Layered Transition Metal Thiophosphates as Anodes in Sodium-Ion Batteries:

Evaluation of Electrochemical Properties and Structural Examination of Reaction Mechanisms during Sodium Uptake and Release

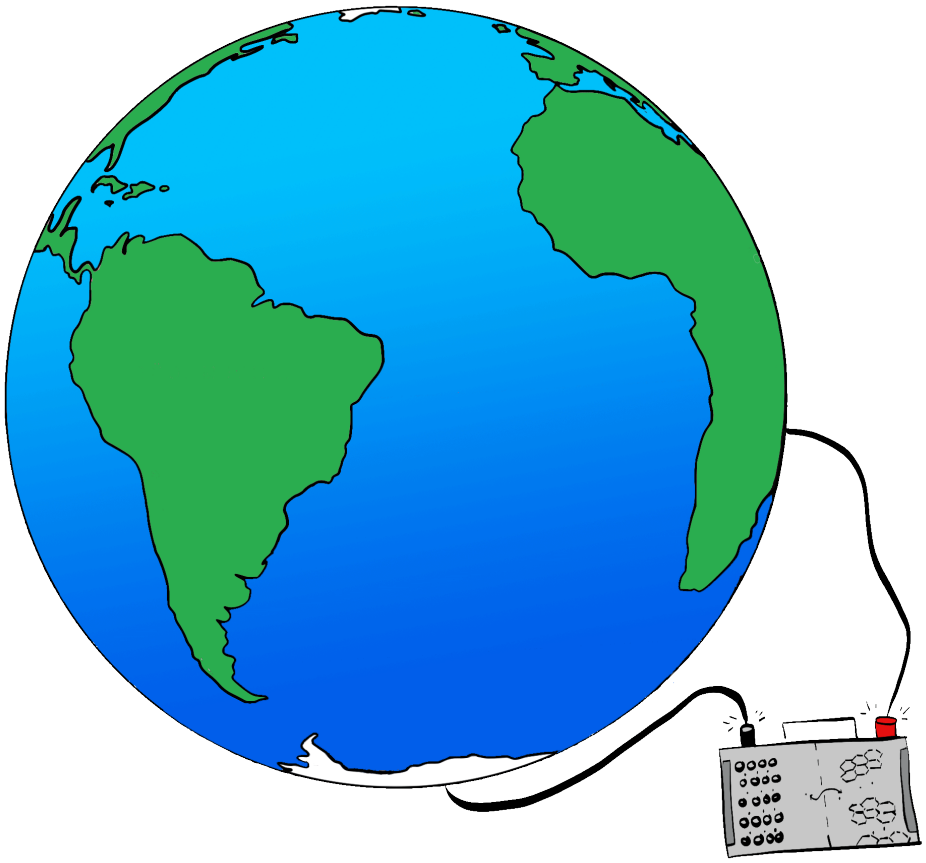

Dissertation submitted to the

Faculty of Mathematics and Natural Sciences of the

Kiel University

for the degree of

Dr. rer. nat.

by

Jonas van Dinter

Kiel, 2022

Referent:	Prof. Dr. Wolfgang Bensch
Korreferent:	Prof. Dr. Norbert Stock
Tag der mündlichen Prüfung:	20.04.2022

Zum Druck genehmigt: Kiel, ..., _____

Der Dekan, Prof. Dr. Frank Kempken

“If you want to assert a truth, first make sure it’s not just an opinion that you desperately want to be true.”

Neil deGrasse Tyson

Abstract

The subject of this thesis is the investigation of the transition metal thiophosphates (MTPs) $Ni_2P_2S_6$, $CrPS_4$ and $CuCrP_2S_6$ as anode materials in sodium-ion batteries (SIBs) with the objective of evaluating their electrochemical performance and understanding the occurring structural changes during sodium uptake and release. Electrochemical characterization was performed using standard galvanostatic and potentiostatic measurements. Besides common characterization methods like X-ray diffraction (XRD), advanced non-standard techniques, such as pair distribution function (PDF) analysis, X-ray absorption (XAS) and solid state nuclear magnetic resonance (NMR) spectroscopy, were utilized for in-depth investigations of structural and electronic changes during discharging and charging. Such a sophisticated approach is necessary, because active materials often transform irreversibly into amorphous phases or nanoparticles upon discharging.

From an electrochemical perspective, it has been described in literature that $Ni_2P_2S_6$ nanosheets represent superior electrode materials in SIBs. Interestingly, this thesis demonstrates that electrodes of the corresponding bulk material provide comparable electrochemical performance. Additionally, the anode materials $CuCrP_2S_6$ and $CrPS_4$ were investigated for the first time in SIBs. The incorporation of Cu^+ cations into electrode materials often affects the electrochemical performance positively. Hence, the potential upside of Cu containing MTP electrodes was evaluated by investigations of $CuCrP_2S_6$. However, only minor advantages were detected in rate capability measurements, whereas long-term performance in fact is inferior to that of $Ni_2P_2S_6$ electrodes. Thus, the anticipated benefits of $CuCrP_2S_6$ are less than expected. Conversely, an excellent overall performance was demonstrated for $CrPS_4$, which additionally does not contain any crucial elements of state-of-the-art electrodes.

From a mechanistic point of view, it was demonstrated that similar reaction pathways occur for different MTPs. During the discharge process, Na^+ ions first intercalate into the layered MTPs, while a transition to intermediate phases takes place in a second step. Finally, the reaction proceeds according to a conversion leading to the formation of Na_2S and metal nanoparticles. Moreover, the loss of structural long-range order was observed after recharging. This thesis disproves the previously assumed formation of Na_xP phases in the discharge step and instead demonstrates a three-step reaction process for the studied MTPs vs. Na. It is noteworthy that each active material generates different intercalation compounds and intermediate phases during discharging. Hence, the reaction pathway follows a similar pattern but does not display a universal reaction mechanism.

Kurzzusammenfassung

Gegenstand dieser Dissertation ist die Untersuchung der Übergangsmetallthiophosphate (MTPs) $Ni_2P_2S_6$, $CrPS_4$ und $CuCrP_2S_6$ als Anodenmaterialien in Natrium-Ionen-Batterien (NIBs). Ziel der Arbeit sind die Bestimmung der elektrochemischen Leistungsfähigkeit sowie detaillierte Erkenntnisse über die ablaufenden strukturellen Änderungen während der Aufnahme und Abgabe von Natrium. Die elektrochemischen Eigenschaften wurden mit galvanostatischen und potentiostatischen Messungen untersucht. Neben Standardmethoden, wie Röntgendiffraktometrie, wurden spezielle Techniken (Analyse der Paarverteilungsfunktion, Röntgenabsorptions- und Festkörper-Kernspinresonanzspektroskopie) für tiefergehende Charakterisierung der strukturellen und elektronischen Zustände eingesetzt. Der Einsatz solcher fortgeschrittenen Methoden ist notwendig, da Aktivmaterialien beim Entladen oft irreversibel amorphisiert werden oder Nanopartikel bilden.

Aus elektrochemischer Sicht wurde bisher angenommen, dass $Ni_2P_2S_6$ Nanoschichten außergewöhnliche Elektrodenmaterialien für NIBs darstellen. Interessanterweise zeigt diese Dissertation, dass Elektroden aus dem entsprechenden Volumenmaterial vergleichbare elektrochemische Leistungsfähigkeiten aufweisen. Außerdem wurden in dieser Arbeit erstmalig die Anodenmaterialien $CuCrP_2S_6$ und $CrPS_4$ in NIBs untersucht. Häufig wird die elektrochemische Leistungsfähigkeit durch den Einbau von Cu^+-Kationen in Elektrodenmaterialien positiv beeinflusst. Daher wurde der potentielle Vorteil von kupferhaltigen MTP Elektroden durch Untersuchungen des Materials $CuCrP_2S_6$ systematisch erfasst. Allerdings wurden nur geringfügig verbesserte Eigenschaften in Bezug auf die Ratenstabilität beobachtet, wohingegen die Langzeit-Leistungsfähigkeit sogar unterhalb der von $Ni_2P_2S_6$ Elektroden liegt. Daher sind die vermuteten Vorteile von $CuCrP_2S_6$ geringer als erwartet. Im Gegensatz dazu wurde insgesamt eine hervorragende Leistungsfähigkeit für $CrPS_4$ nachgewiesen, welches außerdem keine wesentlichen Elemente moderner Elektrodenmaterialien beinhalten.

Untersuchungen bezüglich der zugrundeliegenden Reaktionsmechanismen haben gezeigt, dass vergleichbare Prozesse während der Aufnahme von Natrium für die verschiedenen MTP Materialien ablaufen. Während des Entladens werden zunächst Na^+-Ionen in die Schichten der MTP Materialien interkaliert und in einem zweiten Schritt bilden sich anschließend verschiedene intermediäre Phasen. Schließlich erfolgt eine Umwandlung der Intermediate zu Na_2S und Metallnanopartikeln. Nach dem Wiederaufladen wurde keine strukturelle Fernordnung der resultierenden Produkte detektiert. Diese Dissertation widerlegt den zuvor angenommenen Reaktionsmechanismus, der die Bildung von Na_xP

Phasen voraussetzte, und belegt stattdessen einen dreistufigen Entladeprozess für die untersuchten MTP Materialien vs. Na. Es ist allerdings erwähnenswert, dass sich die während des Entladens gebildeten Interkalationsverbindungen und Intermediate für jedes der untersuchten Materialien unterscheiden. Daher ähneln sich die Reaktionspfade zwar, können aber nicht als gemeingültiger Reaktionsmechanismus für die gesamte Stoffklasse aufgefasst werden.

Table of Contents

1. Introduction

1.1 Motivation

Global warming, caused by unsustainable energy production, and related issues have been discussed for several decades and are among the most popular topics for modern society. So far, some political agreements and treaties between numerous nations have been negotiated to address the imminent climate crisis. The Paris Agreement,[1] which entered into force in 2016, defines the aim of limiting global warming to 1.5 °C above pre-industrial average temperatures. However, energy demands of an ever-growing population will increase over time (Figure 1) and must be covered preferably without increasing greenhouse gas emissions. Therefore, moving energy conversion from fossil towards renewable sources and effectively integrating underlying technologies into the electrical grid is mandatory.[2–4] Nevertheless, the ratio of sustainable energy sources in the total primary energy supply (~2%) is still small (Figure 1; left) compared to the share of fossil fuels (~80%) resulting in annual CO_2 emissions of ~33 Gt in 2018. Due to this dependency on fossil fuels, power generation is one of the largest CO_2 emitting sectors (Figure 1; right) accounting for 40% (coal: 29%; gas: 9%; oil: 2%) of total energy-related emissions directly followed by the transport sector (23%) and emission caused by industrial power demands (23%).[5,6] Furthermore, the global coal fleet alone will add an estimated 175 Gt CO_2 to total emissions between 2018 and 2040 (assuming an average plant lifespan of 50 years), although a steady decrease of emissions from coal burning (to ~60% of 2018s emissions) is already taken into consideration.[6]

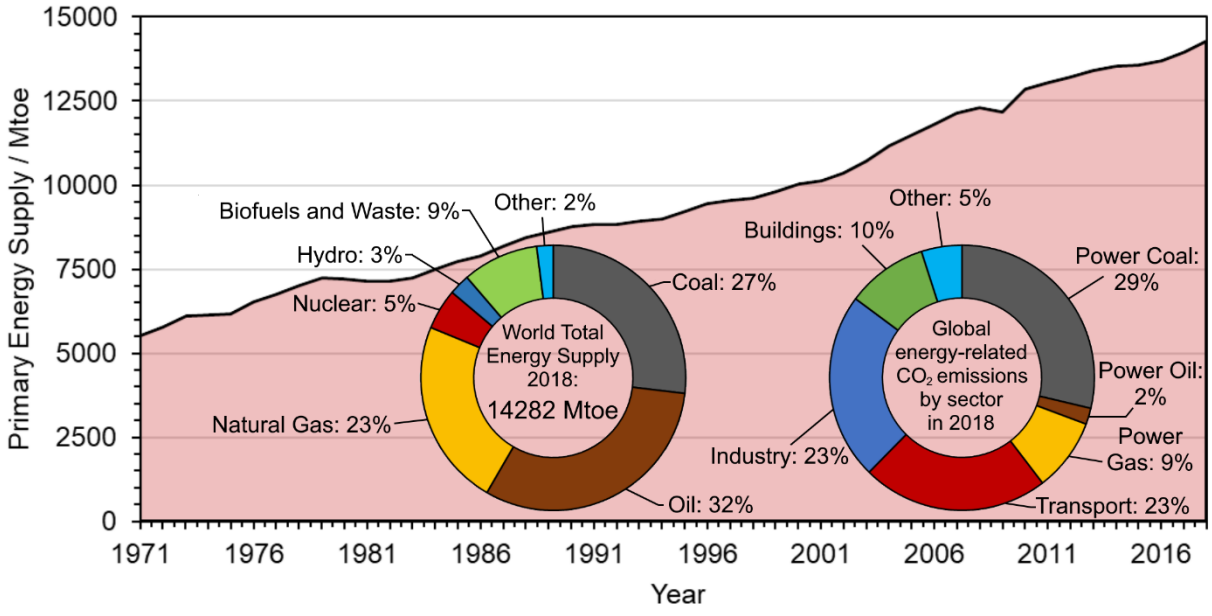

Figure 1. World total primary energy supply by source between 1971 and 2018. The pie charts represent the share of global energy supply by source in 2018 ("coal" includes peat and oil shale; "other" includes major renewable sources like solar, geothermal, wind and tide/wave/ocean; toe = ton of oil equivalent = 10^7 kcal) (left) and percentage of CO_2 emissions by sector in 2018 (right). With alterations from [5,6].

These statistics highlight that transitioning from fossil to renewable energy sources is not only urgent but inevitable as well. While the effective use of some sustainable energy sources like geothermal or hydro energy is limited to certain locations (*e.g.* places with volcanic activity), other renewables, such as wind, tidal or solar energy, are subject to natural fluctuations (*e.g.* weather and seasons). To cope with these intermittent energy sources, it is essential to find suitable energy storage systems (ESS) that are integrated into smart grids and are able to efficiently store excess energy and release it when needed on a large scale and at low costs, preferably built from sustainable materials.[2–4,7,8] The most obvious and promising candidates for ESSs are Lithium-ion batteries (LIBs), which are well developed and already power the majority of portable electronics and electrical vehicles. However, it is widely discussed within the scientific community whether LIBs are the right choice for stationary, large-scale ESS and the prevailing opinion is that batteries based on sodium are better suited for this type of application.[3,4,7–9] Although lithium is not particularly scarce, it indeed is unevenly distributed and mainly accessible from remote regions (Andean states) giving rise to often controversially discussed geopolitical issues regarding resource supply.[2,3,7–10] Establishing another industrial sector (*i.e.* large-scale energy storage) based on LIBs would unavoidably lead to accelerating depletion of Li (and other critical resources) making its integration into large-scale energy storage very expensive and potentially economically unfeasible.[3,7,8,10,11] In contrast, sodium has a substantial natural abundance and is distributed globally leading to easy access at lower price. Moreover, the electrochemical properties of Na are very similar to those of Li. Therefore, Sodium-ion batteries (SIBs) are viewed as the most promising alternative to LIBs for the future usage in large-scale energy storage applications.[2,3,7,9] For this purpose, the established operating principle of LIBs (intercalation) was adopted and applied to SIBs. So far, many possible cathodes have been investigated, which demonstrated appropriate electrochemical performance.[3,4,7,8,12,13] However, finding suitable anodes for intercalation-based systems is far more demanding. Graphite, which is the anode material of choice for state-of-the-art LIBs, does not form sodium-rich intercalation compounds and therefore shows very poor electrochemical performance as anode material in SIBs.[7,14–17] Hence, the identification of new anode materials for SIBs providing high specific capacities and long-term stability is crucial. Ideally, new materials should be composed of abundant, sustainable and inexpensive elements. For that purpose, especially anode materials that undergo so-called conversion reactions or alloy formation have gained intense research attention, due to the high specific capacities and energy densities provided by these multi-electron reaction mechanisms.[3,7,18–20] So far, numerous types of promising anode materials have been studied for the usage in SIBs.[21–29] However, huge volume expansions and voltage hysteresis between the charge and discharge process are the biggest challenges that need

to be addressed before conversion-based batteries can be used efficiently.[7,9,18-20,30] To overcome these challenges, it is imperative to study the origins of these issues. Accordingly, the investigation of underlying reaction mechanisms of a particular material is a vital starting point for a deeper understanding.

1.2 Objective of the Thesis

This thesis focuses on the detailed investigation of different active materials as anodes in SIBs. For this purpose, several transition metal thiophosphate (MTP) compounds were identified as suitable candidates based on their high theoretical specific capacities on the assumption of a full conversion reaction. Until now, research of these compounds as active materials has been focused primarily on electrochemical performance or has been based on LIBs when the reaction mechanism was the objective of investigations.[31–37] Thus, data related to the underlying reaction mechanisms in SIBs is scarce and often speculative.

Here, MTP compounds were synthesized via chemical vapor transport reaction followed by structural characterization of the materials and investigation of their electrochemical properties as anodes against sodium. Additionally, investigations regarding the electrochemical reaction were carried out to get a deeper understanding of the underlying reaction mechanisms during discharging and charging. As electrochemical reactions in SIBs often generate amorphous, nanocrystalline and/or highly defective reaction products, approaches that are more sophisticated are required to address the ongoing reactions. Therefore, various standard and non-standard characterization methods, such as X-ray diffraction (XRD), pair distribution function (PDF) analysis, X-ray absorption (XAS) and solid state nuclear magnetic resonance (NMR) spectroscopy, were applied in an effort to correlate electrochemical properties and behavior with actual reaction steps and products during sodium uptake and release.

2. Scientific Background

2.1 The Rocking Chair Battery

2.1.1 Important milestones leading to the commercialization of Lithium-Ion Batteries

The rechargeable so-called “rocking chair battery” was developed by Whittingham, Goodenough and Yoshino and was commercialized by Sony in 1991.[38–42] It quickly became one of the most important technologies of the past decades[41–43] and even awarded its developers the Nobel prize in Chemistry in 2019.[44] However, first attempts to develop rechargeable LIBs were undertaken already in the 1970s. At that time, the newly proposed concept of using TiS_2 as positive intercalation electrode against metallic Li as anode led to an increasing focus on the development of a rechargeable LIB, although the new system quickly encountered several deficiencies.[38,40,42,45] Dendritic growth of metallic Li on the anode causing short-circuits and consequently internal heating, risk of spontaneous ignition or explosion posed severe safety issues.[42,46–48] Additionally, it was found that cathodes based on oxides were yielding higher energy densities, which eventually led to the identification of Li_xMO_2 (with M = Co, Ni) and $Li_xMn_2O_4$ as promising cathodes in the early 1980s.[39,42,45,49] At about the same time, it was suggested that dendrite formation could be prevented by using intercalation compounds as anodes instead of metallic Li.[42,50,51] For this purpose, graphite emerged as promising intercalation anode, because it was able to intercalate Li at low electrochemical potentials. Nonetheless, a variety of optimizations to the carbonaceous anode, the electrolyte and the overall cell design were necessary before a commercial product was realized.[40,42,45,52] Finally, the first Lithium-ion battery was commercialized in 1991 based on the $LiCoO_2$/C system. The successful adaption of graphite as anode was a major breakthrough at this point, because it prevented safety issues related to dendrite formation during cycling. Additionally, the electrochemical potential of the Li (de)intercalation is high for $LiCoO_2$ (LCO) and low for graphite leading to high cell potentials and energy densities.[39,42,52,53] From then on, LIBs were successively integrated in all major battery-related areas and are the most frequently used technology for powering mobile applications and portable devices today. This success was made possible due to the continuous research on rechargeable batteries, which led to steadily increasing energy densities.[42,43,45,54,55]

2.1.2 Operating Principle

The name “rocking chair battery” is often used to describe the concept of LIBs, because the ions shuttle back and forth between the anode and cathode in a rocking fashion.[53,54] The operating principle of commercial LIBs is based on reversible intercalation reactions, where Li ions are intercalated and deintercalated at the anode and cathode during charging and

discharging.[30,43,53,56,57] The general battery setup (Figure 2) consists of a positive and a negative electrode, which are connected electrically through an external circuit but spatially are separated by a polymer membrane. This separator is permeable to ions and soaked with a liquid electrolyte enabling ion exchange between the electrodes, while forcing electrons to move through the external circuit.[45,56,58] The electrolyte usually consists of a solution of $LiPF_6$ in mixtures of different alkyl carbonates.[43,47,56–59] Commonly-used alkyl carbonate mixtures are ethylene carbonate (EC)[42] mixed with *e.g.* either dimethyl carbonate (DMC),[43,47,57,59] diethyl carbonate (DEC)[56,57,59] or ethyl-methyl carbonate (EMC).[57,59] Li-ion batteries, such as the $LiCoO_2$/C system, are assembled in a discharged state and therefore have to be charged before usage.[45,53,57] Thus, in the charged state, the graphite anode is intercalated with Li (LiC_6),[47,57,60] while the LCO cathode is partially deintercalated ($Li_{1-x}CoO_2$; with x = ~0.5).[7,43,45,61]

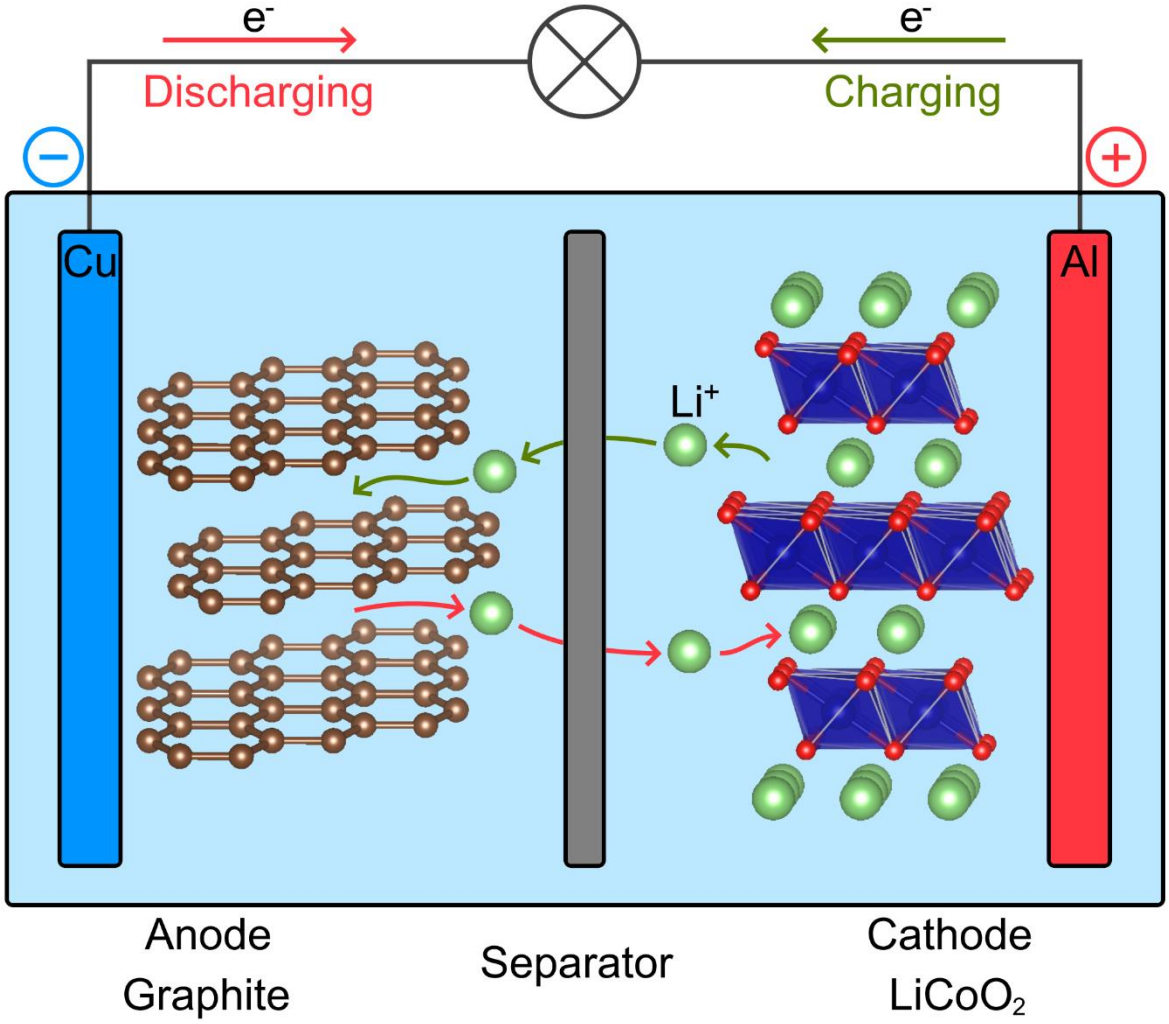

Figure 2. Exemplary depiction of a commercial lithium-ion battery LCO/C system. With alterations from [45].

During discharging, Li is removed from the layered structure of the graphite anode and moves through the electrolyte and separator to the cathode, where the Li^+ ions are

intercalated into $Li_{0.5}CoO_2$. Meanwhile, electrons move through the external circuit from the anode to the cathode, thereby causing electric current and reducing Co^{4+} to Co^{3+} at the cathode. After discharging, the starting materials $LiCoO_2$ and graphite are recovered. During charging, this process happens in reverse (eqs. 1 & 2).[7,39,43,47,57,58]

Anode reaction:
$$xLiC_6 \underset{charge}{\overset{discharge}{\rightleftharpoons}} xC_6 + xLi^+ + x\,e^- \quad (1)$$

Cathode reaction:
$$Li_{1-x}CoO_2 + xLi^+ + x\,e^- \underset{charge}{\overset{discharge}{\rightleftharpoons}} LiCoO_2 \quad (2)$$

As rechargeable batteries work on the prerequisite that electrons pass through an external circuit, it is necessary that the electrolyte does not transport electrons. However, most electrolytes accept electrons at least to some extent leading to different reduction and decomposition processes within the electrolyte solution.[55,62] The products of this process are mostly solids, which accumulate predominantly on the surface of the anode resulting in the formation of the so-called solid electrolyte interphase (SEI).[55,63] The decomposition of the electrolyte usually sets in at low and very high potentials (vs. $Li|Li^+$).[55] A common threshold for SEI formation at the anode is below ~0.8 V for electrolytes containing $LiPF_6$ and/or EC.[64–66] However, the electrolyte decomposition potential depends on many other parameters,[55] such as the exact electrolyte composition (*i.e.* type of solvents and conducting salt)[57] or the applied current rate.[67] The precise constitution of the SEI also strongly depends on the electrolyte solution itself, but normally fractions of both the solvent and the conducting salt are decomposed resulting in the presence of inorganic and organic SEI compounds.[55,57,62] While the SEI formation prevents further reduction of the electrolyte, it enables alkali metal ions to pass through unimpededly.[55,63,68] This process resembles a kinetic stabilization against further electrolyte decomposition, thus enhances long-term cycling stability.[55,62] Another advantageous effect of SEI formation is that co-intercalation of solvents is prevented, which would otherwise lead to exfoliation of the graphite layers. Therefore, the formation of a stable SEI generally is considered beneficial for the performance of a battery.[55,62,66] However, it is noteworthy that SEI formation requires extra electrons, while irreversibly consuming a portion of the cyclable lithium, causing high irreversible capacity losses within the first cycles.[69,70]

2.2 Problems of Lithium-Ion Batteries

2.2.1 Cell Limitations

Despite the broad application of this technology and its obvious success, major drawbacks still remain. While graphite can intercalate 1 Li^+ ion per 6 C atoms resulting in a high specific capacity of 372 mAh g^{-1}, the maximal deintercalation ratio of LCO is limited to 0.5 Li per formula unit (f.u.).[18,47,57,71–75] Below this ratio, the structure of $LiCoO_2$ collapses and Li^+ ions can no longer be intercalated reversibly into the host structure.[74,75] Therefore, the upper cutoff potential is limited to 4.2 V resulting in a low specific capacity of merely ~140 mAh g^{-1}.[57,72,74–76] Although the energy densities of LIBs have been increased continuously since its development (mainly due to improvements in cell design), the maximum energy that can be stored by these systems is limited intrinsically.[7,30,43,45,54]

Further problems are related to charging batteries with high currents, *i.e.* fast charging. Besides considerable heat generation and enhanced mechanical stress within the electrodes induced by Li insertion,[77–81] transport limitations of the electrolyte at high currents make fast charging problematic.[79–81] Applying high currents results in a high concentration gradient, where Li-ion concentration is enhanced at the cathode and reduced at the anode surface leading to strong polarization of the electrodes increasing the cathode while decreasing the anode potential. In this case, the overall cell voltage is artificially elevated and the cutoff voltage is reached before the electrochemical reaction is completed. In addition, when the polarization of the anode forces the electrode surface potential below 0 V vs. $Li|Li^+$, the risk of Li plating becomes imminent.[80–85] Other than that, at low temperatures sluggish Li-ion transport within the electrolyte and electrodes causes similar conditions and resembling problems.[80,81,86] While mechanical stress primarily results in decreasing capacities,[77,79,80,85] strong heating and transport limitations might lead to severe safety concerns like gas evolution and the occurrence of short-circuits caused by side reactions within the battery and dendritic growth of metallic Li, respectively. The latter two incidents can ultimately entail serious consequences, such as thermal runaway and self-ignition.[80,81,87–90]

2.2.2 Resource-related Issues

In addition to these intrinsic cell limitations, there are geographically-related challenges on the resource level. The biggest reserves of lithium are located in South America in Bolivia, Chile and Argentina (often called the lithium triangle).[91–94] Major concerns of lithium extraction are excessive freshwater consumption in already dry environments, soil and water pollution and its impact on local biodiversity and human health.[91–93] Furthermore, a steady supply of battery-grade lithium might not be guaranteed due to political instability and national policies of the Andean states.[94–96] The *Salar de Uyuni,* in Bolivia, which is

estimated to be the single richest deposit of lithium worldwide and yet remains untouched,[97,98] serves as good example for this. On the one hand, due to its nationalistic stance on national resources in the past,[94,95] exploitation of lithium is not attractive for foreign businesses in Bolivia,[99] while on the other hand, Bolivia itself lacks the technology to independently and efficiently produce battery-grade lithium from brine lakes.[94] In addition, the brine of the *Salar de Uyuni* exhibits relative low Li and high Mg concentrations, which makes it even more difficult to extract high-grade lithium.[97] Meanwhile, roughly half of all cobalt deposits are situated in the Democratic Republic of the Congo (DRC), which as well gives rise to unstable situations in terms of resource supply.[100-102] But cobalt extraction has to be considered even more critical. It is estimated that 20% of cobalt mining in the DRC is conducted by the small-scale mining sector, which operates under inhumane conditions, *i.e.* child labor and abuse, modern slavery, often working without any precaution or otherwise helpful equipment (*e.g.* digging by hand), and accounts for roughly 13% of the global cobalt supply.[100,103,104] Besides these working conditions, cobalt mining further dramatically impacts the local environment driving forward water, soil and air pollution through disposal of harmful waste into rivers, wilderness and even near residential areas, which severely affects the health of people living and working in this environment.[100,103,105,106]

In order to conduct a sustainable energy transformation, it is contradictory to rely on resources, whose process of extraction and acquisition fail to abide by the *UN's Sustainable Development Goals 2030*.[107] Admittedly, state-of-the-art technology for LIBs shifted from LCO to Ni-rich so-called NCM ($LiNi_{1-x-y}Co_xMn_yO_2$) and NCA ($LiNi_{1-x-y}Co_xAl_yO_2$) cathodes, where a major portion of Co is substituted by Ni and Mn or Al.[108–112] However, one has to assume that this transition is driven primarily by price development and the need for higher energy densities[108–111] rather than by ethical considerations.[112] While these materials indeed deliver higher energy density with lower Co content (more specifically with higher Ni content), the long-term performance deteriorates due to increasing structural instability.[108,110,113,114] Additionally, the existing limitations in terms of energy density remain valid and Co continues to be a necessary component ensuring structural and electrochemical stability of state-of-the-art materials.[75,108,115,116]

Moreover, as a result of extensive use of a variety of metals (transition, light and alkali metals) for building effective batteries, another issue comes in the form of price development of state-of-the-art battery materials, which predominantly are Cu, Ni, Co, Mn, Al and Li. The biggest concerns arise from high and rising prices of metals and supply chain insecurities of scarce or unevenly distributed resources (*i.e.* Li and Co).[2,3,7,11,117] Therefore, battery recycling was proposed and developed in recent years to mitigate the consequences

of resource depletion and negative environmental impact.[2,7,109,117,118] However, depending on the growth of the battery-related industry, recycling programs might not suffice to prevent negative price development and strong fluctuations.[11,15,119] To overcome the obstacles associated with the current state-of-the-art technology, other approaches are worth considering.[3,4,7,11,18,119] It should be clear that no single technology will meet all requirements in every area of application and hence alternative energy storage systems will most likely be used in certain niche applications.[3,4,7] Especially in terms of energy density and resources, the state-of-the-art technology has room for improvement. Hence, the next chapter covers alternative reaction mechanisms exceeding limited capacities of intercalation-based LIBs and the incorporation of Na instead of Li in rechargeable batteries.

2.3 Alternatives to State-of-the-Art Technology

2.3.1 Reaction Mechanism

As discussed in the previous chapter, new active materials ought to address the issue of restricted energy densities. Enhancing the energy density of a battery can be achieved by increasing either the cell voltage or the specific capacity.[18,120] For this purpose, materials undergoing conversion reactions have been studied intensively since the beginning of the 21st century.[30,121] The conversion mechanism enables the transfer of multiple electrons during an electrochemical displacement reaction through a complete conversion of the active material, yielding superior specific capacities compared to state-of-the-art electrodes. During the discharge process of a conversion electrode, a given metal salt/compound, M_aX_b, is reduced by alkali metal ions A^+ to its metallic state, M^0, embedded in a matrix of the corresponding alkali metal compound, A_zX, according to eq. 3. In the discharged state, the metal is usually obtained in the form of nanoparticles. During charging, the process ideally takes place in reverse.[30,41,71,120–123]

$$M_aX_b + bz \cdot A^+ + bz \cdot e^- \rightleftharpoons a \cdot M^0 + b \cdot A_zX \quad \text{(A = Li, Na)} \tag{3}$$

, with z being the charge of the anion X and M representing a metal (cation).

By comparing $LiCoO_2$ to the comparable conversion material CoO, the advantage of conversion over intercalation reactions becomes clear. While LCO shuttles a mere 0.5 e^- per f.u. (~140 mAh g^{-1}) during charging and discharging,[18,57] CoO is able to deliver 2 e^- per f.u. upon complete reduction yielding a high specific capacity of ~715 mAh g^{-1}.[18,121,123] However, the total amount of transferred electrons is not the only crucial factor in terms of energy density. The molar mass of the active material also plays an important role.[120,122,123] As described by Faraday's law, the theoretical specific capacity (total charge per unit of mass; gravimetric capacity) is proportional to the electron transfer, while being reciprocal correlated with the molar mass (eq. 4).[18,120,122–124] Therefore, in

search of new active materials, these two factors have to be considered together since high electron transfer or low molar mass alone does not guarantee high specific capacity or energy density.

$$Q_{spec} = \frac{x \cdot F}{M} = \frac{I \cdot t}{m} \quad (4)$$

, with x being the amount of transferred electrons, M the molar mass, F the Faraday constant, I the electrical current, t the time, m the mass and Q_{spec} the specific capacity.

Besides other promising battery concepts like alkali metal-air or alkali metal-sulfur, each of which having their own specific challenges,[125–130] especially conversion-type batteries based on alloying reactions are studied extensively.[27,131–135] The basic idea is that every metal, which is able to form alloys with Li or Na can act as electrode material for these batteries according to eq. 5.[20,120,136,137]

$$M^0 + xA^+ + xe^- \rightleftharpoons A_xM \qquad (A = Li, Na) \quad (5)$$

The most noteworthy electrode materials for this type of reaction are silicon and phosphorus for LIBs and SIBs, respectively. Both materials provide extraordinary high theoretical specific capacities (*i.e.* Si: ~4200 mAh g^{-1} vs. Li; P: ~2600 mAh g^{-1} vs. Na) at low average discharge potentials.[134,138–141] Other suitable elements for alloying reactions include Ge, Sn, Pb, As, Sb or Bi for either Li or Na.[119,120,123,131,132] The reason for the remarkably high specific capacities of alloying materials is the advantageous ratio of electron transfer to molar mass (*i.e.* high electron transfer and low molar mass) according to eq. 4. Furthermore, if the composition of the conversion material is chosen carefully, even combined conversion-alloying reactions may take place. Therefore, first metallic particles are provided by a conversion reaction (eq. 3) followed by alloying (eq. 5), if a suitable element combination is present.[27,120,123,135–137] Moreover, it is assumed that the combination of these two mechanisms has a beneficial impact on the electrochemical performance.[142–144]

Altogether, these alternative reaction mechanisms and concepts are of great interest for an advanced battery technology, because they are able to overcome the intrinsic limitations of intercalation-based state-of-the-art batteries. In addition, the combination of these alternative reactions with materials containing more sustainable elements has a beneficial impact on the overall sustainability of those systems. Therefore, one approach is the utilization of materials that undergo conversion reactions together with the incorporation of sodium as basis of an advanced battery technology.

2.3.2 Sodium vs. Lithium

The success story of LIBs evidences the qualification of Li to be the backbone of modern battery technology. The reasons are the low atomic weight, a small ionic radius (0.76 Å[145]),

which benefits solid-state diffusion and the lowest standard potential of E^0 = -3.04 V[146] (vs. standard hydrogen electrode (SHE)).[3,7,9–11] Despite those excellent electrochemical properties, the situation arising from an ever-increasing demand poses challenges and questions for the future usage of Li as basis of the state-of-the-art technology (see chapter 2.2.2). While resource depletion and price development will most likely exacerbate upon the constantly increasing demand for Li,[2,3,7,8,11,15] it is further questioned, if efforts like recycling programs for LIBs will prevent the consequences of this rising demand (*i.e.* price increase and fluctuations).[11,15,119] Therefore, a different approach to solution is the substitution of Li. For this purpose, the heavier homologue Na is the most suitable candidate, because it has a similar, low standard potential of E^0 = -2.71 V[146] (vs. SHE) and its ionic radius of 1.02 Å[145] is only 0.26 Å larger than that of Li^+. Nevertheless, sodium is also three times heavier than lithium. While the electrochemical properties of Na compared to Li are slightly disadvantageous, its natural high availability all over the globe (~23000 ppm Na vs. 20 ppm Li in the continental Earth's crust)[147] is the biggest benefit of Na, which keeps the prices for raw materials significantly lower than for Li resources.[2,7,9,11,15] These raw materials usually are Li_2CO_3 and Na_2CO_3, whereat Na_2CO_3 by itself is about 100 times less expensive than its lithium analogue. However, the decisive economical advantage over lithium is even more pronounced, when price development is taken into consideration. While the price of Na_2CO_3 increased from $128 in 2010 to $150 in 2019, the Li_2CO_3 price nearly tripled from $5180 to $13000 per metric ton.[148] Besides less expensive raw materials, the utilization of sodium instead of lithium further enables the use of cheaper Al instead of Cu as current collector, which reduces costs even more. The reason is that, unlike lithium, sodium does not alloy with aluminum making it a suitable and inexpensive current collector alternative in SIBs.[2,3,7,9,15]

To summarize, resource and price considerations associated with limited lithium supply in the future are primary driving forces for the development of an alternative battery technology. The choice of sodium is not surprising due to its good electrochemical properties and applicability as the basis of an alternative technology. Although sodium has potential advantages over lithium in some areas, various challenges associated with SIBs have been identified so far. These difficulties have to be addressed and overcome before SIBs become commercially available and a serious alternative to LIBs in certain areas of application.

2.4 Challenges for Sodium-Ion Batteries

2.4.1 Intercalation Materials

The usage of sodium instead of lithium is often rendered disadvantageous in literature by comparing the dramatically lower specific capacity of Na vs. Li. However, this argument is only valid, if the alkali metals are directly compared.[9,15,149,150] In this case and according to eq. 4, pure Li metal delivers a specific capacity of 3861 mAh g^{-1}, while Na metal provides 1166 mAh g^{-1}, which is a discrepancy of ~70%. This difference is solely due to the higher mass of sodium vs. lithium.[9,15] For a more realistic estimate, a comparison of actual electrode materials, such as $LiCoO_2$ and $NaCoO_2$, should be undertaken. For these compounds, the masses of the alkali metal ions only make up a fraction of the total molar weight and therefore the theoretical specific capacity for the sodium containing compound is reduced by not more than ~15%.[9,150] For a full cell system, it is estimated that the specific capacity penalty for SIBs can be even further limited to ~10% through material design (*e.g.* using $Na_{0.5}Li_{0.5}CoO_2$ instead of $NaCoO_2$ to reduce the impact of the inactive portion of the alkali metal).[149] Another important parameter worth considering is the lower operating voltage of SIBs and its impact on the energy density.[9,149,150] When taken into consideration, it is estimated that the total specific energy density of a full cell is lowered by ~18% in SIBs compared to LIBs.[149,150] However, it is noteworthy that these considerations are somewhat simplified, yet draw a more realistic picture in contrast to solely comparing the theoretical specific capacities of the alkali metals. Although lower energy densities might prevent SIBs to become directly competitive against LIBs,[4,7,12] this should not be a severe drawback regarding applications like large-scale ESS, where cost-effective batteries are needed and the weight of devices is less important.[12,151] Besides, the development of suitable anode materials is one of the biggest challenges for SIBs. While graphite is used successfully in LIBs as anode material leading to the formation of Li-rich (LiC_6) graphite intercalation compounds (GICs),[47,57,152,153] electrochemical intercalation of Na results in sodium-poor GICs (NaC_{186}[16] at room temperature; NaC_{64}[14] and NaC_{70}[17] at elevated temperatures) and hence very low reversible capacities in SIBs.[14,16,17,153] The poor electrochemical sodium intercalation properties of graphite are caused most likely by thermodynamic hindrance (*i.e.* Na-rich GICs are energetically unstable and their formation only starts below the Na plating potential)[12,152–156] leaving graphite inapplicable as anode material in SIBs. Therefore, new anode materials providing high and reversible specific capacities, long-term stability and high rate capability have to be identified. Besides good electrochemical properties, new anodes should ideally consist of cheap, abundant and sustainable elements.

2.4.2 Conversion Materials

As mentioned previously, the specific capacity can be increased by using materials that undergo conversion instead of intercalation reactions. However, conversion-based anode materials come with its own issues, which so far have prevented them from becoming commercially competitive. Among the biggest challenges are mechanical issues like high volume expansion due to structural rearrangement of the active material during the conversion reaction and electrochemical problems involving high potential plateaus as well as large voltage hysteresis between discharge and charge plateaus.[18,30,71] Volume expansions of ~10%[18] are common for commercial LIBs as well but are way larger for conversion-based materials. Volume expansions occur in the range of ~15 - 200%[18] for conversion materials, while being particularly large for alloying reactions in LIBs (*e.g.* ~300% for Si anode)[157,158] and even more pronounced in SIBs.[7,18] These extreme volume changes potentially lead to inferior long-term stability due to crack formation and eventually pulverization resulting in contact loss between particles of the active material, which causes partial passivation of the electrode.[3,71,135,159] In terms of the electrochemical issues, unfavorable potential plateaus are responsible for reduced energy densities by lowering the operating voltage of the final cell, whereas large potential hysteresis between discharge and charge curves cause low round-trip efficiency.[18,30,43,71] Solution approaches for mitigating the impact of excessive volume expansion usually include improvements of the electrode design, *i.e.* usage of appropriate binders[160–163] as well as nanostructured and/or composite electrodes with carbonaceous nanomaterials (graphene, reduced graphene oxide, carbon nanotubes *etc.*).[164–168] Regarding the electrochemical challenges, especially improvements directed towards the active material are targeted. On the one hand, unfavorable potential plateaus can be tuned by altering the composition of the active material, because the cell potential increases with the ionicity of the M-X bond.[3,18] On the other hand, the occurring potential hysteresis in conversion materials is one of the most complex challenges and its manifold origins are not fully understood. Nevertheless, it is assumed to be closely connected to underlying asymmetric reaction pathways during discharging and charging, diffusion kinetics, ohmic resistance and overpotentials.[169–174] Using nanostructured materials and modifying electrode designs, *e.g.* via surface engineering, are considered promising solution approaches, but further comprehension of this complex phenomenon is required to finally find appropriate and reliable solutions.[120,171-173]

Overall, there are still many challenges to be solved for SIBs and in particular for battery technology based on conversion materials. However, environmental, ethical and economic reasons might open up the market for sodium-based battery technology in the foreseeable future. The approach of using batteries based on sodium in combination with conversion-

type electrodes even holds potential to outperform the current state-of-the-art technology. This progress will take some time and further research is needed to identify promising active materials as well as to address and solve the above-mentioned challenges. For this purpose, the investigation of the underlying reaction pathways is of great importance and contributes to comprehending the origins of the challenges conversion-based SIBs are facing.

2.5 Metal Thiophosphate Compounds

The first documented reports about members of a new substance class, today called metal thiophosphates (MTPs), can be traced back to the late 19th century.[175,176] Later, the proposed compositions of $M_2P_2S_6$[177–179] and M_xPS_4 (x = 1, 1.5, 3)[180–183] were confirmed. Today, a variety of different thiophosphates with diverse anionic compositions (*e.g.* $[PS_4]^{3-}$, $[P_2S_6]^{4-}$, $[P_2S_6]^{2-}$, $[P_2S_x]^{4-}$ with x = 7-10, $[P_3S_9]^{3-}$, $[P_4S_{12}]^{4-}$, *etc.*) and dimensionalities are known.[184,185] Among these compounds, particularly layered MTPs have been studied thoroughly. Investigations focused on a great number of different topics ranging from electronic[186–189] and magnetic properties[187–193] to electrochemical intercalation[31,32,191–194] and different structural aspects.[195-197] More recently, the exfoliation of MTPs yielding few- or monolayers came into focus. These materials are easily exfoliated because of the strong ionic bonds within and weak van der Waals forces between the layers.[198] The resulting 2D materials are studied extensively often regarding the dependence of physical properties on the number of layers.[199–209] However, with respect to energy storage applications like LIBs and SIBs, especially hypothiophosphates $[P_2S_6]^{4-}$ and orthothiophosphates $[PS_4]^{3-}$ containing 3d metals are considered promising electrode materials. The reason is that their beneficial ratios of theoretically transferable electrons to molar mass results in high theoretical capacities ($Ni_2P_2S_6$: 865 mAh g^{-1}; $CuCrP_2S_6$: 870 mAh g^{-1}; $CrPS_4$: 1015 mAh g^{-1}; according to eq. 4 assuming full conversion). Therefore, the focus of this thesis primarily lies on the 1st row transition metal hypothiophosphates $Ni_2P_2S_6$ and $CuCrP_2S_6$ as well as on the orthothiophosphate $CrPS_4$.

2.5.1 Structure of the Hypothiophosphates $M_2P_2S_6$ and $M^IM^{III}P_2S_6$

In hypothiophosphates the phosphorus is tetravalent within the characteristic $[P_2S_6]^{4-}$ anion, while the metal cations' oxidation states range from I to IV including compounds with mixed cation charge (*i.e.* M^IM^{III} and $M^I_2M^{II}$). Usually, hypothiophosphates crystallize in monoclinic space groups, but in some cases trigonal symmetry is observed as well ($Hg_2P_2S_6$ with triclinic symmetry being the only exception). The most common hypothiophosphates are M^{II} and M^IM^{III} compounds (with M^{II} = Mg, Ca, Sr, Ba, Sc, Mn, Fe, Co, Ni, Zn, Pd, Cd, Hg, Sn, Pb; M^I = Cu, Ag; M^{III} = Sc, V, Cr, In).[177,198,210,211]

The structural framework of hypothiophosphates (Figure 3) is mostly independent of the metal cation and basically identical for all compounds of this substance class.[210,211] The crystal structure is related to the $CdCl_2$ structure type.[178,179,192] The lattice is made of a slightly distorted cubic close-packing of S^{2-} anions, where 2/3 of the octahedral sites of every other layer are occupied by metal cations and 1/3 by P-P dimers (Figure 3a). Each P atom has three adjacent S and one P atom generating the ethane-like $[P_2S_6]^{4-}$ anion. A typical honeycomb arrangement (Figure 3b) is formed as every metal cation within the layer is surrounded by three hypothiophosphate anions.[185,192,210–213] The stacking direction of the layers is usually along the *c*-axis.[179,210,211]

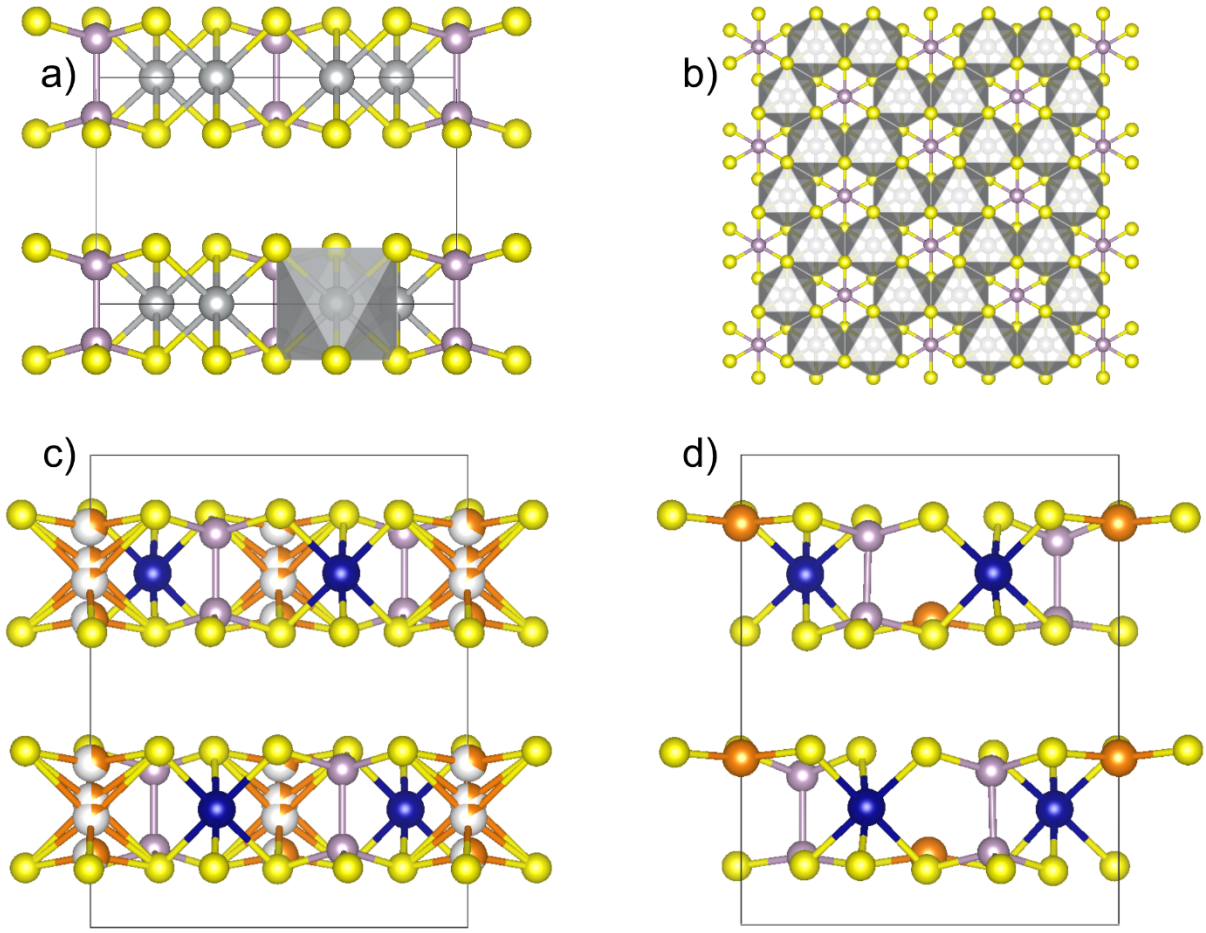

Figure 3. (a, b) Crystal structure of $Ni_2P_2S_6$ (space group: *C/2m*). (a) Unit cell viewed along the *a*-axis showing octahedral coordination of metal cations (grey spheres: Ni^{2+}) and (b) depiction of a single layer viewed along the *c*-axis highlighting the characteristic honeycomb arrangement. (c, d) Unit cells of $CuCrP_2S_6$ (orange: Cu^+, blue: Cr^{3+}) viewed along the *a*-axis. The different metal cation ordering (c) at room temperature (space group: *C2/c*) and (d) below the threshold temperature (space group: *Pc*) are shown. Yellow and purple spheres illustrate sulfur and phosphorus, resp. The structures were created with the software VESTA 3.4.0[218] using crystallographic data from literature.[213,216,217]

While this description is accurate for M^{II} compounds and in general for $M^{I}M^{III}$ compounds as well, slight variations in the cation ordering are observable for $Cu^{I}M^{III}$ compounds. In the structure of these compounds, Cu^+ cations are displaced from the center of the sulfur

defined octahedron depending on the temperature.[210,211,214–217] For $CuCrP_2S_6$, the Cu^+ cations statistically occupy multiple different sites within the octahedron at room temperature (Figure 3c), while being strictly fixed to alternating occupancy between upper and lower sites of the octahedron (Figure 3d) when cooled below a certain temperature threshold.[216,217]

2.5.2 Structure of the Orthothiophosphate $CrPS_4$

The orthothiophosphates exhibit the tetrahedral $[PS_4]^{3-}$ anion, where phosphorus is charged fivefold positive,[198] while the oxidation states of metal cations are usually in the range of I to III. In contrast to hypothiophosphates, M_xPS_4 compounds (with M^{III} = Sc, Cr, B, Al, Ga, In, Bi; M^{I} = Li, Na, K, Ag, Cu; M^{II} = Pd) exhibit a larger variety of crystal symmetries and dimensionalities.[181–183,189,219–226] Due to this structural inhomogeneity, the structure description is based on layered $CrPS_4$ (Figure 4), which crystallizes in the monoclinic space group *C2*. The crystal lattice consists of a hexagonally close-packing of sulfur anions, in which the P^{5+} cations are tetrahedrally coordinated forming the characteristic $[PS_4]^{3-}$ anion, while Cr^{3+} is surrounded octahedrally by sulfur anions (Figure 4a). The resulting CrS_6 octahedra are linked to chains via common edges and connected by PS_4 tetrahedra to layers, which are stacked along the *c*-axis (Figure 4b). It is noteworthy that the sulfur packing of the crystal lattice is slightly distorted, which also results in minor distortion of the tetrahedral and octahedral coordination of P^{5+} and Cr^{3+}, respectively.[183,193]

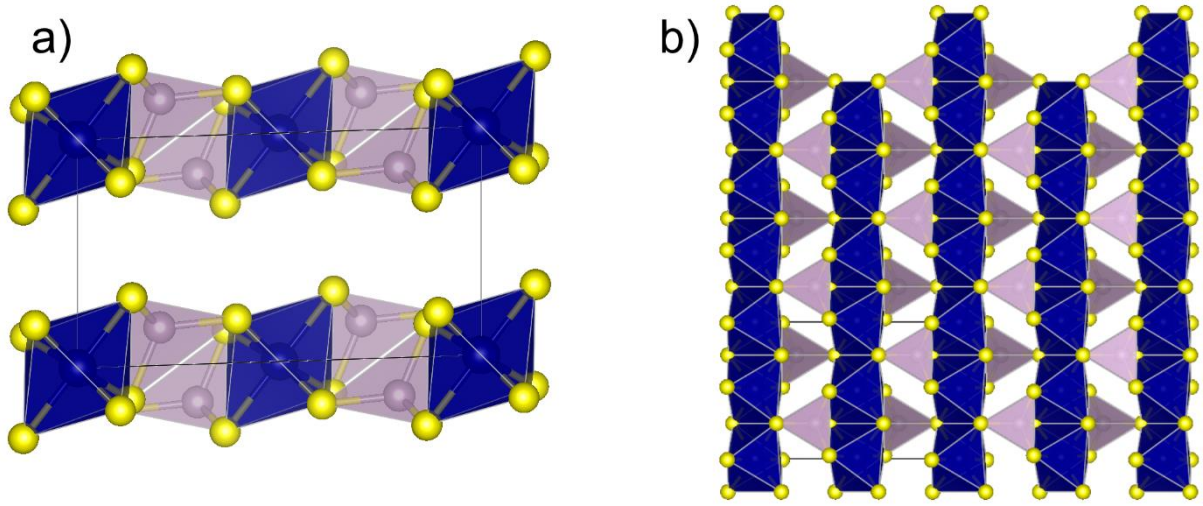

Figure 4. (a) Unit cell of $CrPS_4$ viewed along the *b*-axis and (b) depiction of connected CrS_6 octrahedra to chains (along *b*-axis) and connection of the chains to layers via PS_4 tetrahedra viewed along the *c*-axis. The blue octahedra show the coordination environment of Cr^{3+}, purple tetrahedra indicate the coordination of P^{5+} and yellow spheres form the sulfur lattice. The structure was created with the software VESTA 3.4.0[218] using crystallographic data from literature.[193]

2.5.3 Transition Metal Thiophosphates as Anode Materials

Early investigations of hypothiophosphates as electrodes in LIBs suggested that $M_2P_2S_6$ can reversibly intercalate 3 Li/f.u. generating $Li_xM_2P_2S_6$ ($0 < x < 3$), which was based on the

number of unoccupied octahedral sites in the van der Waals gap.[31,32,192] Accordingly, for the electrochemical intercalation of Li into $Ni_2P_2S_6$, specific capacities of ~216 mAh g^{-1} were reported (508 Wh kg^{-1}; E_{av} = 2.35 V),[31] which is consistent with the theoretical capacity for the uptake of 3 Li/f.u. calculated with eq. 4. Furthermore, some investigations showed that $M_2P_2S_6$ compounds can incorporate up to 18 Li/f.u.[31,32] While the corresponding specific capacities amount to ~1300 mAh g^{-1}, it was suggested that the active material decomposes irreversibly during this process leading to formation of M^0, Li_3P and Li_2S. As a result of the irreversibility of the reaction, it was considered only for primary (non-rechargeable) batteries.[32] However, a reversible reaction including 3 - 6 Li/f.u. was mentioned to be suitable for rechargeable batteries as well.[31,32] Similar to the hypothiophosphates, an intercalation ratio for $CrPS_4$ was estimated based on the number of octahedral interlayer vacancies resulting in Li_xCrPS_4 ($0 < x < 2$). Indeed, these values were achieved by using butyl-lithium, but only low intercalation ratios of $x < 1$ were obtained electrochemically, which made $CrPS_4$ appear to be a poor active material.[193]

More recently, nanosheets of $M_2P_2S_6$ (M = Fe, Co, Ni) were investigated as promising anode materials in LIBs and SIBs. While achieving high and reversible capacities, only few attempts to elucidate the reaction mechanism in LIBs were conducted and the obtained capacities were assigned to the generation of metallic nanoparticles, Li_2S and Li_3P.[33,36] Additionally, no investigations were undertaken to obtain details of the reaction mechanism in SIBs and an analogous process generating Na_2S, Na_xP ($x \leq 3$) and M^0 was assumed.[33] However, due to the distinct discrepancy between specific capacities reported for LIBs and SIBs,[33] it is very likely that the underlying electrochemical reactions are not equal. Hence, in-depth investigations of the sodium uptake mechanism of $Ni_2P_2S_6$ were conducted in the context of this thesis. Moreover, previous studies compared the electrochemical performance of bulk and nanosheet electrodes for the application in LIBs,[36] but only nanosheets or otherwise modified samples of $Ni_2P_2S_6$ were investigated in SIBs,[33] while no data was gathered for the bulk material.

Regarding $CrPS_4$ and $CuCrP_2S_6$, no investigations of the electrochemical performance as conversion electrode and of the corresponding mechanism of sodium uptake and release have been performed until now. Additionally, especially copper containing materials, such as $CuCrP_2S_6$, are of interest for application as active materials. Cu often is extruded from the host material and substituted by Li and Na upon lithiation or sodiation, respectively. As a result, metallic Cu nanoparticles or dendrites are generated in early discharge states,[227-233] which potentially enhances the intrinsic electrical conductivity of the electrode.[229,233] Hence, the material choice of $CuCrP_2S_6$ was inspired particularly by these investigations in order to combine the benefits of Cu containing materials with high theoretical capacities of MTP

compounds. In addition, none of the investigated materials contain critical Co, which indeed should be avoided when conducting research on new active materials for batteries due to its precarious mining conditions and negative influence on the environment.

3. Methods

In order to obtain detailed information about the complex reaction mechanisms occurring during sodium uptake and release in SIBs, usually a combination of different characterization methods is necessary, often requiring various non-standard techniques. Therefore, the fundamentals of non-standard methods applied in this thesis, *i.e.* pair distribution function (PDF) analysis, X-ray absorption spectroscopy (XAS) and solid state nuclear magnetic resonance (NMR) spectroscopy, are discussed here. Further information about the applied standard methods, programs, devices and experimental details can be found in chapter 4.

3.1 Pair Distribution Function

While X-ray diffraction is a very powerful method yielding information about the averaged long-range order of crystalline materials via detection of Bragg reflections, this technique fails when the examined compounds are disordered or do not possess structural periodicity. Amorphous, nanoscopic or strongly disordered solids often exhibit only short- and medium-range order resulting in broadening or absence of Bragg reflections in XRD experiments.[234-237] Therefore, complementary total scattering methods were developed enabling extraction of information from diffraction patterns without Bragg reflections. This is possible because information about the local and medium-range order can be extracted from the weak diffuse scattering within the background of diffraction patterns.[234–236] Extracting those information from total scattering experiments is done by converting the collected data into the so-called pair distribution function (PDF), which translates the structural information from reciprocal (*Q*) space into a real space histogram of bond lengths between pairs of atoms.[234,235,238] However, the collected total scattering data usually contains additional diffuse scattering information from various sources, such as the sample holder, air scattering and contributions from the instrument. In order to account for these contributions to the PDF, an empty sample holder is measured to obtain a background pattern, which then is subtracted from the collected patterns of the samples.[238,239] Besides data corrections regarding the impact of the experimental setup and other undesired contributions (*e.g.* Compton scattering, fluorescence), further processing of the data is necessary (Figure 5). On that account, the corrected data is normalized with respect to the total scattering cross-section of the sample, *i.e.* the squared average atomic form-factor $\langle f(Q)\rangle^2$ (for X-ray experiments), yielding the structure function *S(Q)*. Finally, the pair distribution function *G(r)* is obtained by Fourier transforming *S(Q)* from reciprocal to real space (eq. 6), with *G(r)* representing the probability of the presence of an atom being the distance *r* away from another atom in the real space:[234–236,238,239]

$$G(r) = \frac{2}{\pi}\int_{Q=0}^{Q_{max}} Q[S(Q)-1]\sin\big(Q(r)\big)\,dQ \tag{6}$$

, with Q being the magnitude of the scattering vector.

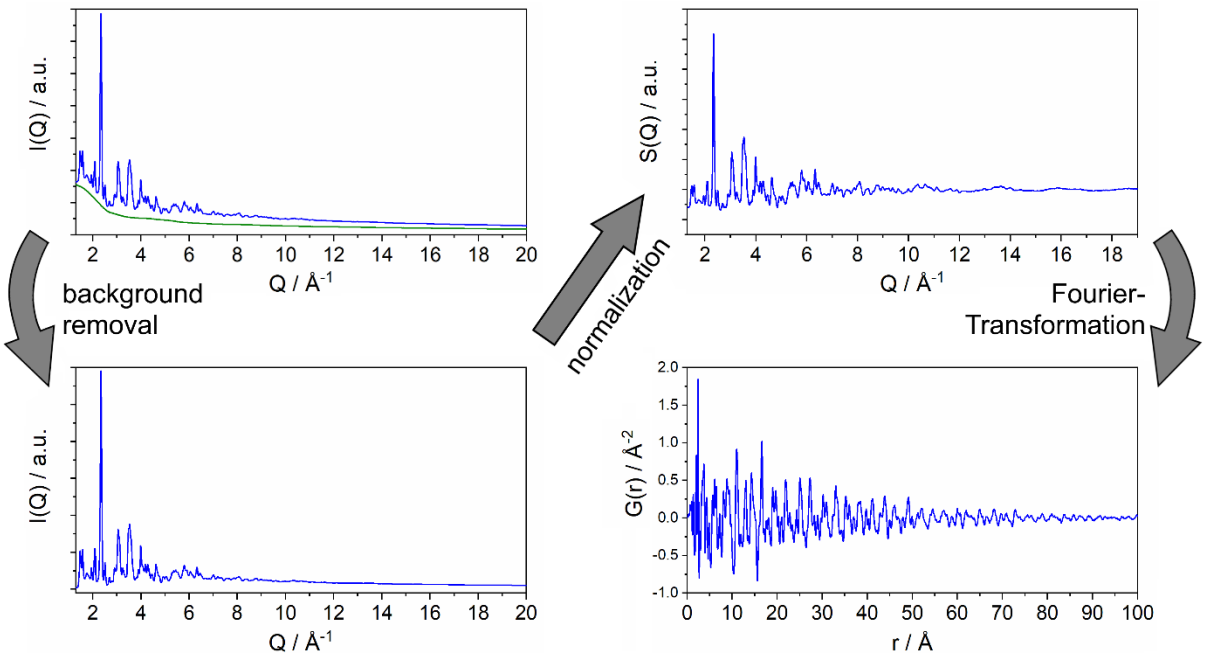

Figure 5. Exemplary data reduction process including background removal (left), normalization (diagonal) and Fourier-transforming (right). The data was obtained from total scattering experiments of $CrPS_4$ and processed with the software xPDFsuite.[240]

The general measurement setup for total scattering experiments is usually very similar to standard XRD experiments. However, due to the transformation from reciprocal to real space, the resolution of the resulting PDF depends on the range of the measured *Q* space. In order to obtain a sufficiently high resolution in real space, measuring a wide range of *Q* space is necessary, which is achieved by using high energy X-rays or neutrons, as *Q* increases with decreasing wavelength ($Q = \frac{4\pi sin\theta}{\lambda}$).[235,238,239] With a high-enough resolution, distances in the range of adjacent atoms up to medium-range order of ~10 - 100 Å can be characterized using the described method of pair distribution function analysis.[234–238]

3.2 X-ray Absorption Spectroscopy

Similar to PDF experiments, X-ray absorption spectroscopy (XAS) is utilized to investigate the local environment of a sample and is not restricted to crystalline materials either. In contrast, XAS is an element-specific method and therefore more detailed information about the local environment of a given element can be obtained. In general, XAS consist of the X-ray near edge absorption spectroscopy (XANES) providing information about the coordination environment and oxidation state as well as the extended X-ray absorption fine-structure spectroscopy (EXAFS), which gives details about the local structure (*i.e.* distances, number and species of neighboring atoms) of a sample.[241,242] Collecting XAS

spectra requires an intense and energy-tunable source of X-rays, which usually is provided by synchrotron radiation. Because XAS is an absorption spectroscopy, it is based on the Lambert-Beer law:[241]

$$I = I_0 e^{-\mu d} \tag{7}$$

, where I is the intensity after absorption, I_0 is the incident intensity (before absorption), d is the thickness of the sample and μ is the absorption coefficient.

Therefore, the measurement setup (Figure 6a) is built in a way to enable the detection of intensity before and after absorption by the sample (and reference). Additionally, the X-ray energy of the incident beam is increased continuously during the XAS measurement.[241] When the incident X-rays reach energies that are equal to the binding energy of core level electrons, the absorption coefficient suddenly and strongly increases. The resulting pronounced feature in the spectrum is called absorption edge and corresponds to the absorption of the incident X-rays by an electron and its transition to unoccupied electronic states (XANES). When the X-ray energy exceeds a certain energy threshold, the absorbing core level electron is emitted as photoelectron according to the photoelectric effect (Figure 6b) resulting in the presence of a core hole (empty core electron level). After leaving the absorber atom, the emitted photoelectron propagates through the sample as a wave and can be scattered by adjacent atoms. The backscattered waves interfere with the outgoing waves influencing the absorption coefficient of the absorber atom, which causes the extended X-ray absorption fine structure (EXAFS).[241–244] The recombination of the core hole usually occurs extremely fast and does not impact the X-ray absorption. The two main mechanisms of recombination are X-ray fluorescence and the Auger effect (Figure 6c). X-ray fluorescence occurs when an electron from a higher core level emits an X-ray photon when filling the core hole. The energy emitted in this process is characteristic for the absorber atom. When recombination occurs through Auger effect, the core hole is also filled by an electron from a higher energy level, but instead of a photon, a second so-called Auger electron is emitted (with characteristic energy for the absorber atom) into the continuum or out of the sample.[241]

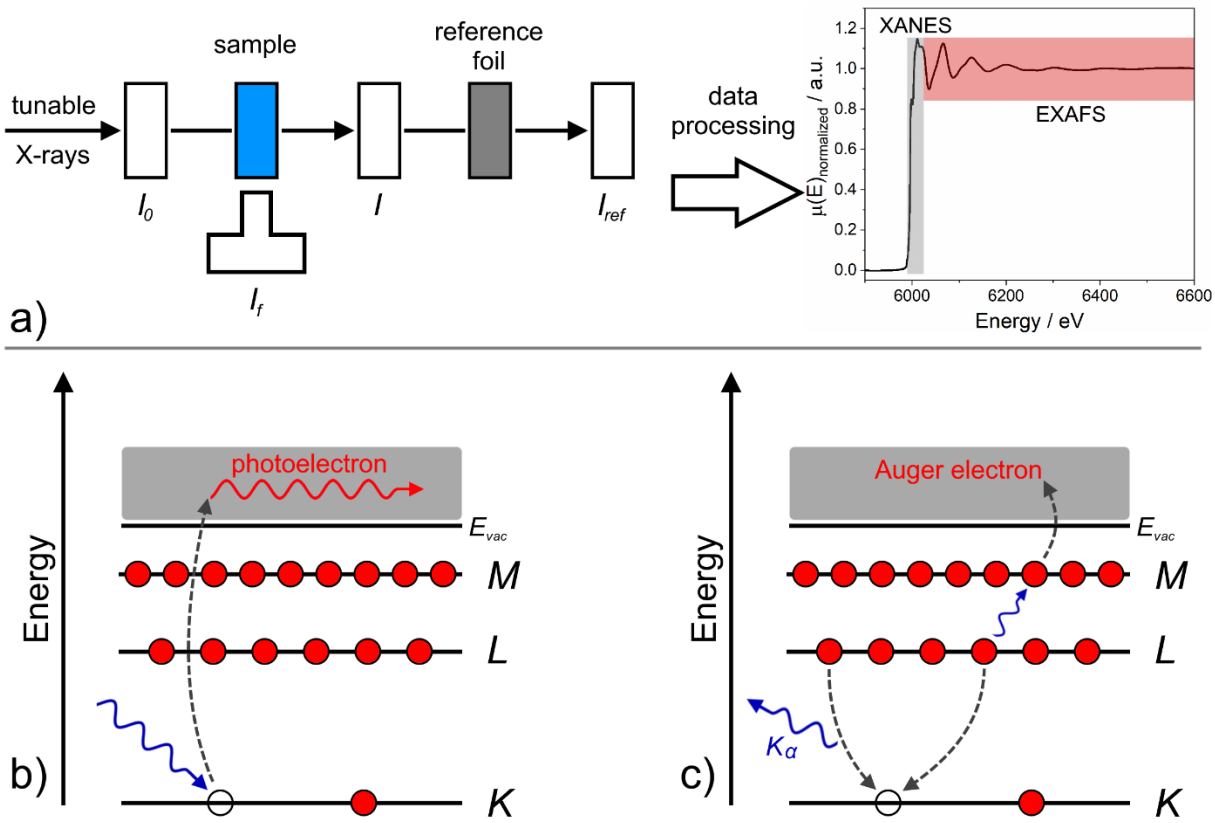

Figure 6. (a) Exemplary depiction of the measurement setup of a XAS experiment. XAS commonly requires collimated, tunable synchrotron radiation. To obtain an X-ray absorption spectrum, the incident intensity (I_0), the intensity transmitted through the sample (I) or intensity of a secondary emission (I_f, *e.g.* fluorescence) and the intensity transmitted through a reference material (I_{ref}) is sampled. (b) Photoelectric effect: X-rays are absorbed by an atom leading to the excitation of an electron, which is emitted from the absorber atom as photoelectron resulting in a core hole. (c) Recombination happens when an electron from a higher energy level moves to the empty core level. The energy difference is emitted via X-rays (fluorescence) or another electron (Auger-effect). With alterations from [241].

In order to extract information from either XANES or EXAFS, processing of the measured data is necessary. For this purpose, the absorption coefficient is retrieved according to eq. 7 and plotted against the incident beam's energy. Afterwards, the data is calibrated to a reference material and normalized with respect to the magnitude of the edge jump to obtain XANES spectra.[241,245] The XANES plot (absorption coefficient vs. energy; $\mu(E)$) is converted into the EXAFS by subtracting a background function (represented by the absorption of an isolated atom $\mu_0(E)$), normalizing by the absorption coefficient of an isolated atom ($\chi(E) = \frac{\mu(E)-\mu_0(E)}{\mu_0(E)}$) and converting the kinetic energy of the photoelectron into wave number ($k = \frac{1}{\hbar}\sqrt{2m_e(E-E_0)}$), which then illustrates the oscillatory part of the absorption coefficient in relation to the wave number.[241,243–245] After applying an appropriate *k*-weighting scheme to account for increasing decay of oscillations at higher *k* values,[241,245] the EXAFS spectrum is Fourier transformed to obtain a partial (*i.e.* element specific) pair distribution function of distances in *R* space. It is noteworthy that the obtained *R* values are not the exact

interatomic distances, because the EXAFS is subject to a phase-shift resulting from the backscattering of the photoelectron wave. Additionally, in order to cancel out abortion effects, which would be caused by the sudden termination of the spectrum at the end of the measuring range, the EXAFS is multiplied by a suitable window function prior to the Fourier transformation.[241]

3.3 Solid State Nuclear Magnetic Resonance Spectroscopy

Nuclear magnetic resonance (NMR) spectroscopy is a powerful standard technique used to characterize the chemical environment especially in fluids and solutions. In order to collect NMR spectra, it is necessary that the nucleus of interest exhibits a nuclear spin ($I > 0$). The fundamental principle of NMR spectroscopy is the splitting of the energy levels of different spin states of a particular nucleus in a strong magnetic field (Zeeman effect) and the corresponding resonance of these energy levels with the external field at certain frequencies.[246] Nuclei with a spin of $I = ½$ (*e.g.* ^{19}F, ^{31}P) normally do not cause major problems, although NMR spectra of these dipolar nuclei are subject to anisotropic interdependencies, such as chemical shift anisotropy (CSA; *i.e.* anisotropic electronic shielding of the nucleus) and magnetic dipole-dipole interactions, causing broadening of the line shapes in the spectrum. In liquids and solutions, however, the broadening due to dipole interaction and CSA is compensated by arbitrary molecular movement, effectively resulting in the same average magnetic field at a particular chemical environment. For quadrupolar nuclei, *i.e.* with a nuclear spin of $I > ½$ (*e.g.* ^{7}Li, ^{23}Na), additional so-called anisotropic quadrupolar broadening becomes effective. This broadening effect is caused by interactions of the quadrupolar moment with the electric field gradient in proximity to the nucleus. For solid state NMR, dipolar coupling and CSA are the primary reasons for line broadening, besides quadrupolar broadening (for nuclei with a spin of $I > ½$).[246–248] In order to account for the line broadening in solids, samples can be rotated rapidly at an angle of ~54.74° with respect to the orientation of the applied magnetic field.[246–250] Spinning around the so-called magic angle cancels out the contributions arising from CSA and dipole-dipole as well as a portion of the quadrupolar interactions.[246–248] This is possible, because the mathematical description of these interaction include angular dependencies containing the term $3\cos^2(\theta)-1$, which becomes zero for $\theta = 54.74°$ ($\cos^{-1}\left(\frac{1}{\sqrt{3}}\right)$) and consequently enhances the resolution of line shapes for dipolar as well as quadrupolar nuclei in solids.[246,247,249,250] Nevertheless, magic angle spinning (MAS) NMR does not completely eliminate the contribution of quadrupolar broadening from the spectrum. Additionally, the spinning of the sample results in the appearance of spinning side bands, which is usually not problematic as their position depends on the spinning speed. Hence, these side bands are easily distinguishable from real resonances.[246-248]

4. Publications

4.1 What happens structurally and chemically during sodium uptake and release by $Ni_2P_2S_6$: a combined X-ray diffraction, X-ray absorption, pair distribution function and MAS NMR analysis

The first study published in the context of this thesis focuses on the application of the layered thiophosphate $Ni_2P_2S_6$ as anode material in SIBs and the investigation of the ongoing reaction mechanism during Na uptake and release. Although previous investigations revealed the promising electrochemical performance for modified $Ni_2P_2S_6$ electrodes in SIBs (*e.g.* nanosheets), neither the electrochemical properties of the bulk material nor the underlying reaction mechanism had been investigated for $Ni_2P_2S_6$ or comparable electrodes in SIBs up to the time of the study presented here. Nevertheless, the ongoing reaction mechanism for SIBs previously had been proposed to be equal to the processes occurring in LIBs. Because this assumption is not necessarily true, the goal here was to shed light on the reaction mechanism of sodium uptake and release. Moreover, the actual merit of $Ni_2P_2S_6$ nanosheet electrodes was evaluated by electrochemical characterization of and comparison to the performance of the bulk material in SIBs.

Electrodes of bulk $Ni_2P_2S_6$ delivered a high reversible capacity of 621 mAh g^{-1} at a current density of 1.0 A g^{-1} after 190 cycles during long-term measurements and an appropriate rate capability of 392 mAh g^{-1} at a current rate of 3.0 A g^{-1} was observed. After switching back to low current rates, a capacity retention of 74% was obtained. Overall, the electrochemical performance of bulk $Ni_2P_2S_6$ is comparable to nanosheet electrodes. Additional electrochemical analysis revealed that long-term cycling induces changes of the reaction mechanism. In order to gain a deeper understanding, the first cycle was targeted for a detailed investigation of the reaction pathway via XRD, PDF analysis, XAS and MAS NMR spectroscopy. During early stages of discharge (0.5 - 3.5 Na/f.u.), an intermediate phase is generated, in which Na is intercalated randomly (staging behavior) into the van der Waals gap of $Ni_2P_2S_6$. Na uptake up to 5 Na/f.u. results in the reduction of Ni^{2+} to Ni^0 nanoparticles and the formation of a second intermediate phase, $Na_4P_2S_6$, which starts as early as after the uptake of 2.5 Na/f.u. Increasing the Na uptake leads to the disappearance of this intermediate after ~9 Na/f.u., while Na_2S is generated between the uptake of 7 - 12 Na/f.u. Despite the postulated occurrence of Na_xP phases during the discharging process of thiophosphates, no signs of such phases were observed and the generation of a P^0 phase as further reaction product in the fully discharged state (12 Na/f.u.) is considered most probable based on the observed specific capacities. Finally, the electrode releases ~11.7 Na/f.u. during recharging and indications of the formation of Ni_3S_2 were found.

However, no phases other than NaF (product of SEI formation) were observed unambiguously, which is due to the nanoscopic and structurally strongly disordered nature of the electrode after completing a full cycle. Therefore, further structural examinations and a detailed prediction of the changing reaction mechanism upon long-term cycling were not feasible. Nevertheless, based on electrochemical data analysis, the successive inactivation of Ni or P is proposed as explanation of the electrochemical behavior.

Reproduced from J. van Dinter, K. Synnatschke, T. A. Engesser, S. Indris, N. Wolff, O. Gronenberg, M. Etter, G. Cibin, L. Kienle, C. Backes and W. Bensch, *J. Mater. Chem. A*, **2020**, *8*, 22401-22415. Permission granted by the Royal Society of Chemistry.

Journal of Materials Chemistry A

ROYAL SOCIETY OF CHEMISTRY

PAPER

Cite this: *J. Mater. Chem. A*, 2020, **8**, 22401

What happens structurally and chemically during sodium uptake and release by $Ni_2P_2S_6$: a combined X-ray diffraction, X-ray absorption, pair distribution function and MAS NMR analysis†

Jonas van Dinter,[a] Kevin Synnatschke,[b] Tobias A. Engesser,[a] Sylvio Indris,[c] Niklas Wolff,[d] Ole Gronenberg,[d] Martin Etter,[e] Giannantonio Cibin,[f] Lorenz Kienle,[d] Claudia Backes[b] and Wolfgang Bensch*[a]

The layered compound $Ni_2P_2S_6$ was electrochemically characterized for application as an anode material in sodium-ion batteries (SIBs). A high reversible capacity of 621 mA h g^{-1} at 1 A g^{-1} was achieved after 190 cycles. The investigation of the complex reaction mechanism of the conversion reaction was performed applying complementary techniques including X-ray powder diffraction, pair distribution function analysis, X-ray absorption spectroscopy, $^{19}F/^{23}Na/^{31}P$ MAS NMR, TEM and nano-EDX. The results highlight that Na uptake for up to 5 Na per formula unit (f.u.) led to reduction of Ni^{2+} to metallic Ni nanoparticles and concomitant formation of an intermediate compound $Na_4P_2S_6$. Increasing the Na content to 12 Na per f.u. generates nanocrystalline Na_2S, which is accompanied by the loss of the long-range order of the pristine sample. In the completely discharged state elemental Ni and Na_2S are present, but in contrast to literature reports, no evidence for the formation of Na_xP phases was found. During the charge process, Ni_3S_2 is formed upon the release of ~11.7 Na per f.u.

Received 11th August 2020
Accepted 1st October 2020

DOI: 10.1039/d0ta07889a

rsc.li/materials-a

1. Introduction

For further development of energy storage devices and clean energy technologies alternatives must be identified beyond the well-established Li-ion batteries (LIBs).[1,2] It can be assumed that LIBs will be the most frequently used storage device in the near future for mobile applications such as cellular phones, laptops or electromobility. Because the amount of electrical energy production by windmills or photovoltaic modules will steadily increase and smart grids will be established, suitable energy storage devices must be developed. In this context, it is questioned in the literature whether Li based electrical storage systems are the best choice. For stationary systems the weight of the devices is less important than for usage in the above mentioned mobile applications. Hence, an alternative for Li is the heavier homologue Na, which came into focus in battery science during the last few years due to its high abundance and low cost. The larger atomic weight, the lower electrochemical potential and the larger radius of Na compared to Li are not severe drawbacks for stationary energy storage devices. A challenge in sodium ion based batteries (SIBs) is the development of a suitable anode material because graphite, which is used in LIBs, has a low specific capacity.[3] An alternative is hard carbon with a specific capacity of about 350 mA h g^{-1} showing good cycle stability. But this material is produced by a high temperature process and the high specific surface area is prone to unwanted side reactions.[4,5] Therefore, research is mainly directed towards identifying anode materials, which provide high specific capacities, good and stable cyclability, and long-term stability and are composed of cheap, abundant and sustainable elements. A large variety of materials was investigated covering *e.g.* carbonaceous materials,[4,6] metal chalcogenides with different compositions and structural dimensionalities,[7–12] alloys[13] or other compounds.[14–16] In particular, binary and ternary metal sulfides were identified as promising electrode materials for SIBs,[17–28] because the M–S bond is less polar than *e.g.* a M–O bond which is beneficial for reversible Na storage. From a mechanistic point of view different types of reactions can be distinguished: intercalation–

[a]*Institute of Inorganic Chemistry, Kiel University, Max-Eyth-Str. 2, 24118 Kiel, Germany. E-mail: wbensch@ac.uni-kiel.de; Fax: +49 431 880-1520; Tel: +49 431 880-2091*

[b]*Institute for Physical Chemistry, Heidelberg University, Im Neuenheimer Feld 253, 69120 Heidelberg, Germany*

[c]*Institute for Applied Materials - Energy Storage Systems, Karlsruhe Institute of Technology, P.O. Box 3640, 76021 Karlsruhe, Germany*

[d]*Institute for Materials Science, Kiel University, Kaiserstr. 2, 24143 Kiel, Germany*

[e]*Deutsches Elektronen-Synchrotron (DESY), Notkestr. 85, 22607 Hamburg, Germany*

[f]*Diamond Light Source, Harwell Science and Innovation Campus, Diamond House, Didcot, Oxfordshire OX11 0DE, UK*

† Electronic supplementary information (ESI) available. See DOI: 10.1039/d0ta07889a

deintercalation, conversion,[29] and alloying.[13,30,31] In a conversion reaction the cations of the electrode material are reduced to the metallic state thus enabling the uptake and release of much more Na atoms than in the intercalation–deintercalation process. In the alloying reaction suitable elements such as Sn, Sb, Si, Ge, Pb and P form alloys with sodium. Another common mechanism is the combination of the conversion and alloying reactions, where first metallic nanoparticles are formed by a conversion reaction followed by alloy formation if a suitable element combination is present, further increasing the specific capacity.

Interesting layered materials for application in batteries are the 1st row transition metal hypothiophosphates (MTPs), $M_2P_2S_6$ (M = Mn, Fe, Co, Ni, Cu, Zn), which were already discovered in the late 19th century[32] and have been widely investigated with respect to their magnetic properties[33–35] and intercalation behavior[33,34,36–38] since 1970.[39,40] MTPs can be classified as M^{II} and $M^{I}M^{III}$ based compounds with M^{II} = Mg, Ca, Sr, Ba, Sc, Mn, Fe, Co, Ni, Zn, Pd, Cd, Hg, Sn, Pb, M^{I} = Cu, Ag and M^{III} = Sc, V, Cr, In.[39,40] M^{II} based MTPs crystallize in the monoclinic space group $C2/m$[34,40–42] whereas MTPs with mixed cations ($M^{I}M^{III}P_2S_6$) also crystallize in trigonal space groups.[39,43] The layers of M^{II} based MTPs are formed by S^{2-} anions in a distorted cubic close-packing providing empty octahedral sites, which are occupied by 2/3 of M^{2+} cations and 1/3 of P–P dimers.[33,39,44,45] Each P atom is surrounded by three S atoms and one P atom forming a $[P_2S_6]^{4-}$ unit similar to the ethane molecule with a covalent P–P bond,[39,43] and the M^{2+} cation is surrounded by three $[P_2S_6]^{4-}$ units leading to a honeycomb arrangement.[43,46,47] Between the layers van der Waals gaps ranging between 3.22 Å and 3.24 Å are observed for the 1st row transition metals.[43]

MTPs came into focus of current research[39,43,48–51] because these materials share many properties with layered 2D transition metal dichalcogenides (TMDCs).[43] The electronic properties of MTPs can be tuned by choosing M leading to bandgaps ranging from 1.3 to 3.5 eV.[52] Due to the layered structure and redox active metal cations, MTPs can be intercalated with cations, making these compounds promising candidates as active materials for lithium ion batteries or sodium ion batteries. For application of MTPs as electrode materials in LIBs or SIBs the three reaction pathways mentioned above may be envisaged depending on the voltage range applied: intercalation–deintercalation, conversion and alloying.[36,48–51,53–58] For Li and Na storage, a reaction pathway (eqn (1)) of the conversion alloying reaction (capacity ≈ 1300 mA h g^{-1} (ref. 37)) was postulated[36,37,43,50] but has not been proven until now.

$$M_2P_2S_6 + 18A^+ + 18e^- \rightarrow 6A_2S + 2A_3P + 2M\ (A = Li, Na) \quad (1)$$

The formal reaction in eqn (1) describes a successive conversion and alloying pathway, whereas the intercalation–deintercalation mechanism should follow eqn (2):[36,37,59]

$$MPS_3 + xLi^+ + xe^- \rightleftharpoons Li_xMPS_3\ (0 \leq x \leq 1.5) \quad (2)$$

For the intercalation–deintercalation reaction, only maximal capacities of around 200 mA h g^{-1} (220 mA h g^{-1} (ref. 59) for $Fe_2P_2S_6$ and 508 W h kg^{-1} (E_{ave} = 2.35 V) (ref. 36) for $Ni_2P_2S_6$) can be obtained, in accordance with values calculated with eqn (2) ($Ni_2P_2S_6$: 216 mA h g^{-1}; $Fe_2P_2S_6$: 220 mA h g^{-1}). Recently MTP nanosheets (M = Fe, Co, Ni) were studied as anode materials for LIBs and SIBs and an improvement of the performance was achieved by intercalating propylamine molecules, but no details on the reaction mechanisms were reported.[50] On the basis of the results of the electrochemical characterization, the formation of Na_2S, Na_xP and metallic nanoparticles was postulated. Assuming that the full conversion (eqn (1)) generates these materials, one would expect specific capacities of 1009 mA h g^{-1} (for Na_xP with x = 1), 1154 mA h g^{-1} (x = 2) and 1298 mA h g^{-1} (x = 3).

In contrast to the general assumption that conversion mechanisms for MTPs are identical in LIBs and SIBs, it is very likely that the mechanisms differ from each other. While the initial capacities found in LIBs[48] support the proposed reaction pathway (eqn (1)), the corresponding values reported for SIBs[50] rather suggest that the proposed mechanism is not applicable for SIBs. For elucidation of the complex reactions occurring during alkali metal uptake and release, characterization by a variety of analytical techniques is required. We and other research groups demonstrated for Li based electrode materials that a combination of methods being sensitive to changes of long-range structural order and of the electronic state is required for understanding the individual steps occurring during alkali metal uptake and release.[60–73]

While a large number of *in situ*, *operando* and *ex situ* studies of reaction mechanisms were performed on Li and Na cathode materials, such experiments are scarce for SIB anodes. Here, we investigated the electrochemical performance of crystalline $Ni_2P_2S_6$ in SIBs and applied *ex situ* X-ray diffraction (XRD), pair distribution function (PDF) analyses, X-ray absorption spectroscopy (XAS), and $^{31}P/^{23}Na/^{19}F$ MAS NMR as well as high resolution transmission electron microscopy with nano-EDX unraveling the step-by-step mechanisms by successive Na uptake.

2. Experimental section

2.1 Synthesis

$Ni_2P_2S_6$ was synthesized *via* a chemical vapor transport reaction. Stoichiometric amounts of elemental nickel (Chempur, 99.99%), red phosphorous (Knapsack AG, 99.9999%) and an excess of sulphur (Chempur, 99.999%) were heated in a quartz glass ampoule, which was sealed under vacuum (10^{-4} mbar). The ampoule was placed in a tube furnace, which was heated within 4 h to 723 K. This temperature was maintained for 24 h and thereafter the temperature was increased to 923 K within 2 h and annealing was carried out for additional 2 weeks. When the furnace reached 923 K, a temperature gradient to 908 K was established in the quartz ampoule to initiate the transport reaction. Excess sulfur was used as the transport agent. Additionally, nanosheets of $Ni_2P_2S_6$ were prepared *via* liquid phase exfoliation from the bulk material (see the ESI for details†).

2.2 Electrochemical tests

Electrodes were prepared by mixing 70 wt% $M_2P_2S_6$, 20 wt% SUPER C65 (Timcal, Switzerland) and 10 wt% polyvinylidene difluoride (PVDF, Solvay, Germany) and suspending the mixture in *N*-methyl-2-pyrrolidone (NMP, Fisher Bioreagens, 99.8%). The suspension was spread on Cu foil using the doctor-blade casting method. After this procedure, the electrode was dried overnight at room temperature and afterwards in a vacuum oven at 333 K for several hours. Spherical electrodes with a diameter of 10 mm (0.6–1.4 mg active material) were punched out and assembled in Swagelok® type cells. The assembly of these cells was performed in an argon glovebox (99.999% Ar, MBraun Unilab) with oxygen and water contents lower than 1 ppm. $M_2P_2S_6$ was used as the testing electrode and a glass fibre filter (Whatman™, United Kingdom) and Celgard® membrane were utilized as separators. A solution of 1 M $NaCF_3SO_3$ (abcr, 98%) in bis(2-methoxyethyl)ether (Diglyme, Acros Organics, 99+%, extra dry) was applied as electrolyte and sodium metal as the counter electrode. Galvanostatic measurements were conducted with an MTI or Neware 8 channel battery analyzer within the voltage range of 3.0–0.1 V at a current density of 1 mA mg^{-1}. A constant current-constant voltage (CCCV) charge mode was applied with a final current of 10% of the initial current. Rate capability measurements were conducted within the same voltage range applying different current densities ranging from 0.2 mA mg^{-1} to 3.0 mA mg^{-1}. Cyclovoltammetric measurements were performed on a Zahner XPOT with a scan rate of 0.1 mV s^{-1} within the same voltage range.

2.3 Materials characterization

X-ray diffraction (XRD) patterns were collected using Cu-K_α radiation (λ = 1.54058 Å) with a PANalytical diffractometer equipped with a 1D PIXcel detector. Elemental analysis was carried out with a vario MICRO cube elemental analyzer (Elementar) using sulphanilamide as a standard material. SEM images and EDX data were collected with a Philips ESEM XL 30 equipped with an EDAX New XL-30 detector. To detect the K-lines of the elements, an acceleration voltage of 20 kV was applied. TEM images were obtained with an FEI Tecnai F30 G^2 microscope (300 kV, field emission cathode) equipped with a Si/Li detector (EDAX system). For *ex situ* nano-EDX measurements samples were transferred without contact to air using a transfer module (double tilt vacuum transfer holder 648; Gatan Inc.). Infrared (IR) spectroscopy was performed with a Bruker IFS 66 infrared spectrometer. Raman spectroscopy was carried out on a Renishaw InVia-Reflex confocal Raman microscope in air under ambient conditions using 532 nm, 633 nm and 785 nm lasers as excitation sources, respectively. Raman emission was collected with a 50× long working distance objective lens in streamline mode and dispersed by a 2400 L mm^{-1} (532 nm) or 1200 L mm^{-1} (633/785 nm) grating with 1% (532 nm) and 10% (633/785 nm) of the laser power (all <25 μW). The spectrometer was calibrated to a silicon reference sample prior to the measurements to correct for the instrument response. For each measurement, 100 spectra were accumulated on 5 different positions and averaged. In the streamline mode, where a larger sample area is probed, no spot to spot variations were observed except for absolute intensities. Additionally, the lateral size and layer number were determined for nanosheets of $Ni_2P_2S_6$ by atomic force microscopy (see the ESI for details; Fig. S1†).

2.4 Calculations

All calculations were performed by using the TURBOMOLE[74] program package. Structure optimizations and calculations of the vibrational frequencies were performed at the RI-PBE0 [75]/def2-TZVPP[76–78] level of theory for $[Cs_2P_2S_6]^{2-}$ and with single point calculations of the electronic structure and calculations of the vibrational frequencies for $[Ni_6S_{18}(P_2S_6)]^{28-}$ at the B3LYP[79,80]/def2-TZVPP and PBE0/def2-TZVPP levels. For the calculations of vibrational frequencies and to prove that the optimized structure is a minimum on the potential energy surface in the case of $[Cs_2P_2S_6]^{2-}$ the AOFORCE module was used, which is included in the TURBOMOLE program package.[81]

2.5 *Ex situ* XRD, PDF, XAS, ^{19}F and $^{23}Na/^{31}P$ MAS NMR

For *ex situ* measurements, samples consisting of 70 wt% $Ni_2P_2S_6$ and 30 wt% SUPER C65 were pressed into pellets and prepared in Swagelok type cells as described above. After the uptake of defined amounts of sodium (discharge), the electrochemical reaction was interrupted and the electrodes were recovered in an argon glove box. To get rid of the electrolyte, the electrodes were rinsed with pure diglyme and dried for one day in the glovebox.

For *ex situ* XRD and PDF analyses, the obtained powders were transferred into borosilicate capillaries with a diameter of 0.7 mm and measured in Debye–Scherrer geometry using high energy synchrotron radiation at beamline P02.1, PETRA III (DESY, Hamburg) at a wavelength of λ = 0.207 Å (60 keV). The sample detector distance (SDD) for XRD experiments was ~1000 mm and the detector used was a PerkinElmer XRD1621 2D detector. Some patterns were collected at different beam time periods and therefore exhibit differences in the background. More precisely, a higher ratio of air scattering for these patterns is present. Hence, a simple spline fit was used to subtract the air scattering. *Ex situ* total scattering data were collected under the same conditions as XRD with a SDD of ~300 mm. The 2D data were processed using DAWN Science.[82] The software xPDFsuite[83] was used to process the total scattering data and to obtain the pair distribution function (Q_{max} = 19 $Å^{-1}$). To account for instrumental contributions to the XRD and PDF data, LaB_6 (NIST 660b) was measured as a standard material. Additionally, to subtract the contribution of the glass capillary, an empty capillary was measured under identical conditions. The single peak fit of the XRD powder pattern was performed using TOPAS Academic 6.0.[84]

For *ex situ* XAS experiments the samples were mixed with carbon and pressed into 10 mm pellets, which were sealed between Kapton foil. XAS spectra were collected at the Ni K-edge at the beamline B18, Diamond Light Source (UK), with a collection time of 3 min at each edge. Each sample was measured three times and these spectra were merged. Energy calibration of the raw data was performed using Ni foil. For an appropriate background subtraction and normalization,

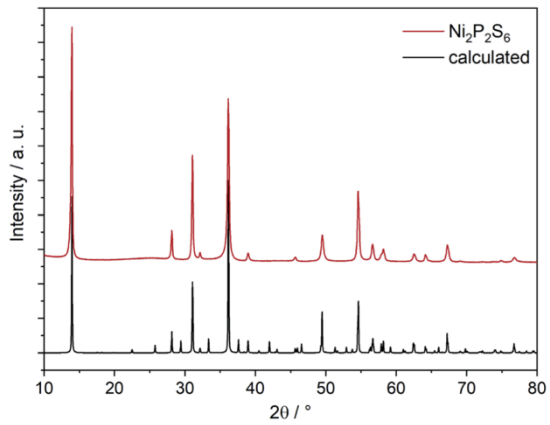

Fig. 1 XRD patterns of $Ni_2P_2S_6$ compared to calculated data from the literature.[44] The data were collected using Cu-K_α radiation (λ = 1.54058 Å).

a linear polynomial fit was used to describe the pre-edge and a cubic polynomial fit was applied to the post-edge region of the absorption spectra. For XAFS data reduction, a suitable background calculated with the Autobk algorithm of the program Athena[85] was used. The k^3 weighting was applied and a fitting range in the k space typically between 3.2 and 12 Å^{-1} was chosen. Afterwards, the previously obtained k^3-weighted $\chi(k)$ function was multiplied by a Kaiser–Bessel window and Fourier transformed into an R space to obtain the pseudo-radial distribution function $|\chi(R)|$.

Ex situ ^{23}Na and ^{31}P magic-angle spinning (MAS) nuclear magnetic resonance (NMR) spectroscopy was performed with a Bruker Avance 200 MHz spectrometer at a magnetic field of 4.7 T corresponding to Larmor frequencies of 52.9 MHz (^{23}Na) and 81.0 MHz (^{31}P). Spinning of the samples was performed in 1.3 mm rotors at 50 kHz. A rotor-synchronized Hahn-echo pulse sequence ($\pi/2$–τ–π–τ–acq.) was used to avoid dead time effects during data acquisition. The $\pi/2$ pulse length was 1.4 µs for ^{23}Na and 0.9 µs for ^{31}P. The recycle delay was 1 s in both cases. Typically, 15 000 scans were acquired for ^{23}Na and 70 000 scans for ^{31}P. The intensities of all spectra were normalized with respect to the sample mass and the number of scans. The spectra were referenced to 1 M NaCl at 0 ppm for ^{23}Na and to H_3PO_4 (85%) at 0 ppm for ^{31}P.

^{19}F MAS NMR was performed with a Bruker Avance 500 MHz spectrometer at a field of 11.7 T, corresponding to a Larmor frequency of 470.6 MHz. Spinning was performed in 2.5 mm rotors at 30 kHz. A single-pulse sequence was used with a $\pi/2$ pulse length of 4.3 µs and a recycle delay of 30 s. 280 scans were acquired and the spectra were referenced to $CFCl_3$ at 0 ppm.

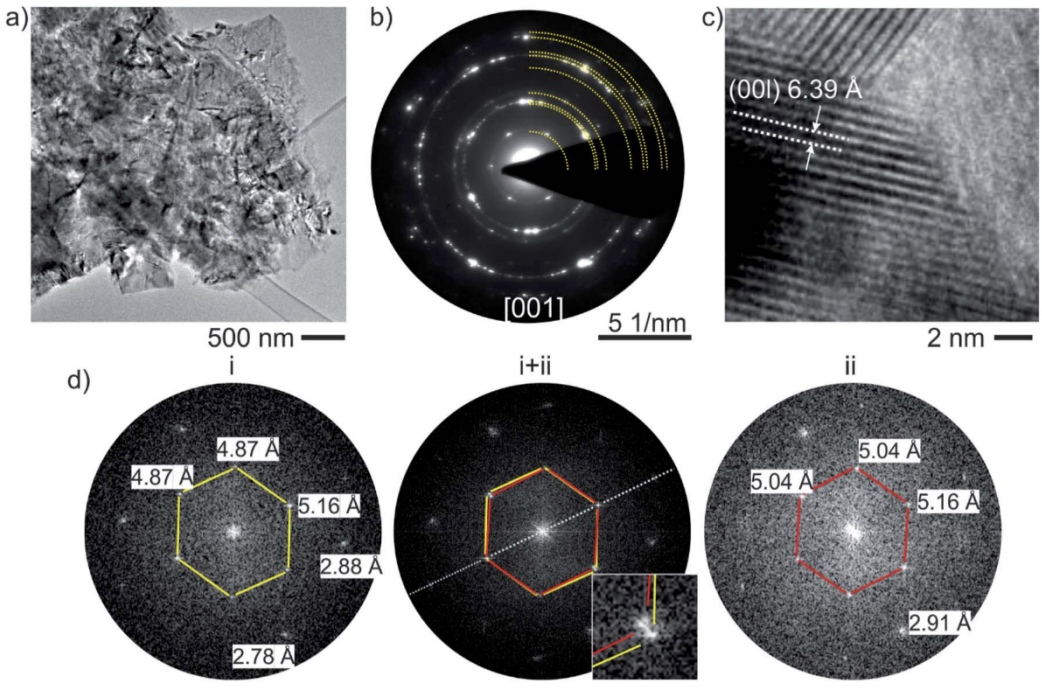

Fig. 2 TEM analysis of pristine $Ni_2P_2S_6$. (a) TEM image showing the plate-like morphology of $Ni_2P_2S_6$ crystals. (b) The SAED pattern exhibits a pseudo-hexagonal symmetry in the [001] orientation. The high intensity reflections are distributed on concentric rings, which are highlighted by the dashed yellow lines. (c) HRTEM study of $Ni_2P_2S_6$ layered crystals oriented along the [100] direction by coincidence. The spacing between the {00l} lattice planes is determined to be 6.39 ± 0.04 Å. (d) Evidence of a distorted variant is indicated by FFT analysis on two neighboring nano-domains (~50 × 50 nm) where the FFT of the domain (i) and (ii) shows metrics of a distorted variant with monoclinic symmetry. The domains are coherently grown together *via* strained lattice planes (5.16 Å).

3. Results and discussion

3.1 Characterization of pristine $Ni_2P_2S_6$

$Ni_2P_2S_6$ crystallizes in the monoclinic space group $C2/m$. Fig. 1 depicts the XRD pattern of the pristine material together with a calculated pattern using data from the literature.[44] Obviously, phase pure $Ni_2P_2S_6$ was obtained. Slightly different intensities as well as extinction of some Bragg reflections are presumably consequences of phenomena such as stacking faults and rotational disorder or twinning. These phenomena are well known for such kinds of materials and were already described in the literature.[86–89] Another possibility of describing the structure of $Ni_2P_2S_6$ is by using hexagonal or trigonal symmetry.[87,88] Accordingly, indications of partially coherent domains with monoclinic to (pseudo-)hexagonal symmetry were found in TEM analysis of plate-like crystals of $Ni_2P_2S_6$ (Fig. 2). The depicted electron diffraction pattern (analysis in Fig. S2†) and the Fast Fourier Transform images (FFTs) indicate nanosized domains by pseudohexagonal [001] patterns according to distorted monoclinic metrics. Heavy structural disorder between the layers is also evident by the streaky and diffuse intensity of second order reflections observable in the FFT (Fig. S3†) of $Ni_2P_2S_6$ observed edge-on.

High-resolution (HRTEM) micrographs (Fig. 2c) display the layered structure of the sample in detail with an interlayer distance of 6.39 Å, measured from the first order FFT reflections which is in agreement with calculated values according to

$$d = c \sin \beta \quad (3)$$

for the monoclinic space group,[44] with c being the length of the unit cell in the stacking direction and β being the monoclinic angle, yielding a value of 6.34 Å for $Ni_2P_2S_6$.

The results of EDX measurements performed on different areas of several crystals (Table S1†) and chemical elemental analysis (Table S2†) yield the composition $Ni_{2.11}P_{1.81}S_{6.10}$ (see the ESI for details†) which is in good agreement with the expected stoichiometry of $Ni_2P_2S_6$. The SEM images (Fig. S4†) show that the sample exhibits a rather unspecific morphology, although the layered nature of $Ni_2P_2S_6$ crystals is observable at the edges of some agglomerates.

The (resonance) Raman and infrared spectra are depicted in Fig. 3. The assignment of the vibrational modes seems to be inconsistent in the literature. For example, bands at 255 cm^{-1}, 561 cm^{-1} and 589 cm^{-1} are assigned to both A_{1g} or E_g by different groups[47,90–94] and different symmetries (*e.g.* D_{3d}[90–93,95,96] or C_{2h}[97,98]) or numbers of modes (6 (ref. 90–93, 95 and 99) or 8 (ref. 47 and 94) Raman active modes for D_{3d} symmetry) are used. Therefore, we decided to perform calculations (Table S3†) to shed light on the nature of the bands observed in the IR and (resonance) Raman spectra. Calculations of the free $[P_2S_6]^{4-}$ anion result in Coulomb explosion accompanied by cleavage of the P–P bond and the formation of two separate $[PS_3]^{2-}$ anions. Therefore, two hypothetical model structures (Fig. S5†) containing the anion were chosen. Based on the crystal structure of $Ni_2P_2S_6$ ($C2/m$), including a D_{3d} ($\bar{3}m$) symmetric $[P_2S_6]^{4-}$ anion, the staggered conformation seemed to be reasonable and was retained in both the presented model structures. To lower the charge and to ensure relatively weak contacts affecting the vibrations two cesium cations were coordinated to $[P_2S_6]^{4-}$ under retention of the D_{3d} symmetry (Fig. S5a,† 2× Cs^+ on C_3). Therefore, an approximately unaffected anion was obtained and Coulomb explosion could be avoided and its structure could be optimized (PBE0/def2-QZVPP) as well as vibrational frequencies could be obtained (Table S3†). To validate the dependency on the size of the basis set, $[Cs_2(P_2S_6)]^{2-}$ was calculated with def2-nZVPP (n = T, Q). As all obtained frequencies differ by no more than 2 cm^{-1}, def2-TZVPP was used for the following calculations.

Additionally, we tried to obtain theoretical data about the anion in its actual crystallographic environment by simulation of a fragment with six nickel(II) ions and additional 18 sulfide anions to saturate the coordination sphere of the metal cations (Fig. S5b†). As this $[(P_2S_6)Ni_6S_{18}]^{28-}$ fragment cut out from the crystal structure of $Ni_2P_2S_6$ is not a minimum structrue, only single point calculations of the energy were possible (PBE0/

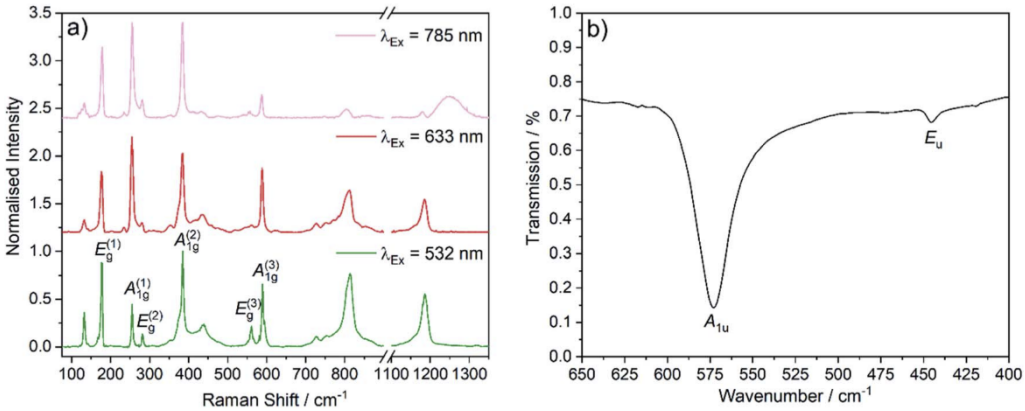

Fig. 3 (a) Resonance Raman spectra with different excitation wavelengths and (b) infrared spectrum displayed between 650 and 400 cm^{-1} of pristine $Ni_2P_2S_6$ at room temperature.

def2-TZVPP and B3LYP/def2-TZVPP) but nevertheless, vibrational frequencies could be obtained and the symmetry of the fragment is D_{3d}. It should be mentioned that only vibrations of the $[P_2S_6]$ unit are discussed, as all other modes represent pseudo lattice vibrations at frequencies below 210 cm^{-1} (one at around 240 cm^{-1}). The experimental bands found in the region below 250 cm^{-1} could indeed also belong to lattice vibrations because their frequencies change significantly, when different metals are included.[92,94,98,99] Therefore, in this area, the assignment was more difficult. In the Raman spectrum for instance, three bands are visible (255, 177, and 133 cm^{-1}) but the calculations gave only two Raman active modes (*e.g.* 219 cm^{-1} (E_g), and 216 cm^{-1} (A_{1g}), with B3LYP/def2-TZVPP). It was reported in ref. 98 that the band at 177 cm^{-1} is depolarized, so it most likely belongs to the less symmetric E_g mode. Based on these depolarisation experiments and the calculations performed here, the bands at 177, 282 and 561 cm^{-1} are assigned to E_g and bands observed at 255, 385 and 589 cm^{-1} to the A_{1g} mode. The band at 133 cm^{-1} corresponds most likely to a lattice vibration.[92]

When D_{3d} symmetry is applied for the isolated $[P_2S_6]^{4-}$ anion, vibrational analysis results in

$$\Gamma_{vib}^{D_{3d}} = 3A_{1g}\,(R) + 3E_g\,(R) + 1A_{1u}\,(\text{inactive}) + 2A_{2u}\,(IR) + 3E_u\,(IR) \quad (4)$$

which is in accordance to the calculated vibrational modes (Table S3†).

Potential overtones (728–833 cm^{-1} (max. 813 cm^{-1}) and 1156–1202 cm^{-1} (max. 1185 cm^{-1})) are typically observed only in a few $M_2P_2S_6$ compounds ($Mn_2P_2S_6$ and $Zn_2P_2S_6$)[94] but clearly seen in the recorded $Ni_2P_2S_6$ spectra in Fig. 3a at all three excitation wavelengths. Surprisingly, the frequencies of the maxima exceed the expected $2A_{1g}$ values ($2 \times 385 = 770$ cm^{-1} and $2 \times 589 = 1178$ cm^{-1}). In the spectrum with an excitation wavelength of 785 nm, an additional broader band is observed at a Raman shift of ≈1250 cm^{-1} corresponding to 870 nm (1.424 eV). Since $Ni_2P_2S_6$ is an (indirect) semiconductor with an experimental absorbance band-edge at 750–800 nm (depending on the thickness[100]), this signal is attributed to fluorescence. The two observed bands in the MIR spectrum of $Ni_2P_2S_6$ (Fig. 3b) can clearly be assigned to E_u (446 cm^{-1}) and A_{1u} (573 cm^{-1}) modes.

3.2 Electrochemical performance

Long-term stability measurements, and electrochemical discharge/charge curves for selected cycles as well as dQ/dV analysis and rate capability measurements of $Ni_2P_2S_6$ are displayed in Fig. 4.

Long-term galvanostatic cycling was performed within a potential range between 3.0 and 0.1 V and a current rate of 1 A g^{-1} was applied (Fig. 4a). After the 3rd cycle the coulombic efficiency reached nearly 100%. A first discharge capacity of 1012 mA h g^{-1} (≈14 Na per f.u.) and a first charge capacity of 842 mA h g^{-1} (≈11.7 Na per f.u.) are obtained. The discharge capacity drops to 575 mA h g^{-1} (≈8 Na per f.u.) within the following 47 cycles. A slight increase of the capacity occurs during further cycling and after 190 cycles a high reversible capacity of 621 mA h g^{-1} (≈8.6 Na per f.u.) was observed.

An initial drop of the specific capacity, which then recovers after further cycling, was also reported for *e.g.* Na–Cu_xS,[17] Na–CuS,[18] Na–$CuCrS_2$ [22] or Na–CuV_2S_4.[23] For the Na–Cu_xS anode, the initial reaction stage is dominated by an intercalation reaction, while at a later stage Na_2S and metallic Cu are formed by a conversion reaction.[17] The unique behavior of the Na–CuS system was explained by a synergistic effect of formation of semi-coherent grain boundaries, stable grains and solid electrolyte interphase (SEI) layers.[18] For the two ternary compounds, extrusion of metallic Cu wires was found at the beginning of discharge, which first do not participate in the electrochemical reaction. After several cycles, most probably Cu sulfides are generated preventing detrimental formation of polysulfides and thus stabilizing the cycling behavior.

For $Ni_2P_2S_6$, the changes of the discharge and charge profiles (Fig. 4b) with increasing cycle number also indicate the formation of different phases accompanied by alteration of the reaction mechanism. The potential of the initial discharge profile drops quickly from 3.0 V to around 1.5 V, where a pseudo-plateau is developed. Afterwards, a drop of the potential occurs leading to a pseudo-plateau at a voltage of approx. 0.75–0.5 V, followed by a steady decrease in the potential until the cell is completely discharged obtaining an initial specific discharge capacity of 1012 mA h g^{-1} (≈14 Na per f.u.). The potential of the initial charge profile rises to approx. 1.7 V where a pseudo-plateau can be observed which is considerably less pronounced than in the discharge profile. After a potential of approx. 1.9 V is reached, the voltage shows a steeper increase than before until an initial specific charge capacity of 842 mA h g^{-1} (≈11.7 Na per f.u.) is reached. Assuming a reaction according to eqn (1), the expected specific capacity of 1298 mA h g^{-1} is significantly larger than the experimentally determined value of 1012 mA h g^{-1}. The experimentally determined irreversible capacity of 170 mA h g^{-1} in the first cycle corresponds to a loss of ≈2.3 Na per f.u. Keeping in mind that a SEI layer is formed on the surface of the electrode material at the beginning of the electrochemical reaction, the experimental value should be indeed larger than the theoretical value.

The observations made here point towards a different reaction mechanism from that proposed in eqn (1) (see Section 3.3). The profiles of the subsequent cycles show clear alterations leading to a loss of the pseudo-plateau in the discharge curve and a shift of the pseudo-plateau starting at 1.8 V in the charge profile of the 10th cycle. For the 50th discharge curve, a pseudo-plateau has developed again at approx. 1.4–1.5 V, which is less pronounced than the plateau of the first discharge. Another pseudo-plateau occurs at about 0.9 V. After reaching 0.8 V the potential drops steadily until the cell is fully discharged. The corresponding charging curve also passes a plateau at 1.9 V, which is more pronounced than the pseudo-plateau of the 10th charge. For the discharge profile of the 100th cycle, the pseudo-plateau at 1.4 V–1.5 V is slightly more evolved than for the 50th, whereas the pseudo-plateau at 0.8–0.9 V has almost disappeared and no significant differences can be identified up to the 100th cycle. A comparison of the discharge curves of the 100th and

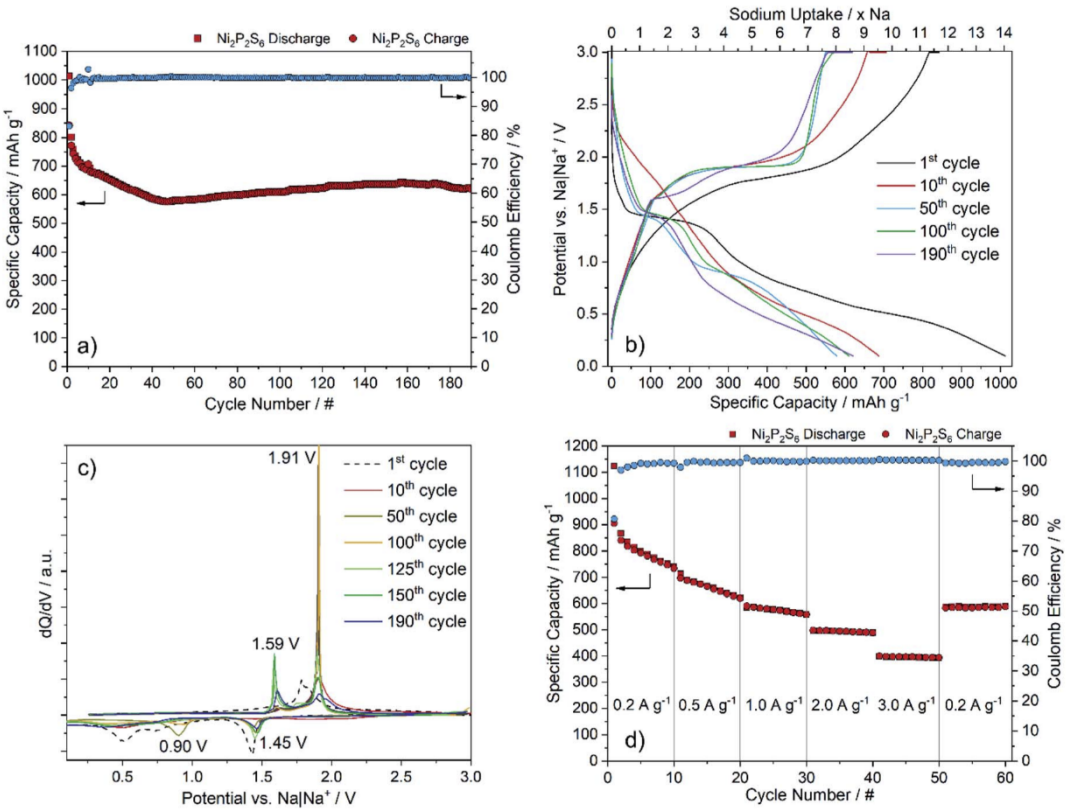

Fig. 4 (a) Electrochemical cycling performance and charge efficiency of $Ni_2P_2S_6$ test cells against Na. A current rate of 1 A g^{-1} was applied within a potential window of 3.0–0.1 V. (b) Discharge and charge profiles of the 1st, 10th, 50th, 100th and 190th cycles of $Ni_2P_2S_6$. (c) dQ/dV analysis of selected cycles. (d) Rate capability at several current rates from 0.2 to 3 A g^{-1} for $Ni_2P_2S_6$.

190th cycles shows that some further alterations occur in the voltage regions 1.4–1.5 V and for 0.8–0.1 V. During charging in the 190th cycle two pseudo-plateaus develop at 1.6 V and at 1.9 V, which are less pronounced compared to those of the 50th and 100th cycles.

The variability of the potential plateaus is clearly seen in the dQ/dV curves (Fig. 4c). The reduction peak at ≈1.4 V in the first cycle shifts to slightly larger potentials during the cycling process, while the less pronounced signals at ≈0.75 and 0.5 V disappear with increasing number of cycles (Fig. 4c, dashed line). The signal for the oxidation process in the first cycle is located at about 1.75–1.85 V and is broad indicating different chemical reactions. These observations are in accordance with cyclic voltammetry (Fig. S6†). Upon further cycling, a new reduction peak at around 1.45 V appears which stays nearly constant at this potential. In the 50th cycle another new reduction peak occurs at 0.9 V, which disappears again upon further cycling. Two oxidation peaks develop during extended cycling which become sharper with the number of cycles first and start to disappear again with increasing cycle number. All these observations indicate changes of the reaction mechanisms during long-term galvanostatic cycling. However, to make a rational assumption on the mechanism in later cycling states, one has to figure out the reaction mechanism of the first cycle to address the amount of lost sodium per formula unit during long-term cycling (see Section 3.3).

Additionally, nanosheets of $Ni_2P_2S_6$ obtained from liquid phase exfoliation were tested, but the electrochemical performance (Fig. S7†) is very poor compared to the bulk sample. The first discharge capacity of 1064 mA h g^{-1} is comparable to the capacity obtained with the bulk material. Like for the bulk electrode the specific capacity first decreases (483 mA h g^{-1}; ≈6.7 Na per f.u.) and then recovers slightly after 100 cycles (510 mA h g^{-1}; ≈7 Na per f.u.). In contrast to the bulk material, the electrodes from few-layered $Ni_2P_2S_6$ nanosheets (~170 nm lateral size, ~8 layers) continuously degrade upon further cycling reaching 227 mA h g^{-1} (≈3.1 Na per f.u.) after 190 cycles. This is in striking contrast to results with $Ni_2P_2S_6$ nanosheets, where the sheet dimensions were controlled *via* the synthesis (200 nm lateral size, 22 nm thickness) which showed a reversible capacity of 450 mA h g^{-1} after 200 cycles at a current rate of 2 A g^{-1}.[50] In the present case, the poor performance may be explained by the poor environmental stability of few layer $Ni_2P_2S_6$ from liquid phase exfoliation as was recently reported.[100] Furthermore, there may be issues with the mechanical stability of the electrodes as frequently observed for liquid-

exfoliated nanosheet networks unless 1-dimensional conductive fillers such as carbon nanotubes are added.[101–103]

The rate capabilities (current rates: 0.2, 0.5, 1.0, 2.0, 3.0 and again 0.2 A g^{-1}) of the $Ni_2P_2S_6$ bulk electrode applied for 10 cycles each are shown in Fig. 4d. At the lowest rate of 0.2 A g^{-1} the specific capacity of 739 mA h g^{-1} after 10 cycles corresponds to ≈10 Na per f.u. A successive increase of the rate leads to decreasing capacities in the 10th cycle: 0.5 A g^{-1}: ≈622 mA h g^{-1}; 1.0 A g^{-1}: ≈558 mA h g^{-1}; 2.0 A g^{-1}: ≈488 mA h g^{-1} and at 3.0 A g^{-1}: ≈392 mA h g^{-1}. Switching back to 0.2 A g^{-1}, the average reversible capacity amounts to 588 mA h g^{-1}. The values correspond to capacity retentions of 79%, 70%, 62%, 50% and 74% in relation to the average specific capacity (792 mA h g^{-1}) of the first current rate of 0.2 A g^{-1}. Within the first 20 cycles, an obvious fading in capacity occurs, which is also present in the long-term measurements (see Fig. 4a) and therefore is no consequence of the applied current rates. The results indicate a good tolerance in terms of cycling stability at higher current rates and a mediocre performance with respect to capacity retention.

3.3 *Ex situ* investigations of $Ni_2P_2S_6$

For the investigation of the reaction pathway of $Ni_2P_2S_6$, electrodes consisting of pressed powder were used instead of electrodes coated on copper foil (see Section 2.5). One has to mention that for these powder cells, different initial capacities were found compared to electrodes deposited on Cu foil. While the electrode on Cu foil showed an initial discharge capacity of 1012 mA h g^{-1}, the value for powder electrodes amounts to 873 mA h g^{-1} (Fig. 5a). These values correspond to an uptake of 14.0 Na per f.u. and 12.1 Na per f.u., respectively. However, as the electrochemical profiles stayed identical for both kinds of electrodes (Fig. 4b *vs.* Fig. 5a), the underlying chemical reaction should be very similar. Therefore, we suppose that the difference in capacity density between the two types of electrodes originates from Na^+ transport limitations caused by the larger electrode loading of the powder electrodes (≈34.12 mg cm^{-2}) *vs.* film electrodes (≈1.78 mg cm^{-2}). In addition, during the investigation of the reaction mechanism, clear evidence was found by XRD investigations that NaF was formed after a full cycle with electrodes on Cu foil (Fig. S8†). In contrast, for both the discharged powder and film electrode samples, only reflections of Na_2S and no indications of NaF were observed (Fig. S9†). Because the Bragg reflections of Na_2S are considerably more intense and are broadened due to the nanoscale character of the particles, it may be possible that the reflections of Na_2S simply superpose the reflections of NaF (Fig. S10†). However, ^{19}F MAS NMR of the discharged powder electrode (Fig. S11†) revealed the presence of NaF. Although the signal is weak, it clearly shows that NaF is formed during discharge. These findings confirm the similarity of the SEI formation process for both types of electrodes used.

In the following sections, the electrochemical reaction mechanism of the $Ni_2P_2S_6$ electrode is analyzed in detail using XRD, PDF, XAS, EDX and MAS NMR methods.

3.3.1 X-ray diffraction and pair distribution function analysis. The XRD patterns of the sodiated samples (Fig. 5b) reveal a continuous decrease of the crystallinity with increasing Na content. Besides this decrease of intensity, a reflection appears at 0.5 Na per f.u. located at a 2θ of 1.6° which increases in intensity up to 1.5 Na per f.u. This reflection is most probably associated with staging phenomena during the insertion of Na, where Na is simultaneously and randomly intercalated between layers of pristine $Ni_2P_2S_6$ resulting in one additional reflection corresponding to the average *d*-value caused by several different stages. In addition, a shoulder starting to develop at a 2θ value of about 4.1° and a slightly increasing background at 2θ values of 3.3 and 5.7° are indicators for the beginning of structural

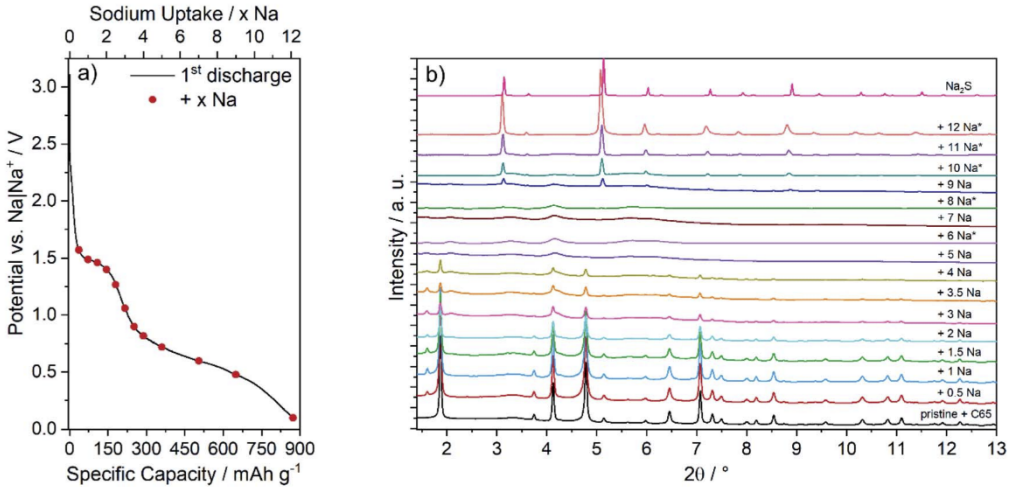

Fig. 5 (a) Discharge profile of the first discharge step of the $Ni_2P_2S_6$ powder electrode. (b) *Ex situ* X-ray diffraction patterns of the $Ni_2P_2S_6$ electrode collected at several states of discharge compared to simulated data for Na_2S.[107] Data marked with * were collected at a different beam time period.

changes at an early stage of discharge of 3 Na per f.u. After uptake of 5 Na per f.u. all reflections disappeared, indicating the formation of either nanoparticles which are too small to be detected by X-rays or of amorphous phases. The XRD patterns of the samples with Na contents between 5 and 8 Na per f.u. display no sharp reflections, but a few broad areas of slightly increased intensity typical for amorphous components having only short-range order. For 9 Na per f.u. reflections of Na_2S appeared, which gain intensity until the material is completely discharged after the uptake of 12 Na per f.u. The size of the coherent scattering domains for Na_2S in the completely discharged state was determined to be about 22.2 nm from a single peak fit of the (220) reflection (Fig. S12†). The single peak fit was necessary because the whole pattern could not be fitted appropriately without using strain parameters, which strongly affects the calculated size of the domains leading to unreliable values. The small shifts of the reflections towards lower scattering angles compared to the calculated pattern are most likely due to the distorted and defective nature of the nanosized sample. The observed formation of Na_2S is in accordance with the assumed conversion reactions in SIBs.[24,29,104] But in the present investigation no reflections of elemental Ni can be identified, indicating very small or amorphous particles as often observed for conversion reactions.[26,69,105,106] After a full cycle only reflections of NaF can be observed (Fig. S8†). The presence of this compound is a result of electrolyte decomposition and SEI formation. No other phases can be determined from the *ex situ* powder pattern of the fully charged sample. *Ex situ* measurements of charged samples cycled for 3 and 6 cycles (film electrodes) show similar diffraction patterns (Fig. S13†) as observed after the first full cycle (Fig. S8†), indicating formation of NaF or a mixture of NaF and Na_2S. NaF is most likely a side product of the SEI formation as discussed above, while Na_2S is a product of the electrode reaction. However, a broad background between 2θ values of ~19.5 and 27.5° without clearly defined Bragg reflections may be caused by amorphous compounds. This observation is not surprising as the electrodes consist of 20% amorphous carbon and the cycling of electrodes usually leads to formation of amorphous or nanoscopic compounds. Noteworthily, the reflections in the X-ray diffraction pattern of the sample after 6 cycles are more intense than those of the electrode recovered after 3 cycles. This finding suggests that with increasing cycle number the amount of Na_2S in the charged samples increases, which could be one reason for the steadily decreasing capacity within the first 48 cycles.

The pronounced reduction of crystallinity is also evident in PDF curves (Fig. 6a). The spatial extension decreases from long-range order for the pristine sample to less than 10 Å after an

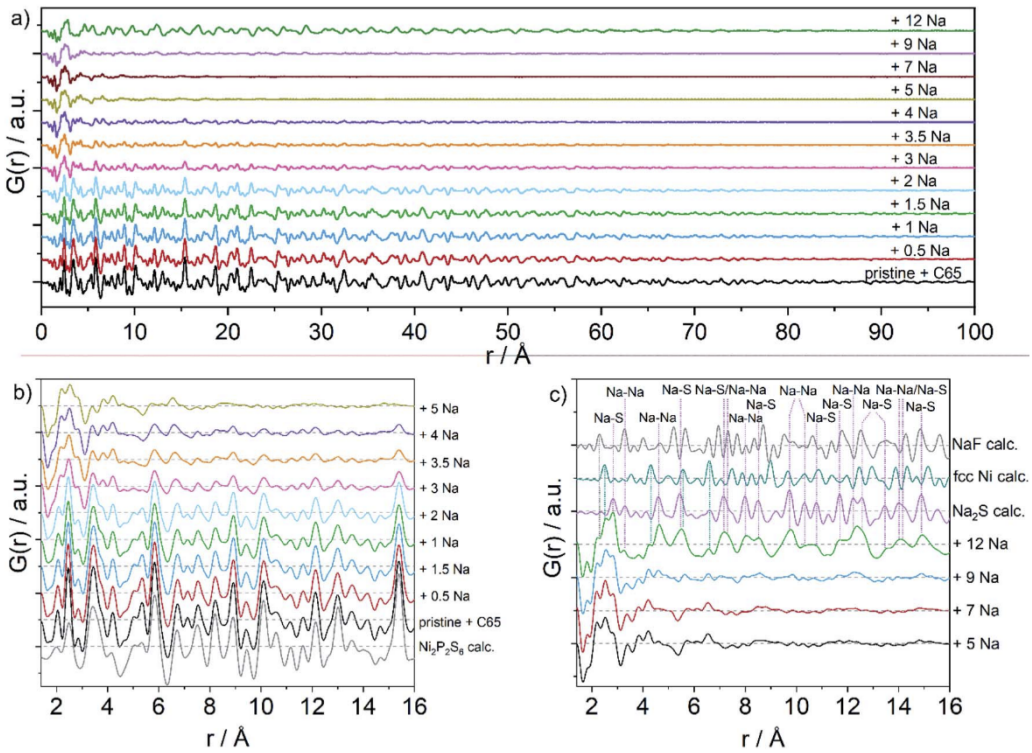

Fig. 6 *Ex situ* pair distribution function of the $Ni_2P_2S_6$ electrode collected at several states of discharge. (a) Overview of all samples measured in a range from 1.5 to 100 Å. (b) *Ex situ* pair distribution function between 1.5 and 16 Å showing the uptake of 0–5 Na per f.u. together with the calculated PDF of the pristine $Ni_2P_2S_6$.[44] (c) *Ex situ* pair distribution function from 1.5 to 16 Å showing the uptake of 5–12 Na per f.u. compared to the calculated PDF data of Na_2S,[107] fcc Ni[108] and NaF.[109]

uptake of 5 Na per f.u. (Fig. 6a). The characteristic interatomic distances of $Ni_2P_2S_6$ (*e.g.* 2.49 Å: Ni–S; 3.28 Å: P–S; 3.37 Å: Ni–Ni; 3.53 Å: Ni–P; 4.18 Å: Ni–S; 5.78 Å: P–S; 5.82 Å: P–P; 5.83 Å: Ni–S) decrease with increasing Na content while the interatomic distances of Na_2S start to develop for >5 Na per f.u. (Fig. 6b and c). The PDF of the fully discharged sample is in very good agreement with the simulated PDF of Na_2S. Only the first two distances are not related to Na_2S (Fig. 6c) and these peaks are probably associated with nano-sized Ni and NaF due to SEI formation. The first distance not related to Na_2S is at 2.24 Å, which is close to the first Na–F distance (~2.31 Å) of NaF, while the second distance not corresponding to Na_2S is at 2.55 Å and fits the Ni–Ni separation (2.49 Å) of metallic Ni. In both cases, the distances do not match perfectly, but these small deviations are most likely caused by the nanoscopic scale of these phases and the overlapping peaks in this region of the PDF. Another indication of the nanoscale character of Ni and NaF is the fact that only the very first distances can be identified in the PDF. These observations are in accordance with the results from XRD and ^{19}F MAS NMR. After a full cycle, mostly distances of NaF can be identified to be in agreement with the XRD data collected after a complete cycle. However, the fully cycled sample cannot be completely explained by the formation of NaF as other compounds must have built up during recharging, which are probably amorphous or nano-sized. As the signal of the first observed distance is much more intense than the corresponding calculated intensity of NaF, it is very likely that compounds with similar distances have formed. Some possibilities are the formation of different nickel and phosphorus sulfides (Fig. S14†) as well as phosphorus polysulfides. Beside the identified compound of the SEI, the PDF of the fully charged sample most probably contains numerous other compounds, which is why it is difficult to formulate a composition for the recharged sample. However, the presence of NaF is evident by PDF analysis, which is in accordance with the results collected by XRD and ^{19}F MAS NMR.

3.3.2 XANES and EXAFS. The X-ray absorption near-edge spectra (XANES) collected at different states of discharge are displayed in Fig. 7a. The Ni XANES curve of the pristine material shows a very weak pre-edge feature at 8332 eV caused by the quadrupole allowed 1s → 3d transition, indicating an octahedral environment of the Ni^{2+} cation.[110] The energy of the K-edge for pristine $Ni_2P_2S_6$ is 8339.7 eV (see Fig. 7b for 1st derivative) and for the white line (1s → 4p transition) the energy is 8349 eV, which are both in good agreement with data published in ref. 111.

For the uptake of up to 5 Na per f.u. the intensity of the 1s → 4p transition significantly decreases and a successive rising of the Ni K-edge at 8332.4 eV is observed, indicating that Ni^{2+} is predominantly reduced to its metallic state. During the further uptake of Na (8–12 Na per f.u.), the alterations of the XANES data are rather small. The intensity of the white line continues to decrease marginally and the intensity of the newly formed Ni K-edge at 8332.4 eV further increases. These observations suggest that after an uptake of 5 Na per f.u., the majority of Ni^{2+} is already reduced to the metallic state and remains in this state during further Na insertion.

During discharge, the XANES data exhibit a rotation around an isosbestic point at 8340 eV, indicating that no intermediate reaction steps occur during the reduction of Ni^{2+}. Compared to the XANES of the reference Ni foil, the Ni K-edge of the discharged sample (+12 Na per f.u.) is less pronounced and the two features of the reference at 8350 eV and 8358 eV are absent. This observation is not surprising taking into account that the Ni foil is highly crystalline fcc Ni, while Ni of the discharged sample is highly disordered and exhibits nano-sized particles causing a large number of surface atoms per defects (see Section 3.3.1). Similar observations were often made for discharged metal nanoparticles and amorphous alloys.[73,112,113] One has to mention that Ni_3S_2 exhibits a pre-edge at 8332 eV,[114] which is very close to the K-edge of metallic Ni at 8333 eV. In addition, the not well developed features in the spectrum of Ni_3S_2, which look slightly similar to the spectrum observed here, might indicate that Ni_3S_2 is formed upon discharge. However, the formation of Ni_3S_2 during the discharge process would not explain the observed capacities of the $Ni_2P_2S_6$ electrode, which reinforces the assumption that rather metallic Ni is formed. For the recharged sample, it can clearly be observed that the Ni K-

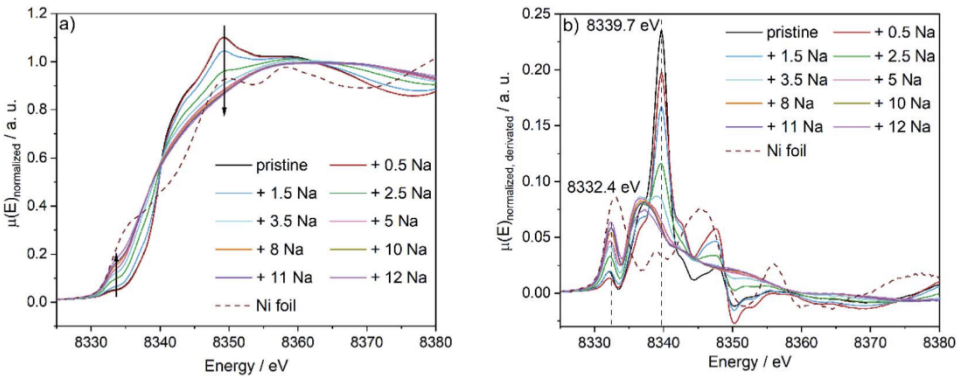

Fig. 7 (a) *Ex situ* XANES spectra at the Ni K-edge of the pristine $Ni_2P_2S_6$ and of various states of discharge and (b) the corresponding first derivatives.

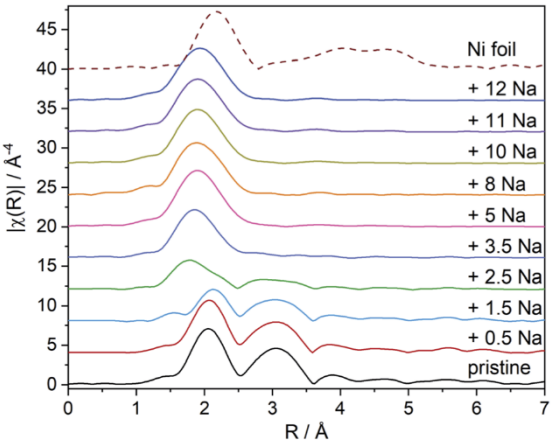

Fig. 8 FT radial distances for Ni absorber atoms of the pristine $Ni_2P_2S_6$ and of various states of discharge.

edge shifts to higher energy in comparison to the fully discharged sample (Fig. S15a†), which indicates the oxidation of metallic Ni. The first derivative shows that the energy of the Ni K-edge of the recharged sample is 8336.3 eV (Fig. S15b†). Additionally, a very weak pre-edge feature is observed at 8332.4 eV. While the spectrum does not match the reference spectrum of NiS, the K-edge energy of the sample is very close to the K-edge energy of Ni_3S_2 (8336 eV)[115] and therefore, we assume that nanoscopic Ni_3S_2 particles are generated upon charging.

The EXAFS data were Fourier-transformed to obtain the pseudo-radial distribution function (pRDF) (Fig. 8). In the pRDF of the pristine material, the first peak positioned around 2.0 Å corresponds to the Ni–S bond at 2.50 Å, and the broad second peak represents the Ni–Ni distance at 3.35–3.37 Å and Ni–P at 3.53 Å. The pRDF reveals the successive conversion of the pristine material during the early stages of discharge (up to 5 Na per f.u.), while a new signal occurs after the uptake of 1.5 Na per f.u. and gains intensity up to 5 Na per f.u. Further discharging (8–12 Na per f.u.) does not affect the signal much, indicating the completed reduction of Ni^{2+} to the metallic state after an uptake of 5 Na per f.u. The signals in the pRDF of the completely discharged state (+12 Na per f.u.) are at smaller distances and only a single distance is observed while the fcc Ni reference foil reveals multiple peaks. As mentioned before, this is not unexpected because the Ni foil is highly crystalline, while the Ni obtained from discharging is highly defective and nanoscopic. Due to the phase shift in the FT R-space and the obtained disordered particles, it is not possible to exactly compare the observed distances with theoretical values. Nonetheless, the EXAFS and XANES data show strong evidence of the reduction of Ni^{2+} to its metallic state during the discharge process. Additionally, the data indicate that the majority of the Ni^{2+} cations are reduced within the early discharge states up to 5 Na per f.u.

3.3.3 ^{23}Na and ^{31}P MAS NMR. The *ex situ* ^{31}P NMR signal of the pristine material is located at −474 ppm (Fig. 9a). A new signal occurs at 102 ppm after insertion of 2.5 Na per f.u. The

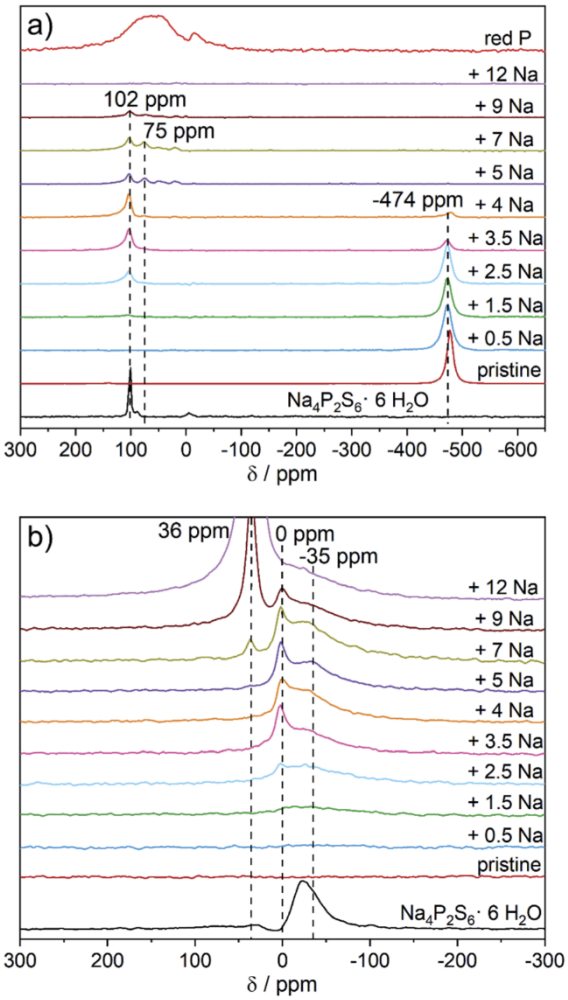

Fig. 9 (a) ^{31}P and (b) ^{23}Na MAS NMR spectra of $Ni_2P_2S_6$ for different Na contents obtained during discharging against Na metal.

signal at −474 ppm nearly disappeared after an uptake of 4 Na per f.u. while the intensity of the signal at 102 ppm significantly increased. The position of the newly formed peak is in very good agreement with that of the peak observed for the reference material $Na_4P_2S_6{\cdot}6H_2O$ (101 ppm). The formation of hydrated compounds is not likely, though. Since the local structure of the phosphorus in $Na_4P_2S_6{\cdot}6H_2O$ and $Na_4P_2S_6$ is similar, chemical shifts in the same range are expected. Additionally, the corresponding lithium compound $Li_4P_2S_6$ shows a very similar chemical shift of 108–110 ppm for the $[P_2S_6]^{4-}$ unit.[116] Therefore, the described peak potentially can be assigned to the formation of $Na_4P_2S_6$. For 5 Na per f.u. the signal at −474 ppm disappeared and another signal appeared at 75 ppm besides the peak at 102 ppm, which decreased in intensity. A further increase of Na per f.u. first leads to the appearance of weak new signals and finally to the full disappearance of the ^{31}P NMR signal. The observations indicate that at lower Na contents

Table 1 Ni, P and S contents of sodiated samples collected by *ex situ* EDX measurements. The values were obtained by averaging several measurements at different spots of the sample

Sample	Ni/at%	P/at%	S/at%	Ratio Ni : P : S
$Ni_2P_2S_6$	19.5 ± 2.6	20.8 ± 1.5	59.7 ± 2.3	1 : 1.07 : 3.06
$Ni_2P_2S_6$ + 4Na	16.7 ± 3.8	20.8 ± 3.8	62.4 ± 3.3	1 : 1.25 : 3.74
$Ni_2P_2S_6$ + 12Na	21.5 ± 2.5	21.5 ± 8.3	57.0 ± 9.7	1 : 1 : 2.65

a new phase, possibly $Na_4P_2S_6$, is formed and that, at the end of the discharge process, the pristine material is totally degraded. Further, there is no evidence for the formation of Na_3P or other phosphide compounds at the fully discharged state. Beside the evidence for the formation of an intermediate phase, all results are in agreement with those obtained with XRD, PDF and XAS discussed above.

The ^{23}Na MAS NMR studies (Fig. 9b) show the development of weak signals after an uptake of 1.5 Na per f.u. at around 0 and −35 ppm. The intensity of these two signals increases up to 5 Na per f.u., while the peak at 0 ppm is more intense and sharper than that at −35 ppm. The reference $Na_4P_2S_6{\cdot}6H_2O$ exhibits a similar chemical shift of −25 ppm. The slight difference of the chemical shift might arise from the proximity of the oxygen to the sodium within the local structure of the hydrated compound, which does not exist for the dehydrated compound $Na_4P_2S_6$. At 7 Na per f.u. another signal developed at 36 ppm which is the most intensive peak for the sample containing 12 Na per f.u., whereas the intensity of the two other signals significantly decreased. The signal at 36 ppm can be assigned to the formation of Na_2S. These results are in accordance with those previously reported.

3.3.4 EDX investigations. To ensure that phosphorus or phosphorus containing phases are not washed away by the electrolyte solution, EDX measurements of sodiated samples were conducted. The results are shown in Table 1.

The results of the EDX measurements clearly prove that no P or P containing phase is washed away by the electrolyte solution as in the average ratio of Ni : P : S stays roughly at 1 : 1 : 3 and no loss of phosphorus is evident from the data. Only the standard deviation increases with higher sodiation, which could indicate a higher particle-to-particle variance.

4. Conclusion

The hypothiophosphate $Ni_2P_2S_6$ was synthesized by chemical vapor transport. The compound is highly crystalline and phase pure which is evident from XRD. Galvanostatic measurements of bulk $Ni_2P_2S_6$ in SIBs revealed good electrochemical performance with a discharge capacity of 621 mA h g^{-1} for 190 cycles. The cyclability, rate capability and specific capacities are in a similar range as reported for $Ni_2P_2S_6$ nanosheets.[50] $Ni_2P_2S_6$ nanosheet samples from liquid phase exfoliation were also investigated in this study, but showed poor performance, which may arise from the different methods used to obtain the nanosheets (LPE *vs.* synthesis controlled[50]). *Ex situ* XRD and PDF measurements demonstrate the decreasing particle size during the uptake of Na (up to 5 Na per f.u.) until only amorphous phases are left. Accordingly, *ex situ* ^{31}P and ^{23}Na MAS NMR experiments show that $Ni_2P_2S_6$ decomposes during early stages of discharge. The formation of an intermediate phase is also evident by ^{31}P and ^{23}Na MAS NMR investigations. The MAS NMR experiments give hints that the intermediate phase might be $Na_4P_2S_6$. *Ex situ* XANES and EXAFS demonstrate that Ni^{2+} is reduced to its metallic state during an uptake of 5 Na per f.u. The XAS studies further suggest that the intermediate phase found by MAS NMR measurements does not contain Ni. Upon further discharging, the metallic Ni remains in its elemental state. Additionally, the formation of Na_2S above an uptake of 7 Na per f.u. could be proven by *ex situ* XRD, PDF analysis and ^{23}Na MAS NMR. Considering the experimentally achieved specific capacity of the first discharge of 873 mA h g^{-1} a reaction involving 12 Na per f.u. (theoretical capacity: 865 mA h g^{-1}) seems reasonable, leading to the following pathway:

$$Ni_2P_2S_6 + 12Na^+ + 12e^- \rightarrow 2Ni + 2P + 6Na_2S$$

Because the formation of Na_2S and the full reduction of Ni^{II} to Ni^0 is evidenced by the results of these investigations, the reduction of P^{IV} to P^0 seems to be most likely. The formation of Na_xP phases should lead to higher specific capacities (up to 1300 mA h g^{-1}) than observed. *Ex situ* EDX investigations of sodiated samples also demonstrate that phosphorus is not dissolved and removed by the electrolyte solution within the first discharge.

Regarding the charge process *ex situ* XANES suggests the formation of Ni_3S_2. *Ex situ* PDF analysis also demonstrates the possibility of the formation of Ni_3S_2 among other phases. This observation is not surprising as there are definitively several other components within the charged sample. Taking these findings into account the pathway of the first charge process might be the following:

$$2Ni + 2P + 6Na_2S \rightarrow \frac{2}{3}Ni_3S_2 + \frac{1}{2}P_4S_9 + 11\frac{2}{3}Na^+ + 11\frac{2}{3}e^- + \frac{1}{6}Na_2S$$

This charging mechanism is postulated based on the assumption of the formation of Ni_3S_2 upon charging and taking the composition of the sample in the discharged state into account. The release of ~11.7 Na per f.u. is in full agreement with the determined first charge capacity of 842 mA h g^{-1} (see Fig. 4a and b). Taking a closer look at the long-term performance, a drop in capacity is observed. While at early cycling stages around 12 Na per f.u. are consumed upon cycling, in later stages only around 8–9 Na per f.u. participate in the electrochemical reaction. This corresponds to a loss of 4–5 Na per f.u., which may be explained by the formation of electrochemically inactive Na_2S. The Na_2S eventually passivates some Ni which cannot be cycled. We note that deactivation of 1 P per f.u. would

also lead to the observed loss of 4–5 Na per f.u. in the later cycling stages.

Conflicts of interest

The authors declare no competing financial interest.

Acknowledgements

Financial support by the State of Schleswig-Holstein is gratefully acknowledged. The authors acknowledge DESY (Hamburg, Germany), a member of the Helmholtz Association HGF, for the provision of experimental facilities. Parts of this research were carried out at PETRA III. We kindly thank Huayna Terraschke for beamtime allocation. This work was carried out with the support of the Diamond Light Source, instrument B18 (proposal SP20060).

References

1 P. K. Nayak, L. Yang, W. Brehm and P. Adelhelm, *Angew. Chem., Int. Ed.*, 2018, **57**, 102–120.
2 J. Deng, W.-B. Luo, S.-L. Chou, H.-K. Liu and S.-X. Dou, *Adv. Energy Mater.*, 2018, **8**, 1701428.
3 D. A. Stevens and J. R. Dahn, *J. Electrochem. Soc.*, 2001, **148**, A803–A811.
4 E. Irisarri, A. Ponrouch and M. R. Palacin, *J. Electrochem. Soc.*, 2015, **162**, A2476.
5 I. El Moctar, Q. Ni, Y. Bai, F. Wu and C. Wu, *Funct. Mater. Lett.*, 2018, **11**, 1830003.
6 D.-Y. Kim, D.-H. Kim, S.-H. Kim, E.-K. Lee, S.-K. Park, J.-W. Lee, Y.-S. Yun, S.-Y. Choi and J. Kang, *Nanomaterials*, 2019, **9**, 793.
7 Y. Xiao, S. H. Lee and Y.-K. Sun, *Adv. Energy Mater.*, 2017, **7**, 1601329.
8 W. Kang, Y. Wang and J. Xu, *J. Mater. Chem. A*, 2017, **5**, 7667–7690.
9 W.-H. Lai, Y.-X. Wang, J.-Z. Wang, S.-L. Chou and S.-X. Dou, *Batteries Supercaps*, 2020, **3**, 236–253.
10 J. Mao, T. Zhou, Y. Zheng, H. Gao, H. kun Liu and Z. Guo, *J. Mater. Chem. A*, 2018, **6**, 3284–3303.
11 Z. Hu, Q. Liu, S.-L. Chou and S.-X. Dou, *Adv. Mater.*, 2017, **29**, 1700606.
12 X. Y. Yu and X. W. Lou, *Adv. Energy Mater.*, 2018, **8**, 1701592.
13 M. Lao, Y. Zhang, W. Luo, Q. Yan, W. Sun and S. X. Dou, *Adv. Mater.*, 2017, **29**, 1700622.
14 N. Yabuuchi, K. Kubota, M. Dahbi and S. Komaba, *Chem. Rev.*, 2014, **114**, 11636–11682.
15 L. Li, Y. Zheng, S. Zhang, J. Yang, Z. Shao and Z. Guo, *Energy Environ. Sci.*, 2018, **11**, 2310–2340.
16 T. Wang, D. Su, D. Shanmukaraj, T. Rojo, M. Armand and G. Wang, *Electrochem. Energy Rev.*, 2018, **1**, 200–237.
17 Z. Yang, T. Chen, C. Wu, J. Qu, Z. Wu, X. Guo, B. Zhong, H. Liu and S. Dou, *ACS Appl. Mater. Interfaces*, 2019, **11**, 3961–3970.
18 J. Y. Park, S. J. Kim, K. Yim, K. S. Dae, Y. Lee, K. P. Dao, J. S. Park, H. B. Jeong, J. H. Chang, H. K. Seo, C. W. Ahn and J. M. Yuk, *Adv. Sci.*, 2019, **6**, 1900264.
19 Y. Zhang, C. Lv, X. Wang, S. Chen, D. Li, Z. Peng and D. Yang, *ACS Appl. Mater. Interfaces*, 2018, **10**, 40531–40539.
20 Z. Shadike, Y.-N. Zhou, F. Ding, L. Sang, K.-W. Nam, X.-Q. Yang and Z.-W. Fu, *J. Power Sources*, 2014, **260**, 72–76.
21 J. Lv, D. Bai, L. Yang, Y. Guo, H. Yan and S. Xu, *Chem. Commun.*, 2018, **54**, 8909–8912.
22 M. Krengel, A.-L. Hansen, F. Hartmann, J. van Dinter and W. Bensch, *Batteries Supercaps*, 2018, **1**, 176–183.
23 M. Krengel, A.-L. Hansen, M. Kaus, S. Indris, N. Wolff, L. Kienle, D. Westfal and W. Bensch, *ACS Appl. Mater. Interfaces*, 2017, **9**, 21283–21291.
24 M. Krengel, P. Adelhelm, F. Klein and W. Bensch, *Chem. Commun.*, 2015, **51**, 13500–13503.
25 J. Deng, Q. Gong, H. Ye, K. Feng, J. Zhou, C. Zha, J. Wu, J. Chen, J. Zhong and Y. Li, *ACS Nano*, 2018, **12**, 1829–1836.
26 C. Yang, X. Ou, X. Xiong, F. Zheng, R. Hu, Y. Chen, M. Liu and K. Huang, *Energy Environ. Sci.*, 2017, **10**, 107–113.
27 Y. Chen, X. Hu, B. Evanko, X. Sun, X. Li, T. Hou, S. Cai, C. Zheng, W. Hu and G. D. Stucky, *Nano Energy*, 2018, **46**, 117–127.
28 K. Zhang, M. Park, L. Zhou, G.-H. Lee, J. Shin, Z. Hu, S.-L. Chou, J. Chen and Y.-M. Kang, *Angew. Chem., Int. Ed.*, 2016, **55**, 12822–12826.
29 F. Klein, B. Jache, A. Bhide and P. Adelhelm, *Phys. Chem. Chem. Phys.*, 2013, **15**, 15876–15887.
30 S. Mukherjee, S. Bin Mujib, D. Soares and G. Singh, *Materials*, 2019, **12**, 1952.
31 E. Edison, S. Sreejith, C. Teck Lim and S. Madhavi, *Sustainable Energy Fuels*, 2018, **2**, 2567–2582.
32 M. C. Friedel, *Compt. Rend.*, 1894, **119**, 260–264.
33 R. Brec, *Solid State Ionics*, 1986, **22**, 3–30.
34 G. Ouvrard, R. Fréour, R. Brec and J. Rouxel, *Mater. Res. Bull.*, 1985, **20**, 1053–1062.
35 E. Durand, G. Ouvrard, M. Evain and R. Brec, *Inorg. Chem.*, 1990, **29**, 4916–4920.
36 Y. V. Kuz'minskii, B. M. Voronin, I. M. Petrushina, N. N. Redin and G. P. Prikhodko, *J. Power Sources*, 1995, **55**, 1–6.
37 Y. V. Kuz'minskii, B. M. Voronin and N. N. Redin, *J. Power Sources*, 1995, **55**, 133–141.
38 A. H. Thompson and M. S. Whittingham, *Mater. Res. Bull.*, 1977, **12**, 741–744.
39 M. A. Susner, M. Chyasnavichyus, M. A. McGuire, P. Ganesh and P. Maksymovych, *Adv. Mater.*, 2017, **29**, 1602852.
40 W. Klingen, R. Ott and H. Hahn, *Z. Anorg. Allg. Chem.*, 1973, **396**, 271–278.
41 E. Prouzet, G. Ouvrard and R. Brec, *Mater. Res. Bull.*, 1986, **21**, 195–200.
42 G. Ouvrard, R. Brec and J. Rouxel, *Mater. Res. Bull.*, 1985, **20**, 1181–1189.
43 F. Wang, T. A. Shifa, P. Yu, P. He, Y. Liu, F. Wang, Z. Wang, X. Zhan, X. Lou, F. Xia and J. He, *Adv. Funct. Mater.*, 2018, **28**, 1802151.

44 R. R. Rao and A. K. Raychaudhuri, *J. Phys. Chem. Solids*, 1992, **53**, 577–583.

45 B. E. Taylor, J. Steger and A. Wold, *J. Solid State Chem.*, 1973, **7**, 461–467.

46 M. Evain, R. Brec and M.-H. Whangbo, *J. Solid State Chem.*, 1987, **71**, 244–262.

47 C.-T. Kuo, M. Neumann, K. Balamurugan, H. J. Park, S. Kang, H. W. Shiu, J. H. Kang, B. H. Hong, M. Han, T. W. Noh and J.-G. Park, *Sci. Rep.*, 2016, **6**, 20904.

48 R. Dangol, Z. Dai, A. Chaturvedi, Y. Zheng, Y. Zhang, K. Ngoc Dinh, B. Li, Y. Zong and Q. Yan, *Nanoscale*, 2018, **10**, 4890–4896.

49 Y. Suto, Y. Fujii, A. Miura, N. C. Rosero-Navarro, M. Higuchi and K. Tadanaga, *J. Ceram. Soc. Jpn.*, 2018, **126**, 568–572.

50 Q. Liang, Y. Zheng, C. Du, Y. Luo, J. Zhang, B. Li, Y. Zong and Q. Yan, *Small Methods*, 2017, **1**, 1700304.

51 Y. Fujii, A. Miura, N. C. Rosero-Navarro, Y. Mizuguchi, C. Moriyoshi, Y. Kuroiwa, M. Higuchi and K. Tadanaga, *J. Electrochem. Soc.*, 2018, **165**, A2948–A2954.

52 R. Brec, D. M. Schleich, G. Ouvrard, A. Louisy and J. Rouxel, *Inorg. Chem.*, 1979, **18**, 1814–1818.

53 M. Armand and J.-M. Tarascon, *Nature*, 2008, **451**, 652–657.

54 R. Malini, U. Uma, T. Sheela, M. Ganesan and N. G. Renganathan, *Ionics*, 2009, **15**, 301–307.

55 J. Cabana, L. Monconduit, D. Larcher and M. R. Palacín, *Adv. Mater.*, 2010, **22**, E170–E192.

56 B. Scrosati and J. Garche, *J. Power Sources*, 2010, **195**, 2419–2430.

57 J. B. Goodenough and K.-S. Park, *J. Am. Chem. Soc.*, 2013, **135**, 1167–1176.

58 K. Takada, Y. Michiue, T. Inada, A. Kajiyama, M. Kouguchi, S. Kondo, M. Watanabe and M. Tabuchi, *Solid State Ionics*, 2003, **159**, 257–263.

59 Y. Fujii, A. Miura, N. C. Rosero-Navarro, M. Higuchi and K. Tadanaga, *Electrochim. Acta*, 2017, **241**, 370–374.

60 Y. Zhang, C. J. Pelliccione, A. B. Brady, H. Guo, P. F. Smith, P. Liu, A. C. Marschilok, K. J. Takeuchi and E. S. Takeuchi, *Chem. Mater.*, 2017, **29**, 4282–4292.

61 D. Bresser, E. Paillard, R. Kloepsch, S. Krueger, M. Fiedler, R. Schmitz, D. Baither, M. Winter and S. Passerini, *Adv. Energy Mater.*, 2013, **3**, 513–523.

62 D. Larcher, G. Sudant, J.-B. Leriche, Y. Chabre and J.-M. Tarascon, *J. Electrochem. Soc.*, 2002, **149**, A234–A241.

63 M. C. Menard, K. J. Takeuchi, A. C. Marschilok and E. S. Takeuchi, *Phys. Chem. Chem. Phys.*, 2013, **15**, 18539–18548.

64 W. Zhang, D. C. Bock, C. J. Pelliccione, Y. Li, L. Wu, Y. Zhu, A. C. Marschilok, E. S. Takeuchi, K. J. Takeuchi and F. Wang, *Adv. Energy Mater.*, 2016, **6**, 1502471.

65 D. Zhou, H. Jia, J. Rana, T. Placke, T. Scherb, R. Kloepsch, G. Schumacher, M. Winter and J. Banhart, *Electrochim. Acta*, 2017, **246**, 699–706.

66 G. Balachandran, D. Dixon, N. Bramnik, A. Bhaskar, M. Yavuz, L. Pfaffmann, F. Scheiba, S. Mangold and H. Ehrenberg, *ChemElectroChem*, 2015, **2**, 1510–1518.

67 A. Ruud, J. Sottmann, P. Vajeeston and H. Fjellvåg, *Phys. Chem. Chem. Phys.*, 2018, **20**, 29798–29803.

68 M. M. Huie, D. C. Bock, L. Wang, A. C. Marschilok, K. J. Takeuchi and E. S. Takeuchi, *J. Phys. Chem. C*, 2018, **122**, 10316–10326.

69 S. Permien, H. Hain, M. Scheuermann, S. Mangold, V. Mereacre, A. K. Powell, S. Indris, U. Schürmann, L. Kienle, V. Duppel, S. Harm and W. Bensch, *RSC Adv.*, 2013, **3**, 23001–23014.

70 S. Permien, S. Indris, M. Scheuermann, U. Schürmann, V. Mereacre, A. K. Powell, L. Kienle and W. Bensch, *J. Mater. Chem. A*, 2015, **3**, 1549–1561.

71 S. Permien, S. Indris, U. Schürmann, L. Kienle, S. Zander, S. Doyle and W. Bensch, *Chem. Mater.*, 2016, **28**, 434–444.

72 S. Permien, S. Indris, A.-L. Hansen, M. Scheuermann, D. Zahn, U. Schürmann, G. Neubüser, L. Kienle, E. Yegudin and W. Bensch, *ACS Appl. Mater. Interfaces*, 2016, **8**, 15320–15332.

73 S. Permien, T. Neumann, S. Indris, G. Neubüser, L. Kienle, A. Fiedler, A.-L. Hansen, D. Gianolio, T. Bredow and W. Bensch, *Phys. Chem. Chem. Phys.*, 2018, **20**, 19129–19141.

74 *Turbomole v6.6 2014*, A Development of University of Karlsruhe and Forschungszentrum Karlsruhe GmbH, Turbomole GmbH, since 2007, 1989–2007, http://www.turbomole.com.

75 J. P. Perdew, K. Burke and M. Ernzerhof, *Phys. Rev. Lett.*, 1996, **77**, 3865–3868.

76 A. Hellweg, C. Hättig, S. Höfener and W. Klopper, *Theor. Chem. Acc.*, 2007, **117**, 587–597.

77 F. Weigend, *Phys. Chem. Chem. Phys.*, 2006, **8**, 1057–1065.

78 F. Weigend and R. Ahlrichs, *Phys. Chem. Chem. Phys.*, 2005, **7**, 3297–3305.

79 J. P. Perdew, *Phys. Rev. B: Condens. Matter Mater. Phys.*, 1986, **33**, 8822–8824.

80 C. Lee, W. Yang and R. G. Parr, *Phys. Rev. B: Condens. Matter Mater. Phys.*, 1988, **37**, 785–789.

81 O. Treutler and R. Ahlrichs, *J. Chem. Phys.*, 1995, **102**, 346–354.

82 J. Filik, A. W. Ashton, P. C. Y. Chang, P. A. Chater, S. J. Day, M. Drakopoulos, M. W. Gerring, M. L. Hart, O. V. Magdysyuk, S. Michalik, A. Smith, C. C. Tang, N. J. Terrill, M. T. Wharmby and H. Wilhelm, *J. Appl. Crystallogr.*, 2017, **50**, 959–966.

83 X. Yang, P. Juhas, C. L. Farrow and S. J. L. Billinge, arXiv:1402.3163, 2014.

84 A. A. Coelho, *Topas Academic (Version 6)*, Coelho Software, Australia, 2016.

85 B. Ravel and M. Newville, *J. Synchrotron Radiat.*, 2005, **12**, 537–541.

86 A. R. Wildes, V. Simonet, E. Ressouche, R. Ballou and G. J. McIntyre, *J. Phys.: Condens. Matter*, 2017, **29**, 455801.

87 C. Murayama, M. Okabe, D. Urushihara, T. Asaka, K. Fukuda, M. Isobe, K. Yamamoto and Y. Matsushita, *J. Appl. Phys.*, 2016, **120**, 142114.

88 A. R. Wildes, V. Simonet, E. Ressouche, G. J. McIntyre, M. Avdeev, E. Suard, S. A. J. Kimber, D. Lançon, G. Pepe, B. Moubaraki and T. J. Hicks, *Phys. Rev. B: Condens. Matter Mater. Phys.*, 2015, **92**, 224408.

89 P. Fragnaud, E. Prouzet and R. Brec, *J. Mater. Res.*, 1992, **7**, 1839–1846.

90 M. Gjikaj and W. Brockner, *Z. Naturforsch., B: J. Chem. Sci.*, 2007, **62**, 1102–1106.

91 C. Sourisseau, J. P. Forgerit and Y. Mathey, *J. Solid State Chem.*, 1983, **49**, 134–149.

92 M. Balkanski, M. Jouanne, G. Ouvrard and M. Scagliotti, *J. Phys. C: Solid State Phys.*, 1987, **20**, 4397–4413.

93 M. Scagliotti, M. Jouanne, M. Balkanski, G. Ouvrard and G. Benedek, *Phys. Rev. B: Condens. Matter Mater. Phys.*, 1987, **35**, 7097–7104.

94 C. C. Mayorga-Martinez, Z. Sofer, D. Sedmidubský, Š. Huber, A. Y. S. Eng and M. Pumera, *ACS Appl. Mater. Interfaces*, 2017, **9**, 12563–12573.

95 M. Gjikaj and C. Ehrhardt, *Z. Anorg. Allg. Chem.*, 2007, **633**, 1048–1054.

96 H. Bürger and H. Falius, *Z. Anorg. Allg. Chem.*, 1968, **363**, 24–32.

97 X. Wang, K. Du, Y. Y. F. Liu, P. Hu, J. Zhang, Q. Zhang, M. H. S. Owen, X. Lu, C. K. Gan, P. Sengupta, C. Kloc and Q. Xiong, *2D Mater.*, 2016, **3**, 031009.

98 M. Bernasconi, G. L. Marra, G. Benedek, L. Miglio, M. Jouanne, C. Julien, M. Scagliotti and M. Balkanski, *Phys. Rev. B: Condens. Matter Mater. Phys.*, 1988, **38**, 12089–12099.

99 G. Kliche, *J. Solid State Chem.*, 1984, **51**, 118–126.

100 K. Synnatschke, S. Shao, J. van Dinter, Y. J. Hofstetter, D. J. Kelly, S. Grieger, S. J. Haigh, Y. Vaynzof, W. Bensch and C. Backes, *Chem. Mater.*, 2019, **31**, 9127–9139.

101 Y. Liu, X. He, D. Hanlon, A. Harvey, U. Khan, Y. Li and J. N. Coleman, *ACS Nano*, 2016, **10**, 5980–5990.

102 S.-H. Park, P. J. King, R. Tian, C. S. Boland, J. Coelho, C. J. Zhang, P. McBean, N. McEvoy, M. P. Kremer, D. Daly, J. N. Coleman and V. Nicolosi, *Nat. Energy*, 2019, **4**, 560–567.

103 C. Gabbett, C. S. Boland, A. Harvey, V. Vega-Mayoral, R. J. Young and J. N. Coleman, *Chem. Mater.*, 2018, **30**, 5245–5255.

104 T. B. Kim, J. W. Choi, H. S. Ryu, G. B. Cho, K. W. Kim, J. H. Ahn, K. K. Cho and H. J. Ahn, *J. Power Sources*, 2007, **174**, 1275–1278.

105 R. Verma, R. K. Raman and U. V. Varadaraju, *J. Solid State Electrochem.*, 2016, **20**, 1501–1505.

106 R. Verma, K. Ramanujam and U. V. Varadaraju, *Appl. Surf. Sci.*, 2017, **418**, 30–39.

107 E. Zintl, A. Harder and B. Dauth, *Z. Elektrochem. Angew. Phys. Chem.*, 1934, **40**, 588–593.

108 E. A. Owen and E. L. Yates, *London, Edinburgh Dublin Philos. Mag. J. Sci.*, 1936, **21**, 809–819.

109 Y. Shirako, Y. G. Shi, A. Aimi, D. Mori, H. Kojitani, K. Yamaura, Y. Inaguma and M. Akaogi, *J. Solid State Chem.*, 2012, **191**, 167–174.

110 W. Niemann, B. S. Clausen and H. Topsøe, *Catal. Lett.*, 1990, **4**, 355–363.

111 P. Fragnaud, E. Prouzet, G. Ouvrard, J. L. Mansot, C. Payen, R. Brec and H. Dexpert, *J. Non-Cryst. Solids*, 1993, **160**, 1–17.

112 W. K. Luo, H. W. Sheng, F. M. Alamgir, J. M. Bai, J. H. He and E. Ma, *Phys. Rev. Lett.*, 2004, **92**, 145502.

113 S. Permien, A.-L. Hansen, J. van Dinter, S. Indris, G. Neubüser, L. Kienle, S. Doyle, S. Mangold and W. Bensch, *ACS Omega*, 2019, **4**, 2398–2409.

114 M. F. Wagenhofer, H. Shi, O. Y. Gutiérrez, A. Jentys and J. A. Lercher, *Sci. Adv.*, 2020, **6**, eaax5331.

115 L. Huang, G. Wang, Z. Qin, M. Dong, M. Du, H. Ge, X. Li, Y. Zhao, J. Zhang, T. Hu and J. Wang, *Appl. Catal., B*, 2011, **106**, 26–38.

116 C. Dietrich, D. A. Weber, S. Culver, A. Senyshyn, S. J. Sedlmaier, S. Indris, J. Janek and W. G. Zeier, *Inorg. Chem.*, 2017, **56**, 6681–6687.

4.2 Long-Term Stable, High-Capacity Anode Material for Sodium-Ion Batteries: Taking a Closer Look at $CrPS_4$ from an Electrochemical and Mechanistic Point of View

In the second study, the layered thiophosphate $CrPS_4$ was investigated as anode material in SIBs and examined regarding the underlying reaction pathway. For this investigation, $CrPS_4$ was chosen, because Cr is a suitable substitution for main elements of state-of-the-art battery technology, such as Ni or Co, while promising electrochemical behavior has been demonstrated previously for the substance class of thiophosphates. Furthermore, this study displays the first investigation of $CrPS_4$ as electrode material in SIBs and the underlying reaction mechanism of Na uptake and release.

Excellent electrochemical performance was found for $CrPS_4$ electrodes against Na metal exhibiting an initial discharge capacity of 1226 mAh g^{-1} (current rate: 0.1 A g^{-1}) and a reversible capacity of 687 mAh g^{-1} after 300 cycles at a current rate of 1.0 A g^{-1}. $CrPS_4$ electrodes further showed good rate capability of 288 mAh g^{-1} at a current density of 3.0 A g^{-1} and demonstrated an extraordinary capacity retention when switched back to lower currents. Moreover, electrochemical experiments indicated changes of the underlying reaction pathway during extended periods of cycling. The analysis of this long-term electrochemical behavior suggests a partial but immediate deactivation followed by a successive reactivation of electrode components within ~130 cycles. By combining complementary characterization techniques (*i.e.* XRD, PDF analysis, XAS and $^{23}Na/^{31}P$ MAS NMR spectroscopy), details of the electrochemical reaction of Na uptake and release during the initial discharge/charge process were revealed. At early stages of the discharge process (0.5 - 3 Na/f.u.), several intercalation compounds are formed, which decompose upon further discharging (5 - 8 Na/f.u.). This decomposition is accompanied by the generation of Na_2S, strongly disordered metallic Cr and NaF (product of SEI formation), whereas no signs of Na_xP phases were observed. Hence, the reduction of P^{5+} to P^0 is assumed based on the obtained specific discharge capacities and ^{31}P MAS NMR investigations. However, the ongoing reaction mechanism exhibits a much higher degree of complexity, which was demonstrated by ^{31}P MAS NMR spectroscopy as well. The uptake of 2 - 8 Na/f.u. generates several P containing phases, some of which are assumed to be related to the formation of intercalated phases, the breakdown of these intermediary intercalation compounds and the formation of a P^0 phase. Admittedly, the origins of some of the signals detected by ^{31}P MAS NMR spectroscopy remain uncertain. Recharging results in the recovery of a short-range order similar to the local environment of $CrPS_4$, although the analysis of the electrochemical data suggests a partial passivation of the electrode after the initial cycles.

ACS APPLIED MATERIALS & INTERFACES

www.acsami.org Research Article

Long-Term Stable, High-Capacity Anode Material for Sodium-Ion Batteries: Taking a Closer Look at $CrPS_4$ from an Electrochemical and Mechanistic Point of View

Jonas van Dinter, Sylvio Indris, Alexander Bitter, David Grantz, Giannantonio Cibin, Martin Etter, and Wolfgang Bensch*

Cite This: *ACS Appl. Mater. Interfaces* 2021, 13, 54936–54950 Read Online

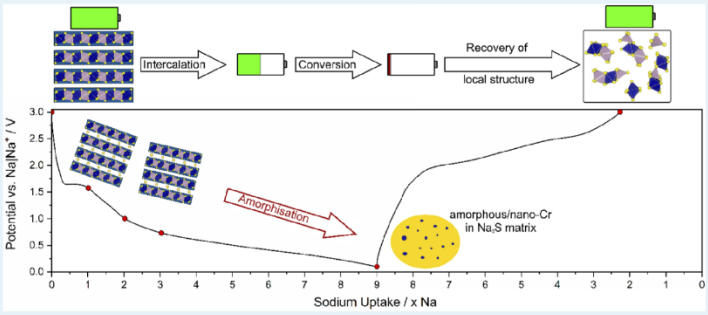

ABSTRACT: Electrochemical performance of the layered compound $CrPS_4$ for the usage as anode material in sodium-ion batteries (SIBs) was examined and exceptional reversible long-term capacity and capacity retention were found. After 300 cycles, an extraordinary reversible capacity of 687 mAh g^{-1} at a current rate of 1 A g^{-1} was achieved, while rate capability tests showed an excellent capacity retention of 100%. Detailed evaluation of the data evidence a change of the electrochemical reaction upon cycling leading to the striking long-term performance. Further investigations targeted the reaction mechanism of the first cycle by applying complementary techniques, i.e., powder X-ray diffraction (XRD), pair distribution function (PDF) analysis, X-ray absorption spectroscopy (XAS), and $^{23}Na/^{31}P$ magic-angle-spinning (MAS) nuclear magnetic resonance (NMR) spectroscopy. The results indicated an unexpectedly complex reaction pathway including formation of several intercalation compounds, depending on the amount of Na inserted at the early discharge states and subsequent conversion to Na_2S and strongly disordered metallic Cr at the completely discharged state. While XAS measurements suggest no further presence of intermediates after formation of Na intercalation compounds, several different phases are detected via MAS NMR upon continued discharging. Especially the data obtained from the MAS NMR investigations therefore point toward a very complex reaction pathway. Furthermore, solid electrolyte interphase (SEI) formation, resulting in the presence of NaF, was observed. After recharging the anode material, no structural long-range order occurred, but short-range order indeed resembled the local environment of the starting material, to a certain extent.

KEYWORDS: *sodium-ion battery, anode material, $CrPS_4$, sodium intercalation, X-ray scattering, pair distribution function, X-ray absorption, MAS NMR*

1. INTRODUCTION

To reach the targeted goal to limit global warming, which was confirmed by most states worldwide in the Paris Agreement, a shift from fossil energy sources toward clean alternative technologies using wind, solar, tidal, or geothermal energy is strongly required. As a part of this transition, suitable energy storage systems must be identified and developed to compensate the natural fluctuation of electrical energy output from sustainable technologies.[1−4] This topic is already discussed in the literature and it remains questionable if the established Li^+ ion batteries (LIBs) are suitable for this purpose. The alternative are systems based on Na, because of its similar chemical properties and the high abundance worldwide. Nonetheless, Na has a higher atomic weight, as well as a larger ionic radius and a lower chemical potential. However, these properties are no major drawbacks, as the total

Received: August 6, 2021
Accepted: October 26, 2021
Published: November 10, 2021

https://doi.org/10.1021/acsami.1c14980
ACS Appl. Mater. Interfaces 2021, 13, 54936−54950

weight of the device is not as important for stationary energy storage as for mobile applications, where a low weight and high energy density is necessary or beneficial. In battery science, sodium-ion batteries (SIBs) have been in focus for several years and one of the biggest challenges is the development of anode materials that provide high specific capacities, long-term stability consisting of inexpensive, earth-abundant, and sustainable elements.[3] To ensure high specific capacities, materials undergoing conversion instead of intercalation reactions are preferred, where the constituents of the active material are completely reduced enabling uptake and release of larger amounts of alkali-metal ions per formula unit (f.u.).[1] Widely investigated conversion materials are, e.g., binary[5−13] and, less often, ternary[14−16] metal chalcogenides, as well as alloys[17,18] and other metal salts such as (fluoro)phosphates or polyanionic compounds.[19,20] Many of these compounds contain elements such as Cu, Ni, and/or Co, which are also key ingredients of LIBs, but in terms of sustainability, availability, and price, these elements are quite problematic. Choosing elements that are less problematic and/or developing efficient battery recycling concepts is a prerequisite for producing inexpensive and sustainable electrode materials in the long term.[3] Regarding the anodes for SIBs, different sulfides were studied intensely and are considered promising active materials in SIBs.[12,15,16,21−25] The M−S bond is less polar than a M−O bond, which is favorable for conversion reactions in SIBs, because lower ionicity leads to decreasing overpotentials during charging and discharging.[26] However, interesting active materials such as transition-metal orthothiophosphates (M_xPS_4) are less often studied, although the presence of phosphorus might be beneficial, because of the possibility to form alloys with sodium, providing higher specific capacities.[18,27] Orthothiophosphates $M^{III}_xPS_4$ (M^{III} = Cr, B, Al, Ga, In, Bi; M^{I} = Li, Na, Ag, Cu; M^{II} = Pd) exhibit various dimensionalities and contain transition or alkali metals, as well as *p*-block elements with oxidation numbers ranging from 1 to 3.[28−38] The layered compound $CrPS_4$ has been thoroughly investigated since its discovery in 1976.[28] The magnetic properties,[39−41] optical behavior,[39,42] and chemical compositions and oxidation states,[43] spin dynamics, and electronic and thermal transport properties[41,44,45] were studied. Applying different exfoliation techniques generates few layer $CrPS_4$ materials, which are mainly studied with respect to changes of the properties, depending on the thickness and/or number of layers.[46−48] Applications in energy storage and conversion such as catalysis[41] and as intercalation electrodes in LIBs were investigated.[39] Although $CrPS_4$ is known to intercalate up to 2 Li/f.u. using butyl-lithium, electrochemical intercalation shows rather poor intercalation behavior with only <1 Li/f.u.[39] However, as far as we know, $CrPS_4$ has never been investigated for the application in SIBs until now. In addition, chromium is not a typical main element of battery technology but has a slightly higher abundance than Ni, Co, or Cu,[19] which makes it a possible substitution for these elements. Although electrochemical intercalation of Li into $CrPS_4$ exhibits very low degrees of intercalation, the application in SIBs is promising, if a conversion mechanism occurs during charging and discharging. Since sodium and phosphorus can form alloys, a conversion-alloying mechanism also seems reasonable. For a conversion reaction with subsequent alloying (eq 1), the theoretically very high specific capacity is calculated to be 1396 mAh g^{-1}.

$$CrPS_4 + 11Na^+ + 11e^- \rightarrow Cr + Na_3P + 4Na_2S \quad (1)$$

A conversion reaction without subsequent alloying theoretically delivers a specific capacity of 1015 mAh g^{-1} and follows eq 2:

$$CrPS_4 + 8Na^+ + 8e^- \rightarrow Cr + P + 4Na_2S \quad (2)$$

Both of these possible reaction pathways provide very high specific capacities in SIBs, which is beneficial for future applications. Therefore, we investigated the electrochemical behavior of crystalline $CrPS_4$ as anode material in SIBs and applied a variety of methods including X-ray diffraction (XRD) and X-ray absorption spectroscopy (XAS), and pair-distribution function analyses (PDF), as well as $^{31}P/^{23}Na$ magic-angle-spinning (MAS) nuclear magnetic resonance (NMR) spectroscopy to elucidate the reaction mechanism during the sodiation process.

2. EXPERIMENTAL SECTION

2.1. Synthesis. $CrPS_4$ was synthesized via chemical vapor transport. Stoichiometric amounts of chromium (Alfa Aesar, 99.94%), red phosphorus (Knapsack AG, 99.9999%), and excess sulfur (Chempur, 99.999%) were heated in a quartz glass ampule, which was previously sealed under vacuum ($<10^{-4}$ mbar). The ampule was placed in a tube furnace and heated to 723 K within 4 h. This temperature was maintained for 24 h and afterward increased to 973 K within 2.5 h. After this temperature was reached, a temperature gradient to 953 K was established within the quartz glass ampule to start the transport reaction. Excess sulfur was utilized as transport agent and the transport reaction was performed for 2 weeks.

2.2. Electrochemical Tests. 70 wt % of $CrPS_4$, 20 wt % SUPER C65 (Timcal, Switzerland), and 10 wt % polyvinylidene difluoride (PVDF, Solvay, Germany) were mixed and subsequently suspended in *N*-methyl-2-pyrrolidone (NMP, Fisher Bioreagens, 99.8%) for electrode preparation. The obtained slurry was spread on Cu foil applying the doctor-blade casting method. Afterward, the electrode film was dried overnight at room temperature and for several hours in a vacuum oven at 333 K. For test cell assembly, circular electrodes with a diameter of 10 mm (0.88−1.34 mg cm^{-2} active material) were punched out of the film. The electrochemical reaction was conducted in Swagelok-type cells, which were assembled in an argon-filled glovebox (99.999% Ar, MBraun Unilab, <1 ppm of H_2O; <1 ppm of O_2). Glass fiber filters (Whatman, United Kingdom) and Celgard membranes were used as separators. Sodium metal foil was used as a counter electrode and a 1 M solution of $NaCF_3SO_3$ (abcr, 98%) in bis(2-methoxyethyl)ether (Diglyme, Acros Organics, 99+%, extra dry) was used as an electrolyte. Galvanostatic cycling within the potential range of 3.0−0.1 V was performed on Neware 8 channel battery analyzers. For battery performance tests, a current rate of 0.1 A g^{-1} for the first and 1 A g^{-1} for subsequent cycles were used. For rate capability tests, current rates of 0.1, 0.2. 0.5, 1.0, 1.5, 2.0, and 3.0 A g^{-1} were applied. Constant current−constant voltage (CCCV) charge mode was applied for all cycles with current rates of ≥0.5 A g^{-1}. The final current rate of the CCCV mode was set to 0.1 A g^{-1} for the long-term stability tests and to 0.2 A g^{-1} for the rate capability measurements. Cyclic voltammetry (CV) measurements were performed on a Zahner XPOT within the same voltage range as mentioned above and at a scan rate of 0.1 mV s^{-1}.

2.3. Material Characterizations. Powder XRD was conducted using Cu Kα radiation (λ = 1.54058 Å) with a PANalytical diffractometer equipped with a 1D PIXcel detector. SEM and EDX experiments were performed on a Philips ESEM XL 30 system that was equipped with an EDAX New XL-30 detector. Raman spectra were recorded at RT on a Bruker Vertex70 RAM II FT-Raman spectrometer using an Nd:YAG laser with an excitation wavelength of λ = 1064 nm and a liquid-nitrogen-cooled, highly sensitive Ge detector with a resolution of 3 cm^{-1}.

https://doi.org/10.1021/acsami.1c14980
ACS Appl. Mater. Interfaces 2021, 13, 54936−54950

ACS Applied Materials & Interfaces www.acsami.org Research Article

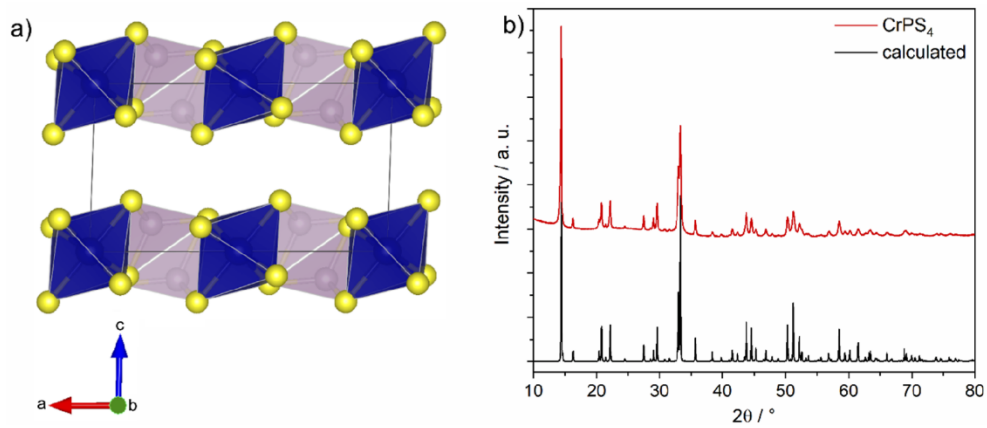

Figure 1. (a) Crystal structure of $CrPS_4$ along the *b*-axis. Blue octahedra indicate Cr^{3+}, purple tetrahedra P^{5+} coordination and yellow spheres illustrate the sulfur lattice. The structure was plotted using the software VESTA 3.4.0[52] and crystallographic data from the literature.[39] (b) XRD pattern of $CrPS_4$ compared to a pattern calculated from literature data.[39]

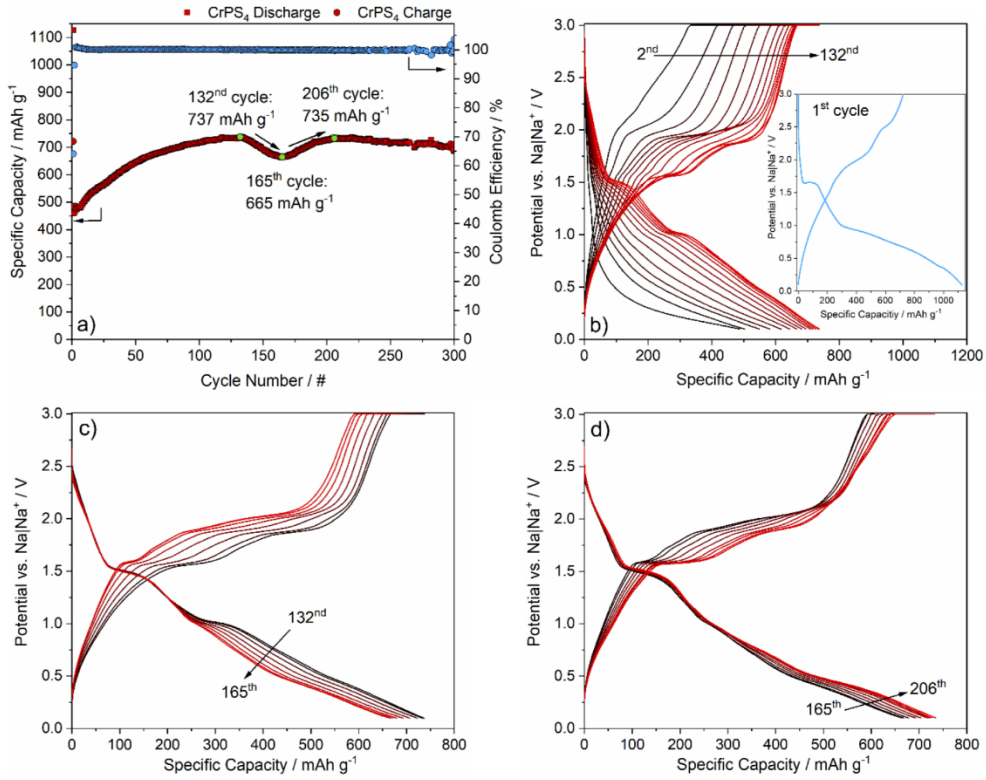

Figure 2. (a) Electrochemical cycling performance and Coulombic efficiency of $CrPS_4$ test cells against Na. A current rate of 1 Ag^{-1} was applied within a potential window of 3.0 − 0.1 V. Discharge and charge profiles of (b) cycles 1−132 (inset shows the first cycle), (c) cycles 132−165, and (d) cycles 165−206 of the $CrPS_4$ electrode. In panel (b), every 10th cycle is displayed; in panels (c) and (d), every 5th cycle is displayed.

2.4. Investigation of the Mechanism by XRD, PDF, XAS, and $^{23}Na/^{31}P$ MAS NMR. For the investigation of the reaction mechanism, samples were prepared by pressing 70 wt % $CrPS_4$ and 30 wt % SUPER C65 into pellets and assembling them in Swagelok-type cells. The electrochemical reaction was interrupted after uptake of a distinct amount of sodium (discharge) and afterward the Swagelok cells were disassembled in an argon glovebox. To remove the electrolyte, electrodes were rinsed with pure diglyme and dried for 1 day. These air-sensitive samples were permanently handled and transported in an inert atmosphere.

XRD and PDF experiments were performed in Debye−Scherrer geometry using high-energy synchrotron radiation at beamline P02.1, Petra III (DESY, Hamburg) at a wavelength of $\lambda = 0.207$ Å (60 keV). Samples were prepared in borosilicate capillaries with a diameter of

https://doi.org/10.1021/acsami.1c14980
ACS Appl. Mater. Interfaces 2021, 13, 54936−54950

0.7 mm. The sample-to-detector distance (SDD) for XRD experiments was 1010 mm and 350 mm for PDF experiments. The detector used was a PerkinElmer XRD1621 2D detector. The obtained 2D data were processed using the software DAWN Science,[49] and xPDFsuite[50] was used to obtain the PDF (Q_{max} = 19 Å^{-1}). To account for instrumental contributions to XRD, a LaB_6 (NIST 660b) standard was measured. An empty capillary was measured under identical conditions to subtract the contribution of the glass capillary from the PDF.

XAS experiments on the Cr K-edge were performed at the beamline B18, Diamond Light Source (U.K.). The samples were diluted with carbon, pressed into pellets with a diameter of 8 mm, and sealed between Kapton foil. Each sample was measured three times at the minimum with a collection time of 3 min and these spectra were merged. For energy calibration of the raw data, Cr foil was used. To ensure appropriate normalization and background subtraction, the pre-edge region was described by a linear fit, and for the post-edge region, a cubic polynomial fit was applied. XAFS data reduction was performed by using a calculated background from the Autobk algorithm of the program Athena.[51] A fitting range in k-space between 3.0 Å^{-1} and 12.5 Å^{-1} was chosen by applying k^3 weighting. The k^3-weighted $\chi(k)$ function was then multiplied by a Kaiser−Bessel window and Fourier-transformed into R-space in order to obtain the pseudoradial distribution function (pRDF) $|\chi(R)|$ without correcting the distances by a phase shift.

^{23}Na and ^{31}P magic-angle spinning (MAS) nuclear magnetic resonance (NMR) spectroscopy was performed on a Bruker Avance neo 200 MHz spectrometer at a magnetic field of 4.7 T, corresponding to resonance frequencies of 52.9 MHz (^{23}Na) and 81.0 MHz (^{31}P). Spinning was done in 1.3 mm rotors at 60 kHz. Spectra were acquired with a rotor-synchronized Hahn-echo pulse sequence, a recycle delay of 1 s, and $\pi/2$ pulse durations of 1.3 μs (^{23}Na) and 0.95 μs (^{31}P). The NMR shifts of ^{23}Na and ^{31}P were referenced to an aqueous 1 M NaCl solution and to H_3PO_4 (85%), respectively.

3. RESULTS AND DISCUSSION

3.1. Characterization of Pristine $CrPS_4$. $CrPS_4$ crystallizes in the monoclinic noncentrosymmetric space group $C2$.[28,39,41,42] The crystal structure (Figure 1a) is based on a hexagonal close packing of puckered sulfur layers. The trivalent Cr^{3+} ions are located in a distorted octahedral environment of S^{2-} anions, and P^{5+} is arranged in a distorted tetrahedral coordination of S^{2-}. The CrS_6 octahedra are connected via common edges forming chains, which are linked by the PS_4 tetrahedra to layers along the [001] direction.[28,39,42,44] The XRD pattern (Figure 1b) of the pristine material, compared to a calculated pattern using data from the literature,[39] reveals that phase-pure and crystalline $CrPS_4$ was obtained.

Raman spectroscopy also confirms the presence of $CrPS_4$ (see Figure S1 in the Supporting Information) and EDX measurements (see Table S1 in the Supporting Information) demonstrate ratios of Cr, P, and S close to the expected values, yielding the composition $Cr_{0.98}P_{1.06}S_{3.95}$. In addition, SEM investigations (Figure S2 in the Supporting Information) confirm the layered nature of the compound.

3.2. Electrochemical Performance. For galvanostatic long-term cycling, a current rate of 0.1 A g^{-1} for the first cycle and a rate of 1.0 A g^{-1} for subsequent cycles were applied (Figure 2a). The capacity of the first discharge of 1226 mAh g^{-1} corresponds to ~9.7 Na/f.u., while the first charge process only yields 722 mAh g^{-1} (~5.7 Na/f.u.). The discharge and charge capacities of the second cycle are significantly lower at 486 mAh g^{-1} (~3.8 Na/f.u.) and 460 mAh g^{-1} (~3.6 Na/f.u.), respectively. Nevertheless, starting from the third cycle, the Coulombic efficiency reached ~100% and within the following 130 cycles, the discharge capacity rises to 737 mAh g^{-1} (~5.8 Na/f.u.) and afterward drops again to 665 mAh g^{-1} (~5.2 Na/f.u.) in the 165th cycle. After passing this minimum, the capacity recovers, increasing to 735 mAh g^{-1} (~5.8 Na/f.u.) in the 206th cycle, followed by a slight but steady decrease, reaching a reversible specific capacity of 687 mAh g^{-1} (~5.4 Na/f.u.) in the 300th cycle. The initial decrease and subsequent recovery of the specific capacity was already observed for several electrode materials in SIBs and was explained by different phenomena.[15,21,25,53,54] In most cases, the underlying reaction mechanism during long-term cycling changes and the capacity recovery occurs over a large number of cycles.[15,25,53] For the Na-CuS system, a relatively fast recovery of the initial capacity loss was observed, which was explained by a combination of synergistic effects, i.e., the formation of semicoherent phase interfaces arising from multiphase transitions causing stress relaxation and preventing random pulverization.[21] Because a similar behavior is found for $CrPS_4$, at least comparable effects may play a key role. The evolution of the discharge and charge profiles (Figures 2b−d) clearly indicates changes of the reaction mechanism during long-term cycling. The initial discharge profile (see Figure 2b, inset) shows a potential decrease from 3.0 V to 1.65 V, where an electrochemical plateau is developed, typical for a two-phase reaction caused by intercalation of Na into the empty layers of $CrPS_4$. Further Na uptake leads to a steep decrease of the potential until ~0.98 V is reached, followed by a steady decrease, finally reaching a discharge capacity of 1226 mAh g^{-1} (~9.7 Na/f.u.). The potential of the first charge profile quickly rises from 0.1 V to 1.98 V, where a pseudoplateau is developed. Afterward, the potential rises again until the next pseudoplateau occurs at 2.51 V. Further charging exhibits a potential increase delivering an overall charge capacity of 722 mAh g^{-1} (~5.7 Na/f.u.). Considering the possible reaction pathways represented by eqs 1 and 2, the discharge capacity is lower than expected for the reaction described by eq 1, but is larger assuming a pathway according to eq 2. However, solid electrolyte interphase (SEI) formation should lead to a discharge capacity larger than the theoretical value, making a reaction according to eq 1 highly unlikely (i.e., the formation of Na_3P can be most probably excluded). However, if only NaP is generated, the theoretical capacity of 1142 mAh g^{-1} matches the experimental value, taking SEI formation into account. Moreover, a contribution to the specific capacity by cointercalation of solvent molecules from the electrolyte into the active material cannot be excluded and might be a possible explanation for the high specific capacity of the first discharge step. Therefore, a reaction mechanism according to eq 2, in which the difference between expected and observed specific capacity is contributed by a combination of SEI formation and cointercalation of solvent molecules seems possible as well. However, the irreversible capacity decrease for the first cycle of 504 mAh g^{-1} corresponds to a loss of ~4.0 Na/f.u. Usually, the capacity loss between initial discharging and charging due to SEI formation is not as large as that observed, indicating a strongly altered reaction mechanism for the first charge process. The profiles of the following 131 cycles (Figure 2b) significantly differ from the first one and no distinct potential plateaus can be identified during early cycling stages: the potential steeply decreases from 3.0 V to 0.5 V, followed by a continuous reduction until the cell is discharged. In the charging curve, the potential significantly increases from 0.1 V to 2.1 V, where the slope flattens slightly with further rising

https://doi.org/10.1021/acsami.1c14980
ACS Appl. Mater. Interfaces 2021, 13, 54936−54950

ACS Applied Materials & Interfaces www.acsami.org Research Article

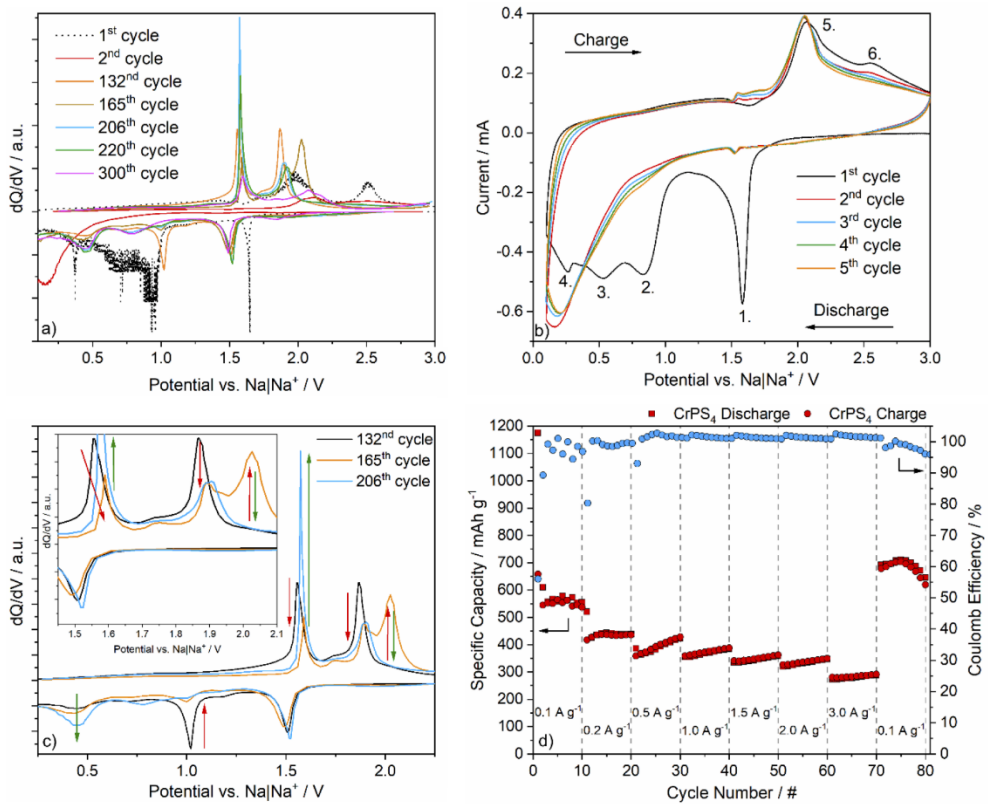

Figure 3. (a) dQ/dV analysis of selected cycles during long-term cycling, (b) CV curves recorded with a scan rate of 0.1 mV s^{-1} within a potential range between 3.0 V and 0.1 V and (c) dQ/dV curves of the 132nd, 165th, and 206th cycles. The red and green arrows indicate the redox processes responsible for capacity decrease (red) and increase (green). (d) Rate capability at several current rates ranging from 0.1 A g^{-1} to 3.0 A g^{-1} for $CrPS_4$ test cells against Na within a potential window of 3.0 V to 0.1 V.

potential, until the cell is completely charged. Toward the 132nd cycle, two pseudoplateaus in the discharge profile develop at ∼1.51 and 1.02 V, as well as at ∼1.56 and 1.87 V in the charge profile, accompanied by an increasing specific capacity. Another change of the discharge and charge curves occurs from the 132nd cycle to the 165th cycle (Figure 2c). While the first pseudoplateau at 1.51 V does not show any changes, the second pseudoplateau at ∼1.02 V nearly disappeared in the discharge profile reaching the 165th cycle. The pseudoplateau in the charge curves at ∼1.56 V slightly shifts to 1.59 V and the plateau itself is somewhat smaller, whereas the pseudoplateau at 1.87 V shifts to 2.02 V and is considerably more pronounced in the 165th cycle, compared to the 132nd cycle. These alterations cause a decreasing specific capacity between the 132nd cycle and the 165th cycle. Finally, a further change of the curves is observed between the 165th cycle and the 206th cycle (Figure 2d). While the pseudoplateau in the discharge profiles at ∼1.51 V is not affected, at lower potentials, a very weak pseudoplateau at ∼0.44 V develops. In the charge curves, the small pseudoplateau at 1.59 V becomes more intense and shifts to ∼1.57 V, while the broad pseudoplateau at ∼2.02 V shifts back to 1.89 V and is less pronounced again. These changes of the electrochemical behavior between the 165th cycle and the 206th cycle are accompanied again by an increase in specific capacity.

The alterations of the potential plateaus are better identified in the dQ/dV curves (Figure 3a). All events already discussed above appear as well-pronounced reduction and oxidation signals. More interestingly, the dQ/dV curves clearly show that the 206th and 220th cycles exhibit identical signals for oxidation and reduction process, indicating that no further changes of the mechanism occur. Regarding the 300th cycle, no alterations for the reduction process can be detected, but the signal for the second oxidation process has changed from 1.89 V to ∼2.07 V. Since this signal is the only one changing, it is most likely an early sign of electrode degradation during long-term cycling. Nevertheless, after the 300th cycle, a high reversible specific discharge capacity of 687 mAh g^{-1} is obtained. The observations made here point toward a steadily changing reaction mechanism during long-term cycling. To account for not well-resolved dQ/dV curves of the first cycle, additional CV measurements (Figure 3b) were performed. The CV curves clearly show four reduction processes but only two oxidation processes in the first cycle. The first and most intense reduction peak at ∼1.58 V (peak 1) is assigned to the intercalation of Na^+ into the interlayer space of $CrPS_4$, which is accompanied by the reduction of Cr^{3+}. The reduction of $Cr^{2+/3+}$ and Cr^{3+} was recently confirmed to occur at a potential of ∼0.4 V for Cr_3S_4 and $NiCr_2S_4$ against sodium.[55] Therefore, we assign the reduction process at ∼0.53 V (peak 3) to the reduction of Cr^{2+} to the metallic state. The origin of the

https://doi.org/10.1021/acsami.1c14980
ACS Appl. Mater. Interfaces 2021, 13, 54936−54950

reduction peaks occurring at ~0.83 V (peak 2) and ~0.26 V (peak 4) remains uncertain. A stepwise reduction of P^{5+} as well as SEI formation are possible explanations for the occurrence of these peaks. During the charging process, an intensive oxidation peak is observed at ~2.06 V, while a smaller and not well-resolved second oxidation event is detected at a potential of ~2.55 V. Taking the initial capacity drop (Figure 2b, inset) into account, we suggest a two-step oxidation of phosphorus to its starting oxidation state of P^{5+} in the first charge process, while the oxidation of Cr^0 is kinetically hindered. The expected oxidation peak for Cr^0/Cr^{3+} is ~1.2 V[55] or slightly above at ~1.5 V, which potentially is the reason for the very small oxidation and reduction peaks in the CV curve (Figure 3b) at this potential. In the second and subsequent cycles, the oxidation process at ~2.55 V disappears, which might be an indication that phosphorus is only oxidized to P^{3+} after the first cycle. The CV curves of cycles 2−5 have an almost uniform appearance, but differ strongly from the first cycle, which is typical for a conversion mechanism. The CV curves exhibit only one peak for the reduction (~0.19 V) and oxidation (~2.04 V), which, in the context of our assumptions, is related to the oxidation and reduction of P^0/P^{3+}. The corresponding Na uptake amounts to 3.6 Na/f.u. in the second cycle, which is in agreement with the oxidation of P^0 to P^{3+}, as well as a minor portion of Cr^0 to Cr^{3+}. With increasing cycle number, deactivated Cr^0 gradually starts to participate in the electrochemical reaction again, potentially leading to the development of a second pseudoplateau in the charge profiles (Figure 2b), as indicated by the peak in the dQ/dV curve of the 132nd cycle at 1.56 V (see Figures 3a and 3c). Consequently, the specific capacity steadily increases until the majority of Cr is involved in the electrochemical reaction again. The corresponding uptake in the 132nd cycle is 5.8 Na/f.u., which is nearly the expected value of 6 Na/f.u. for the proposed reaction. Furthermore, after the majority of Cr is activated again, the electrochemical reaction obviously is subject to mechanistic changes, causing a temporary decrease in capacity, which is evidenced by the changes occurring in the dQ/dV curves of the 132nd, 165th, and 206th cycles (Figure 3c, inset).

However, it is noteworthy that CV curves and dQ/dV analysis alone are not capable of providing deep insights into mechanistic aspects of the electrochemical reaction, but rather give indications about occurring redox processes. The reaction mechanism of the first cycle is discussed in more detail in section 3.3.

Rate capability measurements (current rates = 0.1, 0.2, 0.5, 1.0, 1.5, 2.0, 3.0, and again 0.1 A g^{-1}, applied for 10 cycles each) are shown in Figure 3d. The lowest rate (0.1 A g^{-1}) delivers a specific discharge capacity in the 10th cycle of 555 mAh g^{-1} (~4.4 Na/f.u.), while increasing the current rate leads to lower values after 10 cycles (see Table 1). We note that the initial capacity increases for every rate within the 10 cycles applied, and by switching back to 0.1 A g^{-1}, a capacity retention of 116% is reached. However, a decrease of capacity is observed after the first 5 cycles at this current rate. This decrease in capacity potentially has the same origin as the temporary reduced capacity during long-term cycling. In contrast, this capacity decrease occurs earlier in the rate capability experiments than in the long-term measurements, which might be caused by the high current rates overcoming the assumed kinetic hindrance more quickly, because of a higher energy input into the system. Nevertheless, the results indicate a good cycling stability at higher current rates, as well as an extraordinary capacity retention after applying high current rates.

Table 1. Observed Specific Discharge Capacities at Different Current Rates and Corresponding Capacity Retentions

current rate (A g^{-1})	specific capacity (mAh g^{-1})	capacity retention (%)
0.1	555	–
0.2	438	79
0.5	422	76
1.0	384	69
1.5	359	65
2.0	346	62
3.0	288	52
0.1	645	116

It is noteworthy that the electrochemical data measured for $CrPS_4$ is comparable with high-performance binary sulfides (see Table 2), even though those binary compounds are often improved by adding highly conductive additives, such as reduced graphene oxide (rGO) or carbon nanotubes (CNT) or are parts of other advanced carbonaceous composites.

Table 2. Comparison between Selected Indicators of Electrochemical Performance of $CrPS_4$ and Binary Sulfide Anode Materials

anode	long-term stability: capacity [mAh g^{-1}]/ current rate [mA g^{-1}] /cycle number [#]	rate capability: capacity [mAh g^{-1}]/current rate [mA g^{-1}]	reference
$CrPS_4$	687/1000/300	288/3000	this work
NiS/C[a]	208/1475/500	250/2950	56
NiS/rGO	483/200/100	393/2000	57
NiS/CNT	394/200/100	331/2000	57
FeS_x@CS[b]	639/100/100	404/2000	58
Fe_7S_8/C-G[c]	478/100/100	306/2000	59
CoS_xNF@GF[d]	491/500/100	479/2000	60

[a]Composite derived from parent MOF structure. [b]Material embedded in porous carbon hollow spheres. [c]3D carbon-wrapped iron sulfide interlocked graphene composite. [d]Nanoflakes grown on graphite foam.

3.3. Investigations of the Reaction Mechanism. Electrodes of pressed powder were used to obtain a larger amount of material necessary for the variety of characterization methods. The initial discharge capacities are lower than for electrodes cast on Cu foil and the specific discharge capacities are lower than expected according to eq 2, in contrast to film electrodes. Therefore, to be sure that the completely discharged state is reached, film electrodes were also prepared for characterization. The initial average discharge capacity for the film electrodes of 1167 mAh g^{-1} (~9.2 Na/f.u.) is larger than that for powder electrodes (785 mAh g^{-1}; ~6.2 Na/f.u.) (see Table S2 in the Supporting Information), but the discharge profiles are very similar (see Figure S3 in the Supporting Information). Beside early termination of the electrochemical reaction in powder electrodes, the first electrochemical plateau occurs at slightly lower potentials (~1.4 V) and decreases continuously in contrast to film electrodes, which exhibit a very stable potential plateau at ~1.65 V. These deviations between the two electrode types are potentially caused by Na^+ transport limitations in the powder electrodes, because of higher mass loading (~30.4 mg cm^{-1} vs ~0.88 mg cm^{-1}). The average capacity for the first charge

https://doi.org/10.1021/acsami.1c14980
ACS Appl. Mater. Interfaces 2021, 13, 54936−54950

process (see Table S2) is 774 mAh g^{-1} (~6.1 Na/f.u.) for film electrodes, whereas, for powder electrodes, no complete cycle could be obtained (see Figures S3–S6 in the Supporting Information for details on powder cells). An exemplary discharge/charge profile and corresponding sodium uptake and release of the $CrPS_4$ electrode is depicted in Figure 4.

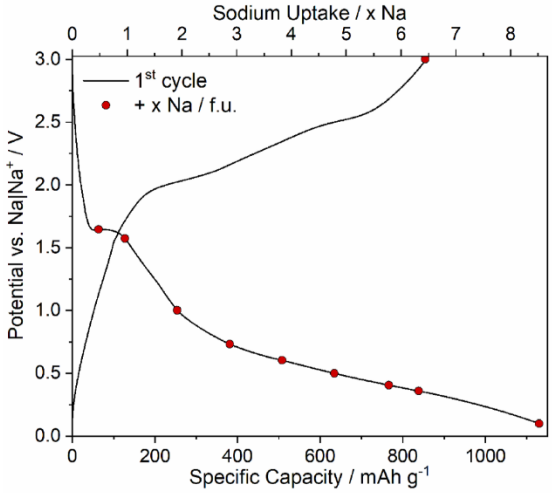

Figure 4. Exemplary depiction of discharge and charge profiles of a typical $CrPS_4$ film electrode during sodium uptake and release. The investigated discharge and charge states are marked as red dots.

3.3.1. X-ray Diffraction Experiments. XRD patterns (Figure 5; see Figure S4 in the Suporting Information for full range) reveal a slight reduction of crystallinity upon uptake of 1 Na/f.u. as well as the appearance of new reflections at 1.7° 2θ and 1.8° 2θ (shoulder), which gain intensity after insertion of 2 Na/f.u. and the reflection at 2.2° 2θ becomes more intense at this stage. In addition, new reflections developed between 5.9°

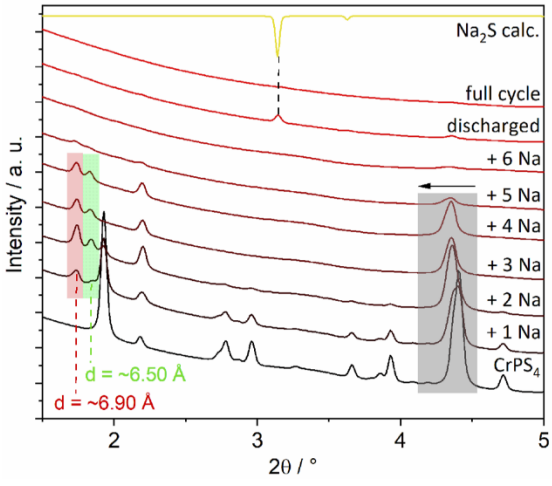

Figure 5. XRD patterns of the $CrPS_4$ electrode collected at different discharge states compared to the pattern of Na_2S calculated from literature data.[61]

2θ and 6.7° 2θ (Figure S4), as well as a slight shift of the reflection of the starting material at 4.40° 2θ to 4.36° 2θ, indicating the formation of a new phase. After the uptake of 3 Na/f.u. reflections of the pristine material disappeared and the most intense reflection is now located at 4.35° 2θ, which is less intense than for 2 Na/f.u. During further Na insertion, the intensity of the reflections continuously decreases until no crystalline phase can be observed after an uptake of 6 Na/f.u. and only reflections of Na_2S can be observed in the discharged state (see Figure 5 and Figure S4). Characterization of discharged powder cells indicate that the crystallization of Na_2S starts between 6 and 6.2 Na/f.u. (see Figure S4). In addition to these observations, some peculiarities should be briefly discussed: (i) the most intense reflections at 4.40° 2θ shifted to lower scattering angles; (ii) the final position is reached after 3 Na/f.u.; and (iii) the highest intensity of the new reflections is observed after an uptake of 2 Na/f.u.

In the following analysis of the XRD data, we assume that the crystal symmetry is not changed during Na uptake. We are aware that this is not necessarily the case, as demonstrated especially for transition-metal dichacolgenides, where, in the equilibrium state, different structure types and even superstructures were observed.[62−64]

A closer look at the development of the XRD patterns at the early discharge states (Figure 6) evidences the formation and

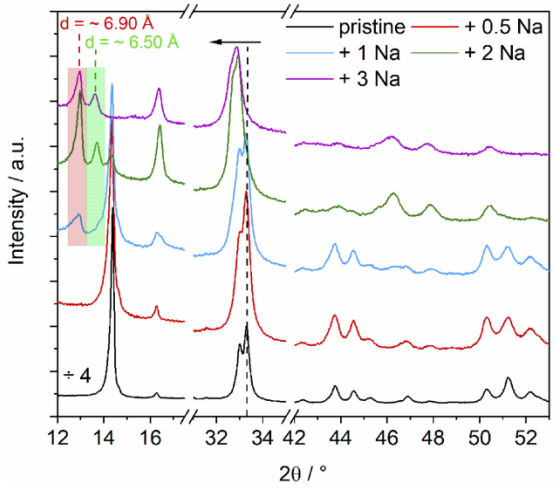

Figure 6. XRD patterns of the $CrPS_4$ electrode collected at early states of discharge. 2θ ranges of 12°−17.5° 2θ, 31°−35° 2θ. and 42°−53° 2θ are shown. Intensities of the pristine sample were divided by 4 for better visibility.

development of new reflections at 12.9° 2θ and 13.7° 2θ, which strongly suggest an intercalation process. The first new reflection at 12.9° 2θ ($d \approx 6.90$ Å) occurs after insertion of 1 Na/f.u., while the second one is observed as a shoulder and is only clearly visible after the uptake of 2 Na/f.u. at 13.7° 2θ ($d \approx 6.50$ Å). For pristine $CrPS_4$, the d-value of the (001) planes is calculated as ~6.14 Å, using eq 3:

$$d = c \sin \beta \tag{3}$$

A possible candidate for a Na inserted intermediate phase is Na_3PS_4 with a c-axis of 7.075 Å,[35] which is very similar to the d-value of 6.90 Å of the first observed new reflection. Despite

https://doi.org/10.1021/acsami.1c14980
ACS Appl. Mater. Interfaces 2021, 13, 54936−54950

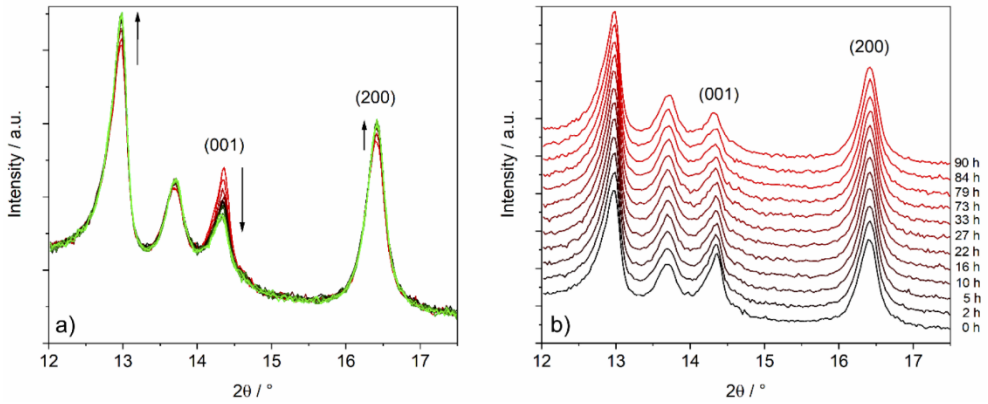

Figure 7. Time-dependent XRD measurements of the $CrPS_4$ electrode after insertion of 2Na/f.u. depicted (a) on top of each other and (b) stacked for better visibility. The (001) and (200) reflections of the pristine $CrPS_4$ are labeled.

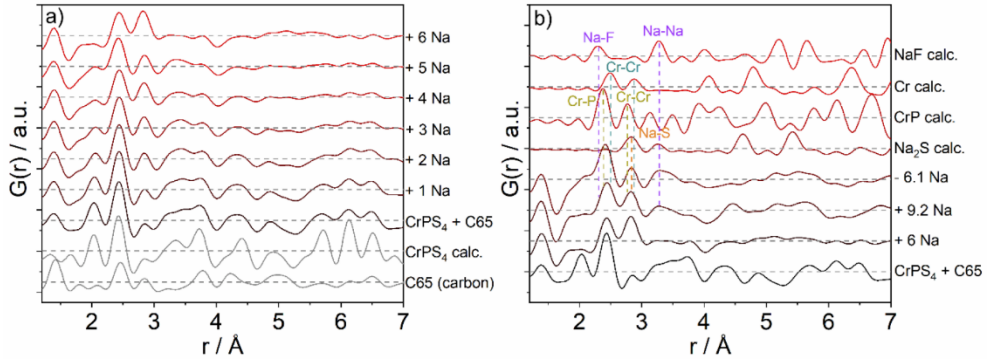

Figure 8. Pair distribution function (PDF) of $CrPS_4$ electrodes after uptake of several amounts of Na/f.u. (a) PDF in the range of 1.5−7 Å. The uptake of 1−6 Na/f.u. as well as the starting material, pure carbon and the PDF calculated from the structure of $CrPS_4$[39] is shown. (b) PDF in the range of 1.5−7 Å, showing the starting material, the uptake of 6 Na/f.u. and the discharged film electrode (+9.2Na/f.u.), and the PDF after a complete cycle (−6.1 Na/f.u.). For comparison, PDFs calculated from the structures of Na_2S,[61] CrP,[68] bcc Cr,[69] and NaF[70] are shown as well.

the differing crystal structures between Na_3PS_4 and $CrPS_4$ the expansion of the *c*-axis of $CrPS_4$ is a clear hint for Na^+ intercalation. Simultaneously with the Na^+ intercalation, the (200) reflection gains intensity, because of the scattering power of Na in the van der Waals gaps. Along with this change, the intensity of reflections in stacking direction increases and shifts toward larger *d*-values. Assuming that the symmetry of the structure was not changed during Na insertion, we assign the reflection at d = 6.90 Å as (001) of the intercalated compound. For transition-metal dichalcogenides, it was proposed that the expansion of layers by intercalation of A^+ cations is proportional to the radius of A^+.[65] In addition to this geometrical effect, electronic effects cannot be neglected, such as, e.g., repulsive interactions between the negatively charged layers after uptake of the electrons during intercalation. The interlayer expansion of Δc = 0.71 Å observed after insertion of 1 Na/f.u. is lower than expected, considering the effective ionic radius of Na^+ in 6-fold coordination geometry of 1.02 Å,[66] pointing to an intercalation of ca. 0.7 Na/f.u. For the reflection located at d = 6.50 Å, Δc amounts to 0.31 Å, i.e., these domains contain a lower Na content. However, these explanations are based on the assumption that no structural phase transitions occur as observed, e.g., for Na intercalation in TiS_2.[67]

Indeed, some further changes are observed in different regions of the XRD patterns, which may indicate a phase transition and/or shifting of the slabs. But one should also keep in mind that electron transfer leads to a reduction of Cr^{3+} (d^3) to Cr^{2+} (d^4), changing the ionic radius and, consequently, the Cr−S bond length affecting reflection positions and intensities. The decreasing intensities after an uptake of 2 Na/f.u. are caused by significant reduction of coherently scattering domains and finally amorphization, which is completed after the uptake of 5−6 Na/f.u. (compare Figure 5).

Electrochemical intercalation results in host−guest complexes, which are not in equilibrium, considering the intercalation time. Increasing the waiting time after Na uptake leads to a relaxation similar to annealing at room temperature and changes of reflection intensities can be expected. This was investigated for a sample after insertion of 2 Na/f.u. (Figure 7). Several alterations occur within 90 h of relaxation time: (i) the (001) reflection of $CrPS_4$ loses intensity; (ii) the two reflections indicative for intercalated $CrPS_4$ become more intense; (iii) the intensity of the (200) reflection slightly increases; and (iv) no shift of the reflection position can be observed. This behavior might be explained by initial intercalation into edge regions of $CrPS_4$ domains and

https://doi.org/10.1021/acsami.1c14980
ACS Appl. Mater. Interfaces 2021, 13, 54936−54950

ACS Applied Materials & Interfaces www.acsami.org Research Article

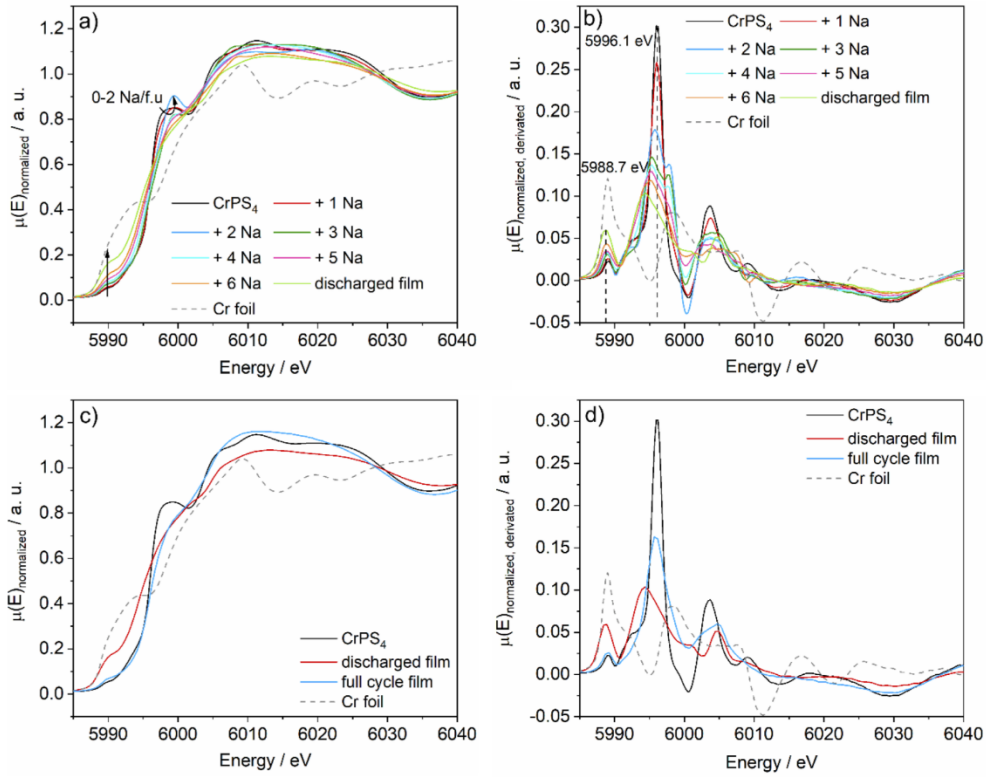

Figure 9. (a) XANES spectra at the Cr K-edge of $CrPS_4$ electrodes at different states of discharge and (b) the corresponding first derivatives. (c) XANES spectra of the pristine $CrPS_4$, compared with the electrode after a complete discharge and a full cycle, as well as bcc Cr foil, and (d) the corresponding first derivatives.

subsequent slow movement of Na^+ from these regions into the differently intercalated phases, thus reducing the amount of pristine $CrPS_4$.

Summarizing the findings led to the following conclusions:

(i) Na is intercalated into the van der Waals gaps of $CrPS_4$ during early stages of discharge, which was already suggested by the plateau in the discharge curve (Figure 2b, inset).

(ii) The occurrence of two intense reflections at 2 Na/f.u. indicates the formation of domains containing different amounts of Na within the interlayer space visualized by eq 4.

(iii) Beyond 3 Na/f.u., first domain sizes of $CrPS_4$ are successively reduced followed by amorphization and formation of Na_2S. After a complete cycle, no distinct reflections can be observed in the XRD pattern.

$$CrPS_4 + 2Na^+ + 2e^- \rightarrow Na_xCrPS_4 + Na_yCrPS_4$$
$$(x + y = 2 \text{ and } x \neq y) \quad (4)$$

The loss of crystallinity, as well as the observed structural alterations during the electrochemical reaction, are confirmed by PDF data (Figure 8; see Figure S5 in the Supporting Information for full range). After uptake of 6 Na/f.u., the spatial extension is decreased to ~7 Å (Figure 8) and no peaks corresponding to characteristic interatomic distances of $CrPS_4$ are detected. Only three distinct signals are left and two of them (1.42 and 2.44 Å) most likely correspond to amorphous carbon. During the uptake of Na up to 3 Na/f.u., rather subtle changes occur in the PDF curves (Figure 8a). The most pronounced alterations are the decreasing intensities of the signals at 2.04, 3.73, 4.32, 7.22, 11.02, and 13.01 Å, as well as increasing intensities at 2.84, 3.42, 6.87, and 12.01 Å. The PDF curve for 3 Na/f.u. exhibits only a few sharp signals at small distances up to ~4 Å, while, at larger distances, the signals are rather broad but still fit the distances of $CrPS_4$ quite well, indicating residual $CrPS_4$. On the other hand, a signal of an intercalation compound is expected at ~3.5 Å, according to XRD investigations. Indeed, increasing intensities at 3.42 Å for 2 Na/f.u. is a clear hint for the intercalation of Na^+ into $CrPS_4$ resulting in one or more Na_xCrPS_4 phases (see eq 4). XRD experiments suggested that the formation of Na_2S sets in after the uptake of 6 Na/f.u., which is confirmed by signals developing after this stage. However, only some of these signals match the calculated distances of Na_2S, which is caused by the highly defective nature of this compound (Figure 8b). For the fully discharged sample, only few signals are clearly developed. The signals at 2.41 and 2.83 Å match calculated PDF curves of Na_2S (2.83 Å: Na−S), Cr (2.50/2.88 Å: Cr−Cr), and NaF (2.32 Å: Na−F), as well as CrP (2.38/2.77 Å: Cr−P/Cr-Cr). The signal at 3.28 Å might correspond to the Na−Na distance of NaF and Na_2S. The PDF curve of a full cycled electrode (Figure 8b) is very similar to that of the discharged sample and only significant changes occurred for the intensity ratio of the

https://doi.org/10.1021/acsami.1c14980
ACS Appl. Mater. Interfaces 2021, 13, 54936−54950

ACS Applied Materials & Interfaces www.acsami.org Research Article

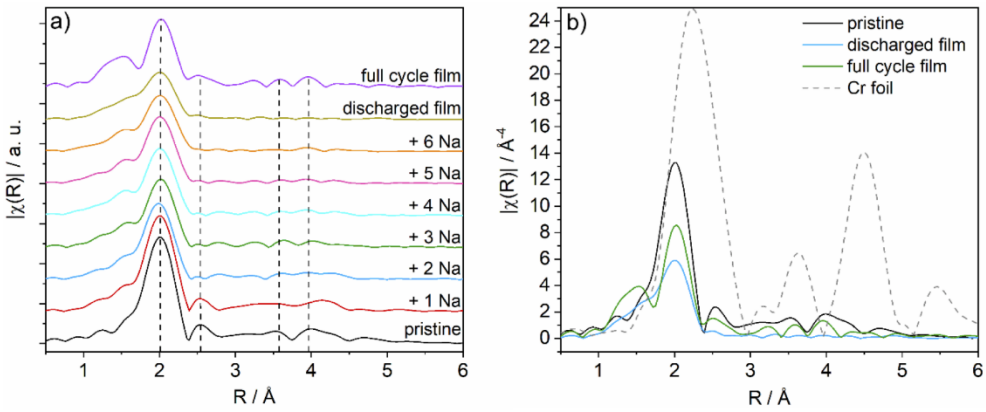

Figure 10. (a) FT pseudoradial distances for Cr absorber atoms of $CrPS_4$ electrodes at different discharge/charge states. (b) Comparison of pRDF of the pristine, completely discharged, full-cycled electrode and Cr foil.

signals at 2.41 and 2.83 Å, i.e., the former is much more intense than the latter indicating formation of phases with similar distances during charging. In addition, the intensity of the peak at 2.83 Å decreases but does not disappear, which is a hint that phases present in the discharged state do not fully participate in the charge process. The formation of a shoulder at 2.04 Å and the increasing intensity at 2.41 Å indicate the recovery of $CrPS_4$ (2.01/2.09 Å: P−S; 2.40/2.48 Å: Cr−S) on a local scale. At this stage of analyses of the PDF curves, it becomes clear that the expected complex mixture prevents assignment of distinct phases. To summarize the complex reactions, the XRD and PDF data indicate the formation of different compounds on the nanoscale and only Na_2S could be identified for >6 Na/f.u. However, after an intercalation reaction at the beginning (eq 4), a general conversion mechanism according to eq 2 generating amorphous Cr and Na_2S, as well as SEI formation accompanied by the formation of NaF is most probable, while recharging might lead to recovery of the local environment of $CrPS_4$.

3.3.2. X-ray Absorption Experiments. The X-ray absorption near-edge spectra (XANES) were collected at the Cr K edge at different states of discharge and first derivatives were used to determine XANES features and edge energy positions (Figure 9). Pristine $CrPS_4$ exhibits a weak pre-edge feature at 5989.1 eV, because of the dipole-forbidden but quadrupole-allowed 1s → 3d transition and the Cr K-edge is located at 5996.1 eV. A clearly defined white line (1s → 4p transition) can be observed at 6011.2 eV.

During Na uptake (see Figures 9a and 9b), the Cr−K edge shifts to lower energy (5995.8 eV) and gains intensity after insertion of 2 Na/f.u., while the 1s → 4p transition exhibits a slight decrease in intensity (Figure 9a). Further Na uptake leads to rotation around an isosbestic point at 5997.2 eV, accompanied by a steady decrease of the edge energy due to the reduction of Cr^{3+}, until no clearly defined edge feature is detectable, while the first derivative (Figure 9b) displays a signal at ∼5994.2 eV. Simultaneously, the pre-edge signal slightly shifts toward 5988.7 eV gaining intensity and reaching maximum intensity at the discharged state, resembling that of nanocrystalline elemental Cr. The differences between the spectrum of the discharged sample and the Cr foil is a phenomenon known for metal nanoparticles and amorphous alloys[54,71−73] caused by strong disorder and large amounts of surface atoms/defects altering scattering paths, compared to well-crystalline phases. At this point of data analysis, the formation of CrP instead of elemental Cr cannot be ruled out, because the present spectrum shows similarities with that of literature data for crystalline CrP.[74] In addition, investigation of transition-metal monophosphides MP (M = Cr, Mn, Fe, Co) have shown that the oxidation state of these compounds is better formulated as $M^{1+}P^{1-}$ instead of $M^{3+}P^{3-}$,[75] and the reduction of Cr^{3+} to a lower oxidation state is consistent with a possible CrP formation besides the generation of nanosized Cr.

The analysis of the XRD and PDF data suggest that some residual $CrPS_4$ and an intercalated compound Na_xCrPS_4 is present after the uptake of 2 Na/f.u. The intercalation of Na^+ clearly results in the reduction of constituents of $CrPS_4$. Because the edge energy and the specific features on the rising edge are affected by the interatomic bond length (covalency) and defects, the assignment of a certain oxidation state is barely possible and phosphorus might be reduced upon intercalation of Na as well. However, based on the redox couples Cr^{3+}/Cr^{2+} and $H_3PO_4/H_4P_2O_6$ (E^0 = −0.424 V vs E^0 = −0.933 V),[76] we suggest that Cr^{3+} is reduced before P^{5+}. The data gathered so far demonstrate the high complexity of the present system, preventing an unambiguous assignment to distinct phases. However, based on the results from XRD, PDF, and XANES, the formation of intercalation compounds at the early discharge states can be safely stated. The occurrence of an isosbestic point after the uptake of 3 Na/f.u. and onward clearly demonstrates that no intermediates are formed during further discharging.

After a complete cycle (Figures 9c and 9d), the XANES is nearly featureless, which is often observed for nanoparticles. In the first derivative (Figure 9d), the signal at 5988.7 eV for the discharged sample decreased dramatically and shifted slightly to 5989.1 eV after recharging, while also a second peak at ∼5996 eV emerged for the recharged sample. These signals match with that of $CrPS_4$ and are in accordance with the findings of PDF data, suggesting that, during the charging, a nanoscopic phase was generated with a local structural order and electronic situation similar to that observed in $CrPS_4$.

The information gathered from XANES spectra is consistent with the results of the XRD investigations, as the formation of intermediate phases within the uptake of 2 Na/f.u. and its subsequent decomposition upon further Na insertion is

https://doi.org/10.1021/acsami.1c14980
ACS Appl. Mater. Interfaces 2021, 13, 54936−54950

observed in XRD patterns and is supported by XANES data. In addition, in the discharge process, a reduction of Cr^{3+} occurs. Furthermore, the recovery of a material resembling the structural characteristics of the starting material after a full cycle is in accordance with PDF analysis.

The EXAFS R-space plot (Figure 10) of $CrPS_4$ shows an intense peak at 2.01 Å corresponding to Cr−S bonds in the CrS_6 octahedron, while the less intense signal at 2.54 Å is due to the first Cr−P distance. The other signals at 3.53 and 3.99 Å with a shoulder at 4.25 Å are assigned to the second Cr−P distance and different Cr−S separations, respectively. During the uptake of Na (Figure 10a), the signal at 2.01 Å decreases and for 2−3 Na/f.u. distances beyond 2.5 Å almost disappeared. Nevertheless, weak newly formed signals (for 2 and 3 Na/f.u.) at ∼2.78, ∼3.26, ∼3.64, and ∼4.02 Å support the formation of an intercalation compound. Taking a closer look at the discharged state (Figure 10b), less signals than for bcc Cr are detected, because of the nanoscopic/amorphous and strongly disordered nature of the particles. After a full cycle, distances of 2.52, 3.59, and 3.96 Å appeared and the intensity of the signal at 2.01 Å increased. Because these signals match those of $CrPS_4$, the recovery of a local structure similar to that of $CrPS_4$ is very likely, which is also backed by PDF and XANES data.

3.3.3. Magic-Angle-Spinning Nuclear Magnetic Resonance Experiments. In order to further address the underlying reaction mechanism, ^{23}Na and ^{31}P MAS NMR studies were conducted (Figure 11). For the pristine sample, the ^{23}Na MAS NMR spectrum reveals, as expected, only a flat baseline. For some of the sodiated samples, the ^{23}Na MAS NMR spectra (Figure 11a) reveal a small narrow peak at −12.1 ppm (marked with an asterisk (*)), which can be assigned to residues of the electrolyte salt sodium triflate.[25] After uptake of 2 Na/f.u., a new broad signal at −12.4 ppm is observed, demonstrating the formation of an intermediate phase. It has been shown that chemical shifts of −4.4 ppm can be associated with Na_3PS_4 as well as amorphous and crystalline $Na_2P_2S_6$.[77] However, this signal most likely arises from intercalation compounds, as indicated also by the other methods described above. In accordance with XRD investigations, the highest intensity of this signal is reached after the uptake of 2 Na/f.u. and disappears again upon further sodiation. In addition, the sodiated samples (4−6 Na/f.u.) show the successive formation of a broad signal in the range between +200 ppm and −100 ppm. The large width of this signal is probably caused by the presence of an increasing amount of magnetic compounds in proximity to the Na-containing phases. Similar broad signals have been observed for sodiation of CuV_2S_4[25] and $Ni_2P_2S_6$.[54] At later stages of sodiation (starting at +6 Na/f.u.), a narrow signal appears at 49.5 ppm, which is in agreement with NMR spectra of pure, well-crystallized Na_2S[25,78] revealing its formation during the investigated reaction. After the full discharge, the spectrum is dominated by this narrow signal, which shows that a larger amount of Na_2S has been formed experiencing less influence of other phases. An additional small signal at 6.9 ppm appearing after full discharge reveals the formation of some NaF[78,79] caused by SEI formation. The formation of $NaCrS_2$ can be excluded since the spectrum of this compound would exhibit a strong peak at 1654 ppm (Figure S7 in the Supporting Information) which was not observed for any of the sodiated samples.

The ^{31}P MAS NMR investigations (Figure 11b) show no signal for the starting material. This is surprising because the

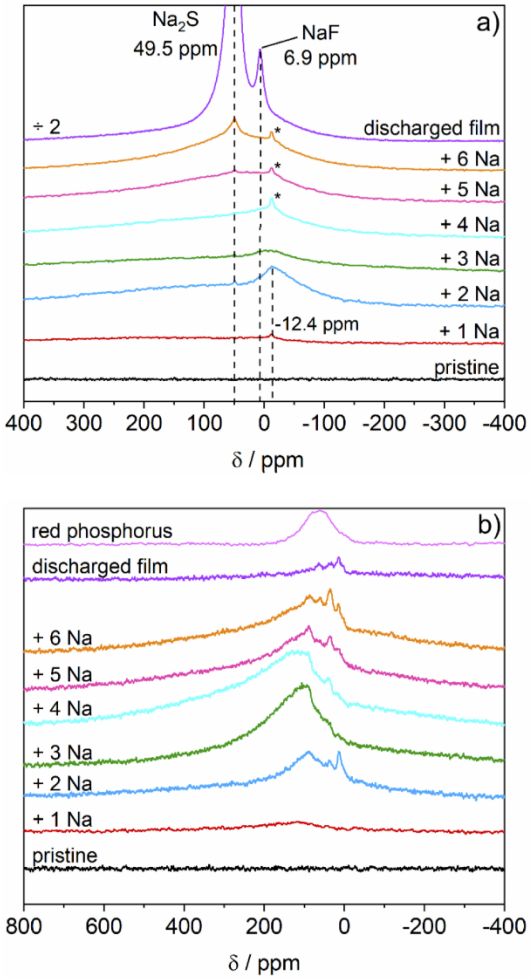

Figure 11. (a) ^{23}Na and (b) ^{31}P MAS NMR spectra of $CrPS_4$ for different sodiation states. The peak marked with an asterisk (*) in the ^{23}Na MAS NMR spectrum is caused by residues of the electrolyte salt sodium triflate.

paramagnetic behavior of $CrPS_4$ at room temperature[80] should lead at least to the appearance of broad NMR signals. However, nonexistent signals might be the consequence of strong magnetic coupling within the $CrPS_4$ layers. After an uptake of 2 Na/f.u., a broad peak in the range between +200 and −100 ppm with its center at ∼90.8 ppm and smaller signals at 13.4 and 35.3 ppm were detected. Considering the results from XRD, this change in the spectrum is related to the alteration of the local environment of phosphorus due to the formation of two sodium intercalation compounds. The smaller signals disappeared after the uptake of 3 Na/f.u. and the broad signal shows some left shift, which might indicate ordering of sodium within the intercalation compounds and eventually a phase transition. After an uptake of 4 Na/f.u., new signals occurred at 39.4 and 15.2 ppm and after the insertion of 5 Na/f.u. another signal at ∼89.4 ppm has formed. This is consistent with isolated $[PS_4]^{3-}$ tetrahedra.[81,82] In addition, the broad underlying signal between +200 ppm and −100 ppm

https://doi.org/10.1021/acsami.1c14980
ACS Appl. Mater. Interfaces 2021, 13, 54936−54950

shows a small right shift and upon the uptake of 6 Na/f.u., the smaller signals slightly gain intensity. This signal occurring after the uptake of 5−6 Na/f.u. and disappearing for the completely discharged sample is similar to the signal of red phosphorus, in terms of chemical shift and shape (see Figure 11b). The disappearance of this signal is most likely caused by the formation of magnetic nanoparticles disrupting the signal or a high degree of structural disorder in the sample. The origin of the smaller and sharper signals is uncertain. Another expected phase to form upon discharging is Na_3P, which was not observed here. The chemical shift for this phase is expected at approximately −208 ppm,[83,84] which is not present in the ^{31}P MAS NMR and neither are the corresponding chemical shifts (75 and 100 ppm)[83] in the ^{23}Na MAS NMR.

The ^{31}P MAS NMR experiments reveal the complex nature of the reaction mechanism. Considering the obtained results of MAS NMR with XRD and XANES data reinforces the presence of several stages of an intercalation compound during early discharge resulting in Na_xCrPS_4 phases. In this intercalation compound, the coupling within the layers is not as strong as in the starting material causing the observed sharp signals after uptake of 2 Na/f.u. ^{31}P MAS NMR experiments further suggest several phase transitions for P-containing phases throughout the discharge process and indicate the formation of elemental phosphorus after the uptake of 5 Na/f.u. Accordingly, ^{23}Na MAS NMR measurements indicate the formation of at least one new compound within the uptake of 2 Na/f.u. and further confirm the presence of Na_2S and NaF for the completely discharged sample, which is in accordance with XRD and PDF analysis.

4. CONCLUSION

In this study, we presented the electrochemical behavior of $CrPS_4$ and gave insights in the ongoing reaction mechanism. The thiophosphate $CrPS_4$ was successfully synthesized by chemical vapor transport using excess sulfur as a transport agent. The synthesis delivered highly crystalline and phase-pure $CrPS_4$, as evidenced by XRD. Galvanostatic measurements of $CrPS_4$ electrodes in SIBs proved to exhibit extraordinary electrochemical performance with reversible specific capacities up to 687 mAh g^{-1} after 300 cycles. Rate capability measurements showed a good tolerance against higher currents, as well as an exceptional capacity retention after high currents were applied. However, a temporary decrease of the specific capacity was observed, which is likely caused by the changing of the reaction mechanism, which was proven by dQ/dV analysis. Beside these electrochemical investigations, we also have gained insights in the ongoing reaction mechanism during the initial sodium uptake and release. Despite the application of advanced characterization methods, we must note that the system investigated here turned out to be extremely complex and the obtained data are not unambiguous. XRD and ^{23}Na MAS NMR clearly proved the presence of Na_2S in the discharged state, which was supported by PDF analysis, while XANES indicated the reduction of Cr(III) and suggested that nanoscopic and probably strongly disordered Cr was formed during discharging. Furthermore, signs of NaF were found by ^{23}Na MAS NMR, which is most likely caused by SEI formation. XRD measurements of the early discharge states (0−3 Na/f.u.) show strong indications of the formation of several intercalation compounds, which is also supported by PDF, XANES, EXAFS, and MAS NMR investigations. The obtained specific discharge capacity corresponds to an uptake of 9.2 Na/f.u. As no Na_xP phases were detected, the reaction likely proceeds according to eq 2 (consumption of 8 Na/f.u. in total), while intermediate formation occurs as described in eq 4. The observed difference in sodium uptake (1.2 Na/f.u.) could be caused by SEI formation, together with cointercalation of solvent molecules into the layered structure. In summary, the reaction mechanism might be summarized accordingly as follows:

$$CrPS_4 \xrightarrow{+2Na} Na_xCrPS_4 + Na_yCrPS_4 \xrightarrow{+6Na} Cr + P + 4Na_2S \quad (5)$$

Nevertheless, ^{31}P MAS NMR clearly reveals the complexity of the occurring reaction mechanism. Therefore, we note that a simple chemical equation as provided in eq 5 is not suited to describe this complex system properly and should only be seen as a simplified model and for visualization purposes.

PDF, XANES, and EXAFS investigations of the charge process suggest that a nanoscopic local environment and electronic structure similar to $CrPS_4$ is recovered after the first cycle. The obtained charge capacity corresponds to only 6.1 Na/f.u., which might be caused by, e.g., Na_2S partly not participating in the charging process, because of an incomplete oxidation of Cr or P during charging. In this context, CV curves suggest that most of the metallic Cr might be passivated during early cycling. Hence, only a minor portion of Cr is oxidized in the first cycle and merely vague signs of recovered $CrPS_4$ are detectable.

■ ASSOCIATED CONTENT

Supporting Information

The Supporting Information is available free of charge *in the online version of the paper*. Results of EDX measurements and Raman spectroscopy of pristine $CrPS_4$; comparison of film vs powder electrodes; full view of XRD and PDF data of $CrPS_4$ electrodes at different discharge/charge state; ^{23}Na MAS NMR spectrum of $NaCrS_2$. The Supporting Information is available free of charge at https://pubs.acs.org/doi/10.1021/acsami.1c14980.

(PDF)

■ AUTHOR INFORMATION

Corresponding Author

Wolfgang Bensch − *Institute of Inorganic Chemistry, Kiel University, 24118 Kiel, Germany;* orcid.org/0000-0002-3111-580X; Phone: +49 431 880-2091; Email: wbensch@ac.uni-kiel.de; Fax: +49 431 880-1520

Authors

Jonas van Dinter − *Institute of Inorganic Chemistry, Kiel University, 24118 Kiel, Germany*

Sylvio Indris − *Institute for Applied Materials - Energy Storage Systems, Karlsruhe Institute of Technology, 76021 Karlsruhe, Germany;* orcid.org/0000-0002-5100-113X

Alexander Bitter − *Institute of Inorganic Chemistry, Kiel University, 24118 Kiel, Germany*

David Grantz − *Institute of Inorganic Chemistry, Kiel University, 24118 Kiel, Germany*

Giannantonio Cibin − *Diamond Light Source, Didcot, Oxfordshire OX11 0DE, United Kingdom*

Martin Etter − *Deutsches Elektronen-Synchrotron (DESY), 22607 Hamburg, Germany*

Complete contact information is available at: https://pubs.acs.org/10.1021/acsami.1c14980

https://doi.org/10.1021/acsami.1c14980
ACS Appl. Mater. Interfaces 2021, 13, 54936−54950

Notes

The authors declare no competing financial interest.

■ ACKNOWLEDGMENTS

Financial support by the State of Schleswig-Holstein is gratefully acknowledged. The authors acknowledge DESY (Hamburg, Germany), a member of the Helmholtz Association HGF, for the provision of experimental facilities. Parts of this research were carried out at PETRA III. We kindly thank Huayna Terraschke for beamtime allocation. This work was carried out with the support of the Diamond Light Source, instrument B18 (proposal SP20060).

■ REFERENCES

(1) Nayak, P. K.; Yang, L.; Brehm, W.; Adelhelm, P. From Lithium-Ion to Sodium-Ion Batteries: Advantages, Challenges, and Surprises. *Angew. Chem., Int. Ed.* **2018**, *57* (1), 102−120.

(2) Deng, J.; Luo, W.-B.; Chou, S.-L.; Liu, H.-K.; Dou, S.-X. Sodium-Ion Batteries: From Academic Research to Practical Commercialization. *Adv. Energy Mater.* **2018**, *8* (4), 1701428.

(3) Larcher, D.; Tarascon, J.-M. Towards Greener and More Sustainable Batteries for Electrical Energy Storage. *Nat. Chem.* **2015**, *7* (1), 19−29.

(4) Panwar, N. L.; Kaushik, S. C.; Kothari, S. Role of Renewable Energy Sources in Environmental Protection: A Review. *Renewable Sustainable Energy Rev.* **2011**, *15* (3), 1513−1524.

(5) Peng, S.; Han, X.; Li, L.; Zhu, Z.; Cheng, F.; Srinivansan, M.; Adams, S.; Ramakrishna, S. Unique Cobalt Sulfide/Reduced Graphene Oxide Composite as an Anode for Sodium-Ion Batteries with Superior Rate Capability and Long Cycling Stability. *Small* **2016**, *12* (10), 1359−1368.

(6) Zhou, Q.; Liu, L.; Guo, G.; Yan, Z.; Tan, J.; Huang, Z.; Chen, X.; Wang, X. Sandwich-like Cobalt Sulfide-Graphene Composite - an Anode Material with Excellent Electrochemical Performance for Sodium Ion Batteries. *RSC Adv.* **2015**, *5* (88), 71644−71651.

(7) Li, X.; He, X.; Shi, C.; Liu, B.; Zhang, Y.; Wu, S.; Zhu, Z.; Zhao, J. Synthesis of One-Dimensional Copper Sulfide Nanorods as High-Performance Anode in Lithium Ion Batteries. *ChemSusChem* **2014**, *7* (12), 3328−3333.

(8) Kim, N. R.; Choi, J.; Yoon, H. J.; Lee, M. E.; Son, S. U.; Jin, H.-J.; Yun, Y. S. Conversion Reaction of Copper Sulfide Based Nanohybrids for Sodium-Ion Batteries. *ACS Sustainable Chem. Eng.* **2017**, *5* (11), 9802−9808.

(9) Qin, W.; Chen, T.; Lu, T.; Chua, D. H. C.; Pan, L. Layered Nickel Sulfide-Reduced Graphene Oxide Composites Synthesized via Microwave-Assisted Method as High Performance Anode Materials of Sodium-Ion Batteries. *J. Power Sources* **2016**, *302*, 202−209.

(10) Mahmood, N.; Zhang, C.; Hou, Y. Nickel Sulfide/Nitrogen-Doped Graphene Composites: Phase-Controlled Synthesis and High Performance Anode Materials for Lithium Ion Batteries. *Small* **2013**, *9* (8), 1321−1328.

(11) Tao, H.; Zhou, M.; Wang, R.; Wang, K.; Cheng, S.; Jiang, K. TiS_2 as an Advanced Conversion Electrode for Sodium-Ion Batteries with Ultra-High Capacity and Long-Cycle Life. *Adv. Sci.* **2018**, *5* (11), 1801021.

(12) Xiao, Y.; Lee, S. H.; Sun, Y.-K. The Application of Metal Sulfides in Sodium Ion Batteries. *Adv. Energy Mater.* **2017**, *7* (3), 1601329.

(13) Hu, Z.; Liu, Q.; Chou, S.-L.; Dou, S.-X. Advances and Challenges in Metal Sulfides/Selenides for Next-Generation Rechargeable Sodium-Ion Batteries. *Adv. Mater.* **2017**, *29* (48), 1700606.

(14) Yu, X. Y.; Lou, X. W. D. Mixed Metal Sulfides for Electrochemical Energy Storage and Conversion. *Adv. Energy Mater.* **2018**, *8* (3), 1701592.

(15) Krengel, M.; Hansen, A.-L.; Hartmann, F.; van Dinter, J.; Bensch, W. Elucidation of the Sodium - Copper Extrusion Mechanism in $CuCrS_2$: A High Capacity, Long-Life Anode Material for Sodium-Ion Batteries. *Batteries Supercaps* **2018**, *1* (5), 176−183.

(16) Krengel, M.; Adelhelm, P.; Klein, F.; Bensch, W. FeV_2S_4 as a High Capacity Electrode Material for Sodium-Ion Batteries. *Chem. Commun.* **2015**, *51* (70), 13500−13503.

(17) Li, L.; Zheng, Y.; Zhang, S.; Yang, J.; Shao, Z.; Guo, Z. Recent Progress on Sodium Ion Batteries: Potential High-Performance Anodes. *Energy Environ. Sci.* **2018**, *11* (9), 2310−2340.

(18) Mao, J.; Zhou, T.; Zheng, Y.; Gao, H.; Liu, H. K.; Guo, Z. Two-Dimensional Nanostructures for Sodium-Ion Battery Anodes. *J. Mater. Chem. A* **2018**, *6* (8), 3284−3303.

(19) Yabuuchi, N.; Kubota, K.; Dahbi, M.; Komaba, S. Research Development on Sodium-Ion Batteries. *Chem. Rev.* **2014**, *114* (23), 11636−11682.

(20) Wang, T.; Su, D.; Shanmukaraj, D.; Rojo, T.; Armand, M.; Wang, G. Electrode Materials for Sodium-Ion Batteries: Considerations on Crystal Structures and Sodium Storage Mechanisms. *Electrochem. Energy Rev.* **2018**, *1* (2), 200−237.

(21) Park, J. Y.; Kim, S. J.; Yim, K.; Dae, K. S.; Lee, Y.; Dao, K. P.; Park, J. S.; Jeong, H. B.; Chang, J. H.; Seo, H. K.; Ahn, C. W.; Yuk, J. M. Pulverization-Tolerance and Capacity Recovery of Copper Sulfide for High-Performance Sodium Storage. *Adv. Sci.* **2019**, *6* (12), 1900264.

(22) Shadike, Z.; Zhou, Y.-N.; Ding, F.; Sang, L.; Nam, K.-W.; Yang, X.-Q.; Fu, Z.-W. The New Electrochemical Reaction Mechanism of Na/FeS_2 Cell at Ambient Temperature. *J. Power Sources* **2014**, *260*, 72−76.

(23) Deng, J.; Gong, Q.; Ye, H.; Feng, K.; Zhou, J.; Zha, C.; Wu, J.; Chen, J.; Zhong, J.; Li, Y. Rational Synthesis and Assembly of Ni_3S_4 Nanorods for Enhanced Electrochemical Sodium-Ion Storage. *ACS Nano* **2018**, *12* (2), 1829−1836.

(24) Yang, C.; Ou, X.; Xiong, X.; Zheng, F.; Hu, R.; Chen, Y.; Liu, M.; Huang, K. V_5S_8-Graphite Hybrid Nanosheets as a High Rate-Capacity and Stable Anode Material for Sodium-Ion Batteries. *Energy Environ. Sci.* **2017**, *10* (1), 107−113.

(25) Krengel, M.; Hansen, A.-L.; Kaus, M.; Indris, S.; Wolff, N.; Kienle, L.; Westfal, D.; Bensch, W. CuV_2S_4: A High Rate Capacity and Stable Anode Material for Sodium Ion Batteries. *ACS Appl. Mater. Interfaces* **2017**, *9* (25), 21283−21291.

(26) Klein, F.; Jache, B.; Bhide, A.; Adelhelm, P. Conversion Reactions for Sodium-Ion Batteries. *Phys. Chem. Chem. Phys.* **2013**, *15* (38), 15876−15887.

(27) Qian, J.; Wu, X.; Cao, Y.; Ai, X.; Yang, H. High Capacity and Rate Capability of Amorphous Phosphorus for Sodium Ion Batteries. *Angew. Chem., Int. Ed.* **2013**, *52* (17), 4633−4636.

(28) Diehl, R.; Carpentier, C.-D. The Crystal Structure of Chromium Thiophosphate, $CrPS_4$. *Acta Crystallogr., Sect. B: Struct. Crystallogr. Cryst. Chem.* **1977**, *33* (5), 1399−1404.

(29) Weiss, A.; Schäfer, H. Notizen: Zur Kenntnis von Bortetrathiophosphat BPS_4. *Z. Naturforsch., B: J. Chem. Sci.* **1963**, *18* (1), 81−82.

(30) Weiss, A.; Schäfer, H. Zur Kenntnis von Aluminiumthiophosphat $AlPS_4$. *Naturwissenschaften* **1960**, *47* (21), 495−495.

(31) Buck, P.; Carpentier, C. D. The Crystal Structure of Gallium Thiophosphate, $GaPS_4$. *Acta Crystallogr., Sect. B: Struct. Crystallogr. Cryst. Chem.* **1973**, *29* (9), 1864−1868.

(32) Carpentier, C. D.; Diehl, R.; Nitsche, R. Die Kristallstruktur des InPS. *Naturwissenschaften* **1970**, *57* (8), 393−393.

(33) Zimmermann, H.; Carpentier, C. D.; Nitsche, R. The Crystal Structure of Bismuth Thiophosphate $BiPS_4$. *Acta Crystallogr., Sect. B: Struct. Crystallogr. Cryst. Chem.* **1975**, *31* (8), 2003−2006.

(34) Mercier, R.; Malugani, J.-P.; Fahys, B.; Robert, G.; Douglade, J. Structure Du Tetrathiophosphate de Lithium. *Acta Crystallogr., Sect. B: Struct. Crystallogr. Cryst. Chem.* **1982**, *38* (7), 1887−1890.

(35) Jansen, M.; Henseler, U. Synthesis, Structure Determination, and Ionic Conductivity of Sodium Tetrathiophosphate. *J. Solid State Chem.* **1992**, *99* (1), 110−119.

https://doi.org/10.1021/acsami.1c14980
ACS Appl. Mater. Interfaces 2021, 13, 54936−54950

(36) Jörgens, S.; Mewis, A. $Ag_5PS_4Cl_2$ and $Ag_{15}(PS_4)_4Cl_3$ - Crystal Structures and Their Relation to Ag_3PS_4. *Solid State Sci.* **2007**, *9* (2), 213−217.
(37) Pfitzner, A.; Reiser, S. Refinement of the Crystal Structures of Cu_3PS_4 and Cu_3SbS_4 and a Comment on Normal Tetrahedral Structures. *Z. Kristallogr. - Cryst. Mater.* **2002**, *217* (2), 51−54.
(38) Bither, T. A.; Donohue, P. C.; Young, H. S. Palladium and Platinum Phosphochalcogenides—Synthesis and Properties. *J. Solid State Chem.* **1971**, *3* (2), 300−307.
(39) Louisy, A.; Ouvrard, G.; Schleich, D. M.; Brec, R. Physical Properties and Lithium Intercalates of $CrPS_4$. *Solid State Commun.* **1978**, *28* (1), 61−66.
(40) Zhuang, H. L.; Zhou, J. Density Functional Theory Study of Bulk and Single-Layer Magnetic Semiconductor $CrPS_4$. *Phys. Rev. B: Condens. Matter Mater. Phys.* **2016**, *94* (19), 195307.
(41) Mayorga-Martinez, C. C.; Sofer, Z.; Sedmidubský, D.; Huber, Š.; Eng, A. Y. S.; Pumera, M. Layered Metal Thiophosphite Materials: Magnetic, Electrochemical, and Electronic Properties. *ACS Appl. Mater. Interfaces* **2017**, *9* (14), 12563−12573.
(42) Wu, H.; Chen, H. Probing the Properties of Lattice Vibrations and Surface Electronic States in Magnetic Semiconductor $CrPS_4$. *RSC Adv.* **2019**, *9* (53), 30655−30658.
(43) Ohno, Y.; Mineo, A.; Matsubara, I. Reflection Electron-Energy-Loss Spectroscopy, x-Ray-Absorption Spectroscopy, and x-Ray Photoelectron Spectroscopy Studies of a New Type of Layer Compound $CrPS_4$. *Phys. Rev. B: Condens. Matter Mater. Phys.* **1989**, *40* (15), 10262−10272.
(44) Pei, Q. L.; Luo, X.; Lin, G. T.; Song, J. Y.; Hu, L.; Zou, Y. M.; Yu, L.; Tong, W.; Song, W. H.; Lu, W. J.; Sun, Y. P. Spin Dynamics, Electronic, and Thermal Transport Properties of Two-Dimensional $CrPS_4$ Single Crystal. *J. Appl. Phys.* **2016**, *119* (4), 043902.
(45) Susilo, R. A.; Jang, B. G.; Feng, J.; Du, Q.; Yan, Z.; Dong, H.; Yuan, M.; Petrovic, C.; Shim, J. H.; Kim, D. Y.; Chen, B. Band Gap Crossover and Insulator-Metal Transition in the Compressed Layered $CrPS_4$. *npj Quantum Mater.* **2020**, *5* (1), 1−8.
(46) Lee, J.; Ko, T. Y.; Kim, J. H.; Bark, H.; Kang, B.; Jung, S.-G.; Park, T.; Lee, Z.; Ryu, S.; Lee, C. Structural and Optical Properties of Single- and Few-Layer Magnetic Semiconductor $CrPS_4$. *ACS Nano* **2017**, *11* (11), 10935−10944.
(47) Kim, S.; Lee, J.; Jin, G.; Jo, M.-H.; Lee, C.; Ryu, S. Crossover between Photochemical and Photothermal Oxidations of Atomically Thin Magnetic Semiconductor $CrPS_4$. *Nano Lett.* **2019**, *19* (6), 4043−4051.
(48) Budniak, A. K.; Killilea, N. A.; Zelewski, S. J.; Sytnyk, M.; Kauffmann, Y.; Amouyal, Y.; Kudrawiec, R.; Heiss, W.; Lifshitz, E. Exfoliated $CrPS_4$ with Promising Photoconductivity. *Small* **2020**, *16* (1), 1905924.
(49) Filik, J.; Ashton, A. W.; Chang, P. C. Y.; Chater, P. A.; Day, S. J.; Drakopoulos, M.; Gerring, M. W.; Hart, M. L.; Magdysyuk, O. V.; Michalik, S.; Smith, A.; Tang, C. C.; Terrill, N. J.; Wharmby, M. T.; Wilhelm, H. Processing Two-Dimensional X-Ray Diffraction and Small-Angle Scattering Data in DAWN 2. *J. Appl. Crystallogr.* **2017**, *50* (3), 959−966.
(50) Yang, X.; Juhas, P.; Farrow, C. L.; Billinge, S. J. L. xPDFsuite: An End-to-End Software Solution for High Throughput Pair Distribution Function Transformation, Visualization and Analysis. *arXiv* 1402.3163, **2014**.
(51) Ravel, B.; Newville, M. ATHENA, ARTEMIS, HEPHAESTUS: Data Analysis for X-Ray Absorption Spectroscopy Using IFEFFIT. *J. Synchrotron Radiat.* **2005**, *12* (4), 537−541.
(52) Momma, K.; Izumi, F. VESTA 3 for Three-Dimensional Visualization of Crystal, Volumetric and Morphology Data. *J. Appl. Crystallogr.* **2011**, *44* (6), 1272−1276.
(53) Yang, Z.; Chen, T.; Wu, C.; Qu, J.; Wu, Z.; Guo, X.; Zhong, B.; Liu, H.; Dou, S. Interpreting Abnormal Charge-Discharge Plateau Migration in Cu_xS during Long-Term Cycling. *ACS Appl. Mater. Interfaces* **2019**, *11* (4), 3961−3970.
(54) van Dinter, J.; Synnatschke, K. A.; Engesser, T.; Indris, S.; Wolff, N.; Gronenberg, O.; Etter, M.; Cibin, G.; Kienle, L.; Backes, C.; Bensch, W. What Happens Structurally and Chemically during Sodium Uptake and Release by $Ni_2P_2S_6$: A Combined X-Ray Diffraction, X-Ray Absorption, Pair Distribution Function and MAS NMR Analysis. *J. Mater. Chem. A* **2020**, *8* (42), 22401−22415.
(55) Hartmann, F.; Etter, M.; Cibin, G.; Liers, L.; Terraschke, H.; Bensch, W. Superior Sodium Storage Properties in the Anode Material $NiCr_2S_4$ for Sodium-Ion Batteries: An X-Ray Diffraction, Pair Distribution Function, and X-Ray Absorption Study Reveals a Conversion Mechanism via Nickel Extrusion. *Adv. Mater.* **2021**, 2101576.
(56) Dogrusoz, M.; Devic, T.; Şems Ahsen, A.; Demir-Cakan, R. A Gallic Acid Based Metal Organic Framework Derived NiS/C Anode for Sodium Ion Batteries. *Sustainable Energy Fuels* **2021**, *5* (13), 3363−3372.
(57) Wang, J.; Cao, D.; Yang, G.; Yang, Y.; Wang, H. Synthesis of NiS/Carbon Composites as Anodes for High-Performance Sodium-Ion Batteries. *J. Solid State Electrochem.* **2017**, *21* (10), 3047−3055.
(58) Tan, Y.; Wong, K.-W.; Zhang, Z.; Ng, K. M. In Situ Synthesis of Iron Sulfide Embedded Porous Carbon Hollow Spheres for Sodium Ion Batteries. *Nanoscale* **2017**, *9* (48), 19408−19414.
(59) Huang, W.; Sun, H.; Shangguan, H.; Cao, X.; Xiao, X.; Shen, F.; Mølhave, K.; Ci, L.; Si, P.; Zhang, J. Three-Dimensional Iron Sulfide-Carbon Interlocked Graphene Composites for High-Performance Sodium-Ion Storage. *Nanoscale* **2018**, *10* (16), 7851−7859.
(60) Wang, H.; Liu, J.; Wang, H.; Cai, X.; Ye, X.; Zhang, L.; Chen, Z.; Shen, Z. X. Cobalt Sulfide Nanoflakes Grown on Graphite Foam for Na-Ion Batteries with Ultrahigh Initial Coulombic Efficiency. *J. Mater. Chem. A* **2020**, *8* (30), 14900−14907.
(61) Zintl, E.; Harder, A.; Dauth, B. Gitterstruktur der Oxyde, Sulfide, Selenide und Telluride des Lithiums, Natriums und Kaliums. *Z. Elektrochem. Angew. Phys. Chem.* **1934**, *40* (8), 588−593.
(62) Hibma, T. Ordering of the Alkali-Ions in Na_xTiS_2 and Li_xTiS_2. *Physica B+C* **1980**, *99* (1-4), 136−140.
(63) Leblanc-Soreau, A.; Danot, M.; Trichet, L.; Rouxel, J. Les Intercalaires A_xTiS_2 et A_xZrS_2. Structure et Liaisons. (A = Li, Na, K, Rb, Cs). *Mater. Res. Bull.* **1974**, *9* (2), 191−197.
(64) Brec, R.; Dugast, A.; Le Mehauté, A. Chemical and Electrochemical Study of the Li_xFeS_2 Cathodic System ($0 < x \leqslant 2$). *Mater. Res. Bull.* **1980**, *15* (5), 619−625.
(65) Rouxel, J.; Molinie, P.; Top, L. H. Mechanistic Studies of Reversible Layer-Type Electrodes. *J. Power Sources* **1983**, *9* (3), 345−357.
(66) Shannon, R. D. Revised Effective Ionic Radii and Systematic Studies of Interatomic Distances in Halides and Chalcogenides. *Acta Crystallogr., Sect. A: Cryst. Phys., Diffr., Theor. Gen. Crystallogr.* **1976**, *32* (5), 751−767.
(67) Molinie, P.; Trichet, L.; Rouxel, J.; Berthier, C.; Chabre, Y.; Segransan, P. The Na-TiS_2 System: A Critical Discussion of the Phase Boundaries, Structural and NMR Studies. *J. Phys. Chem. Solids* **1984**, *45* (1), 105−112.
(68) Selte, K.; Kjekshus, A.; Andresen, A. F. Structural and Magnetic Properties of CrP. *Acta Chem. Scand.* **1972**, *26* (10), 4188−4190.
(69) Kugler, W.; Knorr, K.; Prandl, W. Röntgenbeugungsuntersuchungen an der magnetostriktiven Verzerrungswelle in Chrom: Amplitude und Temperaturabhängigkeit. *Z. Kristallogr.* **1983**, *162* (1−4), 151−153.
(70) Shirako, Y.; Shi, Y. G.; Aimi, A.; Mori, D.; Kojitani, H.; Yamaura, K.; Inaguma, Y.; Akaogi, M. High-Pressure Stability Relations, Crystal Structures, and Physical Properties of Perovskite and Post-Perovskite of $NaNiF_3$. *J. Solid State Chem.* **2012**, *191*, 167−174.
(71) Luo, W. K.; Sheng, H. W.; Alamgir, F. M.; Bai, J. M.; He, J. H.; Ma, E. Icosahedral Short-Range Order in Amorphous Alloys. *Phys. Rev. Lett.* **2004**, *92* (14), 145502.
(72) Permien, S.; Neumann, T.; Indris, S.; Neubüser, G.; Kienle, L.; Fiedler, A.; Hansen, A.-L.; Gianolio, D.; Bredow, T.; Bensch, W. Transition Metal Cations on the Move: Simultaneous Operando X-Ray Absorption Spectroscopy and X-Ray Diffraction Investigations

https://doi.org/10.1021/acsami.1c14980
ACS Appl. Mater. Interfaces 2021, 13, 54936−54950

during Li Uptake and Release of a $NiFe_2O_4$/CNT Composite. *Phys. Chem. Chem. Phys.* **2018**, *20* (28), 19129−19141.
(73) Permien, S.; Hansen, A.-L.; van Dinter, J.; Indris, S.; Neubüser, G.; Kienle, L.; Doyle, S.; Mangold, S.; Bensch, W. Unveiling the Reaction Mechanism during Li Uptake and Release of Nanosized "$NiFeMnO_4$": Operando X-Ray Absorption, X-Ray Diffraction, and Pair Distribution Function Investigations. *ACS Omega* **2019**, *4* (1), 2398−2409.
(74) Grosvenor, A. P.; Cavell, R. G.; Mar, A. Next-Nearest Neighbour Contributions to the XPS Binding Energies and XANES Absorption Energies of P and As in Transition-Metal Arsenide Phosphides $MAs_{1-y}P_y$ Having the MnP-Type Structure. *J. Solid State Chem.* **2008**, *181* (10), 2549−2558.
(75) Grosvenor, A. P.; Wik, S. D.; Cavell, R. G.; Mar, A. Examination of the Bonding in Binary Transition-Metal Monophosphides MP (M = Cr, Mn, Fe, Co) by X-Ray Photoelectron Spectroscopy. *Inorg. Chem.* **2005**, *44* (24), 8988−8998.
(76) Bard, A. J.; Parsons, R.; Jordan, J. *Standard Potentials in Aqueous Solution*; Marcel Dekker, 1985.
(77) Fritsch, C.; Hansen, A.-L.; Indris, S.; Knapp, M.; Ehrenberg, H. Mechanochemical Synthesis of Amorphous and Crystalline $Na_2P_2S_6$ - Elucidation of Local Structural Changes by X-Ray Total Scattering and NMR. *Dalton Trans.* **2020**, *49* (5), 1668−1673.
(78) Dec, S. F.; Maciel, G. E.; Fitzgerald, J. J. Solid-State ^{23}Na and ^{27}Al MAS NMR Study of the Dehydration of $Na_2O{\cdot}Al_2O_3{\cdot}3H_2O$. *J. Am. Chem. Soc.* **1990**, *112* (25), 9069−9077.
(79) Tabeta, R.; Saito, H. ^{23}Na Chemical Shifts of some Inorganic and Organic Compounds in the Solid State as Determined by the Magic Angle Spinning and High Power NMR Methods. *Chem. Lett.* **1984**, *13* (2), 293−296.
(80) Calder, S.; Haglund, A. V.; Liu, Y.; Pajerowski, D. M.; Cao, H. B.; Williams, T. J.; Garlea, V. O.; Mandrus, D. Magnetic Structure and Exchange Interactions in the Layered Semiconductor $CrPS_4$. *Phys. Rev. B: Condens. Matter Mater. Phys.* **2020**, *102* (2), 024408.
(81) Stöffler, H.; Zinkevich, T.; Yavuz, M.; Senyshyn, A.; Kulisch, J.; Hartmann, P.; Adermann, T.; Randau, S.; Richter, F. H.; Janek, J.; Indris, S.; Ehrenberg, H. Li^+-Ion Dynamics in β-Li_3PS_4 Observed by NMR: Local Hopping and Long-Range Transport. *J. Phys. Chem. C* **2018**, *122* (28), 15954−15965.
(82) Stöffler, H.; Zinkevich, T.; Yavuz, M.; Hansen, A.-L.; Knapp, M.; Bednarčík, J.; Randau, S.; Richter, F. H.; Janek, J.; Ehrenberg, H.; Indris, S. Amorphous versus Crystalline Li_3PS_4: Local Structural Changes during Synthesis and Li Ion Mobility. *J. Phys. Chem. C* **2019**, *123* (16), 10280−10290.
(83) Morita, R.; Gotoh, K.; Dahbi, M.; Kubota, K.; Komaba, S.; Tokiwa, K.; Arabnejad, S.; Yamashita, K.; Deguchi, K.; Ohki, S.; Shimizu, T.; Laskowski, R.; Ishida, H. States of Thermochemically or Electrochemically Synthesized Na_xP_y Compounds Analyzed by Solid State ^{23}Na and ^{31}P Nuclear Magnetic Resonance with Theoretical Calculation. *J. Power Sources* **2019**, *413*, 418−424.
(84) Marbella, L. E.; Evans, M. L.; Groh, M. F.; Nelson, J.; Griffith, K. J.; Morris, A. J.; Grey, C. P. Sodiation and Desodiation via Helical Phosphorus Intermediates in High-Capacity Anodes for Sodium-Ion Batteries. *J. Am. Chem. Soc.* **2018**, *140* (25), 7994−8004.

https://doi.org/10.1021/acsami.1c14980
ACS Appl. Mater. Interfaces 2021, 13, 54936−54950

4.3 A Combined Sodium Intercalation and Copper Extrusion Mechanism in the Thiophosphate Family: $CuCrP_2S_6$ as Anode Material in Sodium-Ion Batteries

The third study is focused on the layered anode material $CuCrP_2S_6$ and its application in SIBs. Similar to the previous works, the electrochemical performance as electrode and the reaction mechanism of Na uptake and release were investigated. This particular anode material was chosen to combine the promising electrochemical properties of layered thiophosphates with the potential benefits arising from the incorporation of Cu^+ into anode materials. Moreover, this study depicts the first investigation of the active material $CuCrP_2S_6$ in SIBs.

Although the electrochemical long-term performance of $CuCrP_2S_6$ is not as high as for $Ni_2P_2S_6$ or $CrPS_4$, the reversible capacity is still fairly large yielding 409 mAh g^{-1} after 200 cycles when a current rate of 1.0 A g^{-1} is applied. The rate capability (422 mAh g^{-1} @ 3 A g^{-1}) is comparable to that of $Ni_2P_2S_6$, although the percentage decrease is slightly smaller for $CuCrP_2S_6$ at current densities greater than 0.5 A g^{-1}. The capacity retention of 79% after reapplying low current rates indicates a good tolerance against high currents and is slightly higher than for $Ni_2P_2S_6$ (74%). Additionally, the discharging and charging process of the initial cycles was investigated by XRD and CV analysis, which revealed an interesting and rare reaction mechanism. The uptake of sodium leads to the intercalation of ~1 Na/f.u. into the interlayer space of the $CuCrP_2S_6$ electrode. Further Na uptake results in the extrusion of Cu^+ by Na^+ and consequently in the generation of metallic Cu. Hence, after a total uptake of 2 Na/f.u., Na^+ completely occupies the van der Waals gap as well as the octahedral space within the layer, in which Cu^+ was distributed formerly. It is noteworthy that most likely Cu^+ is not extruded completely and therefore some Cu^+ cations remain in the structure of the intermediate phase. Further discharging (3 - 12 Na/f.u.) follows the pathway of a conventional conversion, which is accompanied by the generation of Na_2S. The discharge process of $CuCrP_2S_6$ electrodes therefore can be described as combined intercalation-reduction-extrusion mechanism followed by a conversion reaction. Similar to previous studies, the formation of NaF as well-known SEI component and no generation of Na_xP phases were observed. After recharging the electrode, no crystalline phases except for NaF were detected. However, based on the CV curves and obtained capacities, a reaction involving the oxidation of Cr, P and Cu seems reasonable, although Cu often is considered electrochemically inactive after initial reduction. The similarities between $CuCrP_2S_6$ and $Ni_2P_2S_6$ together with the CV analysis suggest the formation of Cu-, Cr- and P- or Cu-Cr- and P-sulfides after recharging.

A Combined Sodium Intercalation and Copper Extrusion Mechanism in the Thiophosphate Family: $CuCrP_2S_6$ as Anode Material in Sodium-Ion Batteries

Jonas van Dinter,[a] David Grantz,[a] Alexander Bitter[a] and Prof. Dr. Wolfgang Bensch*[a]

[a]*Institute of Inorganic Chemistry, Kiel University, Max-Eyth-Str. 2, 24118 Kiel, Germany, E-mail: wbensch@ac.uni-kiel.de*

Abstract

The layered hypothiophosphate $CuCrP_2S_6$ was identified as promising candidate for the application as anode in sodium-ion batteries exhibiting an appropriate electrochemical performance (409 mAh g^{-1} after 200 cycles @ 1 A g^{-1}). The electrochemical long-term experiments suggest that the reaction mechanism changes upon repeated discharging and charging. The initial discharge and charge process was studied by X-ray diffraction evidencing that at the early discharge stages, Na^+ is intercalated in the interlayer space accompanied by a simultaneous reduction of Cu^+ to metallic Cu, which is extruded from the host. At later stages of discharge, a conversion of the intermediate phase to Cu^0, amorphous Cr^0 and P^0 embedded in nanocrystalline Na_2S occurs. After recharging, only reflections of nanocrystalline NaF could be identified, which is part of the generated solid electrolyte interphase (SEI) layer. In contrast to observation made in literature, elemental Cu seems to be oxidized during the charge process again.

1. Introduction

Although Lithium-ion batteries (LIBs) dominate the market for portable devices and electromobility, this energy storage system is not considered suitable to satisfy climate change related challenges and requirements according to the prevailing opinion in literature. With increasing energy conversion from renewable sources, the necessity for stationary energy storage systems (ESS) will also increase to balance out over- and underproduction of electric energy produced by renewable sources. In this context, the application of Na based storage systems seems to be more reasonable than Li based systems.[1–6] The biggest drawbacks of Na opposed to Li are the higher mass, larger ionic radius and the smaller electrochemical potential of Na, causing lower energy densities for the corresponding Na based battery systems.[4,7,8] However, most of these apparent negative traits are negligible applying sodium-ion batteries (SIBs) for stationary ESS, since *e.g.* weight is less important for stationary applications.

Additionally, the low cost of Na due to its high abundance and wide distribution is an important commercial advantage over Li.[1–4] Nevertheless, while graphite is the anode material of choice in LIBs, it only shows a low specific capacity using Na as guest species.[9] It is assumed that the intercalation of Na^+ cations into graphite is thermodynamically hindered and hence graphite is not suitable for the usage in SIBs as anode material.[9–13] Therefore, identification and development of anode materials for SIBs providing high specific capacities and good long-term performance is necessary. While hard carbon has been identified as promising anode material, which is capable of reversible sodium intercalation, many non-trivial improvements are necessary in order to obtain an ideal electrode. Those improvements include tuning of surface area, interlayer space, amount of defects, size of pores and the choice of the precursor, while the exact impact of the individual treatments is not understood completely.[14–16] In contrast, the use of active materials that undergo conversion reactions leads to higher specific capacities, allowing more electrons to participate in the electrochemical reaction opposed to intercalation reactions.[17] Until now, a large variety of materials have been investigated ranging from carbonaceous materials[4,13–16] to binary and ternary metal chalcogenides,[18–23] alloys,[20,24,25] elemental phosphorous[26,27] and many other compounds.[4,28] Especially the smaller ionicity of sulfides is considered beneficial for conversion reactions and reversible Na storage. Compared to *e.g.* a M-O bond, the M-S bond is less polar, which reduces overpotentials during the charge and discharge processes.[29] However, another interesting substance class exhibiting M-S bonds is represented by layered transition metal (hypo)thiophosphates (MTPs), which are less often studied as active materials in SIBs. Originally already discovered in the 19th century,[30] MTPs initially gained broader research interest during the 1970s[31] because they share many properties with layered transition metal dichalcogenides (TMDCs) and exhibit intermediate to wide bandgaps in the range between 1.3 and 3.5 eV.[31–34] However, MTPs also have been identified as promising anode materials in LIBs and SIBs recently.[32,35,36] Usually, MTPs are categorized as M^{II} ($M_2P_2S_6$) or $M^{I}M^{III}$ ($M'M''P_2S_6$) based compounds. While MTPs with bivalent metallic cations typically crystallize in *C2/m* symmetry, when mixed cations ($M^{I}M^{III}$) occupy the metal sites also trigonal symmetry is common.[31,33,37–40] The structure of monoclinic hypothiophosphates is mostly formed by close-packed S^{2-} anion layers, where the resulting octahedral sites are occupied by metal cations and by P-P dimers. Each P atom is coordinated by three S and one P atom forming an

ethane-like $[P_2S_6]^{4-}$ dumbbell. These units occupy 1/3 of the octahedral sites, whereas the remaining sites are occupied by metal cations. This results in a honeycomb arrangement, where three $[P_2S_6]^{4-}$ units surround one MS_6 octahedron.[31,33,41,42] Interestingly, M^IM^{III} based MTPs with M = Cu^+ often exhibit special behavior, because the Cu^+ cation is not bound to the center, but can occupy different sites in the sulfur defined octahedron dependent on temperature. At room temperature, the Cu^+ cations are unevenly distributed between two different octahedral sites, whereas at low temperatures (Figure 1a), Cu^+ strictly alternates between upper and lower octahedral sites (Figure 1b).[31,33,43,44]

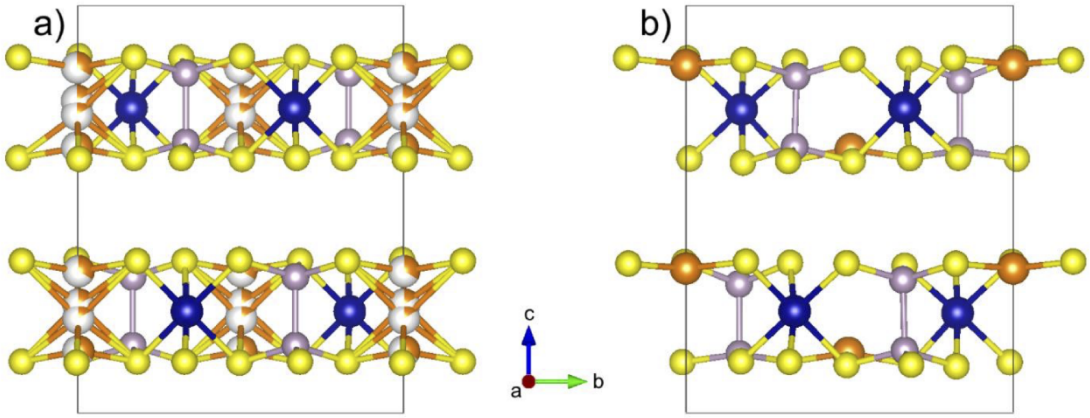

Figure 1. View of the two structural modifications of $CuCrP_2S_6$ (orange: Cu^+; blue: Cr^{3+}; purple: P^{4+}; yellow: S^{2-}) at (a) room temperature (space group *C2/c*) and (b) low temperatures (space group *Pc*). The viewing direction is along the *a*-axis. Structures were created with the software VESTA 3.4.0[45] using crystallographic data from the literature.[43,44]

Concerning possible battery applications, especially ternary Cu containing sulfides might exhibit beneficial properties. The electrochemical reaction during discharging leads to reduction of Cu^+ to metallic Cu, which is extruded as nanoparticles or dendrites.[46–48] As a result, the electric conductivity considerably increases in the electrodes. The presence of elemental Cu enhances the rate capability, capacity retention and long-term stability.[49,50] For example, CuV_2S_4 exhibits a high reversible specific capacity of 580 mAh g^{-1} after 300 cycles at a current rate of 0.7 A g^{-1}.[49] $CuCrS_2$ on the other hand delivered a reversible specific capacity of 252 mAh g^{-1} after 500 cycles at a current density of 1.5 A g^{-1}, which is still 81% of the capacity obtained after the 2nd and 99% of the capacity obtained after the 50th cycle, demonstrating extraordinary electrochemical properties.[50] For these systems, the presence of Cu^+ is considered beneficial by being reduced to elemental Cu during discharge preventing formation of polysulfides and/or enhancing electric conductivity and thus improving

cycling stability and rate capability.[49,50] To incorporate these beneficial properties into MTPs, the most obvious choice as anode material is $CuCrP_2S_6$. To the best of our knowledge, $CuCrP_2S_6$ never has been investigated before as anode material in SIBs. In a recent study, we used $Ni_2P_2S_6$ for the application as anode material in SIBs and thoroughly characterized the underlying reaction mechanisms.[36] Assuming a similar reaction pathway for $CuCrP_2S_6$, the theoretical capacity of $CuCrP_2S_6$ amounts to 870 mAh g^{-1} (eq. 1):

$$CuCrP_2S_6 + 12\,Na^+ + 12\,e^- \rightarrow Cu + Cr + 2\,P + 6Na_2S \quad (1)$$

Based on the idea of beneficial effects of copper containing active materials and the promising results of previously studied MTPs, we present the electrochemical properties of $CuCrP_2S_6$ as potential anode material in SIBs. Additionally, investigations of the reaction products after the discharge and charge process were conducted.

2. Experimental Section

2.1 Synthesis

$CuCrP_2S_6$ was synthesized by chemical vapor transport reaction. Stoichiometric amounts of copper (Chempur, 99.95%) and chromium (Alfa Aesar, 99.94%) were mixed with an excess (6 wt%) of red phosphorus (Knapsack AG, 99.9999%) and sulfur (Chempur, 99.999%) and sealed in a quartz glass ampoule (<10^{-4} mbar). The quartz tube was then placed in a tube furnace and heated to 723 K within 4 h and maintained at this temperature for 24 h. Afterwards, the temperature was increased within 2.5 h to 973 K. When this temperature was reached, a temperature gradient to 953 K was established to start the chemical vapor transport. The reaction was carried out for 14 d. It is noteworthy that this quaternary system is extremely sensitive to the slightest alterations and thus many approaches were necessary to obtain the phase pure product. However, it was always possible to manually separate $CuCrP_2S_6$ from the $CrPS_4$ side product, when the reaction parameters were adjusted optimally. By variation of reaction parameters, the ratio of $CrPS_4$ to $CuCrP_2S_6$ could be altered in favor of $CuCrP_2S_6$, but ultimately the formation of $CrPS_4$ could not be fully avoided. The product was obtained as shiny black plate-like crystals.

2.2 Electrochemical tests

For electrode preparation, 70 wt% of $CuCrP_2S_6$ was mixed together with 20 wt% of SUPER C65 (Timcal, Switzerland) and 10 wt% of polyvinylidene difluoride (PVDF, Solvay, Germany) and afterwards suspended in *N*-methyl-2-pyrrolidone (NMP, Fisher Bioreagens, 99.8%). The obtained suspension was cast onto Cu foil using the doctor-blade method. The electrode was dried over night at room temperature and additionally several hours in a vacuum oven at 333 K. For battery assembly, circular electrodes with diameters of 10 mm were punched out and transferred into Swagelok® type cells together with a Celgard® membrane and glass fibre filter (Whatman™, United Kingdom) both serving as separators. For final assembly, the cells were transferred into an argon glovebox (99.999% Ar, MBraun Unilab, <1 ppm H_2O; <1 ppm O_2) and sodium metal acting as counter electrode and a 1 M solution of $NaCF_3SO_3$ (abcr, 98%) in bis(2-methoxyethyl)ether (Diglyme, Acros Organics, 99+%, extra dry) serving as electrolyte were added. Galvanostatic long-term measurements were conducted using a Neware 8 channel battery analyzer, applying current rates of 1 A g^{-1} within a voltage range of 3.0 to 0.1 V. Constant current-constant voltage (CCCV) charge mode was applied with a cutoff current density of 0.2 A g^{-1}. For rate capability measurements, current densities between 0.2 and 3.0 A g^{-1} were applied within the same voltage range. Cyclovoltammetric (CV) measurements were conducted using a Zahner XPOT with a scanning rate of 0.1 mV s^{-1} between 3.0 and 0.1 V. In order to gather information about the electrochemical reaction, galvanostatic measurements were interrupted after a defined uptake/release of Na. For these experiments, pressed powder electrodes and film electrodes casted on Al foil were used. The electrodes on Al foil were prepared as described above. For powder electrodes, a mixture of 70 wt% $CuCrP_2S_6$ and 30 wt% SUPER C65 was pressed into pellets and used in Swagelok® cells as described for the film cells. A low current rate of C/20 was applied for these experiments. After the uptake/release of a predetermined amount of Na, the electrodes were recovered, rinsed with Diglyme and dried for 24 h in an argon-filled glovebox. The samples were transferred into borosilicate capillaries and sealed in argon atmosphere for further measurements.

2.3 Material characterizations

Powder X-ray diffraction (PXRD) measurements were performed using Cu K_α radiation (1.54058 Å) with a PANalytical diffractometer equipped with a 1D PIXcel detector in Debye-Scherrer geometry. Elemental CHNS analysis was done with a vario MICRO

cube elemental analyzer (Elementar) using sulphanilamide as standard material. EDX and SEM experiments were conducted using a Philips ESEM XL 30 system equipped with an EDAX New XL-30 detector.

3. Results and Discussion

3.1 Characterization of pristine $CuCrP_2S_6$

The compound $CuCrP_2S_6$ could be obtained phase pure through manual separation from $CrPS_4$ as by-product. Despite extensive variation of the synthesis parameters, formation of small amounts of $CrPS_4$ could not be avoided completely (see ESI; Figure S1). $CuCrP_2S_6$ crystallizes in the monoclinic space group *C2/c* at room temperature with lattice parameters of a = 5.916 Å, b = 10.246 Å, c = 13.415 Å and β = 107.09°, V = 777.250 $Å^3$.[43] The PXRD pattern of the sample compared to the calculated PXRD pattern of the room temperature modification of $CuCrP_2S_6$ demonstrates phase purity (Figure 2). However, the intensity ratios of some reflections differ from the calculated pattern and the extinction of less intense reflections can be observed. Structural phenomena such as stacking faults, twinning or rotational disorder most likely cause these deviations in intensity for this kind of layered material. Especially for hypothiophosphates $[P_2S_6]^{4-}$ these phenomena are often observed and were described in literature.[51–54] In a previous study on $Ni_2P_2S_6$, TEM analysis revealed the existence of structurally distorted domains with monoclinic to pseudo-hexagonal symmetry resulting in similar deviations from the expected PXRD pattern.[36] Regarding the structural similarities, such partial distortions of the unit cell in certain domains might occur as well for $CuCrP_2S_6$ and hence intensity ratios are different than expected. Further, a preferred orientation caused by sample preparation may also influence the observed intensity ratios, since the intensities of the (00*l*) reflections are significantly stronger than expected.

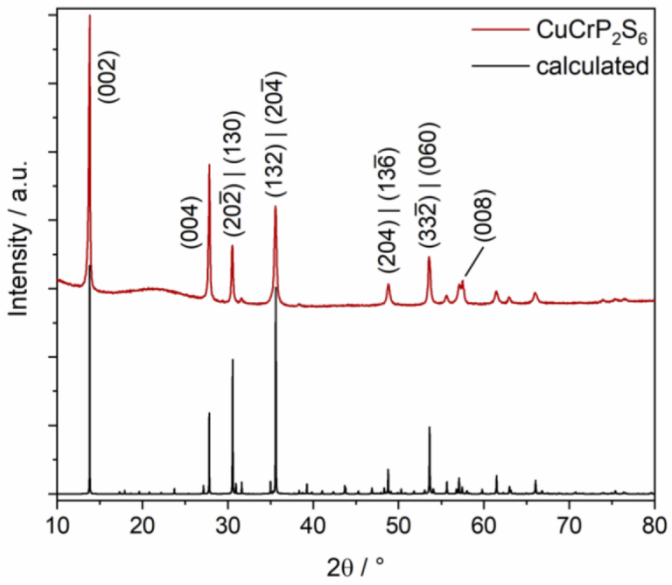

Figure 2. PXRD pattern of $CuCrP_2S_6$ compared to the calculated pattern using literature data.[43]

Additionally, combined EDX data at different spots of the sample and chemical elemental analysis (see ESI; Tables S1, S2) reveal the composition of $Cu_{1.05}Cr_{0.92}P_{1.96}S_{6.07}$, which fits nicely the assumed chemical formula. SEM images (see Figure S2) additionally depict that multiple slabs are stacked on top of each other illustrating the plate-like and layered structure of the compound.

3.2 Electrochemical performance

Results of long-term stability and rate capability measurements of $CuCrP_2S_6$ electrodes are displayed in Figure 3a. Galvanostatic long-term measurements within a potential range between 3.0 and 0.1 V with an applied current density of 1 A g^{-1} showed Coulombic efficiencies close to 100% after the 3rd cycle. The initial discharge capacity is 982 mAh g^{-1} (≈ 13.6 Na/f.u.), while the specific charge capacity of the initial cycle amounts to 810 mAh g^{-1} (≈ 11.2 Na/f.u.). During the first 20 cycles, the capacities quickly drop to 514 mAh g^{-1} (≈ 7.1 Na/f.u.) and remain stable for the following 20 cycles. Thereafter, a local minimum of 461 mAh g^{-1} (≈ 6.4 Na/f.u.) in the 65th cycle is obtained and 504 mAh g^{-1} (≈ 7 Na/f.u.) is reached after 124 cycles. Afterwards, a steady decrease occurs until a reversible capacity of 409 mAh g^{-1} (≈ 5.6 Na/f.u.) is obtained in the 200th cycle. Accordingly, a distinct evolution of the discharge and charge profiles (Figure 3b, c) is observed during the long-term measurement. For the first cycle, the discharge profile quickly drops from 2.8 V to a pseudo-plateau around 1.86 V and further decreases to a potential of ~ 0.6 V, beneath which the potential

decline slows down and is relatively shallow until the initial discharge capacity of 982 mAh g^{-1} is obtained. In the charge profile of the 1st cycle, the potential rapidly increases until a pseudo-plateau at around 2.0 V is reached and afterwards continues to rise until the cell is completely charged delivering an initial charge capacity of 810 mAh g^{-1}, which corresponds to a capacity loss of ~ 172 mAh g^{-1} (≈ 2.4 Na/f.u.). This value seems to be large, but is within the typical order of magnitude for irreversible capacity of these kind of materials[36,55,56] and is mainly caused by formation of a solid electrolyte interphase (SEI) as well as co-intercalation of the solvent molecules of the electrolyte in case of layered active materials. The discharge/charge profiles for the subsequent cycles differ vastly from the profiles of the initial cycle, which is a common observation for conversion-type electrodes. For the 3rd cycle, the potential drops quickly from 3.0 V to ~ 0.5 V and thereafter continues to decrease much slower until the discharged state is reached. The charge profile of the 3rd cycle (pseudo-plateau at ~ 2.08 V) looks very similar to the first cycle, but yields less capacity. From the 3rd cycle onwards, the discharge/charge curves display several alterations. Until the 65th cycle, a new pseudo-plateau at ~ 1.43 V in the discharge profile as well as a small pseudo-plateau at ~ 1.57 V and a more pronounced plateau at ~ 1.99 V in the charge curve are developed. The evolution from the 65th to 124th cycle is less pronounced. However, the pseudo-plateau in the discharge curve slightly shifts to 1.47 V, while being more pronounced. In the charge curve, the pseudo-plateau at ~ 1.57 V is more developed for the 124th compared to the 65th cycle, while the other plateau shifts from ~ 1.99 V in the 65th to ~ 1.94 V in the 124th cycle and is slightly less pronounced. In total, a slight capacity gain is observed comparing the 65th to the 124th cycle. After the 124th cycle, the capacity steadily decreases, which is seen in the discharge/charge profiles as well. The same events observed in the discharge and charge curves of the 124th cycle occur in the 200th cycle, but are less pronounced and rather faint resulting in a lower specific capacity compared to the 124th cycle. The evolution of the potential plateaus are better visible in the *dQ/dV* curves (Figure S3) allowing determination of the exact potentials of the (pseudo-)plateaus.

It is noteworthy that the amount of consumed Na/f.u. for the initial discharging and charging (D/C) is very similar for $CuCrP_2S_6$ (D/C: 13.6 / 11.2 Na/f.u.) and for $Ni_2P_2S_6$ (D/C: 14.0 / 11.7 Na/f.u.),[36] which strengthens the assumption of a similar general reaction pathway for initial discharging and charging. For $Ni_2P_2S_6$ the discharge process delivered Ni, P and Na_2S as reaction products, while charging led to the

formation of Ni_3S_2 besides probably some kind of phosphorus sulfide.[36] For $CuCrP_2S_6$, this would correspond to the formation of Cu, Cr, P and Na_2S in the discharged state, while charging may generate Cu and Cr sulfides or a Cu-Cr sulfides and most probable phosphorus sulfides. However, the mechanistic processes of the initial cycle are described in more detail in section 3.3.

The observed initial dropping and recovery of specific capacity upon cycling is often observed for electrodes in SIBs and in many cases associated with alterations of the underlying conversion reaction mechanisms. However, different synergistic effects as for CuS are known as well causing an increasing capacity at the beginning of long-term measurements after a distinct capacity drop. However, the capacity recovery behavior observed for $CuCrP_2S_6$ differs from that of CuS.[57] Nevertheless, electrodes like $Ni_2P_2S_6$, CuV_2S_4 or $CuCrS_2$ indeed picture similar patterns during long-term cycling.[36,49,50] For these materials, the slow and steady recovery after an initial period of decreasing capacity is caused by changes of the reaction mechanism, which is also very likely for $CuCrP_2S_6$ demonstrated by the shapes of the discharge and charge curves (Figure 3b, c) after an extended period of cycling. In this context, the two Cu containing materials CuV_2S_4 and $CuCrS_2$ are of special interest. It was reported that an extrusion mechanism leads to formation of elemental Cu in the early discharge stages, which first does not participate in the electrochemical reaction upon early long-term cycling, but in later stages presumably prevents detrimental formation and dissolution of polysulfides by formation of Cu sulfides.[49,50] However, we note that the quaternary $CuCrP_2S_6$ compound and its potential electrochemical reactions occurring during long-term cycling are probably more complex than those postulated for the ternary compounds. Therefore, phosphorus might as well play an important role regarding changes of the mechanisms during extended periods of cycling.

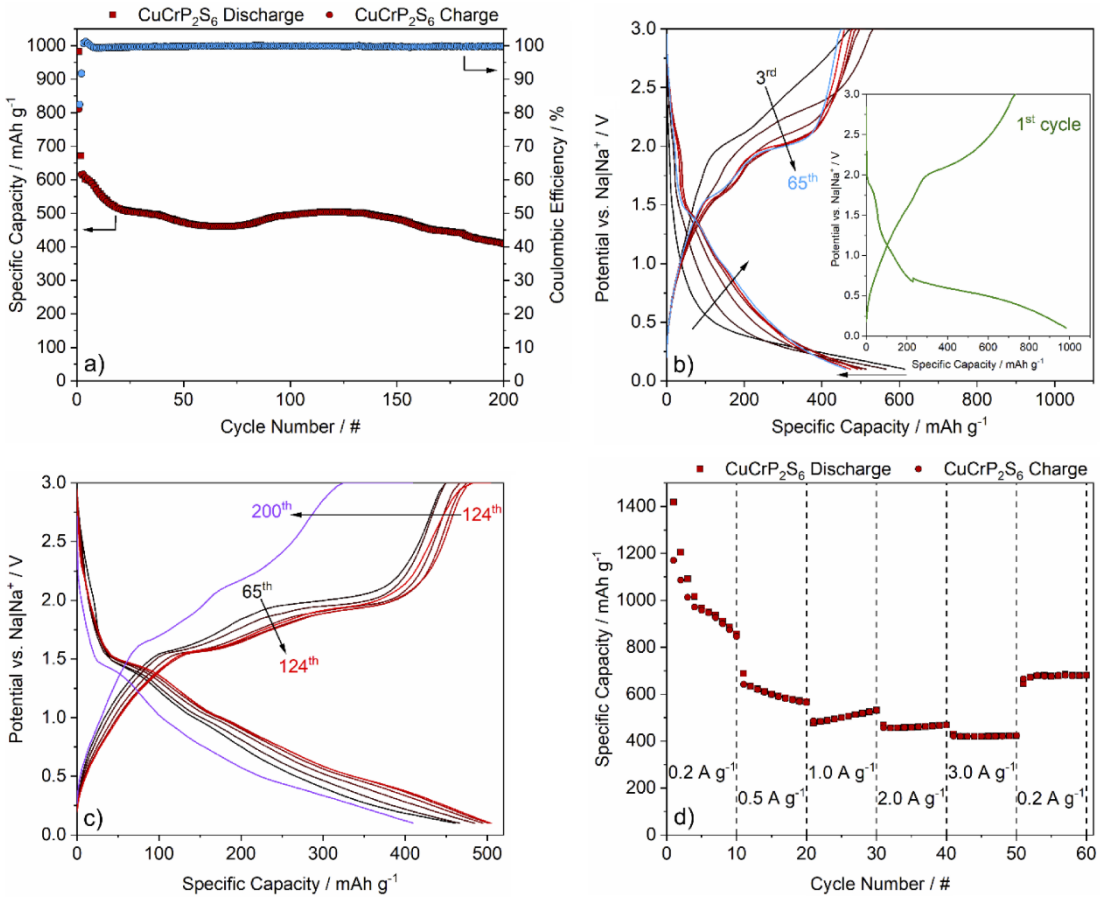

Figure 3. (a) Electrochemical long-term performance and Coulombic Efficiency of $CuCrP_2S_6$ electrode against Na metal. A current rate of 1 A g^{-1} was applied and cycling was performed in a potential range between 3.0 and 0.1 V. Discharge and charge curves of (b) 1st – 65th (inset: 1st cycle) and (c) 65th – 124th and the 200th cycle. Roughly, every 10th cycle is shown between the cycles 3, 65 and 124. (d) Rate capability measurements for several current rates ranging between 0.2 and 3.0 A g^{-1} applied in a potential range between 3.0 - 0.1 V.

To determine the rate capability of the material, current rates of 0.2, 0.5, 1.0, 2.0, 3.0 and again 0.2 A g^{-1} were applied for 10 cycles each (Figure 3d). The 10th cycle of the lowest current rate of 0.2 A g^{-1} delivers a specific discharge capacity of 857 mAh g^{-1}. The successive increase of the applied current leads to lower specific discharge capacities in the 10th cycle of each current rate (Table 1).

Table 1. Observed specific capacities and corresponding capacity retentions at different current rates.

Current Rate / A g^{-1}	Specific Capacity / mAh g^{-1}	Capacity Retention / %
0.2	857	-
0.5	566	66
1.0	531	62
2.0	468	55

3.0	422	49
0.2	681	79

As observed in the long-term measurements, the capacity drops quickly for the first cycles. Because this initial period of declining capacity lasts at least about 20 cycles in the long-term measurement, it can be assumed that this period strongly influences the first two current rates of the rate capability measurement. Accordingly, the value of the capacity retention going from 0.2 A g^{-1} to 0.5 A g^{-1} might be underdetermined. However, the specific capacities obtained from the highest rate of 3.0 A g^{-1} (422 mAh g^{-1}) clearly show an excellent rate capability compared to the capacities obtained from the long-term experiments (current rate of 1.0 A g^{-1}: 409 mAh g^{-1} after 200 cycles; peak performance after initial capacity drop: ~ 500 mAh g^{-1}). Starting from the 10th cycle with a current rate of 1.0 A g^{-1} (531 mAh g^{-1}), the tolerance to higher currents is revealed. The corresponding capacity retentions amount to 88% and 79% for the current densities of 2.0 A g^{-1} and 3.0 A g^{-1} compared to a current rate of 1.0 A g^{-1}. The rate capability measurements clearly evidence that a considerable loss of capacity occurs switching from lower to higher current densities, whereas the capacity loss is quite small when switched between high current rates. After applying all current rates and using the initial current density, the capacity retention amounts to 79%, which in general indicates a good tolerance against high currents. Especially when taking into consideration that the observed specific capacity was still decreasing (as seen in long-term measurement) during the first 10 cycles, the capacity retention of 79% for the last 10 cycles might as well be underdetermined.

Table 2. Comparison between selected indicators of electrochemical performance of different anode materials and $CuCrP_2S_6$.

anode material	long-term stability capacity / current / cycles [mAh g^{-1}] / [mA g^{-1}] / [#]	rate capability[a] capacity / current [mAh g^{-1}] / [mA g^{-1}]	operating potential	reference
$CuCrP_2S_6$	409 / 1000 / 200	422 / 3000 468 / 2000	3.0 – 0.1	This work
$Ni_2P_2S_6$	621 / 1000 / 190	392 / 3000 488 / 2000	3.0 – 0.1	[36]
CuV_2S_4	580 / 700 / 250	232 / 2000	3.0 – 0.01	[49]
$CuCrS_2$	252 / 1500 / 500	158 / 2000	2.5 – 0.1	[50]
$CrPS_4$	687 / 1000 / 300	288 / 3000	3.0 – 0.1	[56]

		346 / 2000		
$NiCr_2S_4$	558 / 500 / 200	399 / 5000 492 / 2000	3.0 – 0.1	[58]
Fe_3S_4	486 / 500 / 300	140 / 9000 359 / 2000	3.0 – 0.5	[59]
$CuFeS_2$	444 / 500 / 700	180 / 5000 352 / 2000	3.0 – 0.3	[60]
$CuFe_2S_3$	422 / 500 / 1000	170 / 5000 301 / 2000	3.0 – 0.3	[61]
NiS_2	319 / 500 / 1000	253 / 5000 420 / 2000	2.9 – 0.4	[62]
NiS/rGO	483 / 200 / 100	393 / 2000	3.0 – 0.01	[63]
NiS/CNT	394 / 200 / 100	331 / 2000	3.0 – 0.01	[63]

[a] rate capability with maximum current and at 2 A g^{-1} is shown.

For comparison of obtained values, the long-term stability and rate capability of $CuCrP_2S_6$ is related to similar anode materials, such as other thiophosphates or pseudo-layered sulfides, and to different ternary as well as binary 3D materials and some composite electrodes as well (Table 2). We note that experiments for distinct materials are usually designed differently and adjusted to the particular electrode (i.e. different current rates and operating potential ranges). Hence, an in-depth comparison would be inappropriate. Nevertheless, it is clearly visible that some materials are more tolerant against high currents, while others show better long-term stability. Besides, it shows that long-term performance and rate capability of $CuCrP_2S_6$ is within the same range of other electrode materials and therefore an appropriate overall electrochemical performance is obtained.

3.3 Investigation of the reaction mechanism *via* X-ray diffraction and CV analysis

X-ray powder diffraction

In order to gain insights into the electrochemical mechanism of the conversion reaction between $CuCrP_2S_6$ and Na in the first cycle, electrodes were discharged and charged to distinct states and subsequently characterized by PXRD. Electrodes of the phase pure sample were prepared on Al foil, while for samples with minor impurities, pressed powder electrodes were prepared. The discharge and charge profile of electrodes on Al foil (Figure 4a) shows minor deviations from the profiles of electrodes on Cu foil (see

Figure 3b; inset) due to the different metal used as current collector (Cu vs. Al). In addition, a slightly larger capacity was obtained from the sample on Al, which is due to the lower current rate. The corresponding PXRD patterns (Figure 4b) reveal interesting details of the electrochemical reaction. At a low uptake of 0.5 Na/f.u., new reflections appeared at ~ 11.9 and ~ 5.9 °2θ and simultaneously the reflections at ~ 30.5, ~ 35.5 and ~ 53.5 °2θ gained intensity compared to the other reflections of $CuCrP_2S_6$. After uptake of 1 Na/f.u. reflections of $CuCrP_2S_6$ have lost a substantial amount of intensity, while the newly emerged reflections at ~ 11.9 and ~ 5.9 °2θ are the most intense reflections and additional reflections at ~ 23.9 and ~ 52.2 °2θ appeared. These reflections reached their maximum intensity after the uptake of 2 Na/f.u., whereas those at ~ 11.9, 23.9 and 52.3 °2θ slightly shift to ~ 11.8, 23.8 and 51.1 °2θ. No distinct reflections of the starting material $CuCrP_2S_6$ can be observed at this state of discharge, but a region of slightly enhanced intensity has developed at ~ 27.8 – 36.0 °2θ. Further discharging leads to diminishing intensities, while the reflection at 51.1 °2θ shifts to ~ 50.8 °2θ after the uptake of 5 Na/f.u. After the uptake of 9 Na/f.u. only minor residues of the intermediate phase remains, while after the complete discharge new reflections at ~ 23.3, 38.6, 43.3 and 55.8 °2θ can be observed. It is noteworthy that the reflection at ~ 43.3 °2θ can be observed as early as ~ 2 Na/f.u. After recharging the electrode, the only observable reflections are located at ~ 38.7 and 55.9 °2θ.

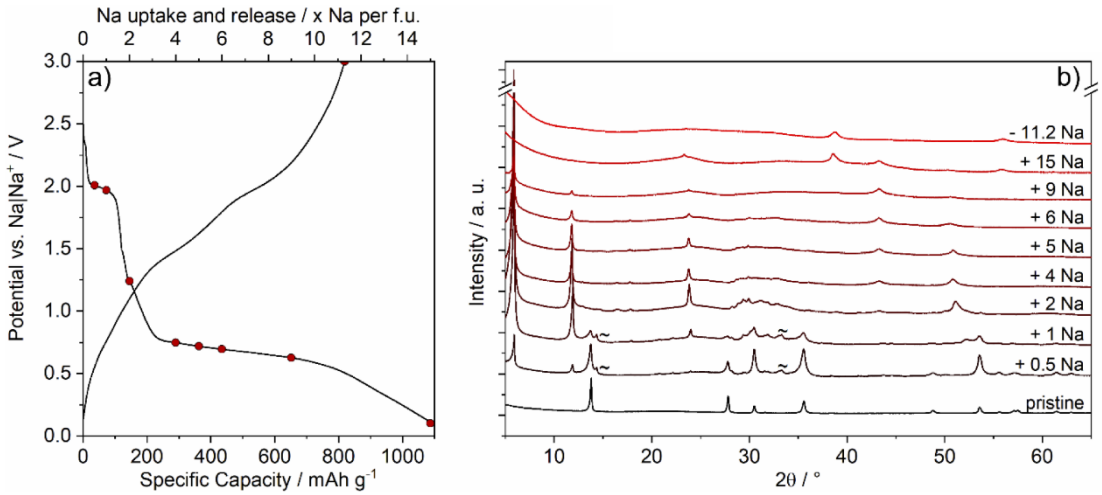

Figure 4. (a) Discharge and charge profile of a $CuCrP_2S_6$ film electrode casted on Al foil. The uptake/release of Na of the investigated samples is indicated by red dots. (b) PXRD patterns of $CuCrP_2S_6$ electrodes collected at different states of charge. The pattern marked with "+15 Na" indicates the completely discharged sample, while the pattern denoted with "-11.2 Na" was obtained from the recharged electrode. Reflections marked with ~ originate from minor impurities of $CrPS_4$.

Taking a closer look at the important states of discharge (Figure 5a-d) gives a more detailed insight of the ongoing mechanisms. PXRD patterns of the $CuCrP_2S_6$ electrode collected after the complete discharge (Figure 5a) evidence the formation of nanoscopic elemental Cu and Na_2S. The high background of the pattern is an indication of amorphous phases present in the discharged sample, which is not surprising as no signs of crystalline phases containing Cr or P are observable. X-ray amorphous elemental Cr in discharged electrodes was previously reported for the anode material $CuCrS_2$.[50] Taking the formation of Na_2S and metallic Cu into account and assuming that Cr is reduced to its metallic state, an electrochemical reaction according to eq. 1 involving 12 Na/f.u. is postulated. However, the actual observed Na uptake of 15 Na/f.u. is larger than required for the proposed reaction. In this context, the uptake of an excess of Na often is explained by Na_3P formation for MTP electrodes. Indeed, no evidence for the formation of Na_3P has been presented yet, and often the experimentally determined specific capacities do not match the required Na uptake for the proposed mechanisms involving Na_3P formation.[35,64–66] In contrast, some investigations of MTPs explicitly noticed that no signs of Na_3P were found after discharging.[36,55,56] Therefore, as long as no reliable evidence of Na_3P is presented, its formation during discharging should be considered at least very carefully. Furthermore, SEI formation and other side reactions can lead to even higher initial discharge capacities. In consequence, when actual Na_3P formation takes place, an enhanced Na uptake is expected. Hence, in the case of $CuCrP_2S_6$, the difference of ~ 3 Na/f.u. is most likely due to a combination of SEI formation and co-intercalation of solvent molecule from the electrolyte. Additionally, the excess of consumed Na in the initial cycle is within the same magnitude as for the previously studied active material $Ni_2P_2S_6$ with an extra consumption of ~ 2 Na/f.u., where no signs of Na_3P were observed either.[36] Regarding the PXRD pattern collected after recharging the $CuCrP_2S_6$ electrode, only Bragg reflections of NaF are observable, which is a commonly observed SEI compound in SIBs.[67–71] The fact that NaF can be observed in the PXRD pattern indicates that a larger amount of SEI must have formed during discharging. Because no crystalline phase other than NaF is observed in the PXRD pattern of the recharged sample, an amorphisation of the electrode material after the first cycle is most probable. The specific capacity for the recharged sample is ~ 820 mAh g^{-1} corresponding to ~ 11.3 Na/f.u.

PXRD patterns of the early discharge states (Figure 5b) clearly show that reflections of the starting material disappeared up to 2 Na/f.u., while new reflections of an intermediate phase successively develop with increasing Na content. Apart from a region with slightly enhanced background intensity (~ 27.8 - 36.0 °2θ), the pattern (2 Na/f.u.) is characterized by three pronounced and relatively sharp reflections located at ~ 5.9, 11.8, 17.8 (very weak) and 23.8 °2θ. Detailed examinations (Figure 5c) of the reflection positions reveal that these belong to the (00*l*) reflection series. Assuming that the space group does not change upon Na uptake maintaining the general reflection condition for the (00*l*) series of *l* = 2*n*, the *c* parameter increases from ~ 13.42 Å to ~ 31.43 Å, while the resulting unit cell likely contains twice as many layers (N = 4) as the unit cell of the pristine $CuCrP_2S_6$ (N = 2). The corresponding interlayer expansion amounts to ~ 1.1 Å, which is in accordance with the ionic radius of Na^+ in four- to sixfold coordination geometry (0.99 Å - 1.02 Å)[72] and indicates the intercalation of ~ 1 Na/f.u. into the van der Waals gap of $CuCrP_2S_6$ after the uptake of 2 Na/f.u. The difference of ~ 1 Na/f.u. most likely occupies the octahedral sites within the layers, where Cu^+ cations have been reduced and replaced by Na^+. As mentioned earlier, another reflection at ~ 51.1 °2θ and the region of enhanced intensity between ~ 27.8 and 36.0 °2θ most likely belong to this intermediate phase. However, based on the few sharp and the region of blurry reflections, it is impossible to propose a reliable structure model for the intermediate phase. Especially, the smeared intensities at ~ 27.8 to 36.0 °2θ are indications for additional structural disorder making a structure prediction even more difficult. Nevertheless, the occurrence of reflections of the (00*l*) series (Figure 5b, c) clearly demonstrates that the layered structure is maintained, and the interlayer expansion suggests intercalation of Na^+. Furthermore, the observed formation of elemental Cu after the uptake of 2 Na/f.u. (Figure 5d) strongly indicates the extrusion of Cu by Na.

Based on the findings in the early discharge states and the presence of Na_2S and elemental Cu at the completely discharged state, we propose the following simplified reaction pathway for the first discharge process:

$$CuCrP_2S_6 \xrightarrow{+2\,Na} Na_2Cu_{1-x}CrP_2S_6 + xCu \xrightarrow{+\,10\,Na} Cu + Cr + \frac{2}{n}P_n + 6Na_2S \qquad (x < 1) \quad (2)$$

We note that some portion of Cu potentially remains in the intermediate phase as observed for e.g. $CuCrS_2$ electrodes.[50] Hence, at 2 Na/f.u., residual Cu^+ and

intercalated Na^+ coexist in $Na_2Cu_{1-x}CrP_2S_6$ and the corresponding reaction is a combination of reduction/extrusion and intercalation. For the reaction pathway towards the end of the process, a conversion is most likely as supported by the detection of Na_2S. We particularly underline that no hints for formation of any Na_xP phases were found. Even if Na_xP was formed in the fully discharged state, one would expect that the capacity delivered upon recharging is larger than observed (~ 11.3 Na/f.u.) and similar to the discharge capacity (~ 15 Na/f.u.). Therefore, the formation of P(0) is assumed in the form of amorphous, polymeric phosphorus. The investigations of the recharged sample only prove the presence of NaF, preventing the postulation of a detailed reaction pathway for the charging process. Nevertheless, assuming a similar pathway as observed for $Ni_2P_2S_6$,[36] the formation of Cu, Cr and P sulfides seems reasonable.

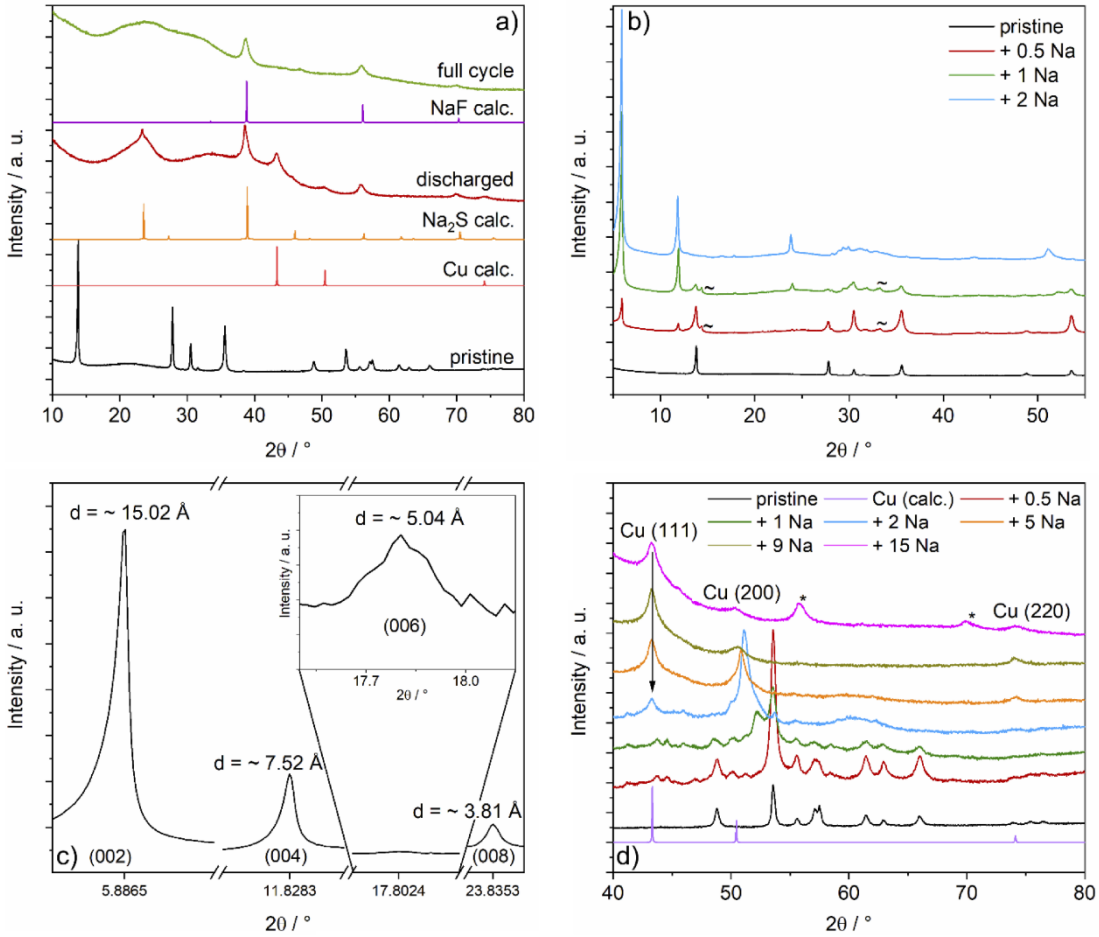

Figure 5. (a) PXRD patterns of pristine $CuCrP_2S_6$, completely discharged and recharged electrode compared with simulated patterns of NaF,[73] Na_2S[74] and fcc Cu.[75] (b) PXRD patterns of the early states of discharge up to 2 Na/f.u. The reflections marked with ~ correspond to minor impurities of $CrPS_4$. (c) Selected areas of the PXRD pattern after an uptake of 2 Na/f.u. to highlight the series of (00*l*) reflections. (d) PXRD patterns of different discharge states compared with a simulated pattern of fcc

Cu[75] evidencing the extrusion of Cu in the early discharge process. Reflections marked with * arise from the formation of Na_2S at the completely discharged state.

Cyclovoltammetry

In order to assess and discuss the results from an electrochemical perspective, CV curves of the $CuCrP_2S_6$ electrode (Figure 6a) were recorded. The curve of the initial cycle exhibits two pronounced and one weak reduction peaks, a shoulder and three broad oxidation events. The first reduction occurs at ~ 1.94 V (peak 1) and is assigned to the intercalation of Na into the structure and the extrusion and resulting reduction of Cu^+ to metallic Cu. The most intense reduction peak at ~0.48 V (peak 3) is assigned to the reduction of Cr^{3+} to Cr^0 in accordance with electrochemical data from Cr_3S_4 and $NiCr_2S_4$.[58] However, this peak is very broad and potentially superposes smaller signals. Furthermore, a shoulder at ~ 0.77 V and a weak signal at ~ 1.21 V (peak 2) occur, which likely are associated with a (two-step) reduction of P^{4+}. Additionally, SEI formation likely contributes to the broadening of reduction peak 3 and/or the formation of the shoulder.

The first oxidation peak is observed at ~ 1.45 V (peak 4), which is assigned to the oxidation of Cr^0. The oxidation events occurring at ~ 2.13 V (peak 5) and ~ 2.54 V (peak 6) arise from the oxidation of P and Cu, respectively. The blurred appearance of peak 5 thereby is an indication of the occurrence of several oxidation processes, which potentially is due to a multi-step oxidation of P, similar to the observation made for the reduction process. We note that the assignment of the redox events was based on the information gathered by PXRD combined with the standard potentials of the redox couples Cu^+/Cu, $H_4P_2O_6/H_3PO_3$, H_3PO_3/P(red) and Cr^{3+}/Cr amounting to E^0 = +0.52 V; E^0 = +0.38 V; E^0 = -0.45 V; E^0 = -0.74 V, respectively.[76]

CV curves of cycles 2-5 differ from the first cycle, but are similar in appearance to each other, which is a typical sign of a conversion-type reaction. The most obvious differences are absence of peak 1 and shifting of peak 2 to lower potentials. Furthermore, the shape of the oxidation peaks strongly changed and their intensity decreased. The shift of the reduction peak 2 accompanied by decreasing intensity likely arises from a changing discharge process during the first cycles. However, SEI formation lasting for several cycles might as well influence peak 2. The shoulder (~ 0.77 V in the 1st cycle), which is still visible in the 2nd cycle, lost intensity and might be a sign of ongoing SEI formation after the 1st cycle as well.

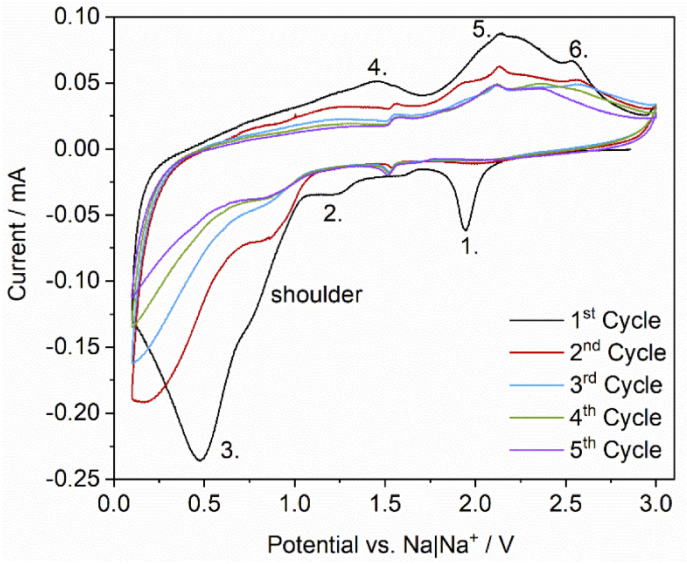

Figure 6. CV curves of the first 5 cycles recorded with a scan rate of 0.1 mV s^{-1} within a potential range of 3.0 to 0.1 V.

To summarize, the findings from the CV experiment support the results obtained from PXRD measurements and shed light on the underlying electrochemical processes. The proposed discharging reaction pathway (eq. 2), which is based on PXRD investigations, match the redox processes visualized by the CV curves and therefore seems plausible. The CV experiment further confirms conversion-like behavior of the electrode, which already was assumed as a result of the electrochemical characterization. However, it is noteworthy that CV measurements usually do not provide sufficient information to unveil details of conversion reactions individually. Therefore, the suggestions made here, which solely were based on CV measurements should be treated as such and must not be over-interpreted.

4. Conclusion

The layered compound $CuCrP_2S_6$ was successfully obtained from chemical vapor transport reaction and phase purity could be significantly improved by varying the synthesis parameters. Galvanostatic measurements yielded the very large specific capacity of 1011 mAh g^{-1} in the first cycle, which dropped to 461 mAh g^{-1} within 65 cycles, followed by a recovery (124^{th} cycle: 504 mAh g^{-1}) and decreased to 409 mAh g^{-1} after 200 cycles. Rate capability measurements delivered 422 mAh g^{-1} at a current density of 3.0 A g^{-1} and revealed a decent tolerance against high current densities. The observed fluctuations of capacities in the long-term measurement are most likely due to changes of the underlying reaction mechanism, which is a common

observation for conversion reactions. At the beginning of Na uptake an intercalation reaction occurs accompanied by an expansion of the interlayer space of the structure. The Na insertion leads to a reduction of Cu^+, which is expelled as nanocrystalline metallic Cu from the host, i.e. the mechanism may be described as intercalation-reduction-extrusion reaction. Increasing the Na content results in a successive decomposition of the intermediate phase and only elemental Cu and nanocrystalline Na_2S can be observed in the PXRD pattern of the completely discharged electrode. For the recharged sample, the presence of NaF is verified in the PXRD pattern, which can be attributed to the formation of a SEI layer.

The large value of the specific charge capacity can be explained by oxidation of Cu, P and Cr, despite no reflections of Cu, P and/or Cr sulfides are observed in the PXRD pattern of the recharged electrode. This observation suggests that the phases containing Cu, P and Cr are in the nanocrystalline/amorphous state. Considering the results and the values of the experimentally obtained specific capacity, a discharge reaction involving 12 Na/f.u. (eq. 2) is most likely, while charging releases 11.3 Na/f.u. and several reactions may be postulated depending on the assumptions made as shown in the formal equations 3-7:

$$Cu + Cr + \frac{2}{n}P_n + 6Na_2S \rightarrow \frac{1}{6}Cu_2S + CrS + \frac{1}{2}P_4S_9 + 11\frac{1}{3}Na + \frac{1}{3}Na_2S + \frac{2}{3}Cu \quad (3)$$

$$Cu + Cr + \frac{2}{n}P_n + 6Na_2S \rightarrow \frac{1}{3}Cu_2S + \frac{1}{3}Cr_3S_4 + \frac{1}{2}P_4S_8 + 11\frac{1}{3}Na + \frac{1}{3}Na_2S + \frac{1}{3}Cu \quad (4)$$

$$Cu + Cr + \frac{2}{n}P_n + 6Na_2S \rightarrow \frac{1}{6}Cu_2S + \frac{1}{2}Cr_2S_3 + \frac{1}{2}P_4S_8 + 11\frac{1}{3}Na + \frac{1}{3}Na_2S + \frac{2}{3}Cu \quad (5)$$

$$Cu + Cr + \frac{2}{n}P_n + 6Na_2S \rightarrow Cu + \frac{2}{3}CrS + \frac{1}{2}P_4S_{10} + 11\frac{1}{3}Na + \frac{1}{3}Na_2S + \frac{1}{3}Cr \quad (6)$$

$$Cu + Cr + \frac{2}{n}P_n + 6Na_2S \rightarrow Cu + \frac{7}{18}Cr_2S_3 + \frac{1}{2}P_4S_9 + 11\frac{1}{3}Na + \frac{1}{3}Na_2S + \frac{2}{9}Cr \quad (7)$$

We note that these are formal reactions, which demonstrate the plethora of possible oxidation products and highlight the enormous difficulties formulating a distinct mechanism in the case where only amorphous/nanocrystalline products are formed. Especially for the P-sulfides, the chemical formula should not imply that these well-known compounds actually are generated, but they rather account for the experimental capacity. The CV curves indicate that at least partial oxidation of Cu, Cr, and P occurs making eq.'s 6 & 7 less likely.

Supporting Information

Details about different synthesis approaches; additional PXRD patterns; results of EDX and elemental analysis, *dQ/dV* curves

Acknowledgements

Financial support by the State of Schleswig-Holstein is gratefully acknowledged.

Conflicts of interest

The authors declare no competing financial interest.

Keywords: anode material, $CuCrP_2S_6$, extrusion, intercalation, reaction mechanisms, sodium-ion battery, X-ray diffraction

References

[1] J.-Y. Hwang, S.-T. Myung, Y.-K. Sun, *Chem. Soc. Rev.* **2017**, *46*, 3529–3614.
[2] E. de la Llave, V. Borgel, K.-J. Park, J.-Y. Hwang, Y.-K. Sun, P. Hartmann, F.-F. Chesneau, D. Aurbach, *ACS Appl. Mater. Interfaces* **2016**, *8*, 1867–1875.
[3] D. Larcher, J.-M. Tarascon, *Nat. Chem.* **2015**, *7*, 19–29.
[4] N. Yabuuchi, K. Kubota, M. Dahbi, S. Komaba, *Chem. Rev.* **2014**, *114*, 11636–11682.
[5] M. D. Slater, D. Kim, E. Lee, C. S. Johnson, *Adv. Funct. Mater.* **2013**, *23*, 947–958.
[6] J. Deng, W.-B. Luo, S.-L. Chou, H.-K. Liu, S.-X. Dou, *Adv. Energy Mater.* **2018**, *8*, 1701428.
[7] Y. Kim, K.-H. Ha, S. M. Oh, K. T. Lee, *Chem. – Eur. J.* **2014**, *20*, 11980–11992.
[8] K. M. Abraham, *ACS Energy Lett.* **2020**, *5*, 3544–3547.
[9] D. A. Stevens, J. R. Dahn, *J. Electrochem. Soc.* **2001**, *148*, A803–A811.
[10] K. Nobuhara, H. Nakayama, M. Nose, S. Nakanishi, H. Iba, *J. Power Sources* **2013**, *243*, 585–587.
[11] J. Sangster, *J. Phase Equilib. Diffus.* **2007**, *28*, 571–579.
[12] Y. Okamoto, *J. Phys. Chem. C* **2014**, *118*, 16–19.
[13] D.-Y. Kim, D.-H. Kim, S.-H. Kim, E.-K. Lee, S.-K. Park, J.-W. Lee, Y.-S. Yun, S.-Y. Choi, J. Kang, *Nanomaterials* **2019**, *9*, 793.
[14] B. Xiao, T. Rojo, X. Li, *ChemSusChem* **2019**, *12*, 133–144.
[15] I. El Moctar, Q. Ni, Y. Bai, F. Wu, C. Wu, *Funct. Mater. Lett.* **2018**, *11*, 1830003.
[16] E. Irisarri, A. Ponrouch, M. R. Palacin, *J. Electrochem. Soc.* **2015**, *162*, A2476–A2482.
[17] P. K. Nayak, L. Yang, W. Brehm, P. Adelhelm, *Angew. Chem., Int. Ed.* **2018**, *57*, 102–120.
[18] Y. Xiao, S. H. Lee, Y.-K. Sun, *Adv. Energy Mater.* **2017**, *7*, 1601329.
[19] W. Kang, Y. Wang, J. Xu, *J. Mater. Chem. A* **2017**, *5*, 7667–7690.
[20] J. Mao, T. Zhou, Y. Zheng, H. Gao, H. kun Liu, Z. Guo, *J. Mater. Chem. A* **2018**, *6*, 3284–3303.
[21] Z. Hu, Q. Liu, S.-L. Chou, S.-X. Dou, *Adv. Mater.* **2017**, *29*, 1700606.
[22] X. Y. Yu, X. W. (David) Lou, *Adv. Energy Mater.* **2018**, *8*, 1701592.
[23] Y. Liu, C. Yang, Q. Zhang, M. Liu, *Energy Storage Mater.* **2019**, *22*, 66–95.

[24] M. Lao, Y. Zhang, W. Luo, Q. Yan, W. Sun, S. X. Dou, *Adv. Mater.* **2017**, *29*, 1700622.
[25] L. Li, Y. Zheng, S. Zhang, J. Yang, Z. Shao, Z. Guo, *Energy Environ. Sci.* **2018**, *11*, 2310–2340.
[26] Q. Xia, W. Li, Z. Miao, S. Chou, H. Liu, *Nano Res.* **2017**, *10*, 4055–4081.
[27] H. Liu, K. Hu, D. Yan, R. Chen, Y. Zou, H. Liu, S. Wang, *Adv. Mater.* **2018**, *30*, 1800295.
[28] T. Wang, D. Su, D. Shanmukaraj, T. Rojo, M. Armand, G. Wang, *Electrochem. Energy Rev.* **2018**, *1*, 200–237.
[29] F. Klein, B. Jache, A. Bhide, P. Adelhelm, *Phys. Chem. Chem. Phys.* **2013**, *15*, 15876–15887.
[30] M. C. Friedel, *C. R. Hebd. Séances Acad. Sci.* **1894**, *119*, 260–264.
[31] M. A. Susner, M. Chyasnavichyus, M. A. McGuire, P. Ganesh, P. Maksymovych, *Adv. Mater.* **2017**, *29*, 1602852.
[32] R. Dangol, Z. Dai, A. Chaturvedi, Y. Zheng, Y. Zhang, K. Ngoc Dinh, B. Li, Y. Zong, Q. Yan, *Nanoscale* **2018**, *10*, 4890–4896.
[33] F. Wang, T. A. Shifa, P. Yu, P. He, Y. Liu, F. Wang, Z. Wang, X. Zhan, X. Lou, F. Xia, J. He, *Adv. Funct. Mater.* **2018**, *28*, 1802151.
[34] K. Du, X. Wang, Y. Liu, P. Hu, M. I. B. Utama, C. K. Gan, Q. Xiong, C. Kloc, *ACS Nano* **2016**, *10*, 1738–1743.
[35] Q. Liang, Y. Zheng, C. Du, Y. Luo, J. Zhang, B. Li, Y. Zong, Q. Yan, *Small Methods* **2017**, *1*, 1700304.
[36] J. van Dinter, K. Synnatschke, T. A. Engesser, S. Indris, N. Wolff, O. Gronenberg, M. Etter, G. Cibin, L. Kienle, C. Backes, W. Bensch, *J. Mater. Chem. A* **2020**, *8*, 22401–22415.
[37] G. Ouvrard, R. Fréour, R. Brec, J. Rouxel, *Mater. Res. Bull.* **1985**, *20*, 1053–1062.
[38] W. Klingen, R. Ott, H. Hahn, *Z. Anorg. Allg. Chem.* **1973**, *396*, 271–278.
[39] E. Prouzet, G. Ouvrard, R. Brec, *Mater. Res. Bull.* **1986**, *21*, 195–200.
[40] G. Ouvrard, R. Brec, J. Rouxel, *Mater. Res. Bull.* **1985**, *20*, 1181–1189.
[41] R. Brec, *Solid State Ionics* **1986**, *22*, 3–30.
[42] M. Evain, R. Brec, M.-H. Whangbo, *J. Solid State Chem.* **1987**, *71*, 244–262.
[43] P. Colombet, A. Leblanc, M. Danot, J. Rouxel, *J. Solid State Chem.* **1982**, *41*, 174–184.
[44] V. Maisonneuve, V. B. Cajipe, C. Payen, *Chem. Mater.* **1993**, *5*, 758–760.
[45] K. Momma, F. Izumi, *J. Appl. Crystallogr.* **2011**, *44*, 1272–1276.
[46] V. Bodenez, L. Dupont, M. Morcrette, C. Surcin, D. W. Murphy, J.-M. Tarascon, *Chem. Mater.* **2006**, *18*, 4278–4287.
[47] V. Bodenez, L. Dupont, L. Laffont, A. R. Armstrong, K. M. Shaju, P. G. Bruce, J.-M. Tarascon, *J. Mater. Chem.* **2007**, *17*, 3238–3247.
[48] W. Bensch, J. Ophey, H. Hain, H. Gesswein, D. Chen, R. Mönig, P. A. Gruber, S. Indris, *Phys. Chem. Chem. Phys.* **2012**, *14*, 7509–7516.
[49] M. Krengel, A.-L. Hansen, M. Kaus, S. Indris, N. Wolff, L. Kienle, D. Westfal, W. Bensch, *ACS Appl. Mater. Interfaces* **2017**, *9*, 21283–21291.
[50] M. Krengel, A.-L. Hansen, F. Hartmann, J. van Dinter, W. Bensch, *Batteries Supercaps* **2018**, *1*, 176–183.
[51] A. R. Wildes, V. Simonet, E. Ressouche, R. Ballou, G. J. McIntyre, *J. Phys.: Condens. Matter* **2017**, *29*, 455801.
[52] A. R. Wildes, V. Simonet, E. Ressouche, G. J. McIntyre, M. Avdeev, E. Suard, S. A. J. Kimber, D. Lançon, G. Pepe, B. Moubaraki, T. J. Hicks, *Phys. Rev. B* **2015**, *92*, 224408.

[53] C. Murayama, M. Okabe, D. Urushihara, T. Asaka, K. Fukuda, M. Isobe, K. Yamamoto, Y. Matsushita, *J. Appl. Phys.* **2016**, *120*, 142114.
[54] P. Fragnaud, E. Prouzet, R. Brec, *J. Mater. Res.* **1992**, *7*, 1839–1846.
[55] W. Brehm, A. L. Santhosha, Z. Zhang, C. Neumann, A. Turchanin, A. Martin, N. Pinna, M. Seyring, M. Rettenmayr, J. R. Buchheim, P. Adelhelm, *Adv. Funct. Mater.* **2020**, *30*, 1910583.
[56] J. van Dinter, S. Indris, A. Bitter, D. Grantz, G. Cibin, M. Etter, W. Bensch, *ACS Appl. Mater. Interfaces* **2021**, *13*, 54936–54950.
[57] J. Y. Park, S. J. Kim, K. Yim, K. S. Dae, Y. Lee, K. P. Dao, J. S. Park, H. B. Jeong, J. H. Chang, H. K. Seo, C. W. Ahn, J. M. Yuk, *Adv. Sci.* **2019**, *6*, 1900264.
[58] F. Hartmann, M. Etter, G. Cibin, L. Liers, H. Terraschke, W. Bensch, *Adv. Mater.* **2021**, *33*, 2101576.
[59] F. Hartmann, M. Etter, G. Cibin, H. Groß, L. Kienle, W. Bensch, *Nanoscale* **2022**, DOI 10.1039/D1NR06950K.
[60] S. Senkale, S. Indris, M. Etter, W. Bensch, *ACS Appl. Mater. Interfaces* **2021**, *13*, 26034–26045.
[61] S. Senkale, G. Cibin, A. V. Chadwick, W. Bensch, *ACS Appl. Mater. Interfaces* **2021**, *13*, 58552–58565.
[62] R. Sun, S. Liu, Q. Wei, J. Sheng, S. Zhu, Q. An, L. Mai, *Small* **2017**, *13*, 1701744.
[63] J. Wang, D. Cao, G. Yang, Y. Yang, H. Wang, *J. Solid State Electrochem.* **2017**, *21*, 3047–3055.
[64] Q. Liang, Y. Zheng, C. Du, Y. Luo, J. Zhao, H. Ren, J. Xu, Q. Yan, *ACS Nano* **2018**, *12*, 12902–12911
[65] Y. Sang, L. Wang, X. Cao, G. Ding, Y. Ding, Y. Hao, N. Xu, H. Yu, L. Li, S. Peng, *J. Alloys Compd.* **2020**, *831*, 154775.
[66] L. Li, H. Jiang, N. Xu, X. Lian, H. Huang, H. Geng, S. Peng, *J. Mater. Chem. A* **2021**, *9*, 17336–17343.
[67] J. Zhang, D.-W. Wang, W. Lv, S. Zhang, Q. Liang, D. Zheng, F. Kang, Q.-H. Yang, *Energy Environ. Sci.* **2017**, *10*, 370–376.
[68] J. Fondard, E. Irisarri, C. Courrèges, M. R. Palacin, A. Ponrouch, R. Dedryvère, *J. Electrochem. Soc.* **2020**, *167*, 070526.
[69] F. Wu, N. Zhu, Y. Bai, Y. Li, Z. Wang, Q. Ni, H. Wang, C. Wu, *Nano Energy* **2018**, *51*, 524–532.
[70] L. A. Ma, A. J. Naylor, L. Nyholm, R. Younesi, *Angew. Chem., Int. Ed.* **2021**, *60*, 4855–4863.
[71] J. Song, B. Xiao, Y. Lin, K. Xu, X. Li, *Adv. Energy Mater.* **2018**, *8*, 1703082.
[72] R. D. Shannon, *Acta Crystallogr. A* **1976**, *32*, 751–767.
[73] Y. Shirako, Y. G. Shi, A. Aimi, D. Mori, H. Kojitani, K. Yamaura, Y. Inaguma, M. Akaogi, *J. Solid State Chem.* **2012**, *191*, 167–174.
[74] E. Zintl, A. Harder, B. Dauth, *Z. Elektrochem. Angew. Phys. Chem.* **1934**, *40*, 588–593.
[75] H. M. Otte, *J. Appl. Phys.* **1961**, *32*, 1536–1546.
[76] A. J. Bard, R. Parsons, J. Jordan, *Standard Potentials in Aqueous Solution*, Marcel Dekker, New York, **1985**.

5. Conclusion and Future Perspective

In the context of this thesis, three materials from the broader substance class of transition metal thiophosphates were studied in detail, while the investigations were aimed to identify their potential as anode materials in SIBs and to understand the underlying reaction pathways of sodium uptake and release. For this purpose, the compounds $Ni_2P_2S_6$, $CrPS_4$ and $CuCrP_2S_6$ were chosen and the corresponding studies were designed to answer several questions. The research concerning $Ni_2P_2S_6$ was focused on reviewing the conversion-alloying reaction mechanism that had been postulated prior to the study and further on comparing the electrochemical performance of bulk with previously reported values for nanosheet electrodes. In contrast, $CrPS_4$ was investigated as new anode material, which does not contain main elements of common state-of-the-art electrodes, while the investigation of $CuCrP_2S_6$ was aimed to determine the benefits of incorporating Cu^+ into a thiophosphate anode material. A brief summary of the most essential findings is given below, which is followed by putting the results into context and answering the research questions. Thereafter, future perspectives based on this thesis are highlighted.

In order to assess the electrochemical performance of the different materials, experiments were focused on long-term cycling and rate capability tests. Each material surpasses its theoretical capacity in the initial cycle, which is ascribed to SEI formation and co-intercalation of solvent molecules into the van der Waals gaps of the layered materials. The observed reversible long-term capacities range between 687 mAh g^{-1} after 300 cycles for $CrPS_4$ and 409 mAh g^{-1} in the 200th cycle for $CuCrP_2S_6$, when current rates of 1.0 A g^{-1} were applied. Rate capabilities vary in similar dimensions from 422 mAh g^{-1} ($CuCrP_2S_6$) to 288 mAh g^{-1} ($CrPS_4$) for maximum current densities of 3.0 A g^{-1}. The electrochemical performance of $Ni_2P_2S_6$ lies in between (621 mAh g^{-1} after 190 cycles; 392 mAh g^{-1} at a rate of 3.0 A g^{-1}). In an effort to unravel the reaction mechanisms of discharging and charging, a variety of complementary characterization techniques was applied to study the occurring changes of structural long- and short-range order as well as of the electronic state. Despite pronounced structural similarities between the starting materials, the occurring reaction mechanisms during Na uptake are different. In early discharge states, the formation of intercalation compounds was observed. For $Ni_2P_2S_6$, arbitrary intercalation of Na^+ into the van der Waals gaps (staging phenomenon) results in a random distribution of Na in the interlayer space, *i.e.* simultaneous formation of multiple intercalation stages. In contrast, only one distinct intercalation stage was observed for $CuCrP_2S_6$, whereas the presence of domains comprising different amounts of intercalated Na (*i.e.* several defined intercalation stages) was detected for $CrPS_4$. Increasing the Na content leads to the transformation of the intercalation compounds into different intermediate phases. For $Ni_2P_2S_6$ electrodes, an

intermediate compound with the local structure of $Na_4P_2S_6$ is formed, and Ni^{2+} is reduced to Ni^0 nanoparticles in the process. For $CuCrP_2S_6$, the layered structure is maintained, and Cu^+ is reduced to Cu^0 and replaced by Na^+ according to an extrusion reaction. Investigations of $CrPS_4$ evidenced an extraordinary complex mechanism with a variety of unknown intermediate phases. For each of the examined electrode materials, completing the discharge process leads to conversion of the previously formed intermediates, resulting in the formation of Na_2S. The discharged samples therefore consist of Na_2S and metal (Ni^0/Cr^0/Cu^0 + Cr^0, resp.) nanoparticles, while the presence of a P^0 phase is postulated based on the experimentally obtained specific capacities. Recharging results in the loss of long-range order. It is most likely that different metal and phosphorus sulfides are formed for $Ni_2P_2S_6$ and $CuCrP_2S_6$. In contrast, recharging the $CrPS_4$ electrode potentially leads to the recovery of its local environment. Moreover, changes of the specific capacities were observed during long-term cycling. For $CrPS_4$, the specific capacity harshly dropped after the initial cycle and started increasing again thereafter, while the initial drop in specific capacity was less pronounced and occurred over a larger number of cycles for $Ni_2P_2S_6$ and $CuCrP_2S_6$. In each case, the observed behavior indicates a changing reaction mechanism during long periods of cycling.

This thesis provides new and deep insights into the potential of transition metal thiophosphates as electrodes and the ongoing processes during Na uptake and release. From an electrochemical perspective, $CrPS_4$ electrodes demonstrated an outstanding long-term performance, proving that crucial state-of-the-art elements can be avoided in high-performance electrodes. As for the other two materials, $CuCrP_2S_6$ does not offer real benefits over $Ni_2P_2S_6$ with respect to long-term performance. Regarding rate capabilities, $CuCrP_2S_6$ delivered the highest absolute numbers but is comparable to $Ni_2P_2S_6$ and inferior to $CrPS_4$ electrodes from a percentage contemplation. Despite the slight advantages of $CuCrP_2S_6$ over $Ni_2P_2S_6$ at higher current rates (>0.5 A g^{-1}), the benefits provided by the incorporation of Cu into MTP electrodes are less than expected. Similarly, bulk $Ni_2P_2S_6$ delivered a comparable electrochemical performance as reported for $Ni_2P_2S_6$ nanosheets, concluding that the previously assumed benefits of MTP nanosheet electrodes have been overestimated to date. In general, the examined MTP electrodes provide appropriate electrochemical performance comparable to or even better than other substance classes, such as binary or ternary transition metal sulfides. From a mechanistic point of view, the investigations of $Ni_2P_2S_6$ did not provide any evidence for the formation of Na_xP phases, which had been postulated previously. Hence, the assumed conversion-alloying reaction in SIBs for hypothiophosphates of certain bivalent transition metals is disproved by this study. Moreover, neither for $CrPS_4$ nor for $CuCrP_2S_6$ any signs of Na_xP phases were found. Therefore, it can be assumed that these materials do not follow a conversion-alloying

pathway either. Admittedly, rephrasing the formerly assumed reaction equation into a uniform mechanism for MTP electrodes would be the most elegant conclusion but is not practical insofar as the discharge processes of the investigated MTPs generate intercalation compounds and intermediate phases, which do not match a common mechanism. However, the discharge processes at the least proceed according to a similar course, which can be summarized by three steps:

i) intercalation of Na into the van der Waals layer
ii) formation of intermediate phase(s)
iii) conversion

Recharging results in the loss of long-range order for all compounds. However, the formation of different sulfides is most probable for $Ni_2P_2S_6$ and $CuCrP_2S_6$, while some data suggest that the local environment of $CrPS_4$ is recovered upon recharging.

It is noteworthy that $Ni_2P_2S_6$ and $CuCrP_2S_6$ electrodes behave fairly similar, especially in terms of electrochemical performance, whereas the behavior of $CrPS_4$ is noticeably different (*e.g.* capacity drop during long-term performance, complex discharging process). These differences certainly are correlated with the oxidation state of P and the structures of the corresponding anions in these compounds ($[P_2S_6]^{4-}$ vs. $[PS_4]^{3-}$). Equally, the similarities between $Ni_2P_2S_6$ and $CuCrP_2S_6$ are attributed to the $[P_2S_6]^{4-}$ anion, while differences between the mechanisms most likely arise from the cations' different properties, such as their oxidation states and the associated standard potentials. Interestingly, so far unpublished work on the reaction mechanism of $Fe_2P_2S_6$ vs. Na, which is not included in this thesis, indicates close resemblance to the reaction mechanism of $Ni_2P_2S_6$ in SIBs. Pursuing this approach, the implied question, whether different types of MTPs ($M_2P_2S_6$, $M^{I}M^{III}P_2S_6$, MPS_4) each follow universal reaction mechanisms, displays an intriguing topic for future research. Moreover, the chemical nature and local structure of the P^0 phase, which is assumed to be present in all discharged MTP electrodes, has not been unraveled conclusively and its identification depicts another interesting objective. Characterization techniques such as X-ray photoelectron spectroscopy (XPS) or XAS investigations at the P K-edge energy potentially are capable of answering this question in upcoming studies. Future research might as well address the observed alterations of the reaction mechanisms during long-term cycling. Since all samples transitioned into amorphous and disordered nanoscopic states after completing the initial cycle, further structural characterization is tedious and most likely requires an even more sophisticated approach. Hence, this topic ought to be addressed properly and not on the side of a study aiming to answer different research questions. However, it can be combined perfectly with evaluating the implications of using MTP nanoparticles as starting material on the long-term performance. Besides,

some structural peculiarities were encountered during this thesis, which are worth investigating in more detail. The observed structure-related phenomenon manifests as extinction of several Bragg reflections in XRD measurements of hypothiophosphates (here: $Ni_2P_2S_6$ and $CuCrP_2S_6$). Possible explanations include the presence of stacking faults, rotational disorder, distortions of the unit cell or combinations thereof, but a valid structural model, which uniformly describes this phenomenon throughout the whole material class, is still lacking and should be viewed as worthwhile research question in future projects.

6. References

[1] *Paris Agreement*, adopted **12.12.2015**, UN Treaty Collection, Chapter XXVII 7d, https://treaties.un.org/Pages/ViewDetails.aspx?src=IND&mtdsg_no=XXVII-7-d&chapter=27&clang=_en (**13.08.21**).

[2] D. Larcher, J.-M. Tarascon, *Nat. Chem.* **2015**, *7*, 19–29.

[3] J.-Y. Hwang, S.-T. Myung, Y.-K. Sun, *Chem. Soc. Rev.* **2017**, *46*, 3529–3614.

[4] J. Deng, W.-B. Luo, S.-L. Chou, H.-K. Liu, S.-X. Dou, *Adv. Energy Mater.* **2018**, *8*, 1701428.

[5] International Energy Agency, *Key World Energy Statistics 2020*, IEA, Paris, **2020**, https://www.iea.org/reports/key-world-energy-statistics-2020 (**18.08.21**).

[6] International Energy Agency, *The role of CCUS in low-carbon power systems*, IEA, Paris, https://www.iea.org/reports/the-role-of-ccus-in-low-carbon-power-systems (**18.08.21**).

[7] P. K. Nayak, L. Yang, W. Brehm, P. Adelhelm, *Angew. Chem., Int. Ed.* **2018**, *57*, 102–120.

[8] E. de la Llave, V. Borgel, K.-J. Park, J.-Y. Hwang, Y.-K. Sun, P. Hartmann, F.-F. Chesneau, D. Aurbach, *ACS Appl. Mater. Interfaces* **2016**, *8*, 1867–1875.

[9] N. Yabuuchi, K. Kubota, M. Dahbi, S. Komaba, *Chem. Rev.* **2014**, *114*, 11636–11682.

[10] J.-M. Tarascon, *Nat. Chem*. **2010**, *2*, 510.

[11] B. L. Ellis, L. F. Nazar, *Curr. Opin. Solid State Mater. Sci.* **2012**, *16*, 168–177.

[12] V. Palomares, P. Serras, I. Villaluenga, K. B. Hueso, J. Carretero-González, T. Rojo, *Energy Environ. Sci.* **2012**, *5*, 5884–5901.

[13] D. Buchholz, A. Moretti, R. Kloepsch, S. Nowak, V. Siozios, M. Winter, S. Passerini, *Chem. Mater.* **2013**, *25*, 142–148.

[14] P. Ge, M. Fouletier, *Solid State Ionics* **1988**, *28–30*, 1172–1175.

[15] M. D. Slater, D. Kim, E. Lee, C. S. Johnson, *Adv. Funct. Mater.* **2013**, *23*, 947–958.

[16] D. A. Stevens, J. R. Dahn, *J. Electrochem. Soc.* **2001**, *148*, A803–A811.

[17] M. M. Doeff, Y. Ma, S. J. Visco, L. C. De Jonghe, *J. Electrochem. Soc.* **1993**, *140*, L169.

[18] F. Klein, B. Jache, A. Bhide, P. Adelhelm, *Phys. Chem. Chem. Phys.* **2013**, *15*, 15876–15887.

[19] P. Adelhelm, P. Hartmann, C. L. Bender, M. Busche, C. Eufinger, J. Janek, *Beilstein J. Nanotechnol.* **2015**, *6*, 1016–1055.

[20] H. Kang, Y. Liu, K. Cao, Y. Zhao, L. Jiao, Y. Wang, H. Yuan, *J. Mater. Chem. A* **2015**, *3*, 17899–17913.

[21] E. Irisarri, A. Ponrouch, M. R. Palacin, *J. Electrochem. Soc.* **2015**, *162*, A2476–A2482.

[22] Y. Xiao, S. H. Lee, Y.-K. Sun, *Adv. Energy Mater.* **2017**, *7*, 1601329.

[23] W. Kang, Y. Wang, J. Xu, *J. Mater. Chem. A* **2017**, *5*, 7667–7690.

[24] W.-H. Lai, Y.-X. Wang, J.-Z. Wang, S.-L. Chou, S.-X. Dou, *Batteries Supercaps* **2020**, *3*, 236–253.

[25] J. Mao, T. Zhou, Y. Zheng, H. Gao, H. Kun Liu, Z. Guo, *J. Mater. Chem. A* **2018**, *6*, 3284–3303.

[26] X. Y. Yu, X. W. D. Lou, *Adv. Energy Mater.* **2018**, *8*, 1701592.

[27] M. Lao, Y. Zhang, W. Luo, Q. Yan, W. Sun, S. X. Dou, *Adv. Mater.* **2017**, *29*, 1700622.

[28] L. Li, Y. Zheng, S. Zhang, J. Yang, Z. Shao, Z. Guo, *Energy Environ. Sci.* **2018**, *11*, 2310–2340.

[29] T. Wang, D. Su, D. Shanmukaraj, T. Rojo, M. Armand, G. Wang, *Electrochem. Energy Rev.* **2018**, *1*, 200–237.

[30] J. Cabana, L. Monconduit, D. Larcher, M. R. Palacín, *Adv. Mater.* **2010**, *22*, E170–E192.

[31] Y. V. Kuz'minskii, B. M. Voronin, I. M. Petrushina, N. N. Redin, G. P. Prikhodko, *J. Power Sources* **1995**, *55*, 1–6.

[32] Y. V. Kuz'minskii, B. M. Voronin, N. N. Redin, *J. Power Sources*, **1995**, *55*, 133–141.

[33] Q. Liang, Y. Zheng, C. Du, Y. Luo, J. Zhang, B. Li, Y. Zong, Q. Yan, *Small Methods* **2017**, *1*, 1700304.

[34] Y. Fujii, A. Miura, N. C. Rosero-Navarro, M. Higuchi, K. Tadanaga, *Electrochim. Acta* **2017**, *241*, 370–374.

[35] Y. Fujii, A. Miura, N. C. Rosero-Navarro, Y. Mizuguchi, C. Moriyoshi, Y. Kuroiwa, M. Higuchi, K. Tadanaga, *J. Electrochem. Soc.* **2018**, *165*, A2948–A2954.

[36] R. Dangol, Z. Dai, A. Chaturvedi, Y. Zheng, Y. Zhang, K. N. Dinh, B. Li, Y. Zong, Q. Yan, *Nanoscale* **2018**, *10*, 4890–4896.

[37] Y. Suto, Y. Fujii, A. Miura, N. C. Rosero-Navarro, M. Higuchi, K. Tadanaga, *J. Ceram. Soc. Jpn.* **2018**, *126*, 568–572.

[38] M. S. Whittingham, *Science* **1976**, *192*, 1126–1127.

[39] K. Mizushima, P. C. Jones, P. J. Wiseman, J. B. Goodenough, *Mater. Res. Bull.* **1980**, *15*, 783–789.

[40] A. Yoshino, *Nat. Energy* **2021**, *6*, 449.

[41] M. Armand, J.-M. Tarascon, *Nature* **2008**, *451*, 652–657.

[42] J.-M. Tarascon, M. Armand, *Nature* **2001**, *414*, 359–367.

[43] B. Scrosati, J. Garche, *J. Power Sources* **2010**, *195*, 2419–2430.

[44] Press release: The Nobel Prize in Chemistry 2019, *NobelPrize.org*, Nobel Prize Outreach AB 2021, https://www.nobelprize.org/prizes/chemistry/2019/press-release/ (**28.08.21**).

[45] J. B. Goodenough, K.-S. Park, *J. Am. Chem. Soc.* **2013**, *135*, 1167–1176.

[46] M. Rosso, C. Brissot, A. Teyssot, M. Dollé, L. Sannier, J.-M. Tarascon, R. Bouchet, S. Lascaud, *Electrochim. Acta* **2006**, *51*, 5334–5340.

[47] M. M. Thackeray, C. Wolverton, E. D. Isaacs, *Energy Environ. Sci.* **2012**, *5*, 7854–7863.

[48] N. Imanishi, Y. Takeda, O. Yamamoto, *Development of the Carbon Anode in Lithium Ion Batteries* in *Lithium Ion Batteries: Fundamentals and Performance* (Eds.: M. Wakihara, O. Yamamoto), Kodansha, Tokyo; Wiley-VCH, Weinheim, **1998**, 98–126.

[49] M. M. Thackeray, W. I. F. David, P. G. Bruce, J. B. Goodenough, *Mater. Res. Bull.* **1983**, *18*, 461–472.

[50] D. W. Murphy, F. J. Di Salvo, J. N. Carides, J. V. Waszczak, *Mater. Res. Bull.* **1978**, *13*, 1395–1402.

[51] M. Lazzari, B. Scrosati, *J. Electrochem. Soc.* **1980**, *127*, 773–774.

[52] R. Yazami, P. Touzain, *J. Power Sources* **1983**, *9*, 365–371.

[53] J. M. Tarascon, D. Guyomard, *Electrochim. Acta* **1993**, *38*, 1221–1231.

[54] T. Placke, R. Kloepsch, S. Dühnen, M. Winter, *J. Solid State Electrochem.* **2017**, *21*, 1939–1964.

[55] P. Verma, P. Maire, P. Novák, *Electrochim. Acta* **2010**, *55*, 6332–6341.

[56] A. S. Aricò, P. Bruce, B. Scrosati, J.-M. Tarascon, W. van Schalkwijk, *Nat. Mater.* **2005**, *4*, 366–377.

[57] V. Etacheri, R. Marom, R. Elazari, G. Salitra, D. Aurbach, *Energy Environ. Sci.* **2011**, *4*, 3243–3262.

[58] M. Saiful Islam, C. A. J. Fisher, *Chem. Soc. Rev.* **2014**, *43*, 185–204.

[59] D. Aurbach, Y. Talyosef, B. Markovsky, E. Markevich, E. Zinigrad, L. Asraf, J. S. Gnanaraj, H.-J. Kim, *Electrochim. Acta* **2004**, *50*, 247–254.

[60] M. Mohri, N. Yanagisawa, Y. Tajima, H. Tanaka, T. Mitate, S. Nakajima, M. Yoshida, Y. Yoshimoto, T. Suzuki, H. Wada, *J. Power Sources* **1989**, *26*, 545–551.

[61] M. S. Whittingham, *Chem. Rev.* **2004**, *104*, 4271–4302.

[62] D. Aurbach, B. Markovsky, A. Shechter, Y. Ein-Eli, H. Cohen, *J. Electrochem. Soc.* **1996**, *143*, 3809–3820.

[63] E. Peled, *J. Electrochem. Soc.* **1979**, *126*, 2047–2051.

[64] S.-H. Kang, D. P. Abraham, A. Xiao, B. L. Lucht, *J. Power Sources* **2008**, *175*, 526–532.

[65] L. Wang, A. Menakath, F. Han, Y. Wang, P. Y. Zavalij, K. J. Gaskell, O. Borodin, D. Iuga, S. P. Brown, C. Wang, K. Xu, B. W. Eichhorn, *Nat. Chem.* **2019**, *11*, 789–796.

[66] J. O. Besenhard, M. Winter, J. Yang, W. Biberacher, *J. Power Sources* **1995**, *54*, 228–231.

[67] C. Liebenow, M. W. Wagner, K. Lühder, P. Lobitz, J. O. Besenhard, *J. Power Sources* **1995**, *54*, 369–372.

[68] R. Fong, U. von Sacken, J. R. Dahn, *J. Electrochem. Soc.* **1990**, *137*, 2009–2013.

[69] P. Arora, R. E. White, M. Doyle, *J. Electrochem. Soc.* **1998**, *145*, 3647–3667.

[70] M. C. Smart, B. V. Ratnakumar, S. Surampudi, Y. Wang, X. Zhang, S. G. Greenbaum, A. Hightower, C. C. Ahn, B. Fultz, *J. Electrochem. Soc.* **1999**, *146*, 3963–3969.

[71] R. Malini, U. Uma, T. Sheela, M. Ganesan, N. G. Renganathan, *Ionics* **2009**, *15*, 301–307.

[72] C.-X. Zu, H. Li, *Energy Environ. Sci.* **2011**, *4*, 2614–2624.

[73] M. Yoshio, H. Wang, K. Fukuda, Y. Hara, Y. Adachi, *J. Electrochem. Soc.* **2000**, *147*, 1245–1250.

[74] G. G. Amatucci, J. M. Tarascon, L. C. Klein, *Solid State Ionics* **1996**, *83*, 167–173.

[75] B. Xu, D. Qian, Z. Wang, Y. S. Meng, *Mater. Sci. Eng. R Rep.* **2012**, *73*, 51–65.

[76] M. Hirooka, T. Sekiya, Y. Omomo, M. Yamada, H. Katayama, T. Okumura, Y. Yamada, K. Ariyoshi, *Electrochim. Acta* **2019**, *320*, 134596.

[77] S. Xia, L. Mu, Z. Xu, J. Wang, C. Wei, L. Liu, P. Pianetta, K. Zhao, X. Yu, F. Lin, Y. Liu, *Nano Energy* **2018**, *53*, 753–762.

[78] K. Zhao, M. Pharr, J. J. Vlassak, Z. Suo, *J. Appl. Phys.* **2010**, *108*, 073517.

[79] T. R. Tanim, E. J. Dufek, M. Evans, C. Dickerson, A. N. Jansen, B. J. Polzin, A. R. Dunlop, S. E. Trask, R. Jackman, I. Bloom, Z. Yang, E. Lee, *J. Electrochem. Soc.* **2019**, *166*, A1926–A1938.

[80] M. Li, M. Feng, D. Luo, Z. Chen, *Cell Rep. Phys. Sci.* **2020**, *1*, 100212.

[81] B. S. Vishnugopi, A. Verma, P. P. Mukherjee, *J. Electrochem. Soc.* **2020**, *167*, 090508.

[82] M.-T. F. Rodrigues, K. Kalaga, S. E. Trask, D. W. Dees, I. A. Shkrob, D. P. Abraham, *J. Electrochem. Soc.* **2019**, *166*, A996–A1003.

[83] I. A. Shkrob, M.-T. F. Rodrigues, D. W. Dees, D. P. Abraham, *J. Electrochem. Soc.* **2019**, *166*, A3305–A3313.

[84] K. P. C. Yao, J. S. Okasinski, K. Kalaga, I. A. Shkrob, D. P. Abraham, *Energy Environ. Sci.* **2019**, *12*, 656–665.

[85] T. Liu, Z. Du, X. Wu, M. M. Rahman, D. Nordlund, K. Zhao, M. D. Schulz, F. Lin, D. L. Wood, I. Belharouak, *Chem. Commun.* **2020**, *56*, 6973–6976.

[86] N. Legrand, B. Knosp, P. Desprez, F. Lapicque, S. Raël, *J. Power Sources* **2014**, *245*, 208–216.

[87] P. Bai, J. Li, F. R. Brushett, M. Z. Bazant, *Energy Environ. Sci.* **2016**, *9*, 3221–3229.

[88] X. He, F. Restuccia, Y. Zhang, Z. Hu, X. Huang, J. Fang, G. Rein, *Fire Technol.* **2020**, *56*, 2649–2669.

[89] Y. Liu, Y. Zhu, Y. Cui, *Nat. Energy* **2019**, *4*, 540–550.

[90] S. Ahmed, I. Bloom, A. N. Jansen, T. Tanim, E. J. Dufek, A. Pesaran, A. Burnham, R. B. Carlson, F. Dias, K. Hardy, M. Keyser, C. Kreuzer, A. Markel, A. Meintz, C. Michelbacher, M. Mohanpurkar, P. A. Nelson, D. C. Robertson, D. Scoffield, M. Shirk, T. Stephens, R. Vijayagopal, J. Zhang, *J. Power Sources* **2017**, *367*, 250–262.

[91] T. C. Wanger, *Conserv. Lett.* **2011**, *4*, 202–206.

[92] V. Flexer, C. F. Baspineiro, C. I. Galli, *Sci. Total Environ.* **2018**, *639*, 1188–1204.

[93] R. B. Kaunda, *J. Energy Nat. Resour. Law* **2020**, *38*, 237–244.

[94] A. Eftekhari, *ACS Sustainable Chem. Eng.* **2019**, *7*, 5602–5613.

[95] F. M. Dorn, F. R. Peyré, *J. Lat. Am. Geogr.* **2020**, *19*, 68–90.

[96] C. Grosjean, P. H. Miranda, M. Perrin, P. Poggi, *Renewable Sustainable Energy Rev.* **2012**, *16*, 1735–1744.

[97] J. W. An, D. J. Kang, K. T. Tran, M. J. Kim, T. Lim, T. Tran, *Hydrometallurgy* **2012**, *117–118*, 64–70.

[98] T. Tran, V. T. Luong, *Lithium Production Processes* in *Lithium Process Chemistry* (Eds. A. Chagnes, J. Światowska), Elsevier, Amsterdam, **2015**, 81–124.

[99] T. P. Narins, *Extr. Ind. Soc.* **2017**, *4*, 321–328.

[100] B. K. Sovacool, *Extr. Ind. Soc.* **2021**, *8*, 271–293.

[101] X. Sun, H. Hao, Z. Liu, F. Zhao, J. Song, *Resour., Conserv. Recycl.* **2019**, *149*, 45–55.

[102] C. W. Babbitt, *Clean Technol. Environ. Policy* **2020**, *22*, 1213–1214.

[103] B. K. Sovacool, *Extr. Ind. Soc.* **2019**, *6*, 915–939.

[104] D. Krummel, P. Siegfried, *J. Geosci. Environ. Protect.* **2021**, *9*, 182–203.

[105] C. B. L. Nkulu, L. Casas, V. Haufroid, T. De Putter, N. D. Saenen, T. Kayembe-Kitenge, P. M. Obadia, D. K. W. Mukoma, J.-M. L. Ilunga, T. S. Nawrot, O. L. Numbi, E. Smolders, B. Nemery, *Nat. Sustain.* **2018**, *1*, 495–504.

[106] S. Squadrone, E. Burioli, G. Monaco, M. K. Koya, M. Prearo, S. Gennero, A. Dominici, M. C. Abete, *Sci. Total Environ.* **2016**, *568*, 679–684.

[107] J. Sachs, C. Kroll, G. Lafortune, G. Fuller, F. Woelm, *The Decade of Action for the Sustainable Development Goals: Sustainable Development Report 2021,* Cambridge University Press, Cambridge, **2021**.

[108] Y. Chen, S. Song, X. Zhang, Y. Liu, *J. Phys.: Conf. Ser.* **2019**, *1347*, 012012.

[109] H.-J. Kim, T. N. V. Krishna, K. Zeb, V. Rajangam, C. V. V. M. Gopi, S. Sambasivam, K. V. G. Raghavendra, I. M. Obaidat, *Electronics* **2020**, *9*, 1161.

[110] K. Park, B. Choi, *J. Alloys Compd.* **2018**, *766*, 470–476.

[111] P. K. Nayak, E. M. Erickson, F. Schipper, T. R. Penki, N. Munichandraiah, P. Adelhelm, H. Sclar, F. Amalraj, B. Markovsky, D. Aurbach, *Adv. Energy Mater.* **2018**, *8*, 1702397.

[112] H.-H. Ryu, H. H. Sun, S.-T. Myung, C. S. Yoon, Y.-K. Sun, *Energy Environ. Sci.* **2021**, *14*, 844–852.

[113] H.-J. Noh, S. Youn, C. S. Yoon, Y.-K. Sun, *J. Power Sources* **2013**, *233*, 121–130.

[114] H.-H. Ryu, K.-J. Park, C. S. Yoon, Y.-K. Sun, *Chem. Mater.* **2018**, *30*, 1155–1163.

[115] M. Li, J. Lu, *Science* **2020**, *367*, 979–980.

[116] S. S. Zhang, *Energy Storage Mater.* **2020**, *24*, 247–254.

[117] E. Fan, L. Li, Z. Wang, J. Lin, Y. Huang, Y. Yao, R. Chen, F. Wu, *Chem. Rev.* **2020**, *120*, 7020–7063.

[118] C.-H. Jo, S.-T. Myung, *J. Power Sources*, **2019**, *426*, 259–265.

[119] T. Perveen, M. Siddiq, N. Shahzad, R. Ihsan, A. Ahmad, M. I. Shahzad, *Renewable Sustainable Energy Rev.* **2020**, *119*, 109549.

[120] H. Wang, S. Chen, C. Fu, Y. Ding, G. Liu, Y. Cao, Z. Chen, *ACS Mater. Lett.* **2021**, *3*, 956–977.

[121] P. Poizot, S. Laruelle, S. Grugeon, L. Dupont, J.-M. Tarascon, *Nature* **2000**, *407*, 496–499.

[122] K. Cao, T. Jin, L. Yang, L. Jiao, *Mater. Chem. Front.* **2017**, *1*, 2213–2242.

[123] X. Deng, Z. Chen, Y. Cao, *Mater. Today Chem.* **2018**, *9*, 114–132.

[124] W. B. Jensen, *J. Chem. Educ.* **2012**, *89*, 1208–1209.

[125] J. Christensen, P. Albertus, R. S. Sanchez-Carrera, T. Lohmann, B. Kozinsky, R. Liedtke, J. Ahmed, A. Kojic, *J. Electrochem. Soc.* **2011**, *159*, R1–R30.

[126] W.-W. Yin, Z.-W. Fu, *ChemCatChem* **2017**, *9*, 1545–1553.

[127] X. Yu, A. Manthiram, *Adv. Funct. Mater.* **2020**, *30*, 2004084.

[128] S.-H. Chung, A. Manthiram, *Adv. Mater.* **2019**, *31*, 1901125.

[129] Q. Pang, X. Liang, C. Y. Kwok, L. F. Nazar, *Nat. Energy* **2016**, *1*, 16132.

[130] A. Manthiram, X. Yu, *Small* **2015**, *11*, 2108–2114.

[131] C.-M. Park, J.-H. Kim, H. Kim, H.-J. Sohn, *Chem. Soc. Rev.* **2010**, *39*, 3115–3141.

[132] L. Ji, Z. Lin, M. Alcoutlabi, X. Zhang, *Energy Environ. Sci.* **2011**, *4*, 2682–2699.

[133] S. Liang, Y.-J. Cheng, J. Zhu, Y. Xia, P. Müller-Buschbaum, *Small Methods* **2020**, *4*, 2000218.

[134] Y. Kim, Y. Park, A. Choi, N.-S. Choi, J. Kim, J. Lee, J. H. Ryu, S. M. Oh, K. T. Lee, *Adv. Mater.* **2013**, *25*, 3045–3049.

[135] Y. Kim, K.-H. Ha, S. M. Oh, K. T. Lee, *Chem. – Eur. J.* **2014**, *20*, 11980–11992.

[136] H. Zhang, I. Hasa, S. Passerini, *Adv. Energy Mater.* **2018**, *8*, 1702582.

[137] M. V. Reddy, G. V. Subba Rao, B. V. R. Chowdari, *Chem. Rev.* **2013**, *113*, 5364–5457.

[138] W.-J. Zhang, *J. Power Sources* **2011**, *196*, 13–24.

[139] X. Zuo, J. Zhu, P. Müller-Buschbaum, Y.-J. Cheng, *Nano Energy* **2017**, *31*, 113–143.

[140] Y. Zhu, Y. Wen, X. Fan, T. Gao, F. Han, C. Luo, S.-C. Liou, C. Wang, *ACS Nano* **2015**, *9*, 3254–3264.

[141] W.-J. Li, S.-L. Chou, J.-Z. Wang, H.-K. Liu, S.-X. Dou, *Nano Lett.* **2013**, *13*, 5480–5484.

[142] M. Hu, Y. Jiang, W. Sun, H. Wang, C. Jin, M. Yan, *ACS Appl. Mater. Interfaces* **2014**, *6*, 19449–19455.

[143] K.-H. Kim, W.-S. Kim, S.-H. Hong, *Nanoscale* **2019**, *11*, 13494–13501.

[144] D. Bresser, S. Passerini, B. Scrosati, *Energy Environ. Sci.* **2016**, *9*, 3348–3367.

[145] R. D. Shannon, *Acta Crystallogr. A* **1976**, *32*, 751–767.

[146] A. J. Bard, R. Parsons, J. Jordan, *Standard Potentials in Aqueous Solution*, Marcel Dekker, New York, **1985**.

[147] R. S. Carmichael, *Practical Handbook of Physical Properties of Rocks and Minerals*, CRC Press, Boca Raton, **1989**.

[148] H. S. Hirsh, Y. Li, D. H. S. Tan, M. Zhang, E. Zhao, Y. S. Meng, *Adv. Energy Mater.* **2020**, *10*, 2001274.

[149] A. Eftekhari, D.-W. Kim, *J. Power Sources* **2018**, *395*, 336–348.

[150] A. Eftekhari, *ACS Sustainable Chem. Eng.* **2019**, *7*, 3684–3687.

[151] D. Kundu, E. Talaie, V. Duffort, L. F. Nazar, *Angew. Chem., Int. Ed.* **2015**, *54*, 3431–3448.

[152] K. Nobuhara, H. Nakayama, M. Nose, S. Nakanishi, H. Iba, *J. Power Sources* **2013**, *243*, 585–587.

[153] Y. Li, Y. Lu, P. Adelhelm, M.-M. Titirici, Y.-S. Hu, *Chem. Soc. Rev.* **2019**, *48*, 4655–4687.

[154] J. Sangster, *J. Phase Equilib. Diffus.* **2007**, *28*, 571–579.

[155] D.-Y. Kim, D.-H. Kim, S.-H. Kim, E.-K. Lee, S.-K. Park, J.-W. Lee, Y.-S. Yun, S.-Y. Choi, J. Kang, *Nanomaterials* **2019**, *9*, 793.

[156] Y. Okamoto, *J. Phys. Chem. C* **2014**, *118*, 16–19.

[157] L. Y. Beaulieu, K. W. Eberman, R. L. Turner, L. J. Krause, J. R. Dahn, *Electrochem. Solid-State Lett.* **2001**, *4*, A137–A140.

[158] W. Huang, W. Wang, Y. Wang, Q. Qu, C. Jin, H. Zheng, *J. Mater. Chem. A* **2021**, *9*, 1541–1551.

[159] M. M. Thackeray, J. T. Vaughey, C. S. Johnson, A. J. Kropf, R. Benedek, L. M. L. Fransson, K. Edstrom, *J. Power Sources* **2003**, *113*, 124–130.

[160] J.-S. Bridel, T. Azaïs, M. Morcrette, J.-M. Tarascon, D. Larcher, *Chem. Mater.* **2010**, *22*, 1229–1241.

[161] S. Komaba, K. Shimomura, N. Yabuuchi, T. Ozeki, H. Yui, K. Konno, *J. Phys. Chem. C* **2011**, *115*, 13487–13495.

[162] S. Komaba, Y. Matsuura, T. Ishikawa, N. Yabuuchi, W. Murata, S. Kuze, *Electrochem. Commun.* **2012**, *21*, 65–68.

[163] S. Komaba, T. Ozeki, N. Yabuuchi, K. Shimomura, *Electrochemistry* **2011**, *79*, 6–9.

[164] W. Wang, X. Zhu, Y. Zhang, Y. Liu, Q. Zhang, L. Fu, *Chin. J. Chem.* **2018**, *36*, 866–874.

[165] Y. Lu, Y. Lu, Z. Niu, J. Chen, *Adv. Energy Mater.* **2018**, *8*, 1702469.

[166] S. Liu, J. Feng, X. Bian, J. Liu, H. Xu, *Energy Environ. Sci.* **2016**, *9*, 1229–1236.

[167] C. Nithya, S. Gopukumar, *J. Mater. Chem. A* **2014**, *2*, 10516–10525.

[168] H. Hou, M. Jing, Y. Yang, Y. Zhu, L. Fang, W. Song, C. Pan, X. Yang, X. Ji, *ACS Appl. Mater. Interfaces* **2014**, *6*, 16189–16196.

[169] H.-C. Yu, C. Ling, J. Bhattacharya, J. C. Thomas, K. Thornton, A. van der Ven, *Energy Environ. Sci.* **2014**, *7*, 1760–1768.

[170] H. Kim, H. Kim, H. Kim, J. Kim, G. Yoon, K. Lim, W.-S. Yoon, K. Kang, *Adv. Funct. Mater.* **2016**, *26*, 5042–5050.

[171] J. Wang, L. Wang, C. Eng, J. Wang, *Adv. Energy Mater.* **2017**, *7*, 1602706.

[172] C. Wu, S.-X. Dou, Y. Yu, *Small* **2018**, *14*, 1703671.

[173] J. Asenbauer, A. Varzi, S. Passerini, D. Bresser, *J. Power Sources* **2020**, *473*, 228583.

[174] Y.-T. Lee, C.-T. Kuo, T.-R. Yew, *ACS Appl. Mater. Interfaces* **2021**, *13*, 570–579.

[175] E. Glatzel, *Z. Anorg. Chem.* **1893**, *4*, 186–226.

[176] M. C. Friedel, *C. R. Hebd. Séances Acad. Sci.* **1894**, *119*, 260–264.

[177] W. Klingen, R. Ott, H. Hahn, *Z. Anorg. Allg. Chem.* **1973**, *396*, 271–278.

[178] W. Klingen, G. Eulenberger, H. Hahn, *Z. Anorg. Allg. Chem.* **1973**, *401*, 97–112.

[179] G. Ouvrard, R. Brec, J. Rouxel, *Mater. Res. Bull.* **1985**, *20*, 1181–1189.

[180] A. Ferrari, L. Cavalca, *Gazz. Chim. Ital.* **1948**, *78*, 283–285.

[181] A. Weiss, H. Schäfer, *Naturwissenschaften* **1960**, *47*, 495.

[182] T. A. Bither, P. C. Donohue, H. S. Young, *J. Solid State Chem.* **1971**, *3*, 300–307.

[183] R. Diehl, C.-D. Carpentier, *Acta Crystallogr. B* **1977**, *33*, 1399–1404.

[184] Y. Yang, M. Song, X. Wu, K. Wu, *J. Phys. D: Appl. Phys.* **2021**, *54*, 463002.

[185] M. Evain, R. Brec, M.-H. Whangbo, *J. Solid State Chem.* **1987**, *71*, 244–262.

[186] J.-H. Yuan, K.-H. Xue, J.-F. Wang, X.-S. Miao, *J. Phys. Chem. Lett.* **2019**, *10*, 4455–4462.

[187] R. Brec, D. M. Schleich, G. Ouvrard, A. Louisy, J. Rouxel, *Inorg. Chem.* **1979**, *18*, 1814–1818.

[188] Q. Chen, Q. Ding, Y. Wang, Y. Xu, J. Wang, *J. Phys. Chem. C* **2020**, *124*, 12075–12080.

[189] C. C. Mayorga-Martinez, Z. Sofer, D. Sedmidubský, Š. Huber, A. Y. S. Eng, M. Pumera, *ACS Appl. Mater. Interfaces* **2017**, *9*, 12563–12573.

[190] E. Durand, G. Ouvrard, M. Evain, R. Brec, *Inorg. Chem.* **1990**, *29*, 4916–4920.

[191] G. Ouvrard, R. Fréour, R. Brec, J. Rouxel, *Mater. Res. Bull.* **1985**, *20*, 1053–1062.

[192] R. Brec, *Solid State Ionics* **1986**, *22*, 3–30.

[193] A. Louisy, G. Ouvrard, D. M. Schleich, R. Brec, *Solid State Commun.* **1978**, *28*, 61–66.

[194] A. H. Thompson, M. S. Whittingham, *Mater. Res. Bull.* **1977**, *12*, 741–744.

[195] P. Fragnaud, E. Prouzet, R. Brec, *J. Mater. Res.* **1992**, *7*, 1839–1846.

[196] A. R. Wildes, V. Simonet, E. Ressouche, G. J. McIntyre, M. Avdeev, E. Suard, S. A. J. Kimber, D. Lançon, G. Pepe, B. Moubaraki, T. J. Hicks, *Phys. Rev. B* **2015**, *92*, 224408.

[197] C. Murayama, M. Okabe, D. Urushihara, T. Asaka, K. Fukuda, M. Isobe, K. Yamamoto, Y. Matsushita, *J. Appl. Phys.* **2016**, *120*, 142114.

[198] R. Gusmão, Z. Sofer, M. Pumera, *Angew. Chem., Int. Ed.* **2019**, *58*, 9326–9337.

[199] K. Du, X. Wang, Y. Liu, P. Hu, M. I. B. Utama, C. K. Gan, Q. Xiong, C. Kloc, *ACS Nano* **2016**, *10*, 1738–1743.

[200] C.-T. Kuo, M. Neumann, K. Balamurugan, H. J. Park, S. Kang, H. W. Shiu, J. H. Kang, B. H. Hong, M. Han, T. W. Noh, J.-G. Park, *Sci. Rep.* **2016**, *6*, 20904.

[201] F. Liu, L. You, K. L. Seyler, X. Li, P. Yu, J. Lin, X. Wang, J. Zhou, H. Wang, H. He, S. T. Pantelides, W. Zhou, P. Sharma, X. Xu, P. M. Ajayan, J. Wang, Z. Liu, *Nat. Commun.* **2016**, *7*, 12357.

[202] Y. Guo, C. Liu, Q. Yin, C. Wei, S. Lin, T. B. Hoffman, Y. Zhao, J. H. Edgar, Q. Chen, S. P. Lau, J. Dai, H. Yao, H.-S. P. Wong, Y. Chai, *ACS Nano* **2016**, *10*, 8980–8988.

[203] G. Long, T. Zhang, X. Cai, J. Hu, C. Cho, S. Xu, J. Shen, Z. Wu, T. Han, J. Lin, J. Wang, Y. Cai, R. Lortz, Z. Mao, N. Wang, *ACS Nano* **2017**, *11*, 11330–11336.

[204] B. Song, K. Li, Y. Yin, T. Wu, L. Dang, M. Cabán-Acevedo, J. Han, T. Gao, X. Wang, Z. Zhang, J. R. Schmidt, P. Xu, S. Jin, *ACS Catal.* **2017**, *7*, 8549–8557.

[205] S. Xue, L. Chen, Z. Liu, H.-M. Cheng, W. Ren, *ACS Nano* **2018**, *12*, 5297–5305.

[206] J. Lee, T. Y. Ko, J. H. Kim, H. Bark, B. Kang, S.-G. Jung, T. Park, Z. Lee, S. Ryu, C. Lee, *ACS Nano* **2017**, *11*, 10935–10944.

[207] S. Kim, J. Lee, G. Jin, M.-H. Jo, C. Lee, S. Ryu, *Nano Lett.* **2019**, *19*, 4043–4051.

[208] H. L. Zhuang, J. Zhou, *Phys. Rev. B* **2016**, *94*, 195307.

[209] A. K. Budniak, N. A. Killilea, S. J. Zelewski, M. Sytnyk, Y. Kauffmann, Y. Amouyal, R. Kudrawiec, W. Heiss, E. Lifshitz, *Small* **2020**, *16*, 1905924.

[210] M. A. Susner, M. Chyasnavichyus, M. A. McGuire, P. Ganesh, P. Maksymovych, *Adv. Mater.* **2017**, *29*, 1602852.

[211] F. Wang, T. A. Shifa, P. Yu, P. He, Y. Liu, F. Wang, Z. Wang, X. Zhan, X. Lou, F. Xia, J. He, *Adv. Funct. Mater.* **2018**, *28*, 1802151.

[212] B. E. Taylor, J. Steger, A. Wold, *J. Solid State Chem.* **1973**, *7*, 461–467.

[213] R. R. Rao, A. K. Raychaudhuri, *J. Phys. Chem. Solids* **1992**, *53*, 577–583.

[214] V. Maisonneuve, M. Evain, C. Payen, V. B. Cajipe, P. Molinié, *J. Alloys Compd.* **1995**, *218*, 157–164.

[215] G. Burr, E. Durand, M. Evain, R. Brec, *J. Solid State Chem.* **1993**, *103*, 514–518.

[216] P. Colombet, A. Leblanc, M. Danot, J. Rouxel, *J. Solid State Chem.* **1982**, *41*, 174–184.

[217] V. Maisonneuve, V. B. Cajipe, C. Payen, *Chem. Mater.* **1993**, *5*, 758–760.

[218] K. Momma, F. Izumi, *J. Appl. Crystallogr.* **2011**, *44*, 1272–1276.

[219] A. Weiss, H. Schäfer, *Z. Naturforsch. B* **1963**, *18*, 81–82.

[220] C. D. Carpentier, R. Diehl, R. Nitsche, *Naturwissenschaften* **1970**, *57*, 393.

[221] R. Mercier, J.-P. Malugani, B. Fahys, G. Robert, J. Douglade, *Acta Crystallogr. B* **1982**, *38*, 1887–1890.

[222] M. Jansen, U. Henseler, *J. Solid State Chem.* **1992**, *99*, 110–119.

[223] H. Schäfer, G. Schäfer, A. Weiss, *Z. Naturforsch. B* **1965**, *20*, 811.

[224] S. Jörgens, A. Mewis, *Solid State Sci.* **2007**, *9*, 213–217.

[225] A. Pfitzner, S. Reiser, *Z. Kristallogr.* **2002**, *217*, 51–54.

[226] S. Lee, R. J. Hilt, *J. Alloys Compd.* **1992**, *189*, 269–271.

[227] V. Bodenez, L. Dupont, M. Morcrette, C. Surcin, D. W. Murphy, J.-M. Tarascon, *Chem. Mater.* **2006**, *18*, 4278–4287.

[228] S. Indris, J. Cabana, O. J. Rutt, S. J. Clarke, C. P. Grey, *J. Am. Chem. Soc.* **2006**, *128*, 13354–13355.

[229] M. Krengel, A.-L. Hansen, M. Kaus, S. Indris, N. Wolff, L. Kienle, D. Westfal, W. Bensch, *ACS Appl. Mater. Interfaces* **2017**, *9*, 21283–21291.

[230] S. Dey, D. Zeng, P. Adamson, J. Cabana, S. Indris, J. Lu, S. J. Clarke, C. P. Grey, *Chem. Mater.* **2021**, *33*, 3989–4005.

[231] V. Bodenez, L. Dupont, L. Laffont, A. R. Armstrong, K. M. Shaju, P. G. Bruce, J.-M. Tarascon, *J. Mater. Chem.* **2007**, *17*, 3238–3247.

[232] W. Bensch, J. Ophey, H. Hain, H. Gesswein, D. Chen, R. Mönig, P. A. Gruber, S. Indris, *Phys. Chem. Chem. Phys.* **2012**, *14*, 7509–7516.

[233] M. Morcrette, P. Rozier, L. Dupont, E. Mugnier, L. Sannier, J. Galy, J.-M. Tarascon, *Nat. Mater.* **2003**, *2*, 755–761.

[234] T. Proffen, S. J. L. Billinge, T. Egami, D. Louca, *Z. Kristallogr.* **2003**, *218*, 132–143.

[235] S. J. L. Billinge, M. G. Kanatzidis, *Chem. Commun.* **2004**, 749–760.

[236] T. Proffen, K. L. Page, S. E. McLain, B. Clausen, T. W. Darling, J. A. TenCate, S.-Y. Lee, E. Ustundag, *Z. Kristallogr.* **2005**, *220*, 1002–1008.

[237] W. Dmowski, K. E. Swider-Lyons, *Z. Kristallogr.* **2004**, *219*, 136–142.

[238] S. J. L. Billinge, *J. Solid State Chem.* **2008**, *181*, 1695–1700.

[239] R. E. Dinnebier, A. Leineweber, J. S. O. Evans, *Rietveld Refinement: Practical Powder Diffraction Pattern Analysis using TOPAS*, De Gruyter, Berlin, Boston, **2018**.

[240] X. Yang, P. Juhas, C. L. Farrow, S. J. L. Billinge, arXiv:1402.3163, **2014**.

[241] M. Newville, *Rev. Mineral. Geochem.* **2014**, *78*, 33–74.

[242] D. Popmintchev, B. R. Galloway, M.-C. Chen, F. Dollar, C. A. Mancuso, A. Hankla, L. Miaja-Avila, G. O'Neil, J. M. Shaw, G. Fan, S. Ališauskas, G. Andriukaitis, T. Balčiunas, O. D. Mücke, A. Pugzlys, A. Baltuška, H. C. Kapteyn, T. Popmintchev, M. M. Murnane, *Phys. Rev. Lett.* **2018**, *120*, 093002.

[243] J. Yano, V. K. Yachandra, *Photosynth. Res.* **2009**, *102*, 241–254.

[244] J. J. Rehr, R. C. Albers, *Rev. Mod. Phys.* **2000**, *72*, 621–654.

[245] S. Calvin, *XAFS for Everyone*, CRC Press, Boca Raton, **2013**.

[246] K. J. D. MacKenzie, M. E. Smith, *Multinuclear Solid-State NMR of Inorganic Materials*, Pergamon - an imprint of Elsevier Science, Amsterdam, **2002**.

[247] D. D. Laws, H.-M. L. Bitter, A. Jerschow, *Angew. Chem., Int. Ed.* **2002**, *41*, 3096–3129.

[248] S. E. Ashbrook, S. Sneddon, *J. Am. Chem. Soc.* **2014**, *136*, 15440–15456.

[249] I. J. Lowe, *Phys. Rev. Lett.* **1959**, *2*, 285–287.

[250] E. R. Andrew, A. Bradbury, R. G. Eades, *Nature* **1959**, *183*, 1802–1803.

7. Appendix

7.1 Electronic Supporting Information

7.1.1 What happens structurally and chemically during sodium uptake and release by $Ni_2P_2S_6$: a combined X-ray diffraction, X-ray absorption, pair distribution function and MAS NMR analysis

Reproduced from J. van Dinter, K. Synnatschke, T. A. Engesser, S. Indris, N. Wolff, O. Gronenberg, M. Etter, G. Cibin, L. Kienle, C. Backes and W. Bensch, *J. Mater. Chem. A*, **2020**, *8*, 22401-22415. Permission granted by the Royal Society of Chemistry.

What happens structurally and chemically during sodium uptake and release by $Ni_2P_2S_6$: a combined X-ray diffraction, X-ray absorption, pair distribution and MAS NMR analysis

Jonas van Dinter[a], Kevin Synnatschke[b], Tobias A. Engesser[a], Sylvio Indris[c], Niklas Wolff[d], Ole Gronenberg[d], Martin Etter[e], Giannantonio Cibin[f], Lorenz Kienle[d], Claudia Backes[b] and Wolfgang Bensch*[a]

[a]*Institute of Inorganic Chemistry, University of Kiel, Max-Eyth-Str. 2, 24118 Kiel, Germany*

[b]*Institute for Physical Chemistry, Heidelberg University, Im Neunheimer Feld 253, 69120 Heidelberg, Germany*

[c]*Institute for Applied Materials - Energy Storage Systems, Karlsruhe Institute of Technology, P.O. Box 3640, 76021 Karlsruhe, Germany*

[d]*Institute for Materials Science, University of Kiel, Kaiserstr. 2, 24143 Kiel, Germany*

[e]*Deutsches Elektronen-Synchrotron (DESY), Notkestr. 85, Hamburg 22607, Germany*

[f]*Diamond Light Source, Harwell Science and Innovation Campus, Diamond House, Didcot, Oxfordshire OX11 0DE, United Kingdom*

Experimental

Liquid phase exfoliation and centrifugation

Ground crystals of $Ni_2P_2S_6$ (500 mg) were sonicated for 8 h in 80 mL of NMP using a sonic tip (Vibracell VCX, 750 W, horn tip, order number Z192732-1EA) at 60% amplitude in a 6 s on/4 s off pulse sequence. The dispersion was kept in a 4 °C cooling cell during sonication in order to avoid heating effects. The resulting dispersion was subjected to a 2-step centrifugation procedure (3000 *g* and 10000 *g*). After centrifugation at 3000 *g* in the first step, the supernatant was used for the subsequent step at 10000 *g*. The sediment obtained after the second centrifugation step was redispersed in reduced solvent volume (~1 mL NMP). The sample prepared according to this protocol is referred to as "exfoliated $Ni_2P_2S_6$". A Hettich Mikro 220R centrifuge equipped with a fixed-angle rotor (1195A) was used for both centrifugation steps for 2 h at 20 °C.

Atomic force microscopy

Atomic force microscopy (AFM) was carried out to determine lateral size and layer number of exfoliated $Ni_2P_2S_6$ on a Dimension ICON3 scanning probe microscope (Bruker AXS S.A.S.) in ScanAsyst in air under ambient conditions using aluminium coated silicon cantilevers (OLTESPA-R3). The concentrated dispersion was diluted with isopropanol to optical densities <0.1 at 500 nm. A drop of the dilute dispersion (15 µL) was deposited on pre-heated (180 °C) Si/SiO_2 wafers (0.5x0.5 cm^2) with an oxide layer of 300 nm. After deposition, the wafer was rinsed with ~10 mL of water and ~10 mL of isopropanol and dried with compressed nitrogen. Typical image sizes were 10x10 μm^2 at scan rates of 0.5 - 0.8 Hz with 1024 lines per image. Step-height analysis from previous work was used to convert the apparent AFM thickness to the layer number.[1] Previously published length corrections were used to correct lateral dimensions for cantilever broadening.[2]

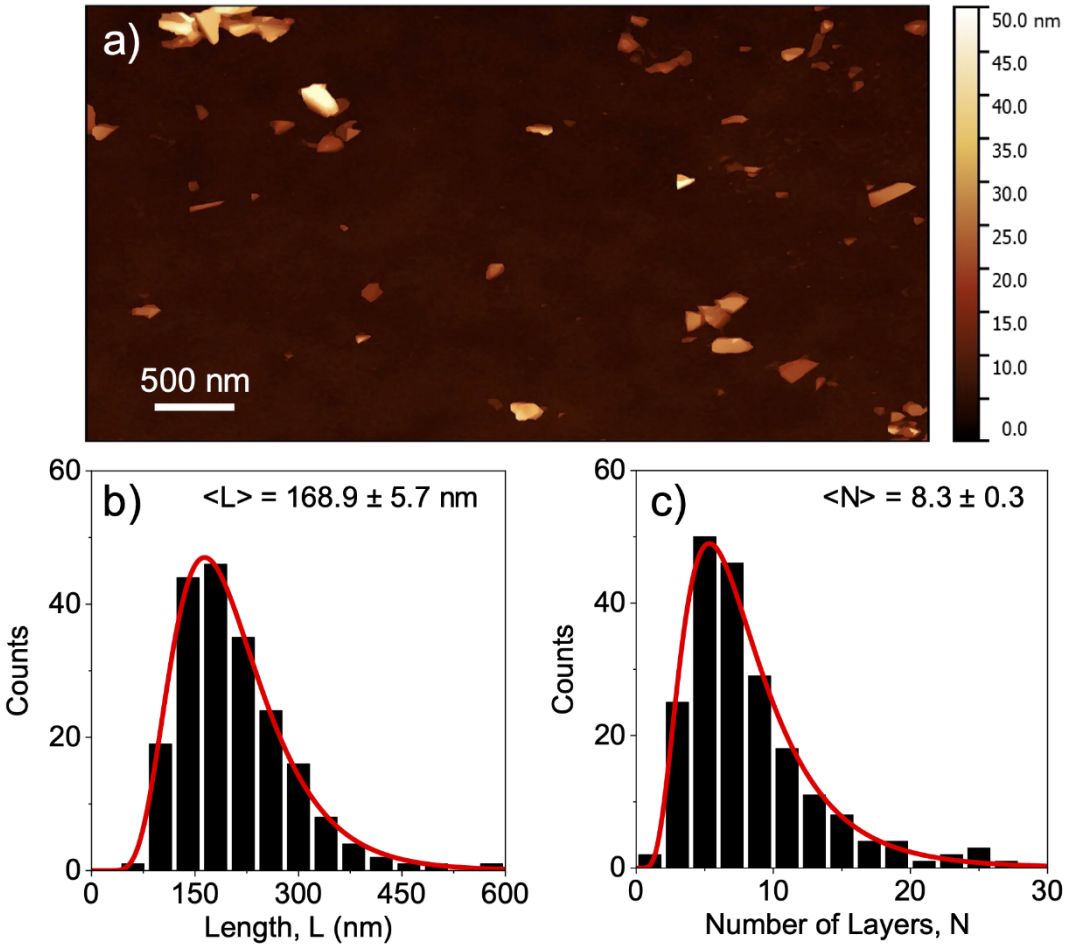

Figure S1. a) Representative AFM image of the exfoliated nanosheets. b, c) Histograms of lateral size, L and layer number, N of the exfoliated $Ni_2P_2S_6$ nanosheets. <L> and <N> are the arithmetic mean of the nanosheet lateral size and layer number.

Transmission electron microscopy

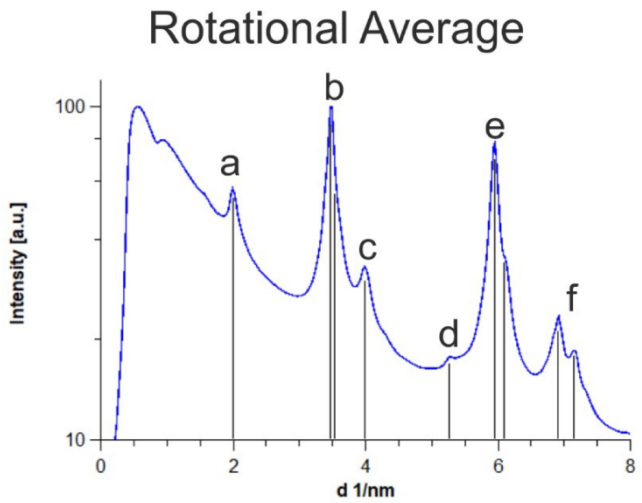

		a	b	c	d	e	f
d [Å]		5.02	2.86 || 2.80	2.51	1.89	1.68 || 1.62	1.44 || 1.40
C2/*m*	(hkl)	(020)	(130) || (200)	(040)	(150) / (240)	(060) || (330)	(260) || (170)
	d [Å]	5.041	2.876 || 2.781	2.520	1.896 / 1.867	1.680 || 1.623	1.438 || 1.394

Figure S2. Rotational intensity average of the diffraction pattern shown in Figure 2. The reflections can be indexed according to the monoclinic space group *C2/m*. The table displays the experimental lattice parameters d as well as a list of lattice parameters and lattice planes (hkl).

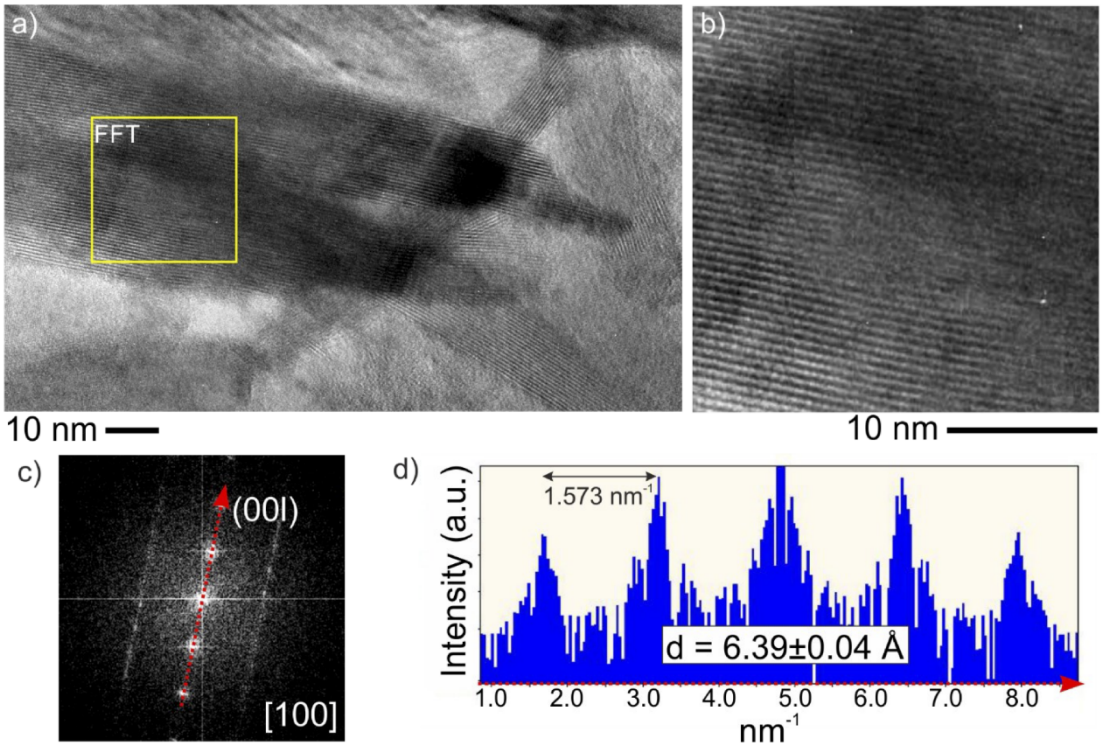

Figure S3. a, b) High-resolution TEM micrographs showing $Ni_2P_2S_6$ crystals coincidentally oriented along the [100] "edge-on" direction. c) In the FFT more or less pronounced diffuse streaking of the intensity in second order reflections is observed which indicates structural disorder between the crystal layers. d) The spacing between {00l} lattice planes was determined by evaluating the first order reflections appearing in the FFT.

Scanning electron microscopy and elemental analysis by EDX and CHNS

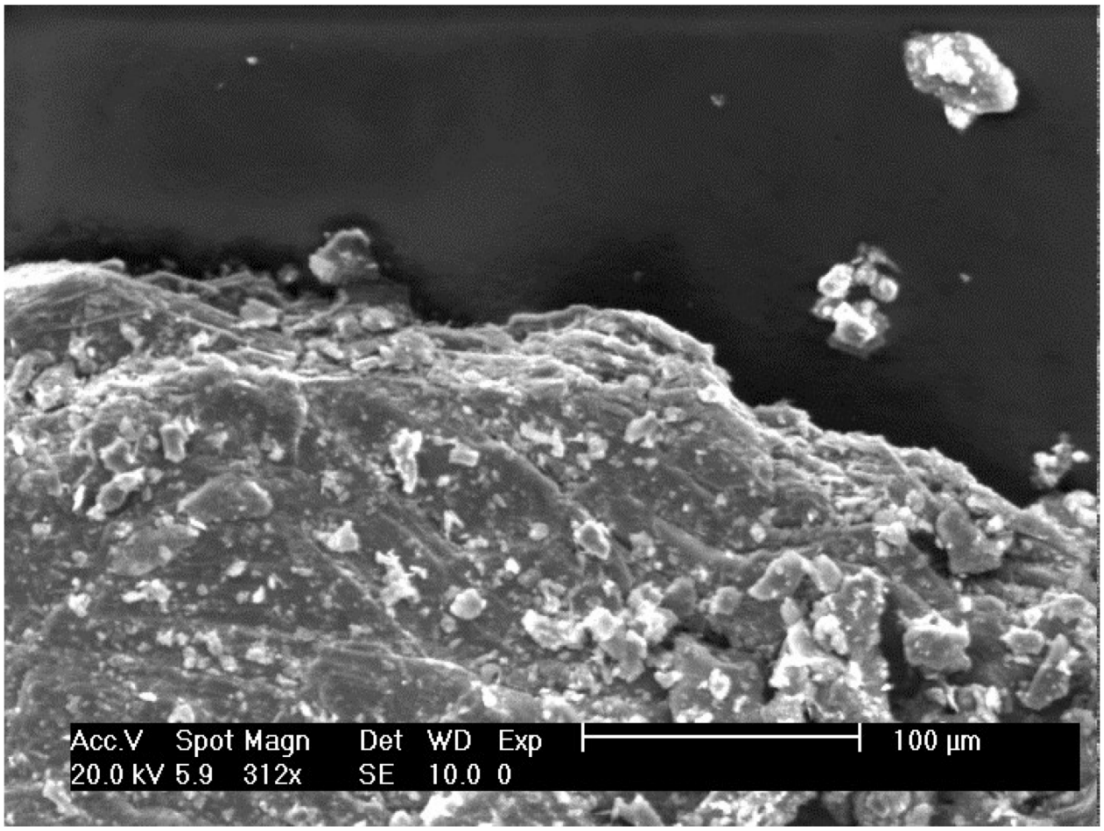

Figure S4. SEM images of $Ni_2P_2S_6$ sample showing its layered structure at the edges of the agglomerate.

Table S1. Results of EDX measurements of $Ni_2P_2S_6$ powder at different spots on the sample.

	Ni / at.%	P / at.%	S / at.%
Spot 1	22.56	21.50	55.94
Spot 2	22.28	20.88	56.84
Spot 3	23.55	20.96	55.49
Average	22.80 ± 0.56	21.11 ± 0.28	56.09 ± 0.56
Composition	$Ni_{2.28}P_{2.11}S_{5.61}$		

The SEM EDX measurements reveal stoichiometric ratios of Ni and P close to 1:1. The S content exhibits smaller values than expected from the target stoichiometry. This might be explained by the low energy of the S K_α emission line and absorption by the matrix. To account the S content properly, additional elemental (CHNS) analysis was conducted (Table S2).

Table S2. Results of the elemental analysis of the $Ni_2P_2S_6$ sample. As reference sulphanilamide was used. For the calculation of the composition, results of the elemental analysis were compared with the theoretical value of 51.76 wt.% S in $Ni_2P_2S_6$. This leads to compositions of $Ni_xP_xS_{6.10}$. Combining these results with the M:P ratio obtained from the EDX measurements, the total compositions of the samples were determined.

Sample	N / wt.%	C / wt.%	H / wt.%	S / wt.%
$Ni_2P_2S_6$	0.0	0.16	0.03	52.63
theoretical	0.0	0.0	0.0	51.76

Taking the results from the elemental analysis into consideration, the composition is calculated to be $Ni_{2.11}P_{1.81}S_{6.10}$.

Raman scattering

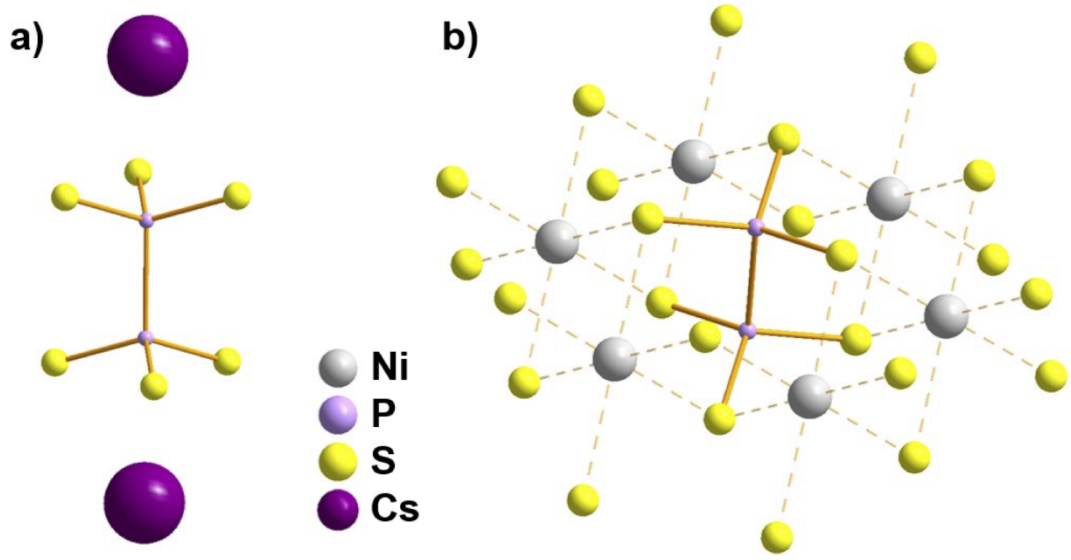

Figure S5. a) $[Cs_2(P_2S_6)]^{2-}$ anion with two Cs^+ cations on C_3 axis. b) $[Ni_6S_{18}(P_2S_6)]^{28-}$ fragment including $[P_2S_6]^{4-}$ anion and six nickel(II) ions as well as additional 18 sulfide anions (coordinates taken from the single crystal structure). Both structures show D_{3d} symmetry.

Table S3. Experimental and calculated frequencies of the Raman (Ra) and IR bands[a] of $Ni_2P_2S_6$ and model structures $[Ni_6S_{18}(P_2S_6)]^{28-}$ (D_{3d}) and $[Cs_2P_2S_6]^{2-}$ (D_{3d}) [cm^{-1}].

$Ni_2P_2S_6$ Exp.		$[Ni_6S_{18}(P_2S_6)]^{28-}$ Calc. PBE0/def2-TZVPP/ B3LYP/def2-TZVPP		$[Cs_2P_2S_6]^{2-}$ Calc. PBE0/def2-TZVPP/ PBE0/def2-QZVPP		Assignment	Activity
Raman	IR[b]	Raman	IR	Raman	IR	Mode Character χ	
-		-	-	-	33	A_{1u}	inactive
133		-	-	-	-	-	-
-		-	130/129	-	135	E_u	IR
-		-	213/217	-	-	A_{1u}	inactive
177		229/219	-	159	-	$E_g^{(1)}$	Ra
255		215/216	-	186	-	$A_{1g}^{(1)}$	Ra
-		-	229/234	-	213	E_u	IR
282		251/253	-	240	-	$E_g^{(2)}$	Ra
-		-	268/264	-	306	A_{2u}	IR
385		411/406	-	373	-	$A_{1g}^{(2)}$	Ra
-	446	-	478/474	-	441	A_{2u}	IR
561	-	618/610	-	555	-	$E_g^{(3)}$	Ra
-	573	-	621/611	-	562	E_u	IR
589	-	608/600	-	532	-	$A_{1g}^{(3)}$	Ra
728-833	-	-	-	-	-	-	overtones/ unclear
1156-1202	-	-	-	-	-	-	overtones/ unclear

[a] Bands which correspond to Cs- or Ni-S- vibrations are assigned as lattice vibrations and not included. [b] IR spectrum was measured between 4000-400 cm^{-1}.

Electrochemical measurements: cyclic voltammetry

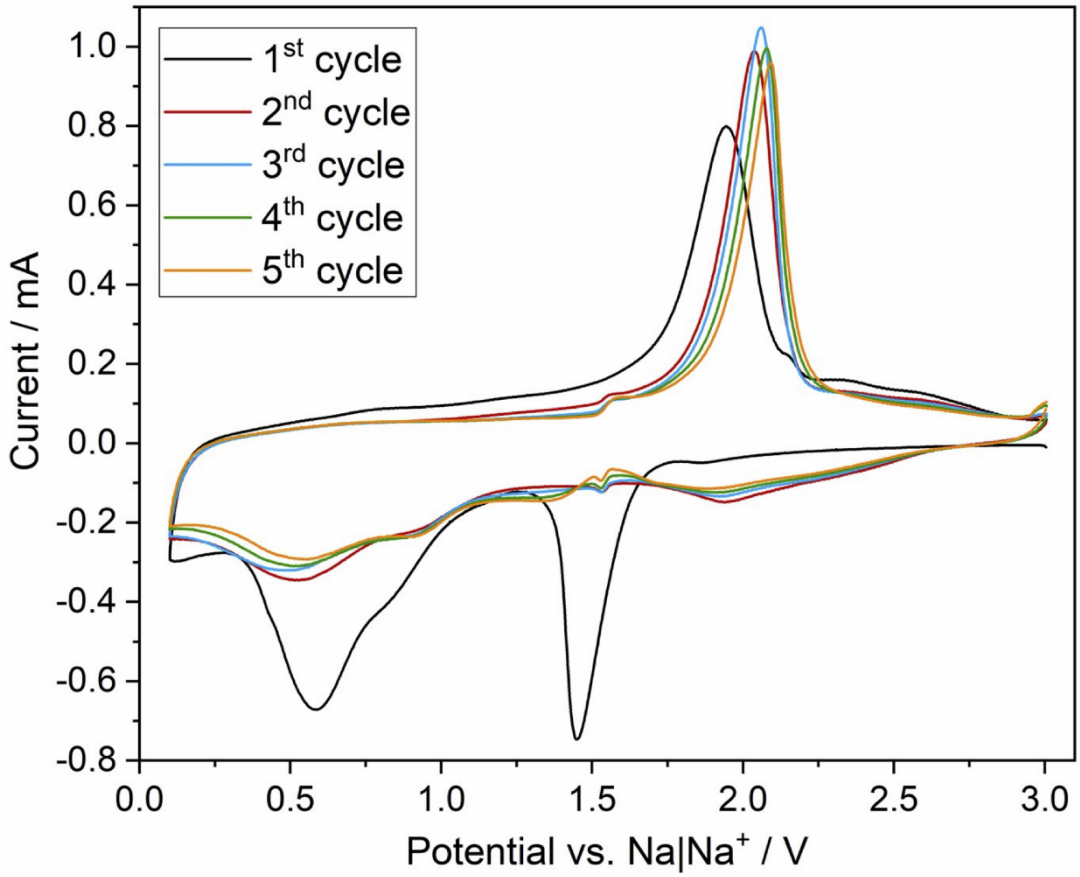

Figure S6. Cyclic voltammetry curves recorded with a scan rate of 0.1 mV s^{-1} in a potential window from 3.0 to 0.1 V.

For further electrochemical characterization, CV curves of the active material were recorded in a potential range from 3.0 V to 0.1 V. The pronounced difference between the first and the following cycles is characteristic for conversion-type reaction mechanisms. During the first discharge, a sharp reduction peak at 1.45 V and several not well-resolved peaks between 0.82 V and 0.43 V are observed. The sharp peak at 1.45 V is assigned to the reduction of Ni^{2+} to Ni, which is in good agreement with conducted *ex situ* measurements as well as with the discharge profile of the 1st cycle (see Fig. 4B). *Ex situ* measurements proof the complete reduction of Ni^{2+} between the uptake of 3.5 to 5 Na/f.u. The discharge profile of the 1st cycle exhibits an electrochemical plateau beginning at 1.45 V, which ends after a specific capacity of ~270 mAh g^{-1} was reached, corresponding to the uptake of roughly 4 Na/f.u. The reduction peaks between 0.82 V and 0.43 V are assigned to the presence of intermediate P and Na containing phases between the uptake of 5 to 9 Na/f.u. as well

as to the formation of Na_2S, which is in good agreement with the *ex situ* ^{23}Na and ^{31}P MAS NMR measurements. During charging, only one sharp oxidation peak occurs at 1.95 V with a very small shoulder at 2.14 V, which might be assigned to desodiation and oxidation of metallic Ni. In the second cycle, the sharp reduction peak slightly shifted to 1.53 V while losing nearly all of its initial intensity. The other reduction events occur at 0.91 V and 0.51 V. The oxidation peak is observed at 2.04 V in the second cycle with increased intensity.

The CV curves clearly demonstrate battery-type rather than pseudocapacitive behavior which is why pseudocapacity was not calculated, as it is not applicable for this type of energy device.[3–5]

Electrochemical long-term cycling of nanosheet $Ni_2P_2S_6$

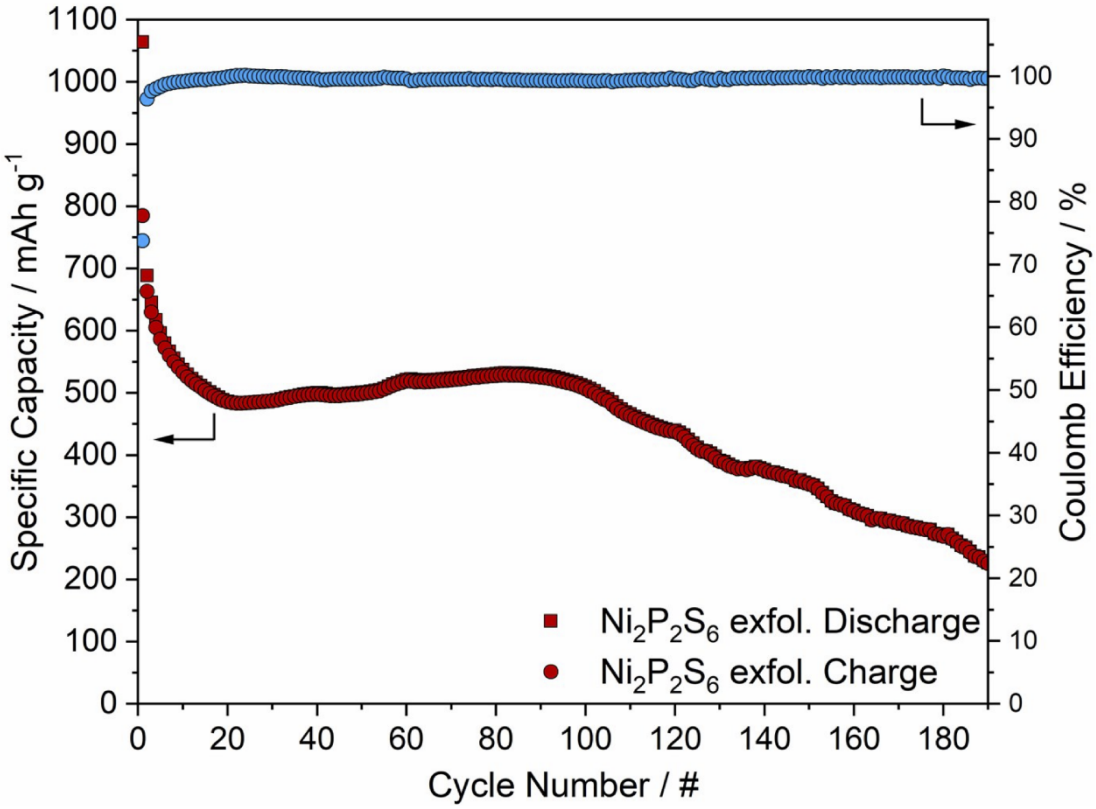

Figure S7. Electrochemical performance of nanosheet samples of $Ni_2P_2S_6$ against Na. Current rates of 1 A g^{-1} were applied within a potential window of 3.0 – 0.1 V.

Ex situ methods: X-ray diffraction, ^{19}F MAS NMR, pair distribution function analysis and X-ray absorption spectroscopy

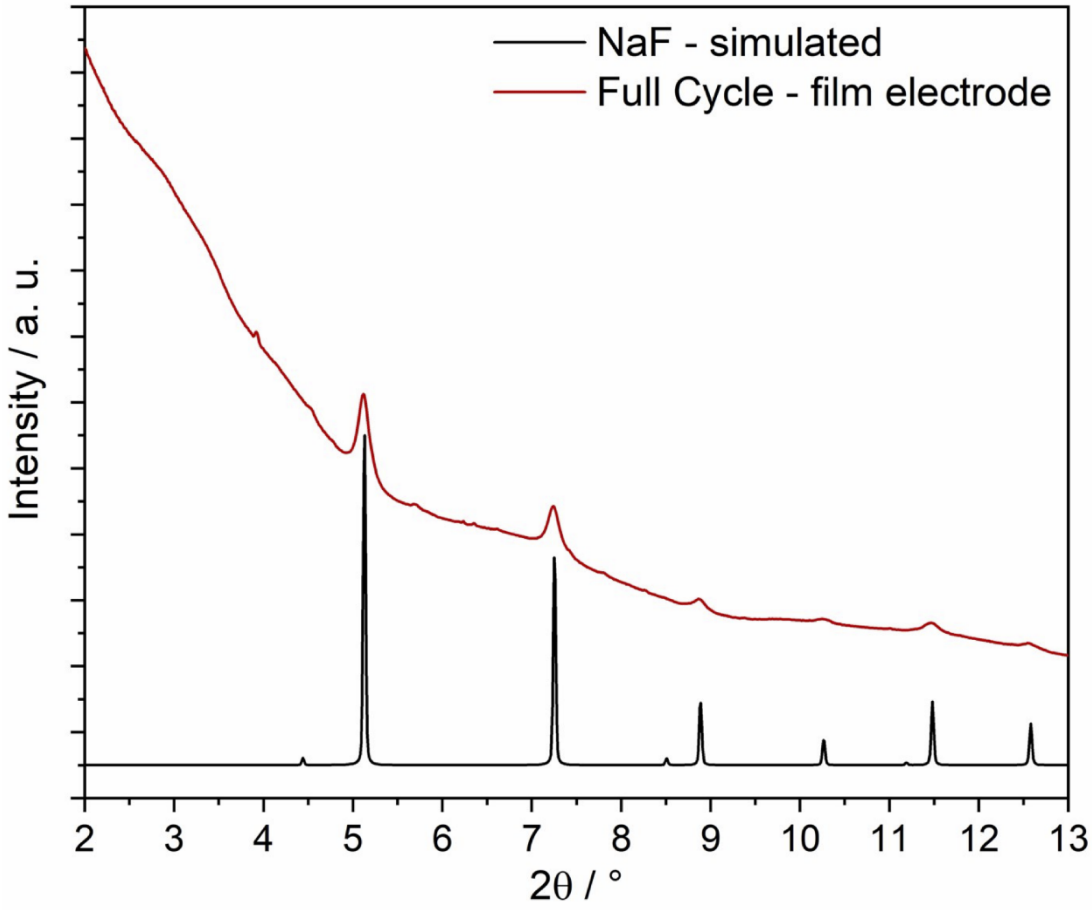

Figure S8. *Ex situ* X-ray diffraction pattern of the $Ni_2P_2S_6$ electrode collected after a full cycle compared to the calculated X-ray diffraction pattern of NaF.[6] Measured at beamline P02.1, DESY using 60 keV (λ = 0.207 Å).

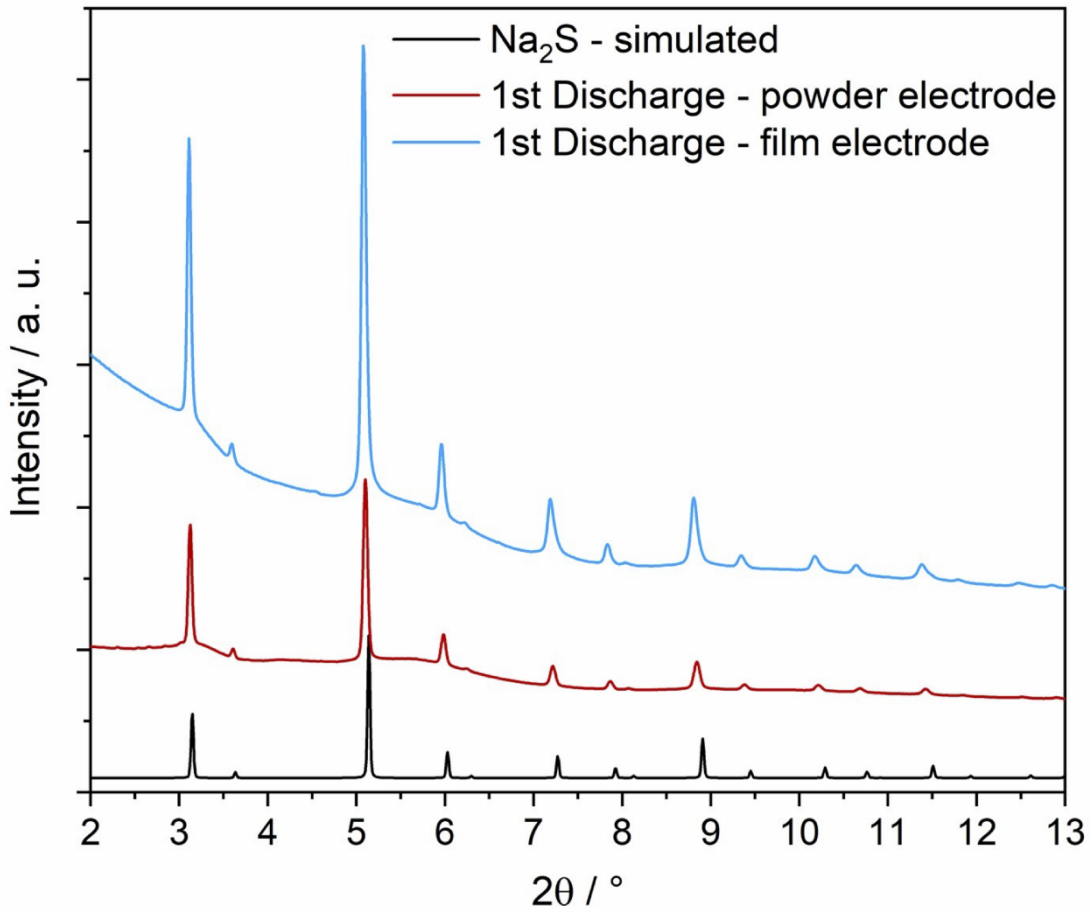

Figure S9. *Ex situ* X-ray diffraction pattern of $Ni_2P_2S_6$ film and powder electrodes collected after complete discharge compared to the calculated X-ray diffraction pattern of Na_2S.[7] The slight variations in peak position are most likely due to the nanoscale and disorder of the particles formed during the electrochemical reaction. The formation of Na_2S is evident in both cases, but no reflections of NaF are observed. Measured at beamline P02.1, DESY using 60 keV (λ = 0.207 Å).

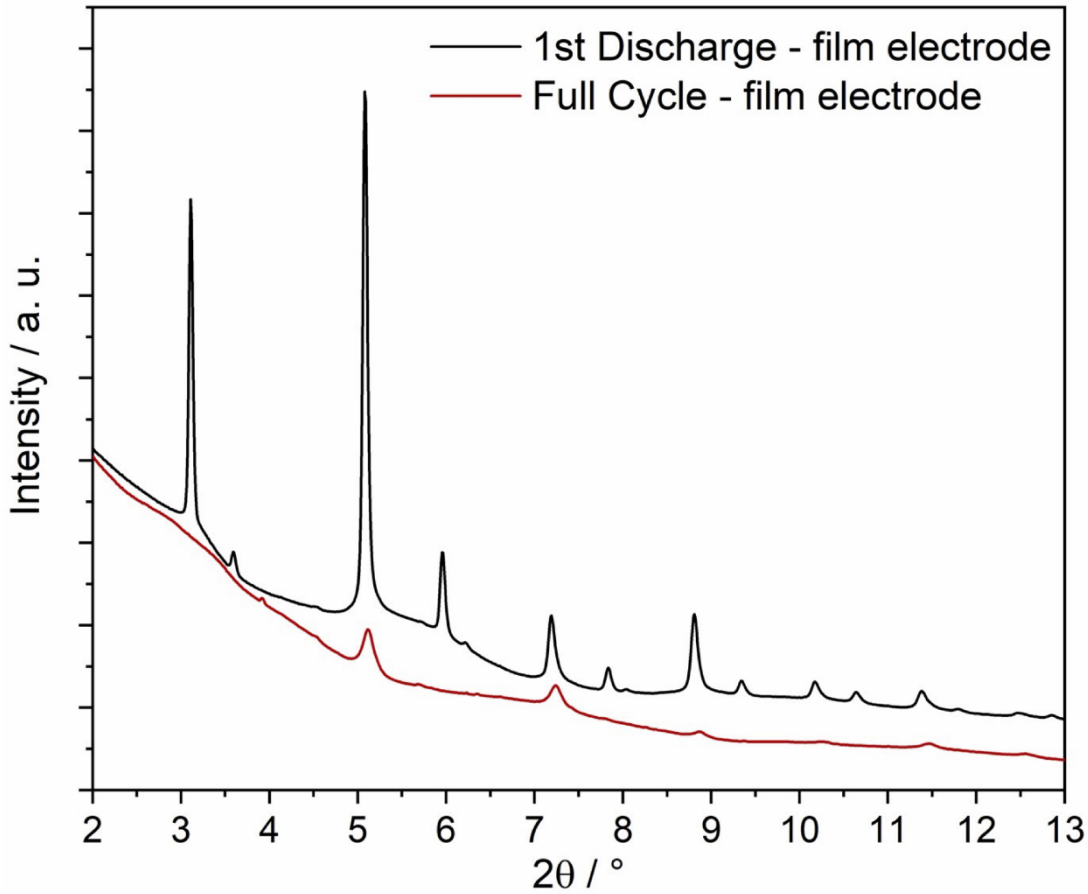

Figure S10. *Ex situ* X-ray diffraction pattern of the $Ni_2P_2S_6$ electrode on copper foil collected after a complete discharge and after a full cycle. In the completely discharged sample, reflections of Na_2S could possibly superpose the less intense reflections of NaF. Measured at beamline P02.1, DESY using 60 keV (λ = 0.207 Å).

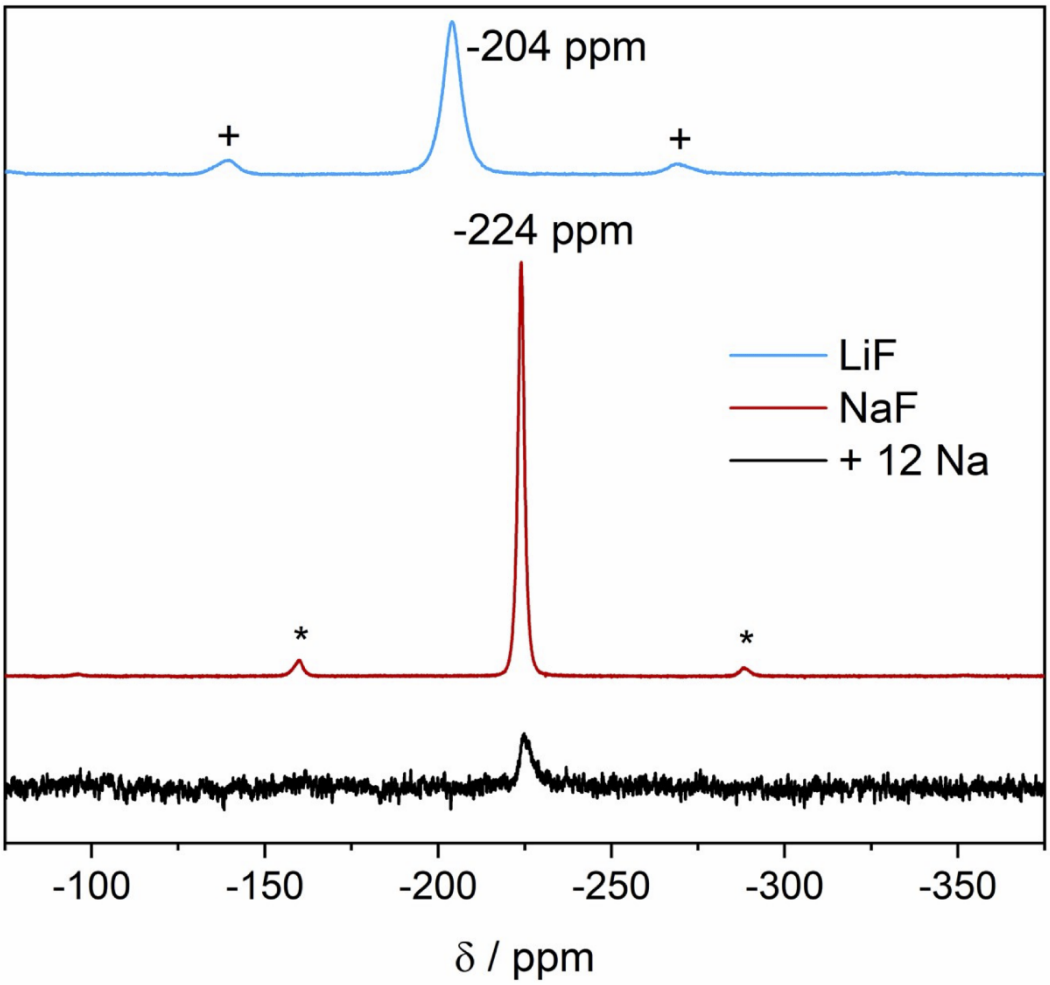

Figure S11. ^{19}F MAS NMR spectra of $Ni_2P_2S_6$ powder electrodes after a complete discharge compared to the references of NaF and LiF. Peaks marked with * and + visualize the spinning sidebands of the reference samples. The spectrum of the discharged sample was magnified by a factor of 200.

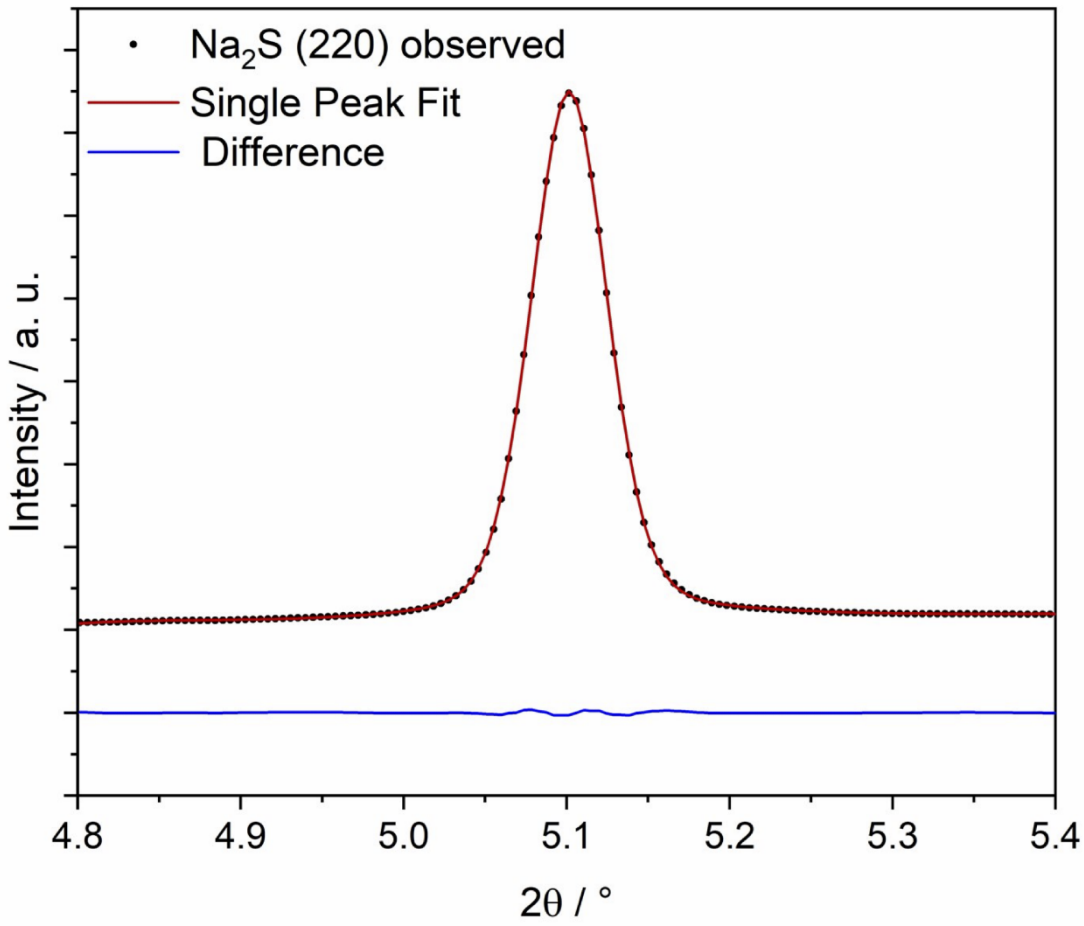

Figure S12. Single peak fit of the *ex situ* X-ray diffraction pattern of the completely discharged $Ni_2P_2S_6$ electrode. The (220) reflection of Na_2S is shown (black) with a single peak fit with a FWHM modelled by the Scherrer formula (red) and difference calculation (blue). Measured at beamline P02.1, DESY using 60 keV (λ = 0.207 Å).

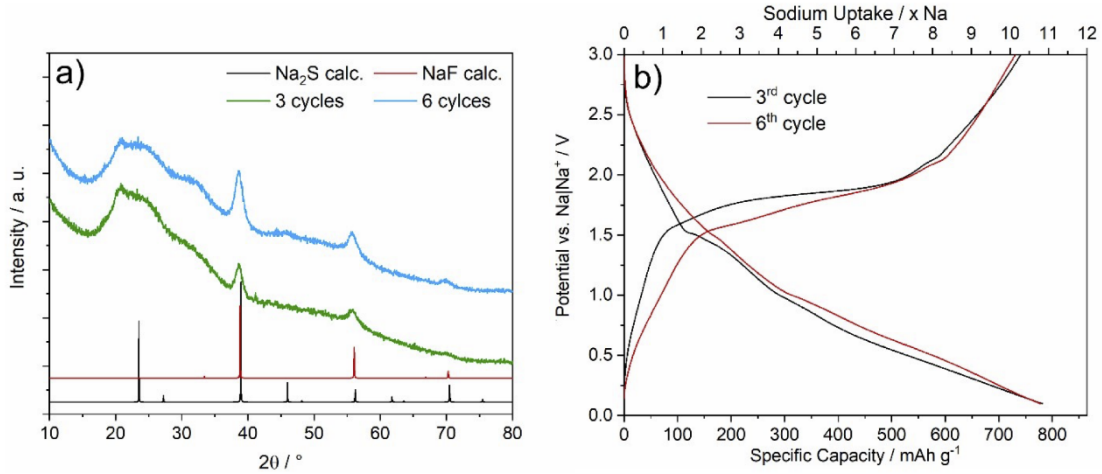

Figure S13. a) *Ex situ* X-ray diffraction pattern (Cu-Kα radiation (λ = 1.54058 Å) of the $Ni_2P_2S_6$ electrode on copper foil collected after 3 and 6 cycles (charged) compared to the calculated X-ray diffraction patterns of NaF[6] and Na_2S.[7] b) Discharge and charge profiles of the 3rd and 6th cycle of $Ni_2P_2S_6$ electrode. C-rates of C/10 and C/5 were applied for the sample cycled for 3 and for 6 cycles, respectively.

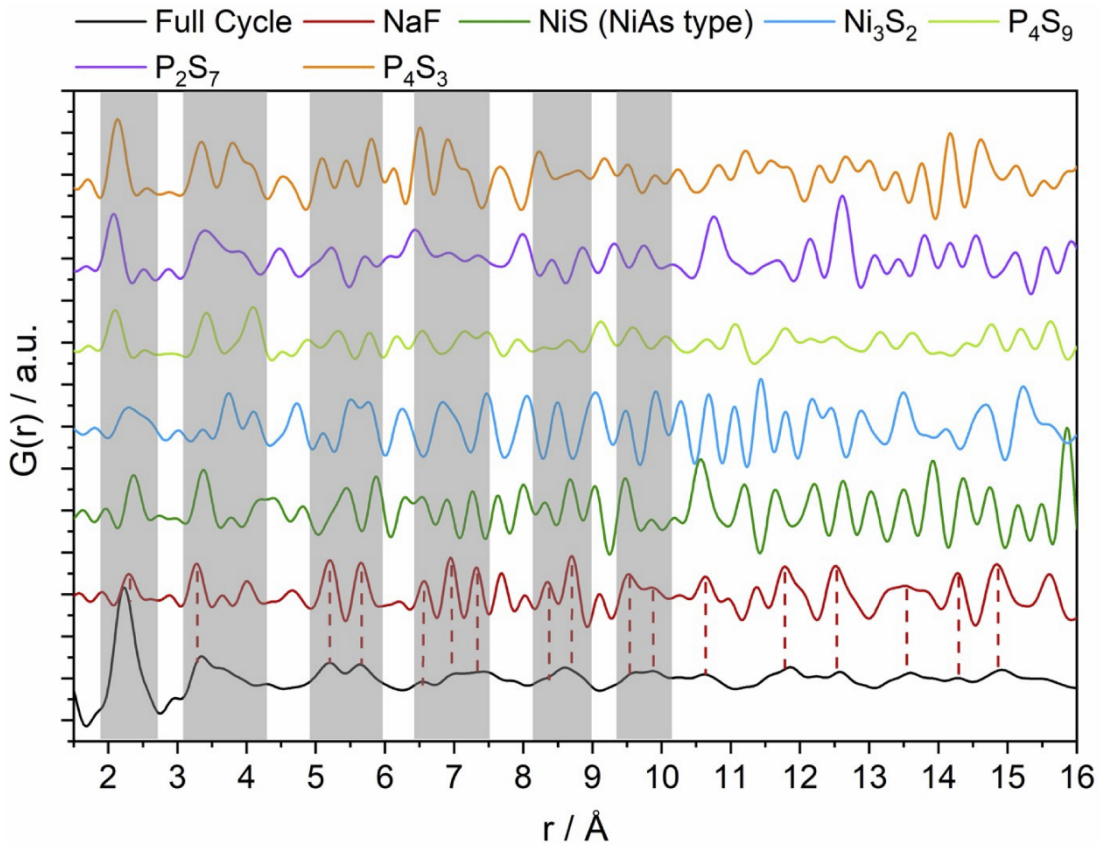

Figure S14. *Ex situ* pair distribution function of the $Ni_2P_2S_6$ electrode collected after a full cycle compared to the calculated PDF of NaF[6], NiS (NiAs type)[8], Ni_3S_2[9] , P_4S_9[10], P_2S_7[11] and P_4S_3[12]. The grey markings show areas where the different compounds have similar distances and therefore could

contribute to the PDF of the sample. The red dashed lines point out distances of NaF, which are in accordance with the PDF of the fully recharged sample.

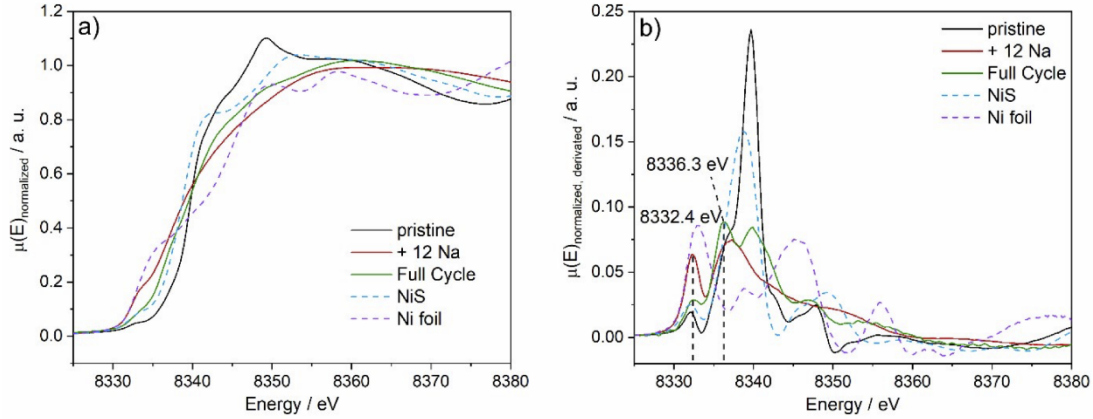

Figure S15. a) *Ex situ* XANES spectra at the Ni K-edge of the $Ni_2P_2S_6$ electrode after a full cycle compared with pristine and completely discharged $Ni_2P_2S_6$ as well as Ni foil and NiS and b) the corresponding first derivatives.

References

1 K. Synnatschke, S. Shao, J. van Dinter, Y. J. Hofstetter, D. J. Kelly, S. Grieger, S. J. Haigh, Y. Vaynzof, W. Bensch and C. Backes, *Chem. Mater.*, 2019, **31**, 9127–9139.

2 L. Ueberricke, J. N. Coleman and C. Backes, *Phys. Status Solidi B*, 2017, **254**, 1700443.

3 P. Simon, Y. Gogotsi and B. Dunn, *Science*, 2014, **343**, 1210–1211.

4 T. Brousse, D. Bélanger and J. W. Long, *J. Electrochem. Soc.*, 2015, **162**, A5185–A5189.

5 C. Costentin and J.-M. Savéant, *Chem. Sci.*, 2019, **10**, 5656–5666.

6 Y. Shirako, Y. G. Shi, A. Aimi, D. Mori, H. Kojitani, K. Yamaura, Y. Inaguma and M. Akaogi, *J. Solid State Chem.*, 2012, **191**, 167–174.

7 E. Zintl, A. Harder and B. Dauth, *Z. Elektrochem. Angew. Phys. Chem.*, 1934, **40**, 588–593.

8 N. Alsén, *Geol. Fören. Förh.*, 1925, **47**, 19–72.

9 M. E. Fleet, *Am. Mineral.*, 1977, **62**, 341–345.

10 W. Hilmer, *Acta Crystallogr., Sect. B: Struct. Sci., Cryst. Eng Mater.*, 1969, **25**, 1229–1232.

11 T. Rödl, R. Weihrich, J. Wack, J. Senker and A. Pfitzner, *Angew. Chem. Int. Ed.*, 2011, **50**, 10996–11000.

12 I. Raabe, S. Antonijevic and I. Krossing, *Chem. – Eur. J.*, 2007, **13**, 7510–7522.

7.1.2 Long-Term Stable, High-Capacity Anode Material for Sodium-Ion Batteries: Taking a Closer Look at $CrPS_4$ from an Electrochemical and Mechanistic Point of View

Supporting Information

Long-Term Stable, High-Capacity Anode Material for Sodium-Ion Batteries: Taking a Closer Look at $CrPS_4$ from an Electrochemical and Mechanistic Point of View

Jonas van Dinter,[†] Sylvio Indris,[‡] Alexander Bitter,[†] David Grantz,[†] Giannantonio Cibin,[§] Martin Etter[‖] and Wolfgang Bensch*[,†]

[†]*Institute of Inorganic Chemistry, Kiel University, Max-Eyth-Str. 2, 24118 Kiel, Germany; wbensch@ac.uni-kiel.de*

[‡]*Institute for Applied Materials - Energy Storage Systems, Karlsruhe Institute of Technology, P.O. Box 3640, 76021 Karlsruhe, Germany*

[§]*Diamond Light Source, Harwell Science and Innovation Campus, Diamond House, Didcot, Oxfordshire OX11 0DE, United Kingdom*

[‖]*Deutsches Elektronen-Synchrotron (DESY), Notkestr. 85, 22607 Hamburg, Germany*

Energy dispersive X-ray spectroscopy

Table S1. Results of EDX measurements of $CrPS_4$ powder at different spots on the sample.

	Cr / at.%	P / at.%	S / at.%
Spot 1	16.61	17.59	65.81
Spot 2	16.54	17.87	65.59
Spot 3	14.44	17.84	67.72
Spot 4	16.46	17.68	65.86
Spot 5	17.95	17.52	64.53
Average	16.40 ± 1.26	17.70 ± 0.02	65.90 ± 1.06
Composition	$Cr_{0.98}P_{1.06}S_{3.95}$		

Raman spectroscopy

The optical properties of $CrPS_4$ were already widely investigated in the past.[1–3] As $CrPS_4$ exhibits *C2* space group symmetry, the lattice vibrations can be reduced according to C_2 point symmetry to

$\Gamma_{\mathrm{vib}}^{C_2}$ = 17A + 19B

resulting in 36 vibrational modes including three Raman inactive modes (A + 2B).[1,2] The experimentally obtained Raman spectrum (Figure S1) shows the characteristic lattice vibrations of $CrPS_4$ in agreement with literature.[1–3] Additionally, recently performed angle-dependent Raman polarization experiments[1] enabled the assignment of the bands (Figure S1) between 100 cm^{-1} and 450 cm^{-1}.

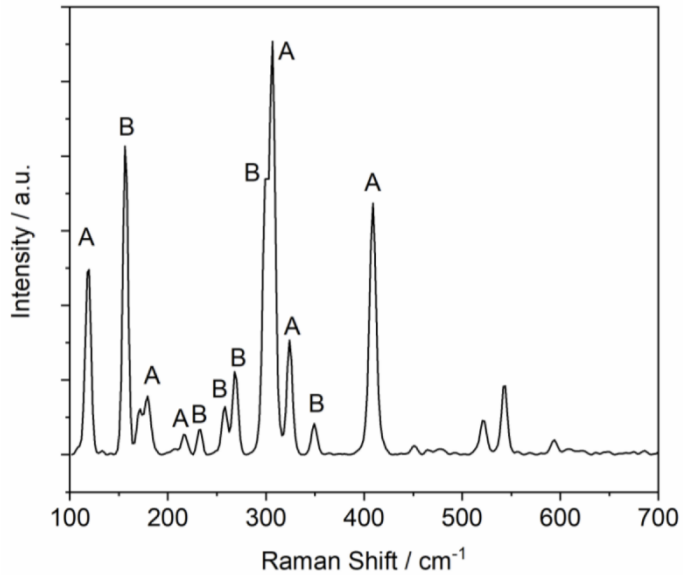

Figure S1. FT-Raman spectrum of the pristine material $CrPS_4$ collected at room temperature with an excitation wavelength of 1064 nm displayed between 100 and 700 cm^{-1}.

Scanning Electron Microscopy

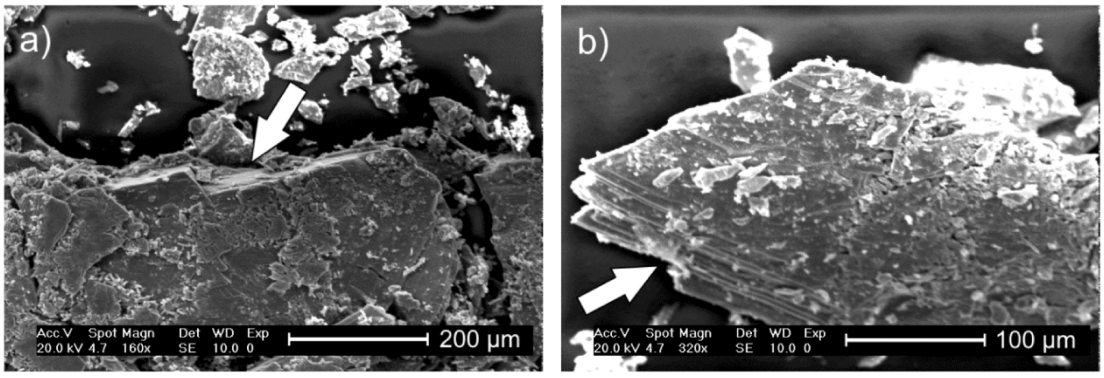

Figure S2. SEM images of the target compound $CrPS_4$ at different magnifications. The white arrows point towards the edges of the agglomerates where the layered nature of the compound is clearly visible.

2

Different types of electrodes

Table S2. Observed specific capacities for different types of electrodes.

#	Type of electrode	Specific discharge capacity [mAh g^{-1}]	Specific charge capacity [mAh g^{-1}]
1	Film	1076	716
2	Film	1056	853
3	Film	1121	826
4	Film	1131	855
5	Film	1278	882
6	Film	1069	514
7	Film	1377	-
8	Film	1232	-
9	Film	1169	-
10	Film	1040	-
11	Film	1356	-
12	Film	1246	-
13	Film	1155	-
14	Film	1237	-
15	Film	1095	-
16	Film	1035	-
Average	Film	1167 (**9.2 Na / f.u.**)	774 (**6.1 Na / f.u.**)
17	Powder	838	-
18	Powder	731	-
Average	Powder	784.5 (**6.2 Na / f.u.**)	-

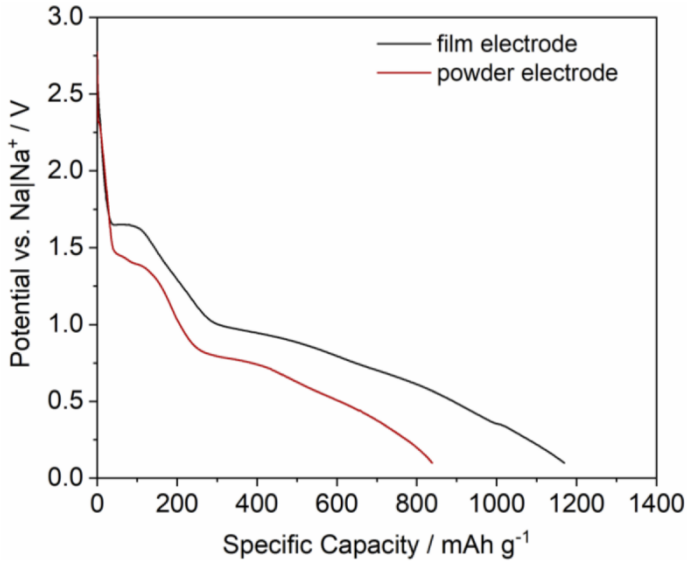

Figure S3. Comparison of the discharge profile of powder vs. film electrodes. The displayed discharge profiles represent the typical appearance of film (black) and powder (red) electrodes.

Comparison discharged powder and film electrode

XRD data (Figure S4) show that Na_2S is not yet formed after the uptake of 6 Na/f.u. The first signs of Na_2S formation can be detected in the XRD pattern of the discharged powder electrode. As powder electrodes only took up ≈ 6.2 Na/f.u. and no reflections of Na_2S can be found in the XRD pattern of the sample after the uptake of 6 Na/f.u., it is very likely that the formation of Na_2S begins approximately between 6 and 6.2 Na/f.u.

By comparing the PDF of the discharged powder (6.2 Na/f.u.) and film (9.2 Na/f.u.) electrode (Figure S5c), it is obvious that the intensity ratio of the signals at 2.41 Å and 2.83 Å are different. For the powder electrode, the signal at 2.83 Å is more intense, while the peak at 2.41 Å is less intense compared to those signals of the film electrode. Further, the intensity at 3.28 Å increased for the film electrode in contrast to the powder electrode. This behavior is a clear indication that the electrochemical reaction is incomplete for the powder electrode. However, the observed alteration during these final discharging processes cannot be assigned clearly to the formation of specific phases as there are too many possibilities.

Another indication of an incomplete electrochemical reaction in powder cells is observed in the XANES data (Figure S6). The signal at 5988.6 eV, which is more intense for the discharged film electrode compared to the discharged powder electrode supports the assumption that the electrochemical reaction during discharging is

incomplete for powder electrodes and is consistent with the obtained lower discharge capacities for these types of electrodes.

Investigation of the reaction mechanism: X-ray diffraction, pair distribution function, X-ray absorption and ^{23}Na MAS NMR spectroscopy

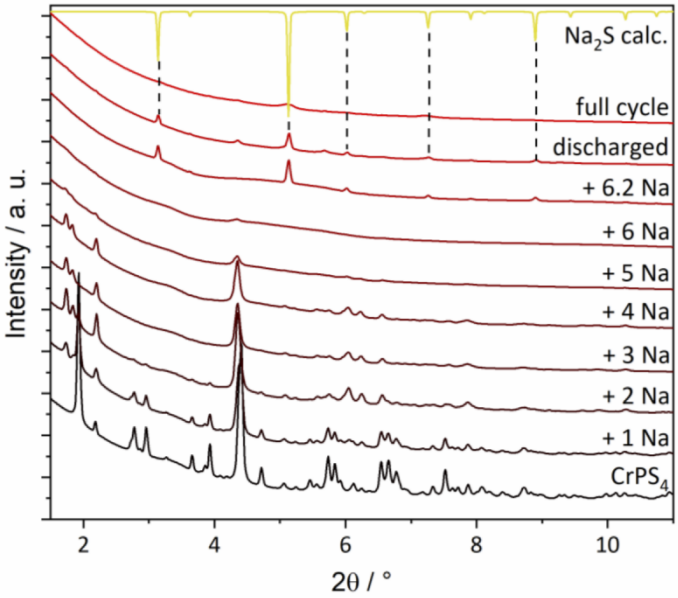

Figure S4. X-ray diffraction patterns of the $CrPS_4$ electrode collected at different states of discharge/charge compared to the calculated pattern of Na_2S from literature data.[4] The sample marked with "+ 6.2 Na" represents a completely discharged powder cell.

5

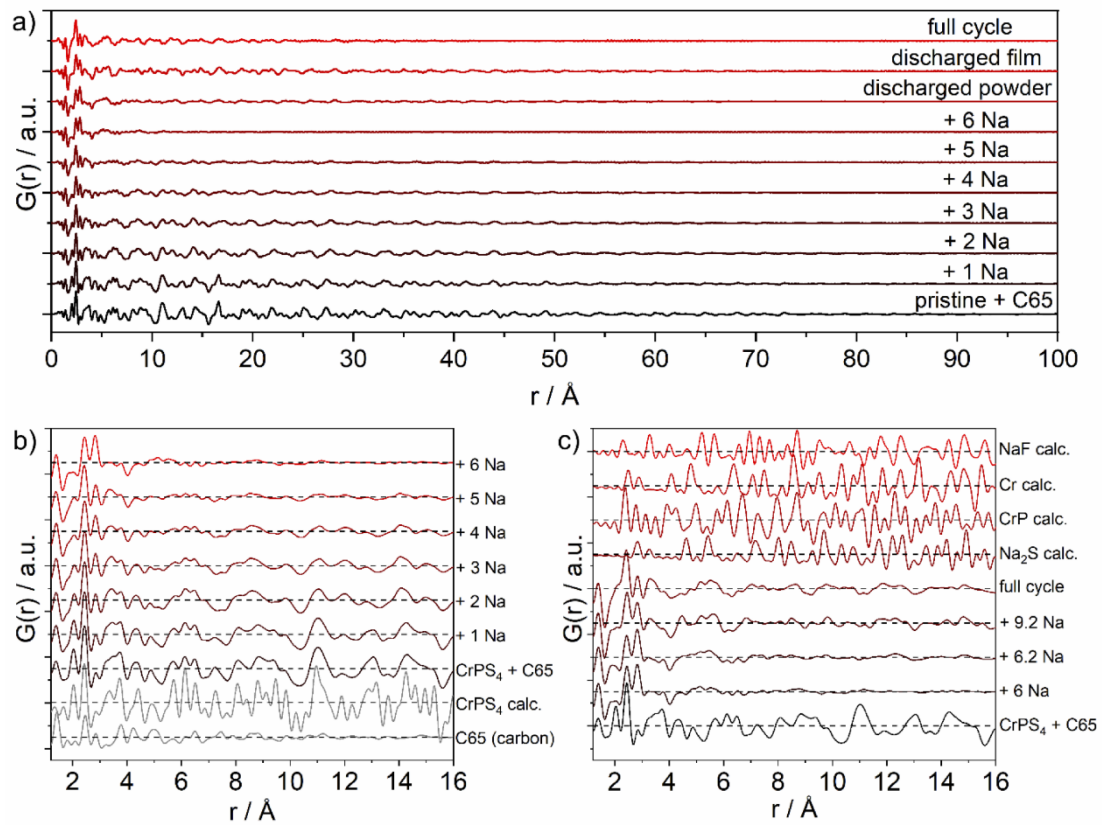

Figure S5. Pair distribution function of $CrPS_4$ electrodes after uptake of several amounts of Na/f.u. (a) Overview of the samples displayed in the range of 0 to 100 Å. (b) PDF in the range of 1.5 Å to 16 Å. The uptake of 1-6 Na/f.u. as well as the starting material, pure carbon and the PDF calculated from the structure of $CrPS_4$[5] is shown. (c) PDF in the range of 1.5 Å to 16 Å showing the starting material, the uptake of 6 Na/f.u., the discharged powder (6.2 Na/f.u.) and film (9.2 Na/f.u.) electrode and the PDF after a complete cycle. For comparison PDFs calculated from the structures of of Na_2S,[4] CrP,[6] bcc Cr[7] and NaF[8] are shown as well.

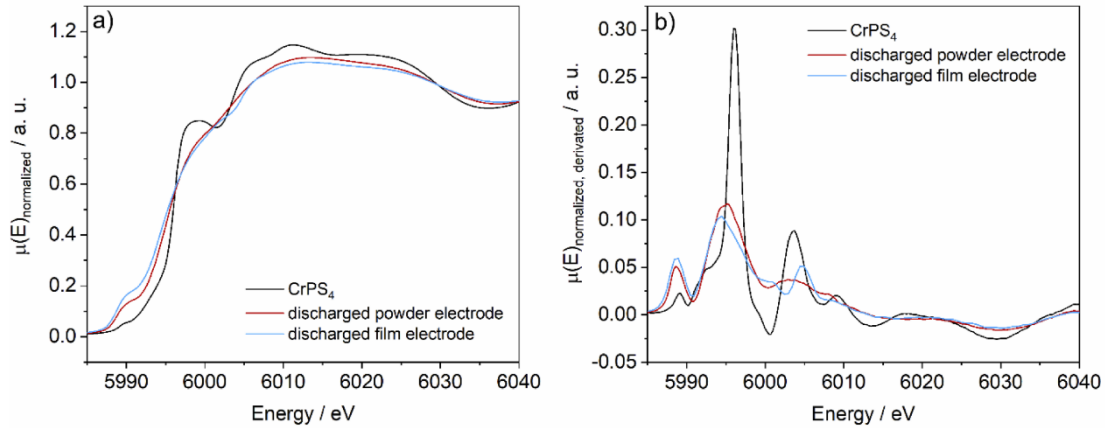

Figure S6. (a) XANES spectra at the Cr K-edge of pristine $CrPS_4$ and the fully discharged powder electrode (6.2 Na/f.u) compared to the fully discharged film electrode (9.2 Na/f.u.) and (b) the corresponding first derivatives.

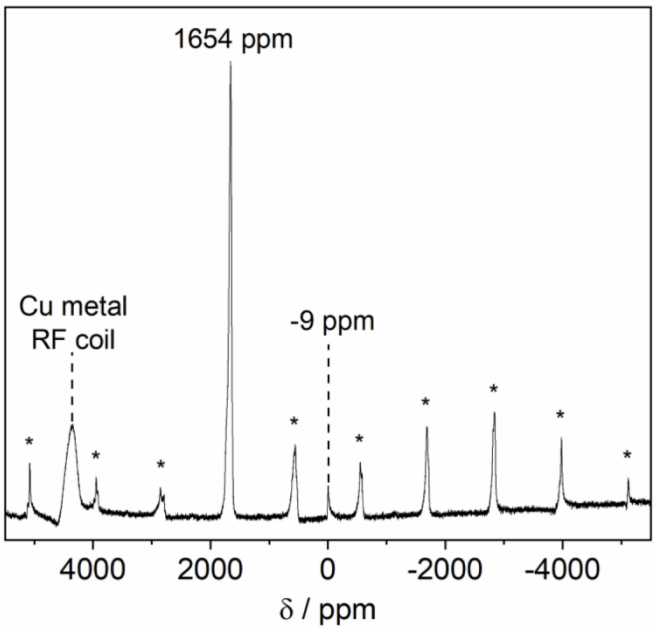

Figure S7. ^{23}Na MAS NMR spectrum of $NaCrS_2$. Spinning sidebands are marked with an asterisk.

References

(1) Wu, H.; Chen, H. Probing the Properties of Lattice Vibrations and Surface Electronic States in Magnetic Semiconductor $CrPS_4$. *RSC Adv.* **2019**, *9* (53), 30655–30658. https://doi.org/10.1039/C9RA05861C.

(2) Lee, J.; Ko, T. Y.; Kim, J. H.; Bark, H.; Kang, B.; Jung, S.-G.; Park, T.; Lee, Z.; Ryu, S.; Lee, C. Structural and Optical Properties of Single- and Few-Layer Magnetic Semiconductor $CrPS_4$. *ACS Nano* **2017**, *11* (11), 10935–10944. https://doi.org/10.1021/acsnano.7b04679.

(3) Budniak, A. K.; Killilea, N. A.; Zelewski, S. J.; Sytnyk, M.; Kauffmann, Y.; Amouyal, Y.; Kudrawiec, R.; Heiss, W.; Lifshitz, E. Exfoliated $CrPS_4$ with Promising Photoconductivity. *Small* **2020**, *16* (1), 1905924. https://doi.org/10.1002/smll.201905924.

(4) Zintl, E.; Harder, A.; Dauth, B. Gitterstruktur der Oxyde, Sulfide, Selenide und Telluride des Lithiums, Natriums und Kaliums. *Z. Elektrochem. Angew. Phys. Chem.* **1934**, *40* (8), 588–593. https://doi.org/10.1002/bbpc.19340400811.

(5) Louisy, A.; Ouvrard, G.; Schleich, D. M.; Brec, R. Physical Properties and Lithium Intercalates of $CrPS_4$. *Solid State Commun.* **1978**, *28* (1), 61–66. https://doi.org/10.1016/0038-1098(78)90328-9.

(6) Selte, K.; Kjekshus, A.; Andresen, A. F. Structural and Magnetic Properties of CrP. *Acta Chem. Scand.* **1972**, *26* (10), 4188–4190. https://doi.org/10.3891/acta.chem.scand.26-4188.

(7) Kugler, W.; Knorr, K.; Prandl, W. Röntgenbeugungsuntersuchungen an der magnetostriktiven Verzerrungswelle in Chrom: Amplitude und Temperaturabhängigkeit. *Z. Kristallogr.* **1983**, *162* (1–4), 151–153. https://doi.org/10.1524/zkri.1983.162.14.i.

(8) Shirako, Y.; Shi, Y. G.; Aimi, A.; Mori, D.; Kojitani, H.; Yamaura, K.; Inaguma, Y.; Akaogi, M. High-Pressure Stability Relations, Crystal Structures, and Physical Properties of Perovskite and Post-Perovskite of $NaNiF_3$. *J. Solid State Chem.* **2012**, *191*, 167–174. https://doi.org/10.1016/j.jssc.2012.03.004.

8

7.1.3 A Combined Sodium Intercalation and Copper Extrusion Mechanism in the Thiophosphate Family: $CuCrP_2S_6$ as Anode Material in Sodium-Ion Batteries

Supporting Information

A combined Sodium Intercalation and Copper Extrusion Mechanism in the Thiophosphate Family: $CuCrP_2S_6$ as Anode Material in Sodium-Ion Batteries

Jonas van Dinter,[a] David Grantz,[a] Alexander Bitter[a] and Wolfgang Bensch*[a]

[a]*Institute of Inorganic Chemistry, Kiel University, Max-Eyth-Str. 2, 24118 Kiel, Germany*

Synthesis

$CuCrP_2S_6$ was synthesized by chemical vapor transport. In general, stoichiometric amounts of Cu, Cr and P were mixed with an excess of S. The mixture was sealed in a quartz glass tube ($<10^{-4}$ mbar) and heated in a tube furnace. To evaporate the sulfur carefully in the quartz tube, the furnace was heated to 450 °C within 4 h. After maintaining this temperature for 24 h, the furnace was heated to the reaction temperature.

The biggest issue of the synthesis of $CuCrP_2S_6$ is that $CrPS_4$ is formed within the same temperature range. Applying chemical vapor transport does not solve this problem, because the transport properties of these compounds seem to be very similar. Therefore, reaction parameters were modified systematically to obtain $CuCrP_2S_6$ with the lowest possible impurities. The best results were obtained with reaction temperatures of 600 and 700°C and a reaction time between 2 and 4 weeks (Figure S1a). It seems beneficial for phase separation to add excess P (beside the excess of S) to the reaction mixture. However, no complete phase separation was achieved by adding excess P. At temperatures above 700°C and below 600°C, compounds other than $CuCrP_2S_6$ and $CrPS_4$ additionally are formed (Figure S1b). We note that phase pure $CuCrP_2S_6$ was obtained by manual separation from $CrPS_4$. The best separation of the reaction products was obtained for the synthesis approach conducted at 700°C for 2 weeks with an excess of P.

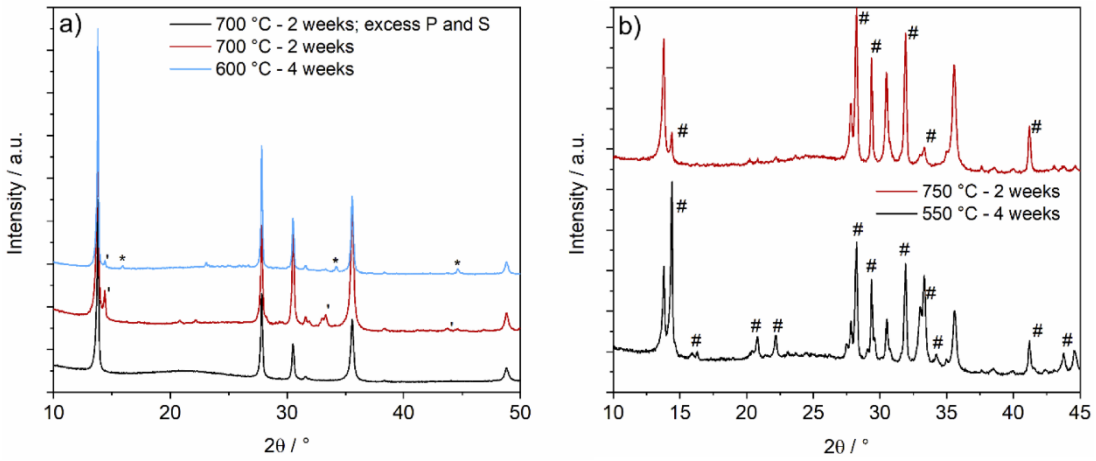

Figure S1. (a) PXRD pattern of reaction products synthesized with different reaction times and temperatures. Reflections marked with ' belong to $CrPS_4$[1] and reflections marked with * can be assigned to Cr_2S_3.[2] (b) PXRD patterns of the products obtained from syntheses with reaction temperatures above 700 °C or below 600 °C, which yield other compounds besides $CrPS_4$ and $CuCrP_2S_6$. Reflection marked with # belong to phases other than $CuCrP_2S_6$.

Characterization of pristine $CuCrP_2S_6$: EDX and elemental analysis

Table S1. Results of EDX measurements of $CuCrP_2S_6$ powder at different spots on the sample.

	Cu / at.%	Cr / at.%	P / at.%	S / at.%
Spot 1	10.59	10.17	21.54	57.70
Spot 2	10.71	10.27	20.75	58.27
Spot 3	11.35	10.22	21.03	57.40
Average	10.88 ± 0.33	10.22 ± 0.04	21.11 ± 0.33	57.79 ± 0.36
Composition	$Cu_{1.09}Cr_{1.02}P_{2.11}S_{5.78}$			

EDX measurements reveal stoichiometric ratios of Cu, Cr and P close to 1:1:2, while the S content exhibits values smaller than expected from the target stoichiometry. This is probably caused by the low energy of the S K_α emission line and absorption by the matrix. To account for the S content properly, additional elemental (CHNS) analysis was conducted (Table S2).

Table S2. Results of the elemental analysis of $CuCr_2P_2S_6$. Sulphanilamide was used as reference.

Sample	N / wt.%	C / wt.%	H / wt.%	S / wt.%
$CuCr_2P_2S_6$	0.0	0.0	0.0	52.65
theoretical	0.0	0.0	0.0	51.01

For the calculation of the composition, results of the elemental analysis were compared with the theoretical value of 51.01 wt.% S in $CuCr_2P_2S_6$, resulting in compositions of

$Cu_xCr_xP_xS_{6.07}$. The total composition of the sample was determined by combining the results of the CHNS analysis with the M^{I}:M^{III}:P ratio obtained from the EDX measurements. The results yield a composition of $Cu_{1.05}Cr_{0.92}P_{1.96}S_{6.07}$.

Characterization of pristine $CuCrP_2S_6$: Scanning Electron Microscopy

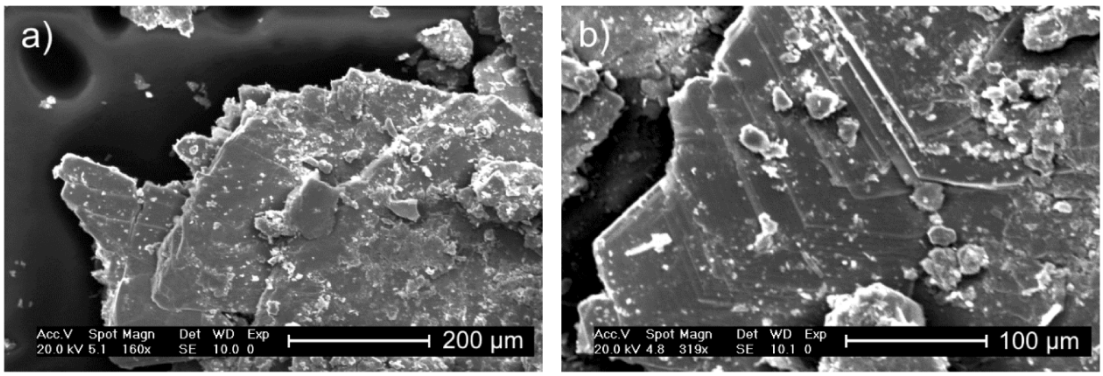

Figure S2. SEM images of the target compound $CuCrP_2S_6$ at different magnifications. (a) The plate-like nature and (b) several slabs stacked on top of each other illustrate the layered structure of the compound.

Electrochemical performance: Evolution of potential plateaus by *dQ/dV*

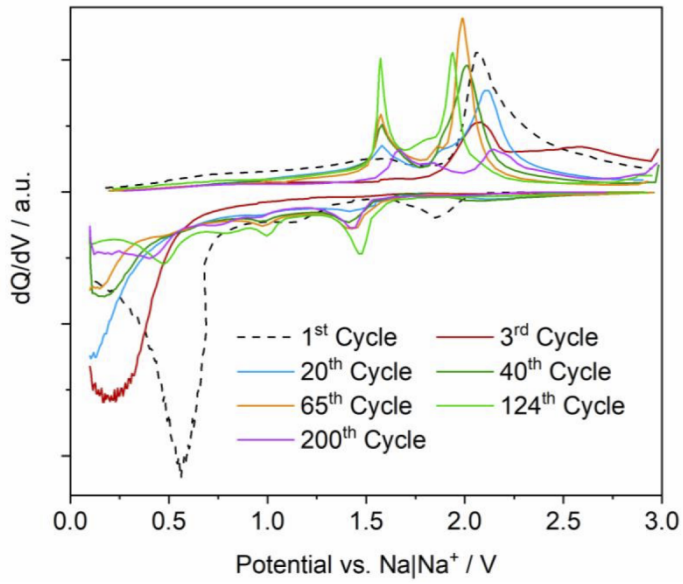

Figure S3. *dQ/dV* analysis of selected cycles indicating the alteration of the underlying reaction mechanism during long-term cycling.

3

References

[1] A. Louisy, G. Ouvrard, D. M. Schleich, R. Brec, *Solid State Commun.* **1978**, *28*, 61–66.
[2] F. Jellinek, *Acta Crystallogr.* **1957**, *10*, 620–628.

4

7.2 List of Publications

1. What happens structurally and chemically during sodium uptake and release by $Ni_2P_2S_6$: a combined X-ray diffraction, X-ray absorption, pair distribution function and MAS NMR analysis

   J. van Dinter, K. Synnatschke, T. A. Engesser, S. Indris, N. Wolff, O. Gronenberg, M. Etter, G. Cibin, L. Kienle, C. Backes, W. Bensch, *J. Mater. Chem. A*, **2020**, *8*, 22401-22415.

2. Long-Term Stable, High-Capacity Anode Material for Sodium-Ion Batteries: Taking a Closer Look at $CrPS_4$ from an Electrochemical and Mechanistic Point of View

   J. van Dinter, S. Indris, A. Bitter, D. Grantz, G. Cibin, M. Etter, W. Bensch, *ACS Appl. Mater. Interfaces*, **2021**, *13*, 54936-54950.

3. A Combined Sodium Intercalation and Copper Extrusion Mechanism in the Thiophosphate Family: $CuCrP_2S_6$ as Anode Material in Sodium-Ion Batteries

   J. van Dinter, D. Grantz, A. Bitter and W. Bensch, *ChemElectroChem*, **2022**, e202200018.

Co-Authorship:

4. Elucidation of the Sodium-Copper Extrusion Mechanism in $CuCrS_2$: A High Capacity, Long-Life Anode Material for Sodium-Ion Batteries

   M. Krengel, A.-L. Hansen, F. Hartmann, **J. van Dinter**, W. Bensch, *Batteries Supercaps*, **2018**, *1*, 176-183.

5. Unveiling the Reaction Mechanism during Li Uptake and Release of Nanosized "$NiMnFeO_4$": Operando X-ray Absorption, X-ray Diffraction, and Pair Distribution Function Investigations

   S. Permien, A.-L. Hansen, **J. van Dinter**, S. Indris, G. Neubüser, L. Kienle, S. Doyle, S. Mangold, W. Bensch, *ACS Omega*, **2019**, *4*, 2398-2409.

6. Liquid Exfoliation of $Ni_2P_2S_6$: Structural Characterization, Size-Dependent Properties, and Degradation

   K. Synnatschke, S. Shao, **J. van Dinter**, Y. J. Hofstetter, D. J. Kelly, S. Grieger, S. J. Haigh, Y. Vaynzof, W. Bensch, C. Backes, *Chem. Mater.*, **2019**, *31*, 9127-9139.

7. Aqueous Flow Reactor and Vapour-Assisted Synthesis of Aluminium Dicarboxylate Metal-Organic Frameworks with Tuneable Water Sorption Properties

   T. Stassin, S. Waitschat, N. Heidenreich, H. Reinsch, F. Pluschkell, D. Kravchenko, J. Marreiros, I. Stassen, **J. van Dinter**, R. Verbeke, M. Dickmann, W. Egger, I. Vankelecom, D. De Vos, R. Ameloot, N. Stock, *Chem. - Eur. J.*, **2020**, *26*, 10841-10848.

7.3 Acknowledgements

At this point, I would like to acknowledge everybody, who contributed to this work in one way or another.

First and foremost, I would like to thank my doctorate supervisor Prof. Dr. Wolfgang Bensch for the possibility of doing my doctorate in his working group as well as for his support and advice. Furthermore, I greatly appreciate the provided large degree of freedom during this time. Finally, I would like to thank for the good food at our working group meetings/barbeques.

Without my cooperation partners, some of the publications wouldn't have been nearly as detailed as they turned out. Therefore, I would like to thank Kevin Synnatschke, Tobias Engesser, Sylvio Indirs, Niklas Wolff, Ole Gronenberg, Martin Etter, Giannantonio Cibin, Lorenz Kienle and Claudia Backes for their support and collaboration.

On a related note, I want to thank Alexander Bitter and David Grantz for contributing to my work during their Bachelor thesis and advanced course, respectively.

In order to process, evaluate and interpret data from advanced characterization techniques, it was necessary to acquire some knowledge about these methods, the evaluation process and required programs. For conducting the corresponding workshops, I would like to thank Reinhard Neder, Thorsten Ressler and Robert Dinnebier.

Furthermore, I would like to say a big thank you to Nicole Pienack not only for the never-ending chocolate supply but also for a friendly ear when things went downhill. Also, thank you for helping me with the madness of bureaucracy related to the numerous business trips and providing advice in general.

Moreover, I particularly thank Anna-Lena and Julian Hansen as well as Felix Hartmann and Markus Krengel for the friendly working atmosphere in the office and the lab. It was a pleasure to share an office and/or lab with you. Additionally, I would like to thank Felix for the always productive beam time sessions, despite some 30+ hour shifts.

I further would like to thank the entire working group for a great work climate, many interdisciplinary discussions and suggestions. In this sense, I especially thank Sebastian Mangelsen and Christoph Teske for being greatly interested in some parts of my research and for the resulting valuable discussions and advice.

Things don't always go as planned and this can be frustrating at times. Therefore, I would love to thank my family and friends for bearing my occasional complaints as well as for creating lasting memories during the time of my thesis. Especially the journeys to México and Southeast Asia as well as the annual trips to Föhr will stick in my memory. Without you, it would have been a lot more difficult to sustain the motivation and the perseverance to get this thesis done. Thank you for that!

7.4 Declaration

I declare that this thesis has been composed solely by myself, apart from the advice of my doctorate supervisor Prof. Dr. Wolfgang Bensch, and according to the rules of good research practice of the German Research Foundation. This dissertation has not been submitted, in whole or in part, in any previous application for a degree, nor has it been published or submitted for publication elsewhere. I further declare that none of my academic degrees have been revoked thus far.

Hiermit versichere ich, Jonas van Dinter, an Eides statt, dass ich die vorliegende Dissertation, abgesehen von der Beratung durch meinen Doktorvater Prof. Dr. Wolfgang Bensch, nach Inhalt und Form selbstständig und gemäß den Regeln guter wissenschaftlicher Praxis der Deutschen Forschungsgemeinschaft verfasst habe. Diese Arbeit wurde, weder ganz noch zum Teil, einer anderen Stelle im Rahmen eines Prüfungsverfahrens vorgelegt, veröffentlicht oder zur Veröffentlichung eingereicht. Ferner erkläre ich, dass mir bisher kein akademischer Grad entzogen wurde.

_____ _____

Ort, Datum Jonas van Dinter